ALMA MATER STUDIORUM
UNIVERSITÀ DI BOLOGNA

DOTTORATO DI RICERCA IN

ASTROFISICA

Ciclo XXXVI

Unveiling the dust-obscured activity of the Universe through cosmic time: the view from the ALMA A^{3}COSMOS Survey

Presentata da:
Alberto Traina

Coordinatore Dottorato:
Prof. Andrea Miglio

Supervisore:
Dott. Carlotta Gruppioni

Co-supervisore:
Dott. Ivan Delvecchio

Esame finale anno 2024

Settore concorsuale: 02/C1 – Astronomia, Astrofisica, Fisica della Terra e dei Pianeti

Settore Scientifico Disciplinare: FIS/05 – Astronomia e Astrofisica

Nella quiete della notte
nasce un legame di spiriti,
un'osmosi di anime
si scatena silenziosa.

L'inventore dell'aritmetica
misura il cosmo con gli occhi.
Guidato dalla speranza,
nella volta celeste
si incarna per un
istante:
l'alba di latte e luce
che col suo bianco riflesso
illumina ogni cosa.

— "Sirio", Giuseppe Traina

Abstract

One of the major unknowns concerning the evolutionary history of the Universe is how galaxies form and on what timescales they build up their baryonic mass over time. In order to tackle this topic, much effort has been put in building large samples of galaxies at different redshifts, aiming at reconstructing their evolutionary history at different epochs. In particular, the derivation of statistical quantities, such as the luminosity function and the star formation rate density, has allowed us to track how the overall galaxy population has undergone a transformation across cosmic time, both in demography and in typical luminosity. In particular, a significant fraction of the star formation rate density has been found to come from dust-obscured sources, with large reservoirs of gas and dust. Only in recent years, thanks to the capability of the ALMA interferometer to perform deep blind surveys in the mm/sub-mm it has been possible to study the evolution of dust obscured galaxies fainter than the sub-mm galaxies (SMGs) detected by Herschel and SCUBA-2, and up to $z \sim 6$. The small field-of-view of ALMA, however, has not allowed the community to simultaneously perform wide-area and deep surveys, thus leading to the observation of sparse and heterogeneous samples of galaxies. In order to overcome this limitation, a recent project, the "Automated pipeline for the mining of the ALMA archival images in the COSMOS field" (A^{3}COSMOS), has been developed with the goal of collecting and using all the ALMA archival images in the COSMOS field to perform statistical studies of ALMA selected galaxies.

In this Thesis, we present the method we developed to homogenize the A^{3}COSMOS heterogeneous collection of pointings to be used for statistical studies as well as for deriving evolutionary properties. Indeed, we were able to obtain the infrared luminosity function of star forming galaxies from the A^{3}COSMOS database, in a wide redshift range ($0.5 < z < 6$), finding strong luminosity and density evolution with redshift over the whole redshift range. We therefore derived the dust-obscured star formation rate density, whose redshift evolution seems to suggest that a significant fraction of the star formation occurs in obscured galaxies even at $4 < z < 6$. Comparing our result with predictions from semi-analytical models and simulations, we found that state-of-the-art models struggle in reproducing the bright, star-forming end of the luminosity and star formation rate functions, being unable to predict the existence of the brightest objects, especially at $z > 2$. To further investigate the properties of the A^{3}COSMOS database, we derived the dust mass function and density up to $z \sim 6$, finding a smooth decreasing trend in the dust mass density from $z \sim 1$ to $z \sim 6$. Finally, we characterized the population of AGN host galaxies ($\sim 35\%$ of the sources) in the A^{3}COSMOS, showing on average, similar properties (SFR and stellar mass), and higher redshift than purely star forming galaxies. In future works, we plan to investigate more

deeply the connection between galaxies and super-massive black holes evolution, by deriving the black hole accretion rate density and by tracing its evolution over the wide redshift range covered by the A^3COSMOS sample.

Contents

CHAPTER 1

Introduction

Our Galaxy, the Milky Way (MW) represents an ideal laboratory to perform detailed studies of most of the processes that are taking place in galaxies.

How did it form? How did it evolve to become what it is today?

To understand the evolutionary history of the MW is important to observe and study large number of galaxies at different cosmic time. This would help in the identification of the MW and of other local galaxies progenitors and to trace back their evolution. Understanding how galaxies form and evolve is therefore one of the key question in modern astrophysics, involving complex processes from several physics field. The basis of each study concerning the formation of these objects rely on the type of Universe considered and on the cosmological assumption regulating it. Moreover, galaxy evolution is also linked to the baryon cycle (i.e., how stars form from gas and dust), thus, the obscured star formation can play a key role in the activity of high redshift galaxies. In this Chapter, we will explore and set up the cosmological framework in which the formation of galaxies is thought to occur and we will describe the processes that cover an important role in the formation of the first luminous objects (Section 1.1). Then, in Section 1.4, the main physical and statistical quantities characterizing the evolution of galaxies will be analyzed. In Section 1.2 we will report the main features of galaxies responsible for the bulk of the star formation. In Sections 1.3 and 1.5 we discuss the evolution of dust in such galaxies, as well as the role played by the presence of an AGN inside them. Finally, we will point out the importance of (blind) surveys to perform statistical studies on the evolution of the main physical parameters of galaxies and describe the main goal of this thesis work (Section 1.6).

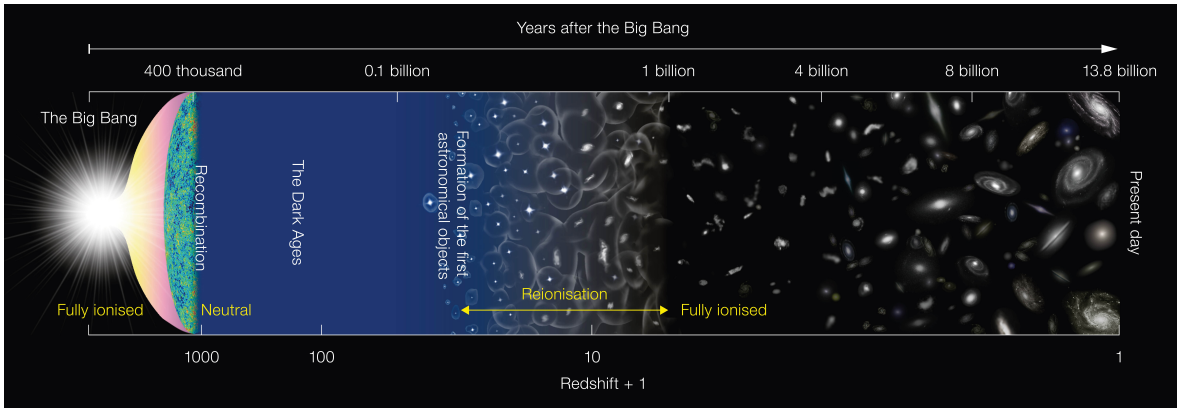

Figure 1.1: Different stages of the Universe evolution, since the Big Bang up to the present day. Credits: Japan National astronomical Observatory (Naoj).

1.1 Cosmological framework: the path to galaxy formation

Nowadays we know galaxies to be a small, but important, piece of a wider Universe picture: indeed they can be seen as luminous points composing the large scale structure of the Universe. In order to characterize the processes and understand the conditions under which galaxy formation could take place, we first need to describe the cosmological framework whose ingredients can lead to the formation of the first structures. The modern view of the Universe is based on two pillars of cosmology, the *Big Bang* and the ΛCDM framework. The combination of the two constitutes what is known as standard cosmology. The main constituents of the Universe in the standard cosmology are baryonic matter, neutrinos, photons, cold dark matter (CDM) and dark energy. Dark Matter weighs as much as 84% of the total matter content of the Universe (Planck Collaboration et al., 2011) and is thought to be made of non relativistic particles only gravitationally interacting with each other and with the other forms of matter. To the previous constituents of the Universe has to be added the dark energy component (Λ), needed to explain the observed acceleration of the Universe. With this in mind, the ΛCDM is described by cosmological parameters determining the geometry of the Universe and the relative contribution of the individual components (5% baryonic matter, 25% DM, 70% dark energy). In this framework, galaxies are the structures resulting from the interaction, across cosmic times, of the different types of matter and energy.

As mentioned before, one of the key "foundation" of the Universe is the Big Bang. The environment of the Universe right after it was a hot bath of fully ionized baryons mixed with photons produced by black body emission (this requires an opacity condition). With the subsequent expansion going on, both temperature and density started to decrease, allowing

the synthesis of the first nuclei to occur. This is known as *primordial nucleosynthesis* and corresponds to the first assembly of matter into nuclei. At this stage, the newly formed gas is ionized, but the constantly decreasing temperature and density permit the formation of neutral atoms (know as *recombination*). With this process, the Universe begins to be transparent (in contrast to the previous opacity), leading to the origin of the *cosmic microwave background* (CMB). With a Universe filled by diffuse neutral gas and DM, it becomes possible to form luminous objects hosted in DM halos. Figure 1.1 shows a sketch representing the key phases of the Universe evolution at different redshift.

It is now fundamental to understand the condition under which a galaxy will form and the main physical processes that make it possible. While, on the one hand, the Universe is expanding, on the other hand the effect of gravity forces matter to act in the opposite direction, tending to aggregate or condense. If in a region of the Universe the gravitational field is sufficiently intense (thus, matter is sufficiently dense) to win against the expansion, DM halos can form. Coupled with the DM pristine, gas is also present in these halos and will fall and settle in their potential wells. However, this is not enough to enable the formation of more compact structures. Indeed, the collapse of gas inside the DM halo should occur rapidly. The collapse is hindered by few factors: the internal pressure and the increase of temperature caused by the densification of the gas work against the collapse itself. Thus, it is important for the gas to cool during this phase and this may happen through the emission of both continuum radiation and spectral lines, favouring the collapse. Chronologically, the first DM halos were sufficiently massive to form the so-called population III (POP III, $M_\star \sim 10 - 1000$ M$_\odot$) stars, but not enough to form more massive objects such as galaxies. The formation of the first galaxies ($z \sim 15$) will indeed originate from DM halos with a minimum mass of 10^8 M$_\odot$, because of the possibility to retain gas and have an extended star formation activity.

The ΛCDM framework for structures formation, predicts a bottom-up scenario, in which galaxies are supposed to form hierarchically (Peebles, 1982): in this scenario, objects with lower masses collapse first and merge with similar ones forming more massive objects. In the hierarchical formation of structures, the initial stages of galaxy formation are governed by the dynamic of DM (well modeled by the so-called N-body simulations, see e.g., Davis et al., 1985; Moore et al., 1999; Springel, 2005; Stadel et al., 2009), which also shapes the subsequent evolution of baryons. Subsequently, physical processes related to the gas component start taking place and dominate the formation of the baryonic part of the galaxy. Mainly, radiative, hydrodynamical and star formation processes affect this moment of the formation and evolution of a galaxy (White and Rees, 1978). Modelling the ensemble of all this processes has revealed to be a very complex task, with a lot of factors to account for (e.g., formation of stars, presence of a black hole, influence of possible feedbacks). Hydro-

dynamical simulations, alongside with semi-analytical models (SAMs) have tried to address these open issues by tracking the growth of galaxies across cosmic time and in large cosmological volumes. Theoretical predictions from cosmological simulations and SAMs set a fundamental ground for both identifying and testing key model predictions against observations.

For instance, studying and interpreting the electromagnetic radiation originated from a galaxy can give us important clues on their formation and evolution. Galaxy light is mostly driven by star-forming processes, which are directly or indirectly traced by stars, gas and dust within the galaxy. In particular, young stars ($\sim 10 - 100$ Myr, see e.g., Hao et al., 2011; Murphy et al., 2011) are traced by ultraviolet (UV) emission, measuring instantaneous star formation. The bulk of the stellar mass, made by sub-solar stars, can be traced using the near-infrared (NIR, $\sim 1 - 3\mu$m). Dust heated by young stars absorbes their light and re-emits it in the infrared band (specifically, in the far-infrared, FIR, $\sim 30 - 1000\mu$m). This opens the possibility to investigate what characterizes the physics of galaxy formation by studying the emission from galaxies and, in particular, by tracing their star formation history, which is crucial to understand their evolution.
In the next Section we will describe the main observational as well as physical properties characterizing the galaxies that are dominating the SFRD contribution (at least at $z < 4.5$), namely the *dusty star forming galaxies* (DSFGs) and the subsample of *submillimeter galaxies* (SMGs).

1.2 Galaxies in the (sub-)mm domain

SMGs are well known to cover an important role in the process of galaxy evolution and their study is crucial to understand the mass assembly of galaxies in the early Universe (see Casey et al., 2014; Hodge and da Cunha, 2020, for reviews). This type of galaxy was firstly discovered using the IRAS telescope in 1983 and became subject of many studies in the next years. They were found to be IR luminous galaxies, with most of them having $10^{11} < L_{\rm IR} < 10^{12} L_{\odot}$, but reaching also higher values ($10^{12} < L_{\rm IR} < 10^{13} L_{\odot}$). Their origin and role in galaxy evolution have immediately been a matter of discussion, because of their extreme luminosities and dust-obscured SFRs, indicating the presence of large reservoirs of dust. Sanders et al. (1988) proposed a scenario in which DSFGs are formed as a result of a wet merger that cause a burst in the star formation in the newly formed galaxy. This scenario has later been furtherly explored and developed also in more recent works (e.g., Hopkins et al., 2008). This process would also fuel the BH growth and, eventually, turns on the AGN activity. Figure 1.7 schematically shows this evolutionary scenario involving a DSFGs phase, after the merger (see Section 1.5 for a more detailed description). The plot highlights

how the brightest quasar phase and the peak of star formation are timely correlated, linking the gas instabilities caused by the merger with star formation and accretion onto the central BH.

1.2.1 Modeling the SED of (sub-)mm galaxies

The IR emission in dust rich galaxies is mainly produced by three constituents: the polycyclic aromatic hydrocarbons (PAH), small grains ($r < 0.01\mu$m) and big grains ($0.01 < r < 0.25\mu$m). These components are responsible for the shape of the IR emission in dusty SF galaxies SEDs. Here we will briefly describe the contribution to the SED by each component.

- ***NIR continuum and PAHs:*** A few percent of the total IR luminosity is emitted in the NIR band, as a continuum between 3 and 5 μm. Since it correlates with the PAH emission (Lu et al., 2003), it is thought to be produced by stochastic heating of PAH or carbon grains (Flagey et al., 2006). It is usually modeled with a grey body emission (da Cunha et al., 2008). The PAHs instead are dominate the SED between ~ 3 and $\sim 13\ \mu$m, with strong emitting features, likely to be produced by excitation due to the absorption of individual UV photons (see e.g., Leger and Puget, 1984; Allamandola et al., 1985; Leger et al., 1989; Allamandola et al., 1999) and are thought to be present outside HII regions, being less affected by the ionizing radiation emitted by stars. This emission is typically modeled by assuming PAH templates spectra.

- ***MIR continuum emission from hot dust:*** Overlapped with PAHs emission, a dust continuum in the MIR is observed. This can be ascribed to small grains, heated by UV photons to high temperatures (Sellgren, 1984) and can be modeled with a multi-temperature grey body (da Cunha et al., 2008).

- ***FIR emission from big grains:*** Big grains are present at lower temperatures, in thermal equilibrium with the radiation field, thus giving us possible informations on the ISM dust temperature. These grains can be present both in the diffuse ISM and in birth clouds, with different temperatures, related to the different radiation fields. This emission is usually modeled with a grey body emission.

Figure 1.2 shows an example of DSFG broad-band SED. The darkgreen (diffuse emission) and limegreen (localized emission) curves are those contributing to the total dust emission (red curve) and are originated as described before. In particular, the inner panel is showing the contribution of different type of grains to the total emission.

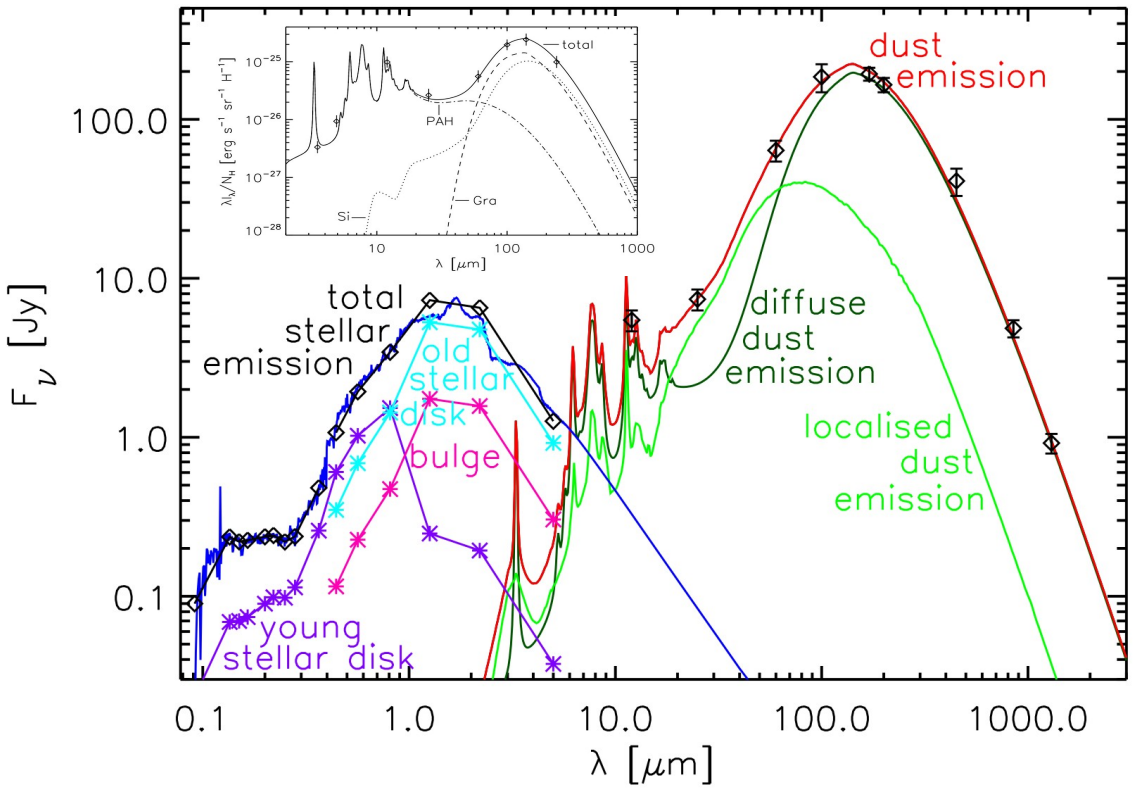

Figure 1.2: Typical SED of a dusty star forming galaxy, with the different components contributing to the total emission, displayed with different colors. In the inner panel, a zoom in the IR part of the SED is reported. Adapted from Popescu et al. (2011).

1.2.2 Observational properties

DSFGs are observed mostly at high redshifts (Ivison et al., 1998): observations in the millimeter regime are favoured in their detection thanks to the negative K-correction (i.e., the conversion from the observed-frame to the rest-frame flux, depending only on the object SED shape) characterizing a DSFG SED in the mm band. This means that the flux density of these galaxies (observed in the mm) increases with redshift, making them easier to detect at high-z rather than at low redshift. They are indeed characterized by a nearly constant brightness from $z \sim 1$ to $z \sim 8$, mainly because of their emission being dominated by a modified black-body (hereafter MBB) peaking at $\sim 100\mu$m, with longer wavelengths being in the Rayleigh-Jeans regime, in which the flux density increases with frequency:

$$S_\nu \propto \nu^{2+\beta}, \tag{1.1}$$

(β is the dust emissivity spectral index: typical values for β are between 1.5 and 2). Figure 1.3 illustrates the K-correction effect on the flux density, in different observing bands, as a function of the redshift. At the shorter wavelengths ($\lambda < 450\mu$m), the flux density steadly decreases with redshift. From $\lambda \sim 500\mu$m to $\lambda \sim 2$mm, the flux densities are characterized by a decrement up to $z \sim 1$ and a flattening towards higher redshifts, varying from $z \sim 6$ up to $z \sim 15$ for longer wavelengths.

Since the discovery of DSFGs, many instruments have been employed in their search and characterization. Most notably, the *SCUBA* telescope helped in the detection of high-z DSFGs, unveiling a population of very luminous ($L > 10^{12.5}$ L$_\odot$) and highly star forming ($SFR > 300$ M$_\odot$ yr^{-1}) galaxies at $\langle z \rangle \sim 2$. The MIPS instrument (working at 24, 70 and 160 μm) onboard of the *Spitzer* observatory identified the so-called highly obscured 24μm sources (see e.g., Yan et al., 2004; Sajina et al., 2008, 2012) and the Dust Obscured Galaxies (DOGs, Dey et al., 2008), which are IR dusty galaxies characterized by an obscured AGN, or an ongoing starburst. The *Herschel* telescope was also important in studying the DSFGs population, with the SPIRE and PACS instruments reaching up to $z \sim 4$. The detection of DFGs also strongly depends on the intrinsic variations in their SED, which is mainly driven by the dust temperature (sub-mm dust temperature selection effect, Blain and Longair, 1996; Blain et al., 2004). In fact, a change in dust temperature can significantly affect the flux density (and the detectability) of a galaxy, since in the sub-mm the flux depends on the dust temperature as: $S_{850} \propto L_{\rm IR} T_{\rm dust}^{-3.5}$ (Chapman et al., 2004; Casey et al., 2009). This effect could create a temperature bias in DSFGs selections. Other properties affecting the SED shape are, for example, the dust distribution and composition, as well as the galaxy structure or the presence of an AGN and its obscuration. These properties can be inferred through SED fitting procedures, by comparing the observed SED shape with model templates (minimizing the χ^2), using a bayesian approach or fitting the FIR SED using MBB

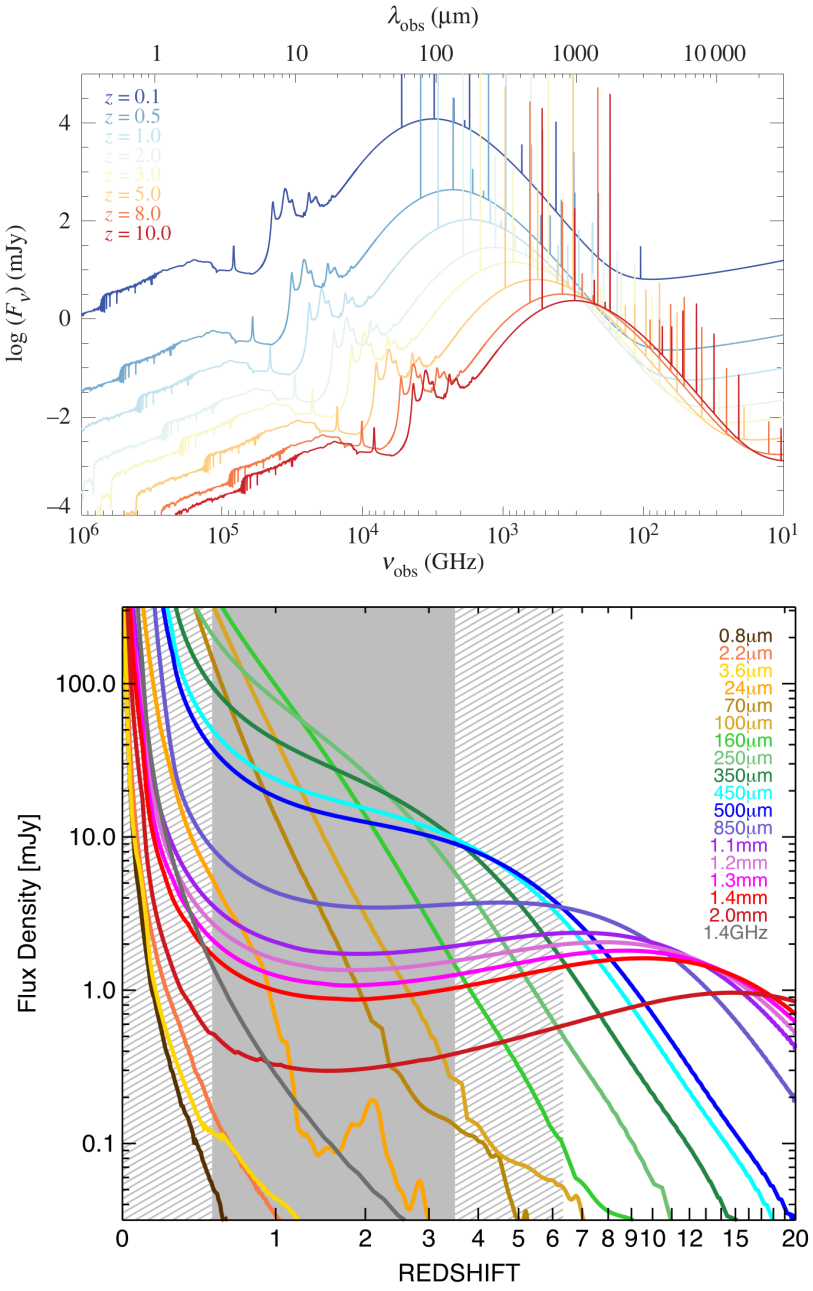

Figure 1.3: *Upper panel:* Same SED at different redshifts, from $z \sim 0.1$ to $z \sim 10$, from Hodge and da Cunha (2020). *Bottom panel:* Flux density at different observing wavelengths and at varying redshift. From Casey et al. (2014).

models.

1.2.3 Physical properties

Studying the physical properties of DSFGs and SMGs is fundamental to understand the extreme nature of these objects and their role in galaxy evolution, as well as to unveil their interplay with BH growth. However, the observations required by these studies are very demanding. As previously discussed, many are the physical properties characterizing star forming galaxies, varying between low and high redshifts. The main physical properties of galaxies observed in the (sub-)mm, in which we are interested for this Thesis are the star formation history (SFH) and SFR, the stellar and dust masses (and dust temperature) and the AGN contribution to the IR part of the SED.

- ***SFR:*** SMGs typically have large SFRs ($> 100\,\mathrm{M}_\odot\ \mathrm{yr}^{-1}$ Swinbank et al., 2014; da Cunha et al., 2015a) and are characterized by short depletion times ($\tau = M_{\rm fuel}/SFR \sim 0.1$ Gyr), even though stellar masses are large ($10^{10} < M_\star < 10^{12}\ \mathrm{M}_\odot$ Simpson et al., 2014; da Cunha et al., 2015a). A possible cause for these extreme episodes of star formation can be found in wet mergers. Depletion times typical of such objects are of the order of ~ 50 Myr (for local galaxies, Solomon and Sage, 1988) and longer ($\tau \sim 100 - 200$ Myr) at higher redshifts (see e.g., Bothwell et al., 2013).

- ***SFH:*** In order to derive other properties as, for example, the stellar mass, several assumptions on the stellar populations as well as on their SFH are required. The latter can be assumed to have different trends with time. The most commonly used are, for example, the exponential decline, the constant one or a SFH consisting of single, or multiple, burst episodes. Different SFHs assumptions can however increase or decrease the mass significantly. A stellar population synthesis (SPS) model also has to be assumed to parametrize the stellar population of the galaxy (Bruzual and Charlot, 2003; Maraston, 2005).

- ***Stellar mass:*** The estimation of the stellar mass takes into account also the IMF of the stellar population (Salpeter, 1955; Chabrier, 2003). All these assumptions can therefore lead to different estimates of the stellar masses, that several works found to be around $M_\star \sim 10^{10} - 10^{12}\ \mathrm{M}_\odot$ (e.g., Borys et al., 2005; Hainline et al., 2011; Michałowski et al., 2012; Béthermin et al., 2013).

- ***Dust properties:*** The longer depletion times observed at high-z suggest larger quantities of gas fueling the star formation (for fixed a SFR). Large quantities of gas also imply the presence of dust, that has to be characterized mainly in terms of temperature and mass. The dust in these galaxies is found to vary in temperature between a

warm and a cold phase ($T_{\rm dust} \sim 20 - 50$K, see e.g., Kovács et al., 2006; Casey, 2012), implying dust masses from $M_{\rm dust} \sim 10^8$ to 10^9 $M_\odot$, at $z \sim 1 - 2$.

1.3 The evolution of dust in galaxies

In the previous Section we discussed the physical properties characterizing the SMGs. The main feature is the presence of large amounts of dust, tightly related to star formation. Studying these objects, from high redshifts to the present days, can give us a trace of the evolution of the dust content of the Universe. The dust emission, which is the UV light absorbed and re-emitted, can be measured in the IR/mm (depending on redshift). By tracing the R-J portion of this MBB emission allows us to compute the dust mass of a galaxy. Several studies have been carried out to investigate in a statistical way how the dust content is evolving with redshift (see e.g., Dunne et al., 2011; Beeston et al., 2018; Driver et al., 2018; Magnelli et al., 2020; Pozzi et al., 2020, 2021): the dust mass function (DMF) and density (DMD) are the key quantities that describe the amount of dust in galaxies within different comoving volumes of the Universe.

Before the advent of the ALMA interferometer, dust emission was traced not further that $z \sim 3$, but ALMA pushed the limit forward to higher redshifts. For example, Dunne et al. (2011) derived the DMD from the *Herschel* ATLAS survey, at $z < 0.5$. Beeston et al. (2018) improved the results at those redshifts combining the ATLAS and GAMA surveys, obtaining constraints on the faint-end slope of the DMF, finding more faint dusty galaxies than previously expected. Driver et al. (2018) studied the DMD in a wide redshift range for the first time ($0.2 < z < 1.5$), while Pozzi et al. (2020) further extended the DMD to $z \sim 2.5$ using *Herschel* photometry. However, all these results are far from being in good agreement to each other.

Using ALMA data, Magnelli et al. (2020) was able to explore the DMD evolution from $z \sim 0.5$ to $z \sim 5$, finding a peak - similar to that of the SFRD - at $z \sim 1 - 3$ followed by a decrease at redshift lower than 1 (in agreement with what was found by *Herschel* works). At $z \sim 5$ Pozzi et al. (2021) studied the DMD from the ALMA ALPINE survey, finding the dust content at that redshift was still relatively high. Figure 1.4 shows a compilation of works devoted to studying the DMD evolution with cosmic time, compared to simulations and models. The general observed trend is an increase of the dust amount from $z \sim 5$ to $z \sim 2$, a broad peak between z 3 and 1, then a decrease toward the local Universe. Few models or simulation are however able to reproduce this trend, in particular, the major discrepancy is in the $z < 1$ range, where the observed DMD shows a drop. Therefore, the dust evolution with redshift needs still to be fully explored, possibly with the same sample ranging from the local Universe, to the higher redshifts. In this thesis, thanks to the nature of the galaxies

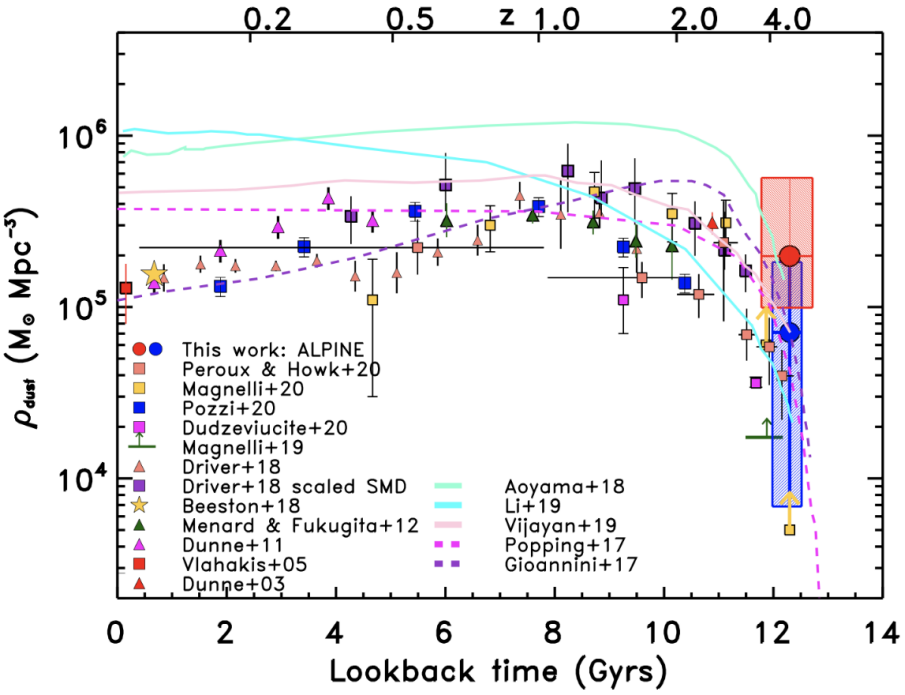

Figure 1.4: Evolution of the comoving dust mass density as a function of the look-back time. Different observational studies are shown with different markers and colors. Curves represent prediction from simulations. From Pozzi et al. (2021).

under investigation, we will explore the redshift evolution of the DMD up to $z \sim 6$.

1.4 The Cosmic Star Formation Rate Density

Studying the star formation is needed to understand how, and at which rate, a galaxy is forming stars. However, using different wavelength tracers implies looking at the light originated by different processes, covering different time scales. In Section 1.4.1 we describe the various methods used to derive the star formation rates of galaxies and the physical processes connected to these methods which are detectable at different wavelengths. In particular, we will mostly focus on the UV, on optical emission lines and on IR tracers, though mentioning also methods using emissions in other part of the spectrum. For an extended review on these topics, we refer to Kennicutt (1998a) and Kennicutt and Evans (2012a).

1.4.1 Star formation tracers

- **UV**

  In the UV range between $\sim$ 1250 Å and $\sim$ 2500 Å, the spectrum light is dominated by

young massive stars and the SFR scales linearly with the UV luminosity. This spectral range is accessible from ground based telescopes at redshifts between $z = 1$ and $z = 5$ (Steidel et al., 1996). At lower redshifts it can be studied using space observatories such as the *GALEX* and the *Hubble Space Telescope*. If we consider a low-mass dominated IMF (e.g., Salpeter, 1955) the UV luminosity of the stellar population is still dominated by the few massive and young O and B stars, characterized by a short lifetime, with their emission lasting a few Myrs. Indeed, considering a typical stellar population, roughly half of the bolometric luminosity radiated over 10 Gyr timescales is emitted in the UV domain during the first 100 Myr (Kennicutt and Evans, 2012a): for this reason, UV light can be used as a SFR tracer of the galaxy. While O stars dominate the emission near 1500 Å for a short time, B and A stars continue emitting for longer times at longer wavelengths ($\sim$ 2500 Å). Other important factors that affect the UV emitted and observed light are the metal enrichment of the stellar population emitting this radiation and the dust extinction caused by the environment surrounding young, newly formed, stars. In particular, a stellar population with a low metal enrichment will produce an higher UV luminosity with respect to a similar population with larger metallicity. For this reason, galaxies with different metallicities should have a different conversion factor to compute the SFR, that accounts for the diverse enrichment. In the same way, also possible different attenuations should be considered. In general we can express the SFR derived by observing the UV emission in the following way:

$$SFR[M_{\odot}\mathrm{yr}^{-1}] = \kappa_{\mathrm{UV}} \times L_{\nu}(\mathrm{FUV})[\mathrm{ergs}^{-1}\mathrm{Hz}^{-1}]. \tag{1.2}$$

The conversion factor κ_{UV} depends on the star formation history (SFH), metallicity and IMF of the stellar populations. The typical value, scaled to a Chabrier (2003) IMF, is 0.77×10^{-28} $\mathrm{M}_{\odot}$ yr^{-1} erg^{-1} s Hz. Therefore, the UV light is potentially one of the best tracers to probe the evolution of the SFR with cosmic time, over a wide redshift range, because it is directly linked to the photospheric emission of young stars. Nevertheless, it is strongly dependent on the IMF of the stellar populations inside the galaxy and on the attenuation caused by the dust present in the interstellar medium (ISM). It can therefore used to trace star formation with several caveats.

- **Emission lines**

  Directly looking at young, massive stars, is not the only way to estimate the star formation. Indeed, the interaction between their light and the surrounding gas can give us important information on the rate at which stars are forming in a galaxy. Optical and near infrared (NIR) emission lines from ionized gas surrounding massive

stars ($M_\star > 15\mathrm{M}_\odot$, with a peak between 30 and 40 $\mathrm{M}_\odot$) probe the young and massive stellar population and provide an instantaneous measure of the star formation rate, with time scales of $3-10$ Myr. Thanks to spectroscopic suveys, it is nowadays possible to derive an emission line based SFR for large samples of galaxies. Several are the lines that can be used as tracers for the SFR. The best indicator in the local Universe, as well as in the high-z Universe, is the Hα line:

$$SFR[M_\odot \mathrm{yr}^{-1}] = \kappa_{\mathrm{H}\alpha} \times L(\mathrm{H}\alpha)[\mathrm{ergs}^{-1}\mathrm{Hz}^{-1}], \tag{1.3}$$

where $\kappa_{\mathrm{H}\alpha}$ is the conversion factor (e.g., $\sim 7.9 \times 10^{42}$ $\mathrm{M}_\odot$ yr^{-1} erg^{-1} s Hz, for a Salpeter IMF). The main feature of the Hα as a tracer of SFR is that it can trace high mass, young, stars with low observational effort, both in the local and distant Universe, as it is produced with the HII recombination in nebular regions.

Other line tracers are, for example, the [O II] forbidden line at 372.7 nm and the Lyα line at 121.6 nm. The former is ideal for intermediate redshift galaxies because it falls in the optical regime. However, it is affected by systematics in its measure since it is strongly affected by dust extinction and the estimates are less accurate than those obtained through Hα. The [O II] SFR can be computed as following:

$$SFR[M_\odot \mathrm{yr}^{-1}] = \kappa_{[\mathrm{OII}]} \times L([\mathrm{OII}])[\mathrm{ergs}^{-1}\mathrm{Hz}^{-1}], \tag{1.4}$$

with $\kappa_{[\mathrm{OII}]} \sim 1.4 \times 10^{-41}$ $\mathrm{M}_\odot$ yr^{-1} erg^{-1} s Hz (for a Salpeter IMF). At high-z, the Lyα enters the optical observed range, and can as well trace the SFR, although it is subject to quenching processes and dust attenuation.

- **IR**

  The UV light produced by young stars, directly tracing the star formation within a galaxy, interacts not only with the gas inside the galaxy, but also with the dust present in star forming regions and diffuse in the whole galaxy. Dust can absorb a large fraction of the luminosity of a galaxy, with its absorption cross-section peaking in the UV. The UV radiation, absorbed by dust, is then thermically re-emitted at longer wavelengths, in the far infrared (FIR) continuum, tipically between 10 and 300 μm, since dust behaves like a black (grey)-body. With the peak of absorption being in the UV, dust emission can then be used as a tracer of the radiation emitted by the young stellar population and, thus, of the SFR. The simplest case in which dust emission directly traces the SFR is under the assumption that only the massive and young stars heat the dust and that the dust opacity is high ($\tau >> 1$). However, in a more realistic case, dust heating can have different origins. Indeed, the emission from warm dust (peaking around $\lambda \sim 60 - 70\mu$m) heated by young stars, is often coupled with a

cooler, more diffuse, dust emission (peaking at $\lambda \sim 100\mu$m) originating from dust heated by the diffuse radiation field in the ISM. In late-type star forming galaxies, the dust emission dominates the $40 - 120\mu$m part of the spectrum and the IR SFR well correlates to the UV and line-based SFRs. In early-type galaxies dust is mainly present in the cooler phase, with the continuum emission - if present - originating form the diffuse stellar radiation field. Other sources of contamination can however be old stars radiation and AGN radiation field. Considering a Salpeter IMF and the luminosity emitted by the dust in the IR between 8 and 1000 μm, the SFR can be computed as:

$$SFR[M_{\odot}\mathrm{yr}^{-1}] = \kappa_{\mathrm{IR}} \times L(\mathrm{IR})[\mathrm{ergs}^{-1}\mathrm{Hz}^{-1}], \tag{1.5}$$

with the conversion factor κ_{IR} having a typical value of 4.5×10^{-44} $\mathrm{M}_{\odot}$ yr^{-1} erg^{-1} s Hz. We now need to understand how to observe and measure the dust continuum. The ideal way would be to fit a dust emission template to observed photometric points just in the MIR/FIR spectral range. However, this method requires the coverage of a wide photometric range in the IR. Otherwise, it is possible to use spectral energy distribution (SED) fitting to reproduce the FIR emission even without having a dense coverage of the IR bands, and reproducing the dust continuum based on the the stellar attenuated emission. Even though this approach could be very powerful in determining the dust emission, on the other hand to model the dust component in SED fitting codes is not straightforward. Dust can indeed be found in a galaxy in different phases, related to its temperature. The bulk in mass of the dust component is found to have a cold temperature (15-60 K), with emission strongly contributing in the sub-millimetric regime ($\lambda \sim 30 - 1000\mu$m) even if its emission is not dominating the IR SED. The MIR continuum can instead be dominated by hotter dust, with the presence also of features produced by PAH and absorptions from silicates, as well as the steep continuum originated from the AGN heating. Combining a good photometric coverage with SED fitting techniques will enable to characterize the dust emission accurately. The only facility that provided deep data in the FIR domain for large number of galaxies is the *Herschel Space Observatory*, with an improved capability of detecting dust in galaxies with respect to it predecessors, *IRAS*, *ISO* and *Spitzer*. *Herschel* was able to trace the dust emission over a wide wavelength range ($70 - 500\mu$m), allowing the detection of dust in galaxies at redshifts las high as $z = 4$. To detect dust at higher redshifts, longer rest-frame wavelengths are needed. The Atacama Large Millimeter Array (ALMA) offers the unique possibility to sample the sub-mm range with very low exposure times, allowing the acquisition of dust emission photometry very quickly. In this way, it is possible to observe dust emission even in very high-z galaxies (up to $z \sim 10$).

- **Other tracers of the SFR**

  In addition to the discussed methods, star formation can be traced also by observations at other wavelengths such as the radio or the X-rays. The radio emission of galaxies is typically composed by a flat free-free component plus a synchrotron emission component. Synchrotron emission from star formation is produced by cosmic ray electrons that are accelerated by shock waves when massive stars explode as SNe, and typically dominates at low frequencies ($\nu < 15$ GHz, assuming a M82 template; e.g., Condon, 1992; Murphy, 2009). Radio synchrotron emission can therefore be used as a SFR tracer (e.g., Bell, 2003), since the number of SNe is related to the SFR of the host, averaged over timescales of 10-100 Myr Murphy (2009). On the opposite side of the spectrum, the hard X-ray emission in star forming galaxies not hosting an AGN is dominated by X-ray binaries, SNe and SNe remnants, which, as for the radio, can be used as tracers of the SFR (see e.g., Ranalli et al., 2003; Mineo et al., 2012a,b; Vattakunnel et al., 2012; Symeonidis et al., 2014; Lehmer et al., 2016).

We described how different observing bands can trace the formation of stars in a galaxy, through direct measurements of the UV light from young stars or detecting its interaction with the ISM (emission lines) and dust (FIR re-emitted radiation). However, when measuring the SFR of a galaxy, one should take into account both the unobscured and obscured component of the star formation. Figure 1.6 shows the effect of correcting for dust attenuation in the UV SFRD estimates. At redshift lower than $z \sim 3$, IR dust-obscured SFRD has a significantly higher normalization than what the UV uncorrected measures. Applying dust attenuation corrections to the UV data (right panel) contribute to address the total SFRD contribution. UV light alone cannot indeed trace the fraction of stars hidden by dense dusty regions, that is instead traced by the IR emission. The total SFR will be computed as:

$$SFR_{\rm TOT} = SFR_{\rm UV} + SFR_{\rm IR} \tag{1.6}$$

with $\kappa_{\rm UV}$ and $\kappa_{\rm IR}$ being the luminosity to SFR conversion factors. UV estimates of the SFRD should then take into account dust attenuation and correct for it to determine the total SFRD.

1.4.2 The luminosity function and its evolution

Tracing back in time the rate at which galaxies are forming stars is a task that requires a large number of data from galaxies at different redshifts, allowing for the derivation of the main statistical properties characterizing galaxy evolution, such as the luminosity function (LF) and star formation rate density (SFRD). Combining the distance information with the galaxies flux it is possible to derive the LF. One of the method that permits to derive the LF

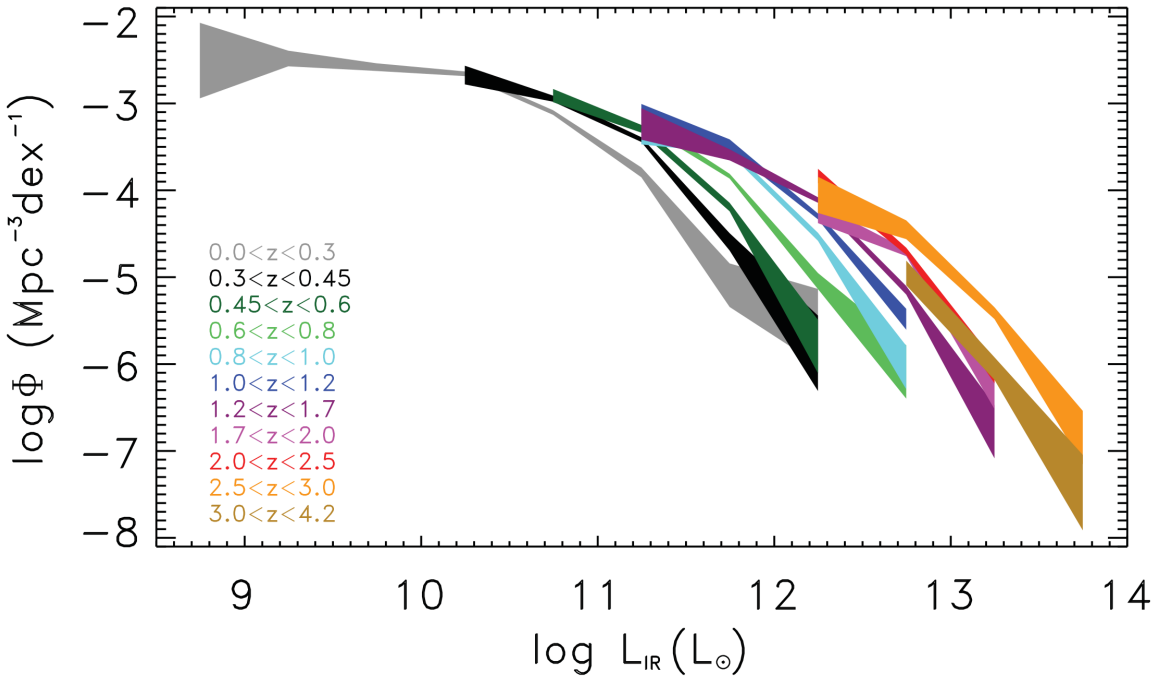

Figure 1.5: Infrared 8-1000 μm luminosity functions at $0 < z < 4.2$, from Gruppioni et al. (2013).

is the well known $1/V_{\rm MAX}$ method, where $V_{\rm MAX}$ is the maximum co-moving volume. For each object, it can be computed as:

$$V_{\rm MAX}(i) = \int_{\Omega}\int_{z_{\rm min}(i)}^{z_{\rm max}(i)} \frac{d^2V}{d\Omega dz} d\Omega dz \tag{1.7}$$

with $z_{\rm min}(i)$ and $z_{\rm max}(i)$ being the minimum and maximum redshifts at which the $i-th$ source is available to be observed in a certain survey. Once the V_{MAX} has been computed, the LF in a z and L bin is given by:

$$\Phi(L,z) = \frac{1}{\Delta logL}\sum_{i=1}^{n_{obj}} \frac{1}{V_{\rm MAX}(i)} \tag{1.8}$$

A typical LF can be modeled using a Schechter function (Schechter, 1976) or a double slope Schechter function (also known as modified Schechter, Saunders et al., 1990a), that is able to reproduce the bright-end found in IR-based works:

$$\Phi(L)dlogL = \Phi^* \left(\frac{L}{L^*}\right)^{1-\alpha} exp\left[-\frac{1}{2\sigma^2}log_{10}^2\left(1+\frac{L}{L^*}\right)\right] dlogL \tag{1.9}$$

The slopes of the faint and bright-ends are parametrized by α and σ, respectively. Φ^* and L^* are instead the normalization and typical luminosity of the population, at a certain redshift and represent the so-called knee of the LF. As it can be seen from figure 1.5, that shows the IR LFs from $z \sim 0.15$ to $z \sim 4$, derived by Gruppioni et al. (2013) using the

PEP/HerMES *Herschel* survey, the knee of the LF is not constant with z, but Φ^* and L^* are evolving with cosmic time. In particular, the normalization, representing the number density of galaxies, is decreasing towards higher redshifts. At the same time, the typical luminosity is increasing in the high-z Universe. This means that moving to the earlier Universe, galaxies were in average more luminous, though less in number, than the local Universe.

1.4.3 The evolution of the star formation rate density

To this end, several surveys have been carried out in the past years, collecting a vast quantity of multi-wavelength data. In particular, surveys in the UV, IR, radio as well as surveys aimed at detecting emission lines have been carried out to investigate the evolution of the SFR with cosmic time. Pioneering studies in the UV have been done by Lilly et al. (1996), Madau et al. (1996), Sawicki et al. (1997), Madau et al. (1998), and Steidel et al. (1999), using large as well as deep surveys to derive the SFRD at redshift $0 < z < 4$. Several recent studies pushed the redshift limits towards higher values (see e.g., Ono et al., 2018; Bouwens et al., 2021, 2022) and, recently, with the James Webb Space Telescope (JWST) even at extreme redshifts ($z \sim 10$, Harikane et al., 2023).

IR surveys have also been carried out to derive IR LFs and SFRD. The first results in the local Universe came from IRAS (Lawrence et al., 1986; Soifer et al., 1987; Saunders et al., 1990b; Rush et al., 1993; Shupe et al., 1998; Sanders et al., 2003) finding the existence of galaxies whose output is dominated by IR emission and also finding the IR LF to be modeled by a modified Schechter functional form, that is able to reproduce the bright-end (which is likely to be dominated by sources with warm dust content, likely being starburst and hosting AGNs). Other studies have been performed in the following years using the *Spitzer* and the *Herschel* observatories improving the knowledge on the IR LF evolution (Pérez-González et al., 2005; Magnelli et al., 2009; Gruppioni et al., 2010; Rodighiero et al., 2010; Gruppioni et al., 2013; Magnelli et al., 2013). *Herschel* works by Gruppioni et al. (2013) and Magnelli et al. (2013) were able to trace the IR LF up to redshift 4.5 and 2.5, respectively, studying the evolution of the main parameters characterizing the IR LF (i.e., the density and luminosity at the knee of the Schechter function). More recentely, the ALMA interferometer allowed us to push the z limit even further ($z > 5$, e.g., Gruppioni et al., 2020; Zavala et al., 2021a; Traina et al., 2024), though finding non-univocal results on the high$-z$ dust-obscured SFRD.

All the efforts put in collecting data for large samples of galaxies in surveys has led to a great quantity and variety of estimates of the SFRD. As highlighted below (see details from the review of Madau and Dickinson (2014)), a coherent picture of the SFR evolution up to $z \sim 3 - 4$ has emerged from the combination of dust-corrected UV and IR surveys

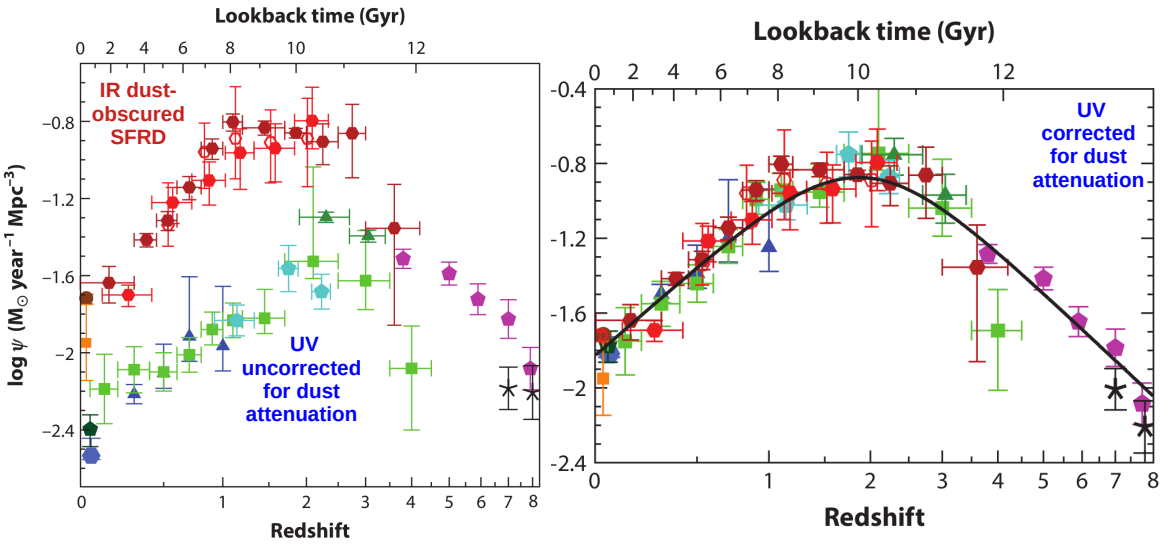

Figure 1.6: UV (blue, green and purple points) and IR (red points) star formation rate density. Both left and right panels show the SFRD evolution with the redshift. In the left panel, UV estimates uncorrected for dust extinction are reported, while the right panel shows the same data but corrected for dust attenuation. Adapted from Madau and Dickinson (2014).

(see Figure 1.6). At higher redshifts, the smaller amount of data has not allowed to put concordant constraints on the SFRD evolution, since large errors characterize the estimates, also finding different trends mostly due to observing biases or corrections difficult to be applied.

In the local Universe, well established SFRD values have been found by Salim et al. (2007) and Robotham and Driver (2011) in the UV, using the GALEX Medium Imaging Survey (1000 deg^2) and in the IR with IRAS (see e.g., Sanders et al., 2003; Takeuchi et al., 2003). These latter studies however struggle in determining the faint-end slope of the IR-LF. The use of the *Herschel* telescope has overcome this problem, at least at low redshift (Eales et al., 2010). At redshifts $0 < z < 1$, several works have been able to characterize the SFRD, thanks to the great availability of data (e.g., Cucciati et al., 2012 in the UV, Magnelli et al., 2009; Rodighiero et al., 2010; Gruppioni et al., 2013 for the IR), finding a steep decline of the SFRD from $z = 1$ to $z = 0$. At higher redshifts ($1 < z < 4$), deeper surveys are needed, especially to probe the knee of the luminosity function and the faintest luminosities. Some fields are particularly well suited for studying high-z LFs, because of their excellent spectroscopic and multi-wavelength coverage. Using the Lyman-Break Galaxies (LBGs) surveys, Reddy and Steidel (2009) were able to trace the UV-LF at $z = 2 - 3$.

At $0 < z < 4$, in the IR bands, the major results on the SFRD evolution are due to *Spitzer*

and *Herschel*, mainly in the GOODS and COSMOS fields, tracing directly the emission from dust in galaxies, but unable to constrain with data the faint-end at $z > 2$. In particular, at $z < 2.3$, Magnelli et al. (2011) derived the SFRD using deep 24 and 70 μm *Spitzer* imaging of the GOODS North and South fields, finding an initial increase and a subsequent flattening of the SFRD, from $z \sim 0$, to $z \sim 2.3$. The same redshift range has been explored by Magnelli et al. (2013), using the PACS instrument onboard of *Herschel* to observe the GOODS field and finding consistent results with the previous study. Exploiting the data of the *Herschel*/Multi-tiered Extragalactic Survey (HerMES Oliver et al., 2012), Gruppioni et al. (2013) were able to derive the IR LF and SFRD up to $z \sim 4$. The results are in agreement with those by Magnelli et al. (2011, 2013), showing a steep increase in the SFRD towards $z \sim 1$ and a flattish behaviour at $1 < z3$, with a decrease at $z > 3$ (traced by an upper-limit at $z \sim 3-4$). Overall, these works have underlined the presence of a broad peak of the star formation rate density, the so-called *cosmic noon*, between $z \sim 1.5$ and $z \sim 3$.

Finally, the higher redshift frontier ($z > 4$) have been mostly explored by UV-based works, exploiting the HUDF and GOODS fields, with HST deep observations being able to reach faint magnitudes, allowing to trace the faint-end even at $6 < z < 8$). Only in recent years the IR-mm studies have succeed in estimating the IR-LF and SFRD at these redshifts. For example, Gruppioni et al. (2020) derived the SFRD in a wide $0.5 < z < 6$ range, thanks to the ALMA observations in the COSMOS field, with the ALPINE survey (Béthermin et al., 2020; Faisst et al., 2020; Le Fèvre et al., 2020). This study has underlined a possible scenario for the evolution of the SFRD with cosmic time, in which, even at $z > 3-4$, the amount of SFR in the Universe is significant and dominated by dusty star-forming galaxies.

The main highlights on the evolution of the SFRD obtained from past surveys can be summarizes as follows:

- the local Universe is mostly populated by galaxies having low SFR, indicating a very small activity in star production by today's galaxies;
- going back in time to $z \sim 1$, the SFR density is found to be quickly increasing by ten times, with a broad peak at $1.5 < z < 3$;
- at $z > 3$, many UV studies point toward a decline of the SFRD with z, though some IR estimates claim a flattening or less steep decrease towards higher z.

At $z > 4$ the lack of data and the lower information on the dust attenuation makes the total SFRD estimates less robust. For this reason, any attempt to enrich the wealth of data aimed at reducing our unknowns on SFRD is worth to be done, since more studies in this field are still needed, especially in the characterization of the distant Universe.

1.5 The role of Active Galactic Nuclei

A key in the study of DSFGs is the AGN presence and the effects of its activity in the host galaxy. This is because a significant fraction ($\sim$ 30 %) of the BH growth is likely to occur in an obscured accretion phase (Treister et al., 2010). In particular, obscured AGN are active galaxies classified as Type 2, namely sources for which the line-of-sight intercepts the obscurig material, which can either be the dusty torus (a "toroidal" structure surrounding the SMBH) or the gas and dust present in the galaxy itself (Gilli et al., 2022). Obscured AGN can be divided into different classes based on the amount of material that provides the obscuration (i.e. the absorbing column density, $N_{\rm H}$). If $N_{\rm H} < 10^{22}$ cm^{-2}, the AGN is called unobscured; if $N_{\rm H} > 10^{22}$ cm^{-2} the obscured AGN is classified as Compton-thin; if $N_{\rm H}$ is higher than 10^{24} cm^{-2}, is defined as Compton-thick. Moreover, from X-ray analysis, $\sim$ 20% of SMGs are found to host an AGN (Laird et al., 2010; Georgantopoulos et al., 2011; Johnson et al., 2013; Wang et al., 2013). Despite this, many AGN may be enshrouded in such large quantities of dust, making them undetectable even through X-ray observations (Gilli et al., 2022). The activity from an AGN is known to be triggered and powered by accretion onto the supermassive black hole (SMBH) at the center of the host galaxy. A possible scenario for the AGN-galaxy co-evolution, has been proposed by Hopkins et al. (2008) (see Figure 1.7). In this evolutionary scenario, the formation of SMBHs and the activity is supposed to be part of a galaxy life-cycle. In particular, as it can be seen in Figure 1.7, isolated galaxies can interact with nearby galaxies through mergers. The merger can either be wet or dry: the former is present when galaxies rich of gas (at least one of the two galaxies); the latter can occur when the merging galaxy are almost gas-free. The fraction of mergers is thought to be higher at high redshift. The merger can cause gas inflow toward the inner region of the newly formed galaxy structure. In regions with high gas density, star formation processes can take place and, if the gas reservoir is large, the galaxy can be classified as a starburst galaxy. If a large amount of gas moves toward the nuclear region, the accretion onto the SMBH could start, favoring its growth and a subsequent activity as an AGN. Finally, in the quasar stage, the nuclear activity can contribute to end the star formation, leading to a quiescent galaxy, ending the "cycle".

The properties of SMBH are not independent from the surrounding environment, as suggested by the tight correlations between SMBH mass and a number of host properties (stellar velocity dispersion, galaxy bulge mass, see, e.g., Magorrian et al., 1998; Ferrarese, 2002; Kormendy and Ho, 2013). In addition, the evolution of galaxies (Thomas et al., 2010a) and AGN (Ueda et al., 2003) seems to follow a similar antihierarchical behaviour called downsizing. In the downsizing scenario, massive galaxies formed earlier and faster than their lower mass counterparts; on the other hand, in the same way, more powerful AGN,

coupled with more massive BH, grew up at earlier times. Another important aspect of such AGN-galaxy "co-evolution" is the co-existence of both AGN-driven and star formation-driven emission within individual sources. Indeed, an additional non-stellar component from an AGN may be needed to reproduce the observed broad-band SED, as well as to explain the integrated properties of the host. In this perspective, the study of the accretion of material onto the SMBH, as well as their growth with cosmic time is crucial. To this purpose, tracing the BH accretion rate density (BHARD) and compare its evolution with redshift with that of the SFRD can provide insightful clues in understanding the interplay between SMBH and galaxy growth through cosmic time.

Most of the galaxies contributing to the SFRD, especially at high redshift, are in the so-called phase of obscured accretion (Vignali, 2014), meaning that part of both the SF and AGN emission is enshrouded by large amounts of dust and gas. Although X-rays is commonly used to select AGN, it can be affected by obscuration, especially in the softer bands. Therefore, X-ray surveys are likely incomplete at high redshifts, missing the most obscured sources. Since the obscured radiation is re-emitted in the IR and mm bands, longer wavelength selection is less biased by dust obscuration than X-rays. In this context, a powerful tool to investigate the evolution of galaxies (and AGN) is the analysis of large samples of IR or sub-mm selected sources, using their observed broad band photometry to reconstruct the SED. A multi-wavelength survey of star-forming galaxies spanning a wide redshift range of the observed galaxies is well suited for these studies. Moreover, as shown in Figure 1.8, some of the theoretical predictions by model are not in agreement with observational results. In particular, X-ray BHARDs (Ueda et al., 2014; Vito et al., 2014; Aird et al., 2015; Vito et al., 2018) find a peak at $z \sim 1.5$ and an evident decrease towards higher redshifts. On the other hand, simulations, if including dark matter halos with a range of different masses (e.g., Lodato and Natarajan, 2006; Volonteri and Begelman, 2010; Shankar et al., 2013; Sijacki et al., 2015; Volonteri et al., 2016) find a peak at higher redshifts ($z \sim 3$) and much higher values at $z > 3$. However, Volonteri et al. (2016) and Bonoli et al. (2014) have estimated the BHARD by considering the massive end of the DMH distribution only and are able to reproduce high-z X-ray observations. Nevertheless, IR studies at $z > 3$ will be fundamental to trace a BHARD unbiased from obscuration, as for now the estimates by Delvecchio et al. (2014) extends up to $z \sim 3$.

1.6 Goal of this Thesis

As it was described throughout the previous Sections, there are many processes undergoing in the evolutionary history of a galaxy, depending on their environment, on their mass and on the presence of a SMBH at their center, whose possible activity is crucial for the host

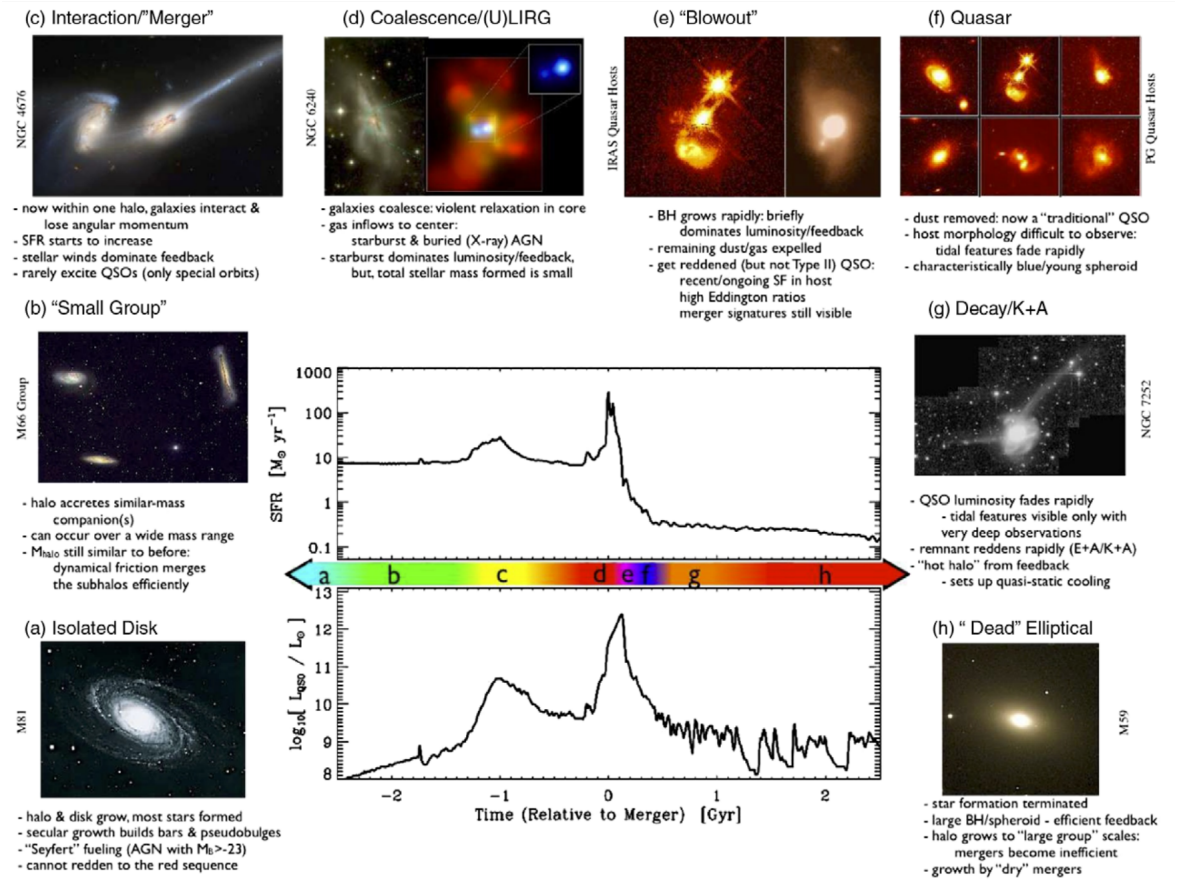

Figure 1.7: Evolution of galaxy scenario, in which the key role is played by wet mergers, leading to star forming processes and BH fueling. The cycle begins with isolated galaxies merging and experiencing bursts of star formation, with a subsequent quasar phase until the star formation quenches. The central plot shows the SFR (upper panel) and quasar luminosity (bottom panel) trends with the time relative to the merger. Taken from (Hopkins et al., 2008).

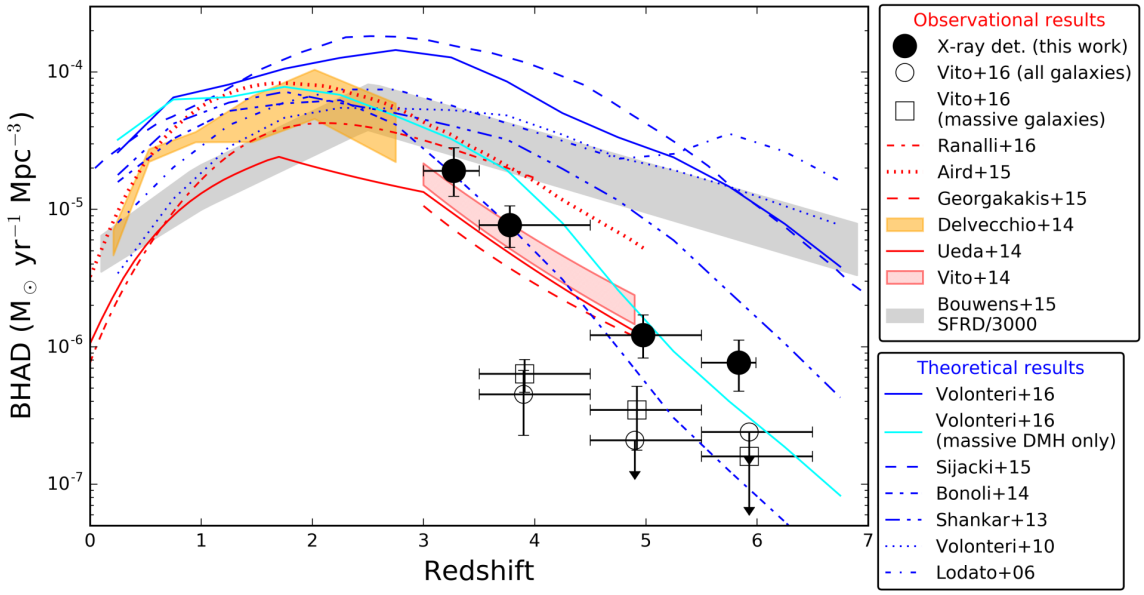

Figure 1.8: BHARD theoretical and observational estimates. The blue and cyan curves represent the theoretical results from different simulations (Lodato and Natarajan, 2006; Volonteri and Begelman, 2010; Shankar et al., 2013; Bonoli et al., 2014; Sijacki et al., 2015; Volonteri et al., 2016). Observational results obtained in the IR and X-ray are instead shown as the orange shaded area (Delvecchio et al., 2014), black filled and empty circles and square (Vito et al., 2016, 2018), red lines (Ueda et al., 2014; Aird et al., 2015; Georgakakis et al., 2015; Ranalli et al., 2016) and the red shaded area by Vito et al. (2014). The rescaled SFRD by Bouwens et al. (2015) is reported as a comparison. Taken from Vito et al. (2018).

galaxy. In the past years, these processes have been explored in great detail, using large samples of galaxies across different cosmic epochs and with several facilities working at different observing bands, but, despite this, key questions on how galaxies evolve are still open. Among these, understanding how the SFRD is evolving at the highest redshift is fundamental to trace back the evolution of galaxies. In particular, it is still unclear if the evolution of the SFRD at $z > 3 - 4$ is characterized by a decrease (steep or smoother) or if it stays flat also at these redshifts. Indeed, recent works by different groups seem to suggest various scenarios for its evolution at $z > 5$, favoring, or not, the existence of large quantities of dust in galaxies even at those redshifts (see e.g., Zavala et al., 2021a). In order to deepen and, possibly, to shed light on this tension, large samples of star-forming galaxies at different cosmic epochs (covering a wide redshift range) have to be studied, and their statistical properties (i.e., LF, SFRD) derived. To this purpose, in this Thesis, we exploited the "Automated pipeline for the mining of the ALMA archival images in the COSMOS field" (A^{3}COSMOS) to obtain, for the first time, the IR-LF, the dust-obscured SFRD and the dust mass density from the ALMA archive. Indeed, the ALMA selection ensure us to study dust-rich, star-forming galaxies, from the local Universe up to $z \sim 6$, allowing us to derive the aforementioned statistical quantities over a broad redshift range.

The main goal of this Thesis work is to obtain a deep and statistically significant sample of sub-mm/mm galaxies to be used to derive the evolutionary properties of DSFGs over a wide range of redshifts (0-6) and SFRs. The sample should have a well now selection function and completeness curve, and the main physical parameters of each sources should be derived. Here we show how we have obtained the sample used in the work from the pointed and heterogeneous ALMA archival survey A^{3}COSMOS. Here we present the investigation of the main physical and statistical properties of a sample of ALMA-selected galaxies observed in the COSMOS field, as part of the A^{3}COSMOS survey, how its areal coverage has been constructed and how the sources have been identified and their main physical properties derived.

This Thesis is structured as follows. In Chapter 2 we will describe the main features of the ALMA interferometer and how the survey has been built. In Chapter 4 we derive the A^{3}COSMOS IR-LF and dust-obscured SFRD, while in Chapter 5 we compare it to the UV estimates as well as to predictions of semi-analytical models and hydrodynamical simulations. In Chapter 6 we investigate the dust properties of the sample, deriving DMF and DMD. The AGN properties of the A^{3}COSMOS galaxies are presented in Chapter 7. Finally, in Chapter 8 we discuss some possible future perpsectives and follow-up of this work.

CHAPTER 2

The A^{3}COSMOS survey

In this Chapter we describe the main features of the ALMA interferometer, the A^{3}COSMOS survey and the method developed to uniform the heterogeneous pointings from the ALMA archive and to obtain the number counts in the different ALMA bands. In Section 2.1, we briefly introduce and describe the ALMA interferometer and its main characteristics. The pipelines and the sources extraction are described in Section 2.2. In Section 2.3 we will describe the recent updated version of the A^{3}COSMOS by Adscheid et al. (2024), the method to reduce possible biases (Section 2.3.1) and the derived number counts (Section 2.3.2) The ALMA interferometer has proven to be a powerful instrument to study dust emission and star forming galaxies. However the field of view (FOV) of ALMA observations is too small to observe wide sky areas and perform deep surveys at the same time, making it difficult to collect data for large sample of galaxies. Indeed, the $FWHM$ of the ALMA primary beam (which can be used as the diameter of the FOV) is between 19" and 33", depending on the observing frequency (but being independent on the observing array configuration). Nevertheless, a number of contiguous deep field ALMA surveys have been carried out in the past years (Hatsukade et al., 2011; Carniani et al., 2015; Aravena et al., 2016; Hatsukade et al., 2016; Walter et al., 2016; Dunlop et al., 2017; Franco et al., 2018a; Hatsukade et al., 2018a), that were able to study small samples of galaxies. On the other hand, the number of individual ALMA observations is continuously increasing: the ALMA archive grows day-by-day, collecting data on large sample of galaxies with a big variety of properties at different epochs, with a total covered area of hundreds arcmin^2. Although the collection of individual pointings suffers from the discreteness of the field of views, leading to selection biases and unpredictable cosmic comoving volume, the variety of data collected on different galaxies allows to widely study several physical properties and processes affecting galaxy formation and evolution. Some studies have already explored the ALMA archive (see e.g., Fujimoto et al., 2017; Scoville et al., 2017; Zavala et al., 2018), but the inhomogeneity of the data affects the outcomes of these analysis. Homogenize the evergrowing ALMA

archival data will lead to the construction of statistically significant samples to study galaxy evolution from a new point of view. With the goal of building an homogeneous set of observations from the ALMA archive, Liu et al. (2019b) developed an automated pipeline for the mining of the ALMA archival images in the COSMOS field (hereafter A^{3}COSMOS).

2.1 The Atacama Large Millimeter Array (ALMA)

The ALMA interferometer, located on the Chajnantor plateau (at 5000 meters), led to a remarkable leap in quality for studying the dusty Universe, with respect to its predecessors, since 2011. The significant height above the sea level and the geographycal location are perfect for (sub-)mm observations, because of the dry atmospherical conditions, with a very low precipitable water vapour percentage. The total number of antennas constituting the ALMA interferometer is 66, of which 54 have a 12 m dish and 12 with a diameter of 7 m. 50 out of 54 12 m antennas are part of the main array, that can be reconfigurated for different observational necessity. The remaining four are instead part of the Total Power Array (TPA). The 12 7 m antennas compose the Atacama Compact Array (ACA).

The main capabilities of ALMA can be ascribed to the following technical quantities: angular resolution, frequency coverage, bandwidth and sensitivity. The *angular resolution* of an interferometer depends on the possible configurations available for the individual antennas. In the case of ALMA, the reconfiguration of the main array allows for a resolution between few arcseconds and 0.01". This angular resolution allows one to perform detailed studies of the star forming regions in galaxies even at high redshifts. The frequencies covered by ALMA are from 35 to 950 GHz (corresponding to ~ 8600 and $\sim 310\mu$m), divided into 10 bands (8 of which are fully operating). This wavelength range is perfectly suited for studying the dust emission in high redshift galaxies (sampling the peak and the Raileigh-Jeans par of their SED). ALMA can also perform spectral scans, useful to measure the redshifts of distant dusty galaxies, thanks to the complementary bandwidth of the ALMA bands. Finally, a significant upgrade, with respect to previous facilities, has been made thank to the sensitivity ALMA can reach (see Figure 2.1). In particular, it can be 10-100x better in the continuum and 10-20x for lines. This improvement makes it possible for ALMA to detect much fainter galaxies.

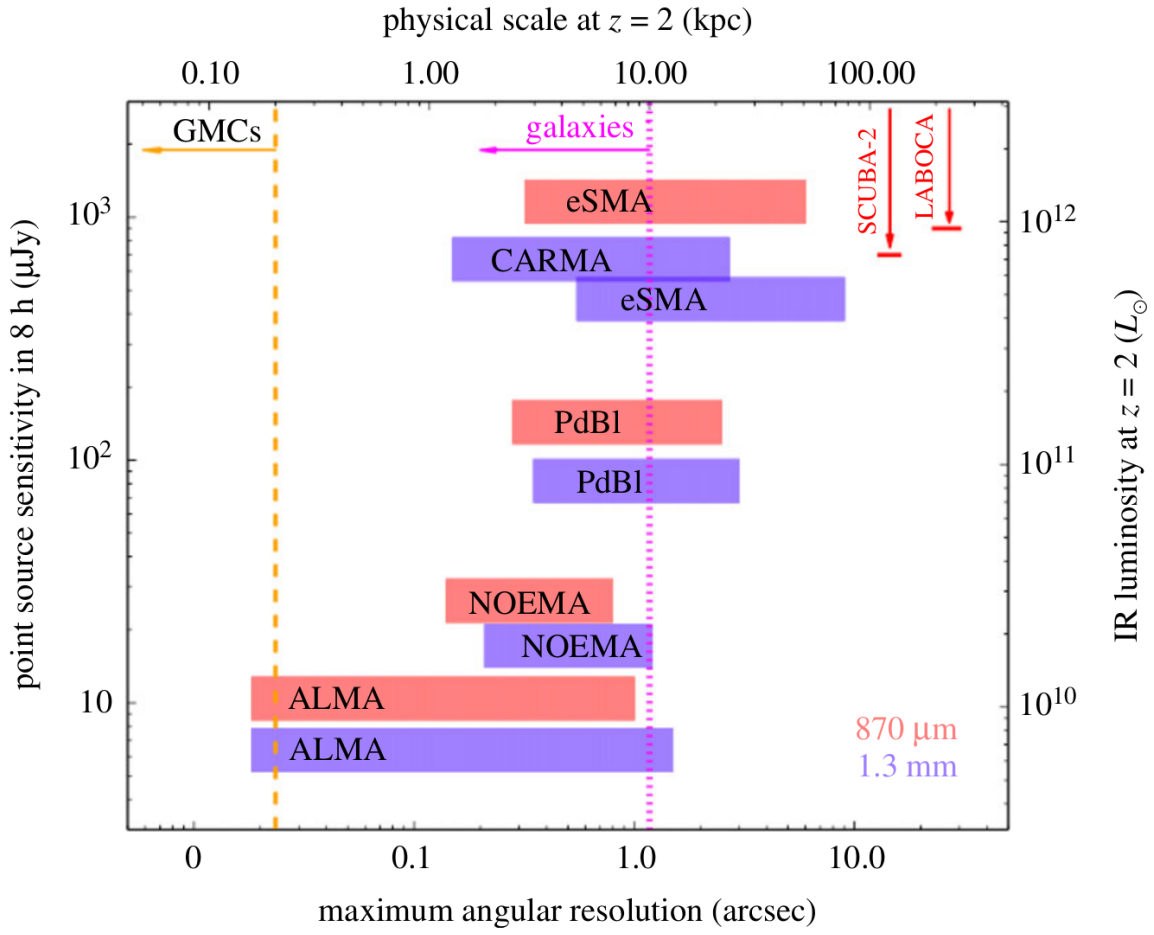

Figure 2.1: Sensitivity for point sources at $\sim 1300\mu$m, with 8hr exposure, for different (sub-)mm facilities.

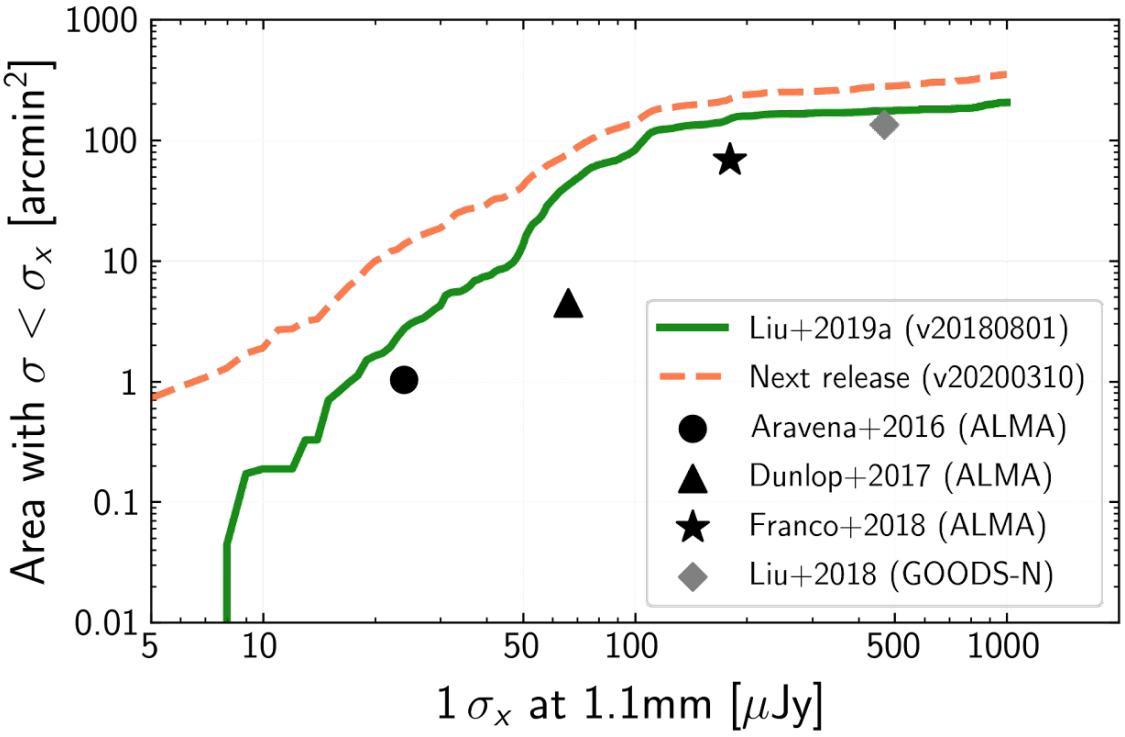

Figure 2.2: Cumulative areal coverage for the v20200310 release of the A^{3}COSMOS survey, compared to the v20180801 release by Liu et al. (2019b) and to the areal coverage of different ALMA surveys.

2.2 The A^{3}COSMOS: survey design and ancillary data

2.2.1 The COSMOS field

The COSMOS field (Scoville et al., 2007) is one of the most studied and observed extragalactic deep fields, which main goal is to investigate the formationa and evolution of galaxies with cosmic time and their environment. The area covered by this field is about 2 deg^2, centered at R.A. = 10h00m28.6s and DEC. = 02°12'2100". In the past years, it benefited from observations all across the electromagnetic spectrum, from the X-rays to the radio band. The COSMOS catalog used by Liu et al. (2019b) to perform the match with the ALMA galaxies is the COSMOS2015 version (Laigle et al., 2016). Adscheid et al. (2024) used instead the updated version of the photometry in the COSMOS field, observed in 2020 (Weaver et al., 2022). In Section 3.2.1 we report in more details the photometrical coverage of the COSMOS filed, as well as the instruments used to build the catalog.

2.2.2 A^{3}COSMOS pipeline

As already pointed out previously, the improving number of ALMA observations, coupled with the poor capability of the interferometer to perform wide and deep field observations of several objects at once, has lead to the need of developing a procedure to collect and homogenise these pointings, which could therefore be used in statistically significant studies. Figure 2.2 shows the areal coverage of different data release of the survey, compared with deep field ALMA surveys, showing a significant improvement with respect to previous surveys. The process of homogenising the ALMA archival images requires several steps to be accomplished. In this Section we summarize the principal points leading to the A^{3}COSMOS constructions (details can be found in Liu et al., 2019b). Before describing the A^{3}COSMOS pipeline, we need to introduce some useful concepts concerning the technical details of ALMA images:

- *Beamsize:* it is parametrised by the primary beam, that is the antenna response as function of the angular distance from the main axis. It can be approximated by a gaussian function and the full-width-at-half-maximum (FWHM) of the primary beam is usually taken as the diameter of the field of view of an interferometer;

- *Primary beam attenuation:* since the response of the antenna is not constant with the distance from the center of the pointing, a correction to the primary beam has to be applied. It can be parametrised as a Gaussian function peaking at the center of the circle with a value of one and decreasing to zero toward the outer regions ($pbcor = e^{-\frac{d^2}{2\sigma^2}}$, with d being the distance of a pixel from the center of the pointing and σ being the $FWHM/2.35$);

- *Noise:* the noise of an ALMA image is a function of the system temperature, the area of each antenna, the number of antennas, the number of polarizations, the available bandwidth and the observing time. Taking into account the primary beam attenuation, the RMS can be computed as the ratio between the noise of the image and the primary beam correction;

- *Signal-to-noise ratio:* having the signal of an ALMA image and knowing in which way the RMS changes across the pointing, it is possible to compute the S/N by dividing these two quantities. In the thesis, we will refer to the peak S/N, which indicates the ration between the peak flux of a source and the noise at its position.

In the A^{3}COSMOS reduction pipeline, at first, the data downloaded from the archive need to be calibrated. Second, sources have to be extracted from the images. Liu et al. (2019b) reported a number of 1534 ALMA pointings, with the most populated bands being

band 6 and 7 and with a mean beam size ranging from ~ 2.2" in band 3, to ~ 0.3 in band 9. Liu et al. (2019b) performed two different extractions: for each image, a prior and a blind extraction have been made. Blind sources were identified by using the Python Blob Detector and Source Finder (PyBDSF, Mohan and Rafferty, 2015), while prior sources have been extracted by doing iterative execution of GALFIT (Peng et al., 2002, 2010). PyBDSF is based on the decomposition of radio interferometry images into individual sources, allowing one to derive quantities as the spectral index, polarizaiton properties or to measure the how the source's PSF change in the image. By using this code, it is then possible to localize sources in a radio image and extract their fluxes, without knowing their position a priori (i.e., blind extraction). The second code, GALFIT, applied instead to perform the prior extraction (i.e., based on the known position of a galaxy, the "prior", taken from a reference catalog), is a two-dimensional fitting algorithm that extracts structural galaxy components from an image. In particular, it allows one to model the galaxy with different possible shapes (e.g., Sérsic profiles, exponential disk, Gaussian profile) and subcomponents (e.g., stellar disk, bars, nuclear sources). With the blind extraction, 930 sources has been found, while the prior extraction lead to 1039 galaxies.

For both catalogs, Monte Carlo (MC) simulations were run to verify the robustness of the extraction. Model galaxies are simulated and then the same method of the main analysis is applied to verify whether they are recovered or not. In particular, the differences between extracted and observed fluxes are studied, in order to find possible offsets, as well as they investigated the fraction of injected sources that are recovered (i.e., the completeness). The positional priors are taken from already existing multiwavelength catalogs in the COSMOS field (i.e., Laigle et al., 2016), using a cross match radius of 1", limiting false match probability. Once both the prior and blind extraction was performed, a cut in signal-to-noise (S/N) has been applied in order to limit spurious detections.

The authors find a cumulative spurious detection rate lower than 8% by cutting at $S/N = 5.40$ (in PyBDSF, blind catalog) and $< 12\%$ for the prior selection (GALFIT), with $S/N = 4.35$ (see Figure 2.3). The remaining sources are then combined with spectroscopic or photometric redshift catalogues, as well as existing photometric ones in the covered field, to obtain multiwavelength photometric coverage from the optical/UV to the mm or even radio bands (see Section 3.2.1). Therefore, they obtained the physical properties (e.g., $M_\star$, SFR, $M_{\rm dust}$) of the sources using the SED fitting code "Multi-wavelength Analysis of Galaxy Physical Properties" (MAGPHYS da Cunha et al., 2008; da Cunha et al., 2015b), that compare a set of libraries of SED models with the observed fluxes, to infer the physical properties of galaxies. Figure 2.4 shows the pipeline workflow, with the iterative processes for the source extraction related to the MC simulations.

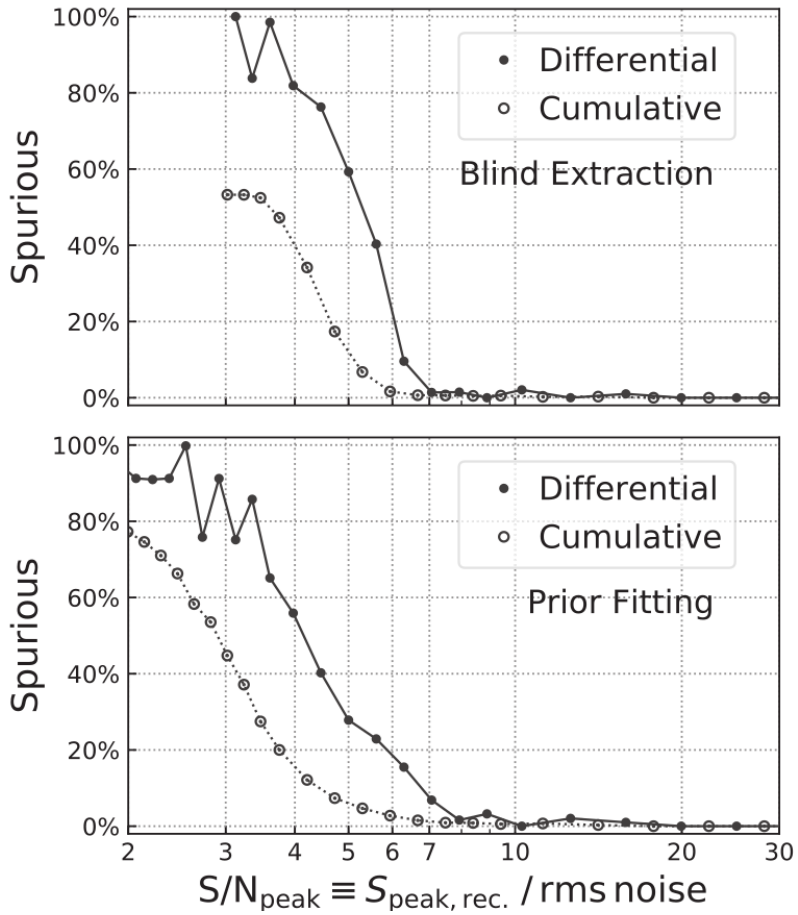

Figure 2.3: A^{3}COSMOS spurious fraction displayed for the prior and blind extraction. Differential (filled circles) and cumulative (empty circles) value are shown. For both extractions, the spurious fraction is low at the S/N threshold adopted. Taken from Liu et al. (2019b).

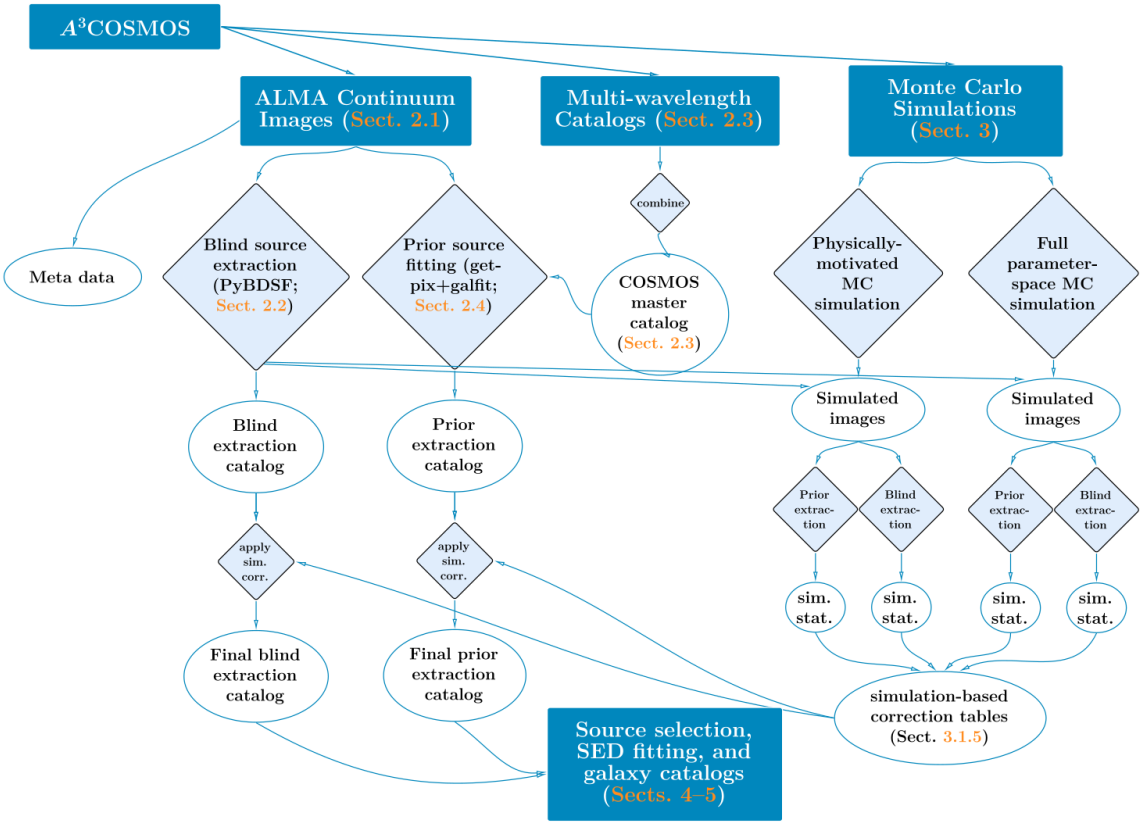

Figure 2.4: Workflow displaying the different steps of the A^{3}COSMOS pipeline, from the images to the final catalogs. Taken from Liu et al. (2019b).

2.3 Number counts from the largest ALMA archival dataset

Recently, in a work published by Adscheid et al. (2024), in which I contributed in the development of the homogeneisation routine, we have updated the A^{3}COSMOS catalog and built a similar A^{3}GOODSS database, by applying the same pipeline to the GOODS-South field. The new version of the database consists of 173 (COSMOS) and 74 (GOODS-S) ALMA projects, with 3232 and 723 images, respectively. The most populated ALMA bands resulted to be 3, 4, 6, 7 and the number of detections is more than doubled with respect to the previous version by Liu et al. (2019b) (1756 in the COSMOS field and 294 in the GOODS-S field). For the A^{3}COSMOS version, the main update is the match with the recent COSMOS2020 (Weaver et al., 2022) that improves the COSMOS2015 photometric coverage (Laigle et al., 2016). With this new version of the A^{3}COSMOS and A^{3}GOODSS database, we were able to derive the mm number counts, thanks to a process of bias reduction aimed at overcoming the problems and possible biases affecting the survey, due to the fact that the individual ALMA images have different observing wavelengths and sensitivities, as well as the fact that most of them are centered to a pre-selected pointed source. In the next Sections we summarize the process of bias reduction (note that a similar procedure will also be used for deriving the luminosity function (LF) and star formation rate density (SFRD), which are the main results of this thesis work), then we show the number counts obtained for the A^{3}COSMOS survey in different (sub-)mm bands.

2.3.1 Reduction of biases

In order to derive the number counts, as well as to derive the other statistical quantities (e.g., LF, SFRD) an unbiased survey is needed. However, the A^{3}COSMOS is an inhomogeneous collection of pointings, with different characteristics depending on the PI selection, far from being free of biases. Nevertheless, it is possible to mitigate these biases by applying a "blinding" procedure, that will be described in this Section. The principal source of bias is related to the targeting of the ALMA observations, since each individual targeted pointing has in the phase center a source that has been observed for some particular reason and, thus, will contribute to an overestimation of the intrinsic number density of sources, especially towards the bright end. Moreover, in order to derive statistical quantities of a sample, the areal coverage of the survey needs to be computed: to this purpose, other sources of bias such as the inhomogeneity in the observing band, depth and overlap between pointings must be taken into account, to avoid double-counting the same area.

In order to overcome target selection biases, observed targets and possible clustering of sources around the target have to be removed from the sample. Although usually in the individual pointings the observed target is expected to be at the phase center of the

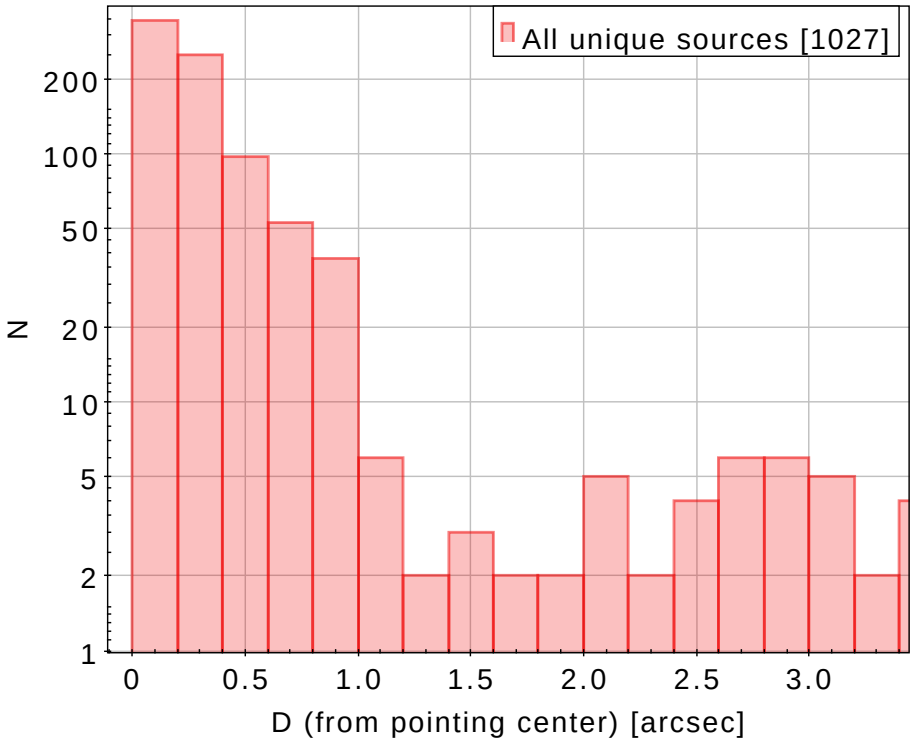

Figure 2.5: Sources distance distribution from the center of the pointings.

observation, some prior sources may suffer from observational offset when observed with ALMA (e.g., sub-mm selected galaxies from single-dish images may have a positional uncertainty of ≥ 3; Hodge et al., 2013). In the A^{3}COSMOS survey we face the problem of having thousands of images in which serendipitous sources may be at few arcsecond from the center and are difficult to be distinguished from the offsetted target. In order to safely identify the central target source, only pointings with a galaxy in the inner 1" radius (from the phase center) are kept. Figure 2.5 shows the distance distribution of each source from the center of the corresponding pointings. At distances larger than $\sim$ 1", the distribution is likely to be dominated by random association.

In this case, the central source is categorized as the target and removed from the sample. To have consistency with the total area, the central circle of 1" radius is also masked and all the inside sources are removed from the catalogue. Note that this masking does not introduce negative biases against bright sources that will still be observed serendipitously in the outer regions of the pointings. Then, one needs to take into account sources that can be clustered with the target. This can be done by using the redshift information of the galaxies inside the same pointing (if available). If a galaxy is found to be at a similar redshift to that of the target, in particular, having a difference in the two redshifts of $\Delta z = 0.06(1 + z)$ (Weaver et al., 2022), it is removed as a clustered galaxy.

After the application of the cuts to the sample for taking into account target biases, the

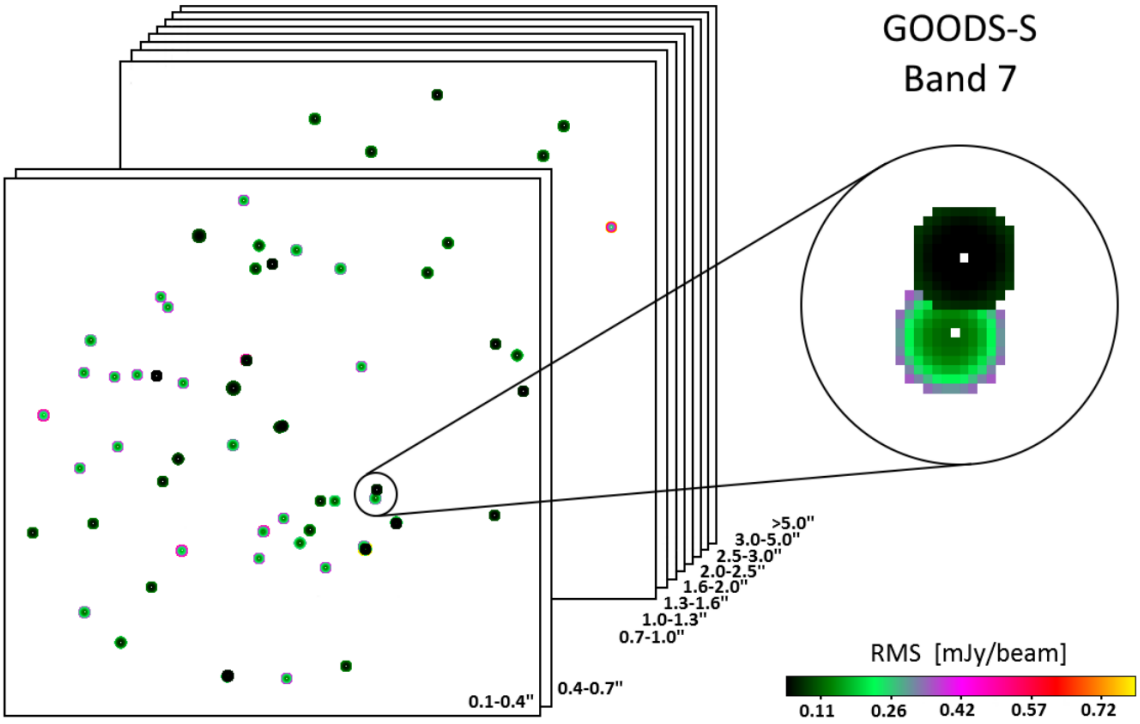

Figure 2.6: Example of a noise map cube, with the ten layers of different angular resolution. The zoom-in panel shows a situation in which two pointings with different RMSs are overlapping. Figure taken from Adscheid et al. (2024).

areal coverage needs to be computed. We know that it depends on three main elements: the completeness, the contamination and the detectability of the sources, which are function of the position, size and S/N. These parameters also change with the observing wavelength and the resolution of the images (which are different in the different pointings of the A^{3}COSMOS survey). In Adscheid et al. (2024) we derived the areal coverage by firstly building noise maps, then filled with ALMA pointings to compute the aforementioned parameters.

The process of building the noise map consists in the following steps: at first, empty COSMOS and GOODSs maps are created, with a fixed pixel scale of 2"; the maps are then divided into 10 layer of increasing angular resolution (from 0.1" to >5", see Figure 2.6) to minimize the overlap of ALMA pointings; next, the maps are normalized to the central reference frequency of its band, with $\sigma_{\nu,\mathrm{ref}} = \sigma_\nu \left(\nu_{\mathrm{ref}}/\nu\right)^{3.8}$, under the assumption of being in the Rayleigh-Jeans regime. Then, a primary beam correction is applied, leading to an increase of the noise from the inner to the outer regions. This is because the primary beam correction is used to account for the non uniform response of the sensitivity in a radio image, and can be computed as $PB_{\mathrm{COR}} = e^{-\frac{d^2}{2\sigma^2}}$, with d being the distance from the center

and $\sigma = FWHM/2.35$. With this map, the areal coverage can be computed by taking into account the previously derived completeness and contamination. The former has been derived by Liu et al. (2019b), by performing MC simulation as described in Section 2.2. The latter is instead determined from the fraction of spurious sources, derived by dividing the negative detections of the A^{3}COSMOS ALMA images (obtained by multiplying the images by -1) by the positive detection in the normal images. The areal coverage is then obtained as:

$$A_{eff} = \frac{A \cdot C_{compl}}{1 - C_{contam}}. \tag{2.1}$$

2.3.2 Mocks and comparison with the literature

In order to test the homogenization method and the selection criteria, simulations have been carried out, using the Simulated Infrared Dusty Extragalactic Sky (SIDES, Béthermin et al., 2017; Gkogkou et al., 2023), based on dark matter simulations and empirical prescriptions. Since this simulation is aimed at reproducing the FIR and mm extragalactic sky and includes also the effect of clustering, it represents a well suited option to perform our tests. In particular, we indeed wanted to verify, by injecting mock ALMA pointings, the number counts retrieved (in three different scenarios) after applying our method.

In order to construct the simulation, we created mock ALMA pointings, with the same characteristics of the A^{3}COSMOS pointings, in the simulated sky region and considered three different situations, each featuring an observational bias: the "Superbias", "Bias" and "Random" realizations. The first one considers brightest sources to be the targets of pointings; the second realization has a targets distribution following the flux density distribution of the targets actually observed in the A^{3}COSMOS pointings, and the "Random" one is not targeting sources specifically, but mocks pointings randomly distributed in the sky. For each of these three parametrization, two different computation of the number counts are made. One is the "uncorrected" computation, that consists in retrieving the mock number counts without applying corrections for the pointings targets, including therefore all the sources inside an ALMA observation. The second is the "corrected" method, which includes all the corrections discussed before on the sources inside a pointing (i.e., the targets and those sources affected by clustering).

The results are shown in Figure 2.7. For the "Random" sample, the retrieved number counts are very similar to the input from the SIDES simulation. "Superbias" and "Bias" (which represents a similar situation as that of the A^{3}COSMOS) samples are instead showing an excess on the number counts (of $\sim$ 1.5 and 1 dex), mostly on the bright-end of the distribution, with the "Bias" sample showing a more spread excess than the "Superbias". For both of them the input distribution is then retrieved once the target corrections are made.

This method has then been applied to the A^{3}COSMOS data in bands 3, 4, 6 and 7.

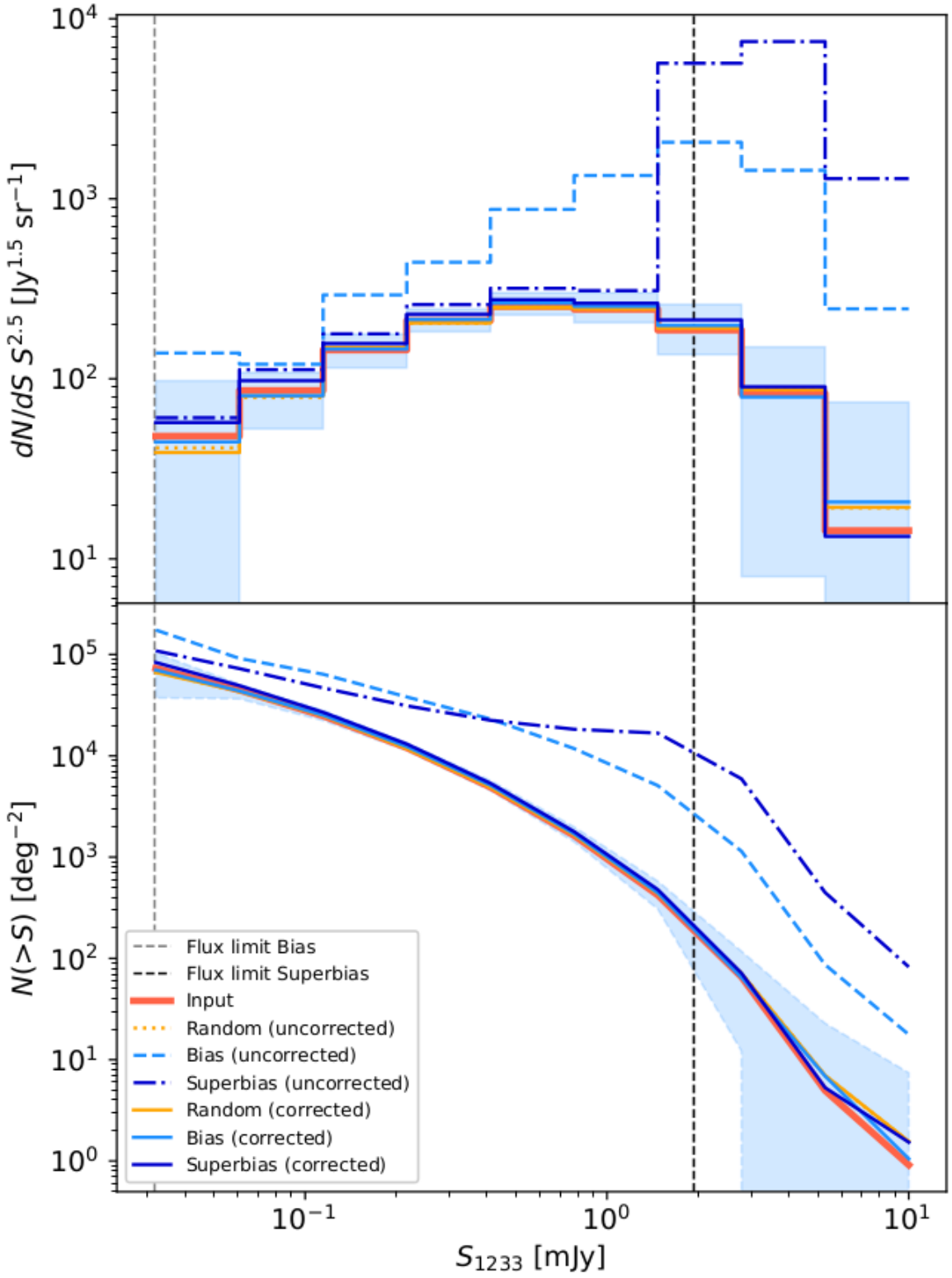

Figure 2.7: Simulated differential (top) and cumulative (bottom) number counts for single pointings in ALMA Band 6 based on the SIDES simulated sky catalogue, taken from Adscheid et al. (2024).

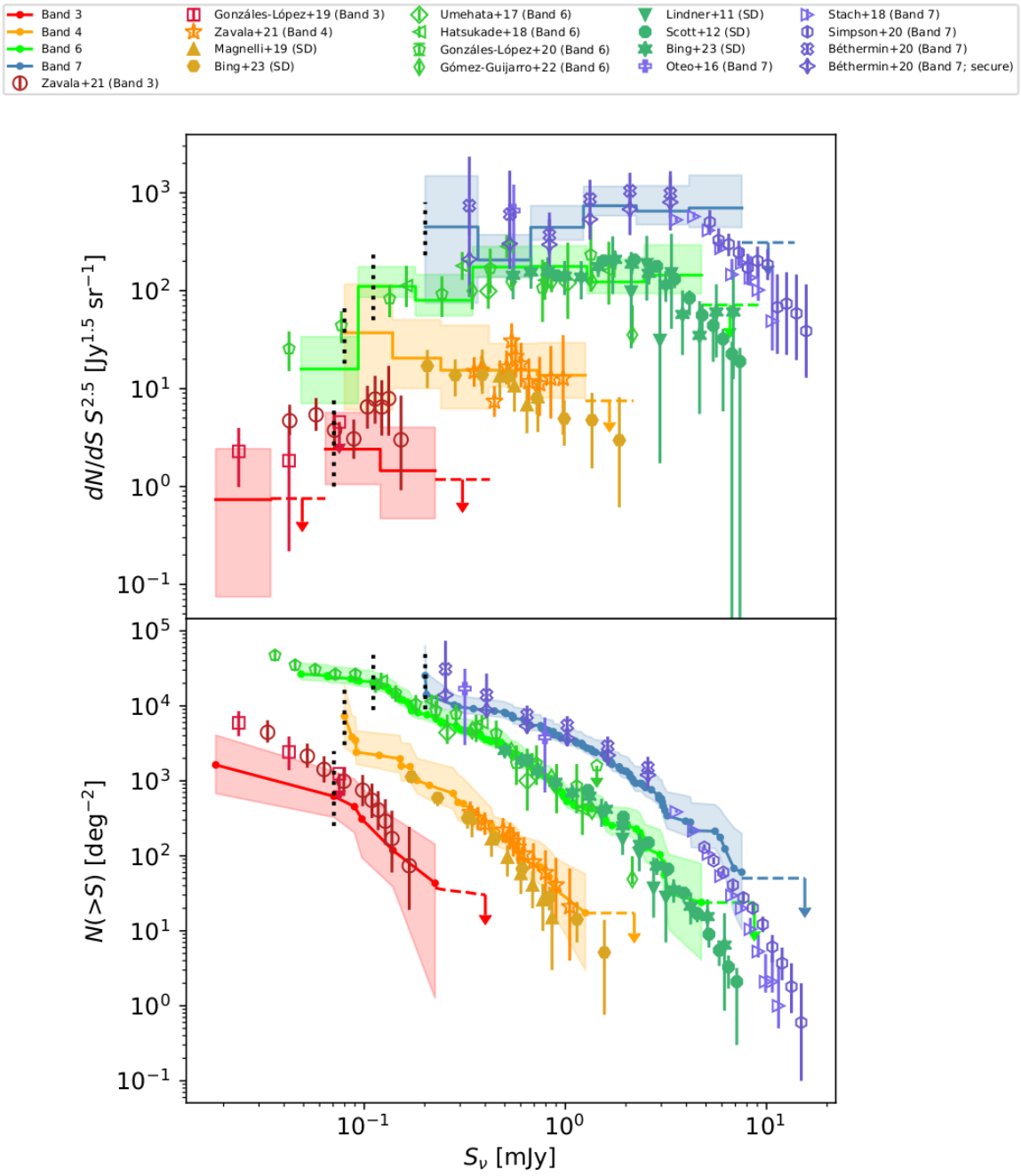

Figure 2.8: A^{3}COSMOS number counts by Adscheid et al. (2024). Different colors represent different ALMA bands (3, 4, 6 and 7) as reported in the legend. Number counts for each band are compared to previous works, displayed with different markers and same colors.

Both cumulative and differential number counts have been derived (see Figure 2.8, taken from Adscheid et al. (2024) and compared to other ALMA or single-dish estimates. Our source counts in band 3 have been compared to those by González-López et al. (2019) and to Zavala et al. (2021b). The former are roughly three times higher than the A^{3}COSMOS number counts, which is likely caused by the line contamination present in most of the sources considered by González-López et al. (2019). The same discrepancy is observed in the comparison with Zavala et al. (2021b) (which includes the ASPECS-LP ALMA at 3mm, by González-López et al., 2019) at low fluxes; a good agreement is instead found at fluxes > 0.06 mJy (where data are only from the MORA survey, not including data by González-López et al. (2019)). The A^{3}COSMOS number counts are also consistent with those obtained by Magnelli et al. (2019a), Zavala et al. (2021b), and Bing et al. (2023) in band 4 (though slightly higher then the single dish estimates). In band 6, the A^{3}COSMOS number counts are able to link the deeper with the shallower survey's estimate and are found to be in good agreement with those by Lindner et al. (2011), Scott et al. (2012), Umehata et al. (2017), Hatsukade et al. (2018b), González-López et al. (2020), Gómez-Guijarro et al. (2022), and Bing et al. (2023). Finally, the A^{3}COSMOS counts in band 7 has been compared with those by Oteo et al. (2016), Stach et al. (2018), Béthermin et al. (2020), and Simpson et al. (2020). The results are consistent with most of the previous estimates, but slightly lower at the faint-end than those by Béthermin et al. (2020) from the ALPINE survey. We note that the A^{3}COSMOS survey is not able to sample the bright-end of the number counts in band 7, as not covering enough area (as the single-dish based survey do instead).

Overall, the combination of the ALMA archival images in the COSMOS and GOODS-S fields, has led to the estimation, for the first time, of the number counts in a wide range in fluxes, bridging the deep estimates (from blind ALMA survey) with the bright-end results from single dish observations. Moreover, especially in band 4, deriving the number counts from the A^{3}COSMOS has contributed to sample deeper fluxes with respect to the previous estimates. This new approach shows a number of advantages over combining results from individual work in different surveys: *i)* all data at different sensitivities and in different bands are reduced in a homogeneous and consistent manner, thus avoiding the need to combine results obtained by using different methods; *ii)* it allows counts to be derived in a wide range of fluxes at the same time; *iii)* the continued increasing of the A^{3}COSMOS and A^{3}GOODS database will make this approach a very useful resource for deriving number counts with greater efficiency and increasing statistics in the future.

Translated with DeepL.com (free version)

2.4 Other results from A^{3}COSMOS survey

In the past five years, since the A^{3}COSMOS survey construction, a number of works have been done investigating the dust and cold gas content and evolution in the high-z Universe. In this Section we report some of the main remarkable results obtained using the data from the A^{3}COSMOS survey.

Molecular gas

Liu et al. (2019a) and Wang et al. (2022) exploited the ALMA archive, through the A^{3}COSMOS survey, to derive statistical properties of the molecular gas in high$-z$ galaxies. In particular, Liu et al. (2019a) studied molecular gas scaling relations and their evolution with cosmic time, combining the A^{3}COSMOS with other sample from the literature. They investigated the fraction of molecular gas to stellar mass ($\mu_{\rm molgas}$) and the depletion time ($\tau_{\rm depl}$) as a function of the cosmic age, stellar mass and SFR. By applying gas fraction scaling relation to the stellar mass function they were able to derive the cosmic cold molecular gas density (see Figure 2.9), for which they found a good agreement with literature, even though the large errors in literature estimates do not allow them to constrain the best scaling relation to use to derive the cosmic molecular gas density.

Wang et al. (2022) investigated for the first time the mean mass and the extent of the molecular gas at $0.4 < z < 3.6$. They found the mass to be evolving with both redshift and stellar mass. In particular, from Figure 2.10 (left panel), it is possible to highlight a decrease of the mean molecular gas from $z \sim 4$ to $z \sim 0$, with a similar rate at which sSFR decreases (for main sequence galaxies). The depletion time (shown in Figure 2.10, right panel) is instead found to be constant ($\tau_{\rm depl} \sim 300 - 500$ Myr) with redshift at $z > 0.5$, but increases toward the local Universe.

Dust attenuation

Fudamoto et al. (2020) used the data of the A^{3}COSMOS sample to derive the relation between the slope of the UV continuum (β) and the infrared excess ($IRX = L_{\rm IR}/L_{\rm UV}$), i.e. the dust attenuation, in galaxies at $z \sim 2.5 - 4$. For massive galaxies ($M_\star > 10^{10}$ M$_\odot$), the IRX-β relation is consistent to what is found in the local Universe, suggesting that the dust properties seem not to evolve with redshift for massive galaxies. For lower stellar masses, the relation is below that of the local Universe. Moreover, they found the IRX to correlate with the stellar mass of the galaxies.

These studies have highlighted how the A^{3}COSMOS survey can be used to infer the sta-

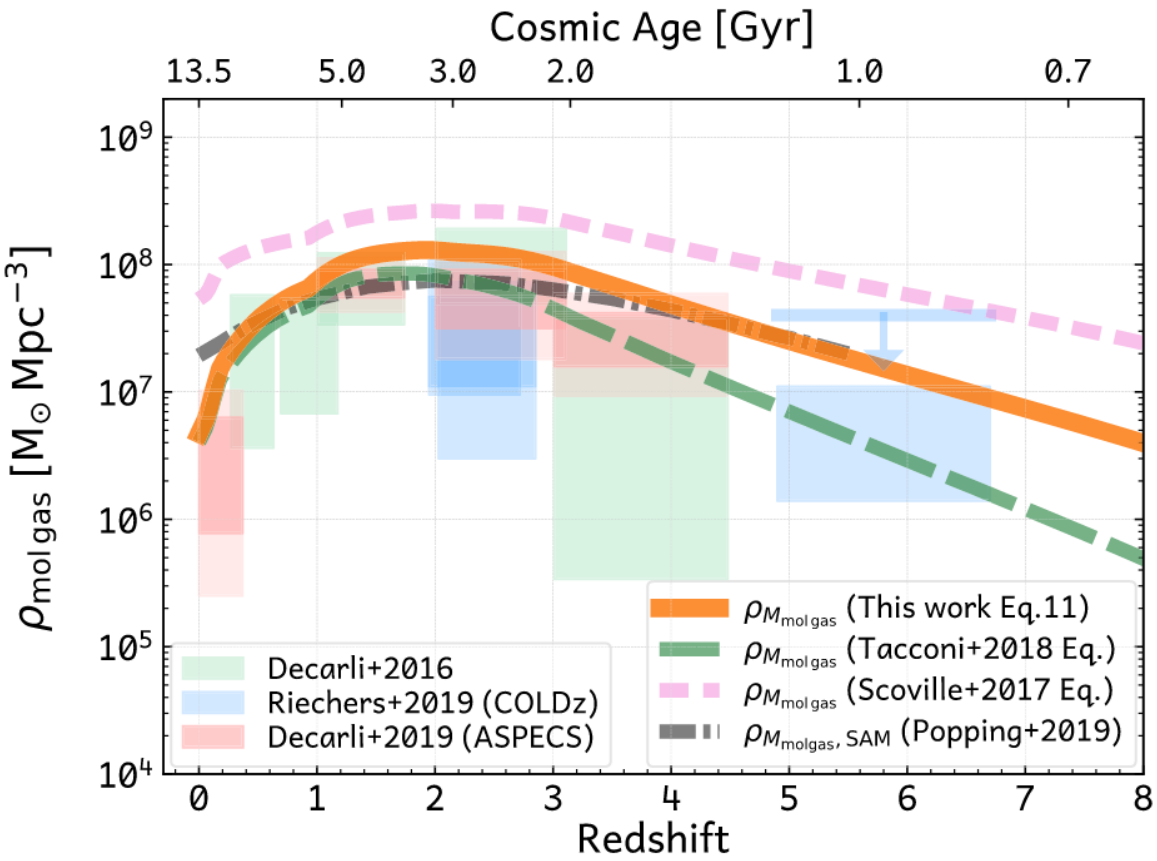

Figure 2.9: Cosmic molecular gas density computed using scaling relations derived for the sample of galaxies in the A^{3}COSMOS survey. From Liu et al. (2019a).

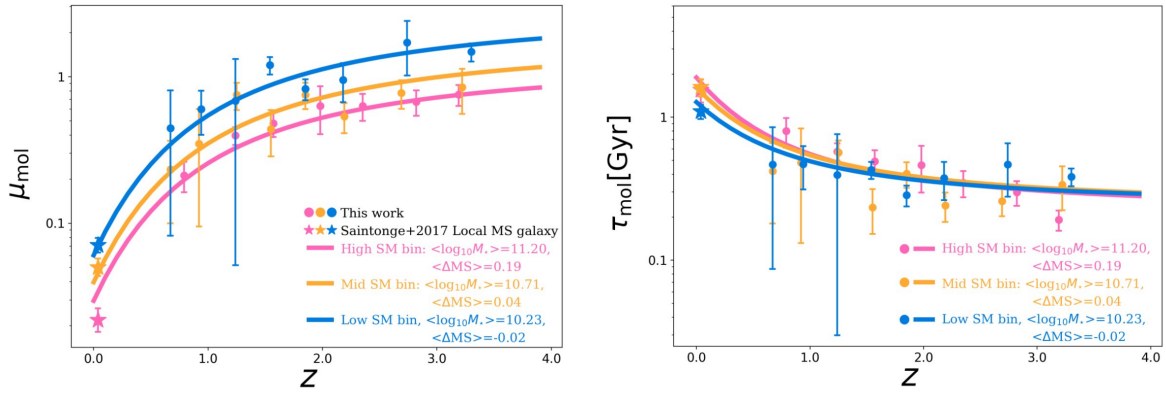

Figure 2.10: Mean molecular gas (left) and its depletion time (right) evolution with redshift. Different colors indicate different stellar masses, with mean values of $< log(M_\star) >= 10.23$, 10.71 and 11.20 (in blue, orange and pink, respectively).

tistical quantities ruling the main processes in the evolution of galaxies, with particular attention to the dust and gas reservoirs in star forming galaxies. In the following Chapters, we will use the data of the A^{3}COSMOS to derive other fundamental quantities for the evolution of galaxies: the cosmic star formation rate density and the dust mass density.

CHAPTER 3

The sample: turning an heterogeneous survey into a blind-like one

Understanding how galaxies form and evolve through cosmic time is one of the open questions of modern astrophysics. This topic can be addressed in many different ways using information across the whole electromagnetic spectrum. In Section 1.4.3 we have shown that one of the best approaches involves the study of galaxy samples over a wide range of redshifts and luminosities, as it enables the derivation of the variation of physical and statistical propertieswith time, such as the LF and the cosmic SFRD, for a large number of objects. These quantities are essential for tracking the demography of the (star-forming) galaxy population over cosmic time, as well as for studying the galaxy mass assembly at different epochs. In this Chapter, we describe how we selected the sample used for this work, and the associated multiwavelength catalogue we used to identify and characterise the sources (Section 3.2). Then we describe the SED fitting procedure and the main results we obtained (Section 3.3). Finally, we present the method developed to turn the A^{3}COSMOS survey into a blind-like survey (in a similar way to what was done by Adscheid et al. (2024), described in section 2.3), that we use to derive the A^{3}COSMOS IR LF (presented in Section 4.1) and the dust obscured SFRD since $z \sim 6$ (presented in Section 4.2). Throughout this Chapter (and this Thesis), we assume a Chabrier (2003) stellar initial mass function (IMF) and adopt a ΛCDM cosmology with $H_0 = 70\ \mathrm{km\ s^{-1}\ Mpc^{-1}}$, $\Omega_\mathrm{m} = 0.3$, and $\Omega_\Lambda = 0.7$.

3.1 Introduction

Up to $z \sim 2 - 3$, the SFRD has been well studied and accurately measured thanks to both optical-ultraviolet and infrared facilities (see Madau and Dickinson, 2014, for a review). These works have revealed an increase of the SFRD with redshift, which at all epochs is

dominated by the obscured IR component ($\sim 80\%$, e.g., Khusanova et al., 2021). In particular, as mentioned in Section 1.2, a key contribution of this IR component comes from DSFGs or submillimeter galaxies (SMGs, defined by a sub-mm excess at 450 and 850 μm; Smail et al., 1997; Barger et al., 1998; Hughes et al., 1998; Blain et al., 2002; Casey et al., 2014). These objects, which are more common at cosmic noon (i.e., $z \sim 2-3$, Chapman et al., 2003; Wardlow et al., 2011; Yun et al., 2012) than locally, are characterized by large IR luminosities ($L_{\rm IR} > 10^{12}$ L$_\odot$), large stellar masses ($M_\star > 10^{10}$ M$_\odot$) (Chapman et al., 2005; Simpson et al., 2014), and high star formation rates (SFRs; > 100 M$_\odot$yr^{-1}; Magnelli et al., 2012; Swinbank et al., 2014), making them the main contributors to the SFRD at these redshifts.

Optical/UV-based studies and recent works with the JWST have made it possible to compute the SFRD up to $z \sim 7-8$ (see e.g., Bouwens et al., 2014; Oesch et al., 2015; Laporte et al., 2016; Oesch et al., 2018) and even $z \sim 10$ (e.g., Harikane et al., 2023), extending our knowledge of star formation activity to very early epochs of the universe. However, these studies may be biased by the band of observation(i.e., the rest-frame UV), which is highly affected by dust obscuration. Indeed, the obscured contribution is only retrieved from dust correction measured in the UV. These corrections are still very uncertain, especially at high-z, where the measurements are scarce and the disagreement large (see, e.g., Magdis et al., 2012; Magnelli et al., 2013; Béthermin et al., 2015; Casey et al., 2018; Zavala et al., 2018; Gruppioni et al., 2020; Algera et al., 2022). Therefore, it is crucial to determine the SFRD contribution of galaxies selected in the IR band, the re-emission of the obscured radiation emerges. While attempts have been made to constrain the SFRD$_{\rm IR}$ at $z > 3$ in the past using single-dish IR-millimeter surveys, only the advent of ALMA opened up this possibility. The unprecedented sensitivity reached by ALMA, coupled with the assembly of unbiased samples in the millimeter bands (Hodge et al., 2013; Staguhn et al., 2014; Franco et al., 2018a; Zavala et al., 2018), allows for the study of the evolution of these galaxies up to high redshifts, thus reaching the $z > 3$ range still affected by many uncertainties (e.g., poor statistics, bias in the IR luminosity). Recent works using submillimeter and millimeter samples (e.g., Gruppioni et al., 2020; Algera et al., 2022) support a scenario in which the SFRD shows a plateau rather than a significant decrease at $z = 2-6$. These studies are, however, limited by statistics, and larger samples are required to better constrain the SFRD at higher redshift by reducing the uncertainties.

In this perspective, the A^{3}COSMOS survey (Liu et al., 2019a,b), which is a compilation of all the ALMA observations in the COSMOS field, represents the largest ALMA survey to date. The fact that the survey is in the COSMOS field (Scoville et al., 2007), where a large wealth of multiwavelength data are available, including deep ancillary UV to near-IR photometry (Weaver et al., 2022, see Section 3.2.1), makes it an ideal source of data for per-

forming statistical studies on the nature and evolution of star-forming galaxies over a large range of redshifts and luminosities. However, A^{3}COSMOS it is not a purely blind survey, (what would be needed to perform statistical studies), because it is composed by individual pointings at different observing wavelengths and with different sensitivities, making it an inhomogeneous survey not suited for statistical studies. For these reasons, within the A^{3}COSMOS collaboration, we developed a new method specifically tailored to turning a targeted survey composed of an arbitrary number of pointings (isolated or overlapping), each with varying sensitivity and observing band, into a "blind-like" (targeted unbiased) survey, thus allowing the derivation of the main statistical properties of large galaxy samples over cosmic time. However, it is important to bear in mind that the conversion into a blind survey can be affected by uncertainties related to the underlying assumptions made (see Section 3.4), with particular regard to the removal of targeted and/or clustered sources, as well as to a robust assessment of the RMS. In order to take advantage of the most recent A^{3}COSMOS[1] and multiwavelength (COSMOS2020 Weaver et al., 2022) catalogs, we have performed a new catalog match and SED-fitting analysis using the PYTHON "Code Investigating GALaxy Emission" (CIGALE; Boquien et al., 2019) SED-fitting tool. We then derived the IR (8-1000 μm) LF, and present new estimates for the dust-obscured SFRD from $z \sim 0.5$ to $z \sim 6$.

3.2 Sample selection

In this Section we briefly summarize the sample used, that was widely described in Chapter 2. In particular, the final catalog has been built by matching the A^{3}COSMOS data with the updated COSMOS2020 photometry (Weaver et al., 2022), and the superdeblended catalog by Jin et al. (2018). Within the A^{3}COSMOS survey, two different catalogs are available. The first contains sources blindly extracted from the images, while the second one is a prior-based catalog using optical/near-IR positional priors (see Section 2.2). In this work, we used the prior version of the catalog (1620 sources) since it allowed us to construct the broad-band (from UV up to submillimeter and millimeter) spectral energy distribution (SED) of our sample.

3.2.1 The COSMOS2020 catalog

The COSMOS field (Scoville et al., 2007) is among the best studied extragalactic deep fields due to an unparalleled multiwavelength photometric coverage that includes X-rays (Elvis et al., 2009; Civano et al., 2012, 2016; Marchesi et al., 2016), UV (Zamojski et al., 2007), opti-

[1] https://sites.google.com/view/a3cosmos

cal (Capak et al., 2007; Leauthaud et al., 2007; Taniguchi et al., 2007; Taniguchi et al., 2015), near-IR (McCracken et al., 2010, 2012), mid-IR (Sanders et al., 2007; Le Floc'h et al., 2009), far-IR (Lutz et al., 2011; Oliver et al., 2012), submillimeter (Geach et al., 2017), millimeter (Bertoldi et al., 2007; Aretxaga et al., 2011), and radio (Schinnerer et al., 2010; Smolčić et al., 2017) bands. This has enabled the construction of large statistical samples of galaxies with measured stellar mass ($M_\star$) and SFR based on their photometric points via the SED-fitting technique. Over the past years, the assembly of COSMOS photometric catalogs has steered from using single-band selections (e.g. i-band, e.g., Capak et al., 2007; Ilbert et al., 2009; Muzzin et al., 2013) to stacking images in several bands (e.g. $JYHK_s$ Laigle et al., 2016). While this approach complicates the selection function due to a mixture of heterogeneous selections, if properly accounted for, it allows us to maximise the completeness in selecting galaxy populations over a wider range of redshifts and physical properties. On this line, the most recent release of the COSMOS photometric catalog (i.e., COSMOS2020; Weaver et al., 2022) is characterized by the addition of new data from the Hyper Suprime-Cam (HSC) Subaru Strategic Program (SSP) PDR2 (Aihara et al., 2019), new data from the DR4 (Moneti et al., 2023) of the Visible Infrared Survey Telescope for Astronomy (VISTA), and all the Spitzer IRAC data in the COSMOS field. Moreover, the catalog contains two independently derived photometric datasets: one (`the CLASSIC`) retrieved with classical aperture photometry on PSF-homogenized images using `IRACLEAN` (Hsieh et al., 2012) and another (`the FARMER`) derived using a PSF-fitting tool (`the Tractor`; Lang et al., 2016) to extract the photometry. The covered area is ~ 1.77 deg^2, and the total number of sources in `the CLASSIC` version is 1,720,700. (See Weaver et al. (2022) for a detailed description of the two methods and catalogs.) In this thesis, we used the `CLASSIC` version of the COSMOS2020 catalog.

3.2.2 Our sample

In this work, we use the latest version of the A^{3}COSMOS database and the latest source extraction by Adscheid et al. (2024). This version combines the already tested process of the automatic mining of the ALMA archive with the new photometry presented in the COSMOS2020 catalog. This version of the catalog consists of 3215 individual pointings coming from 171 different ALMA projects covering ALMA Bands 3 to 9. In Figure 3.1, the wavelength distribution of the different pointings is reported. The ALMA bands are shown with different color-shaded areas. Based on the figure, it is clear that the vast majority ($\sim 80\%$) of the sample comes from ALMA Band 7 (orange area) and Band 6 (blue region), with more than 2500 observations available. In Figure 3.2, we show the spatial distribution of the pointings in the survey, color-coded by observing wavelength. We also highlight three different pointing configurations in the figure that are representative of their complex

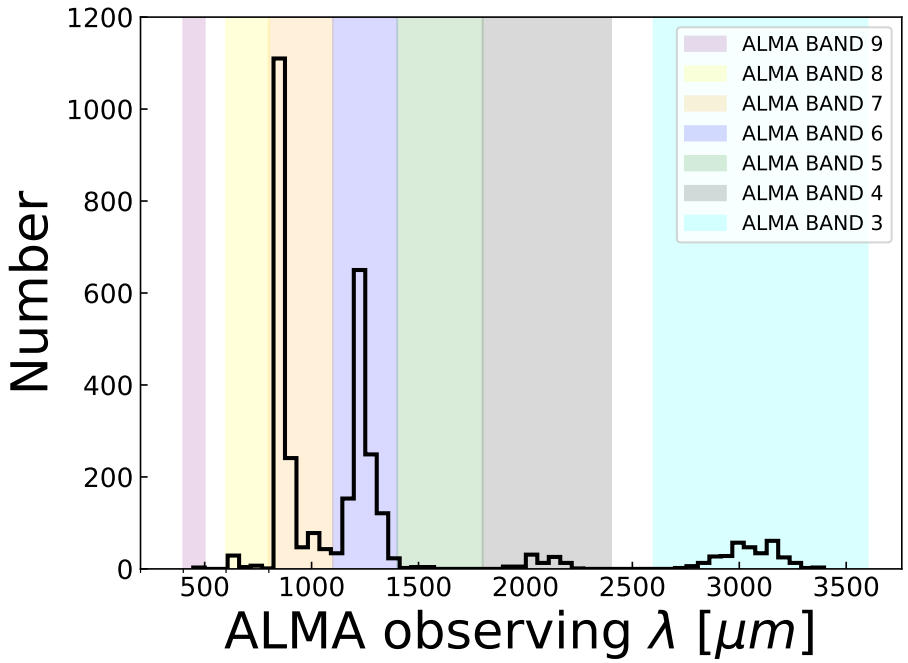

Figure 3.1: Number of pointings as a function of observing wavelength in the A^{3}COSMOS database. The wavelength ranges of the ALMA bands are plotted as color-shaded regions. The most populated bands are 6 and 7, with $\sim$ 2000 pointings each.

spatial distribution in the survey: panel a) shows a case of partially overlapping pointings in the same band; panel b) shows concentric pointings in different bands; and panel c) presents an extreme case of N>10 overlapping pointings in different bands. (For further details see Section 3.4.)

We selected 1620 galaxies with flux at least in one ALMA band above 4.35σ (with σ being the local RMS at the position of each source (see Adscheid et al., 2024). Within the selected sample, 25% (441/1620) of the sources have a spectroscopic redshift (spec-z), while for 1069 out of the 1620 sources, we used the photo-z in the COSMOS2020 catalog. The spec-z in COSMOS2020 are from different works from the literature (e.g., Riechers et al., 2013; Capak et al., 2015; Smolcic et al., 2015; Brisbin et al., 2017; Lee et al., 2017), the catalog by Salvato et al. (version 2017 September 1; available internally to the COSMOS collaboration), and the ALMA archive (Liu et al., 2019b). The photometric redshifts used in this work are from Salvato et al. (2011), Davidzon et al. (2017), Delvecchio et al. (2017), and Jin et al. (2018) and are derived from either the CLASSIC (that use aperture photometry) or FARMER (applying profile-based extraction) version of the COSMOS2020 catalog, which found a similar number of sources. Finally, the remaining 110 of the 1620 sources do not have any redshift information. For this subsample, we computed the photo-z using CIGALE (Boquien et al., 2019) as described in the next section.

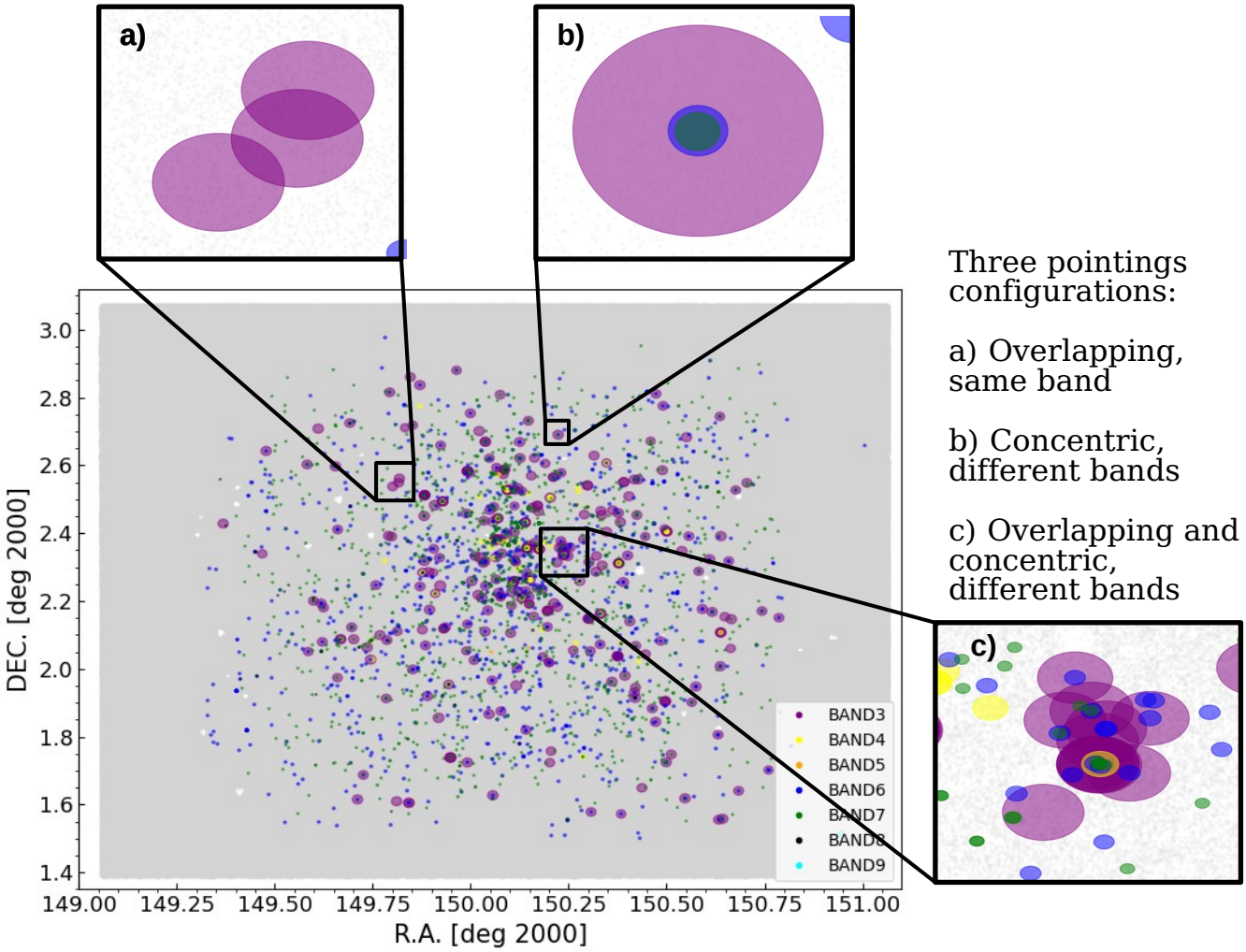

Figure 3.2: Archival ALMA observations in the COSMOS field used in this study. Individual pointings are plotted with different colors representing the observed ALMA bands. In the background, the COSMOS field is shown in gray. We show three zoom-in regions representative of possible classes of pointing configurations. Panel (a): Three overlapping pointings in the same band. Panel (b): Three concentric pointings in different bands. Panel (c): Overlapping and concentric pointings in different bands.

3.3 Galaxy broad-band SED fitting

We decided to perform the SED fitting of the A^{3}COSMOS galaxies using CIGALE, a python SED-fitting code based on the energy balance between the UV and optical emission by stars and the re-emission in the IR and mm by the dust. As CIGALE is a highly flexible code, it allows one to choose among different individual templates for each emission component (e.g., stellar optical/UV emission, cold dust emission, AGN) across a broad parameter space. Furthermore, one of the most important features is the availability of AGN templates, which can be easily included in the fit, allowing a decomposition between star formation-powered and AGN-powered IR emission. We note that deriving the IR luminosity from the SED is crucial to computing the IR LF.

In the following Sections, we report the available photometry and the individual components used to perform the SED fitting following recent SED-based studies (Ciesla et al., 2017; Lo Faro et al., 2017; Małek et al., 2018; Pearson et al., 2018; Buat et al., 2019; Donevski et al., 2020). Moreover, when needed, we included an input grid of redshifts in the fit spanning between $z = 0$ and $z = 8$ (with a step of $\Delta z = 0.1$) in order to derive the best photo-z, if missing. If known already, the redshift is taken from the photometric catalogs.

3.3.1 Photometric coverage

The A^{3}COSMOS catalog, being a combination of the COSMOS2020 catalog and the archival ALMA observations, takes advantage of a large photometric coverage from the UV to the far infrared (FIR)/mm. To perform the SED fitting, we considered the following filters available in the COSMOS2020 catalog (Weaver et al., 2022): CFHT MegaCam *u*; Subaru Suprime-Cam *i*, *B*, *V*, *r*, and *z*; Subaru HSC *y*; VISTA VIRCAM *Y*, *J*, *H*, and *Ks*; and the superdeblended filters (Jin et al., 2018) Spitzer IRAC channel 1, 2, 3, and 4; Spitzer MIPS 24 μm (valid also for those galaxies in the COSMOS2020 that were also detected in the COSMOS2015); *Herschel* PACS at 100 and 160 μm; *Herschel* SPIRE at 250, 350, and 500 μm; JMCT SCUBA2 at 850 μm; ASTE AzTEC (1 mm); and IRAM MAMBO (1.2 mm).

To deal with all the ALMA frequency setups present in the A^{3}COSMOS database, we built artificial filters to be provided to CIGALE, each corresponding to an observing wavelength in the A^{3}COSMOS catalog. The filters are centered at a specific wavelength and are box-like, with their width being equal to 16 GHz. With this procedure, we added up to 330 continuous ALMA filters between 446 μm and 3325 μm to the CIGALE database.

3.3.2 CIGALE input templates and main physical parameters

To build the SED stellar component we modeled the stellar populations with the `bc03` stellar population synthesis model (Bruzual and Charlot, 2003), and a delayed star formation history (SFH) with an optional second burst of star formation. We selected the `dustatt_modified_CF00` (Charlot and Fall, 2000) template to model the attenuation by dust and the `dl2014` (Draine et al., 2014) to model the dust emission, both based on the assumption of having two different attenuation and emission sources represented by birth clouds and diffuse ISM.

Finally, we used the `fritz2006` module (Fritz et al., 2006; Feltre et al., 2012) to model the AGN component in the SED. The AGN emission is described with a radiative transfer model, which takes into account the primary emission coming from the central engine (i.e., the accretion disk), the scattered emission produced by dust, and a thermal component of the dust emission. The individual input parameters are described below.

Stellar population and star formation history

Among the CIGALE options, we selected the `bc03` module (i.e., the stellar population synthesis model by Bruzual and Charlot, 2003) to build the SED stellar component. To parametrize the SFH we used the `sfhdelayed` module. The SFR initially increases up to a certain time, defined as $t = \tau$ (with τ being the e-folding time of the main stellar population model), and then decreases, as described by the following analytical form:

$$\mathrm{SFR(t)} \propto \frac{t}{\tau^2} \times exp(-t/\tau) \;\; for \; 0 \leq t \leq t_0, \tag{3.1}$$

with t_0 being the age of the onset of star formation. An optional burst representing the latest episode of star formation can be added (Małek et al., 2018). However, in this work, we chose to represent the SFH with a nearly constant shape, selecting 10,000 Myr as the value for the e-folding time of the late starburst population model. In Figure 3.3 some of the possible SFHs among which one can choose are shown. The light-purple curve is displaying a SFH similar to that we have choosen.

Dust component

As already explained in Section 1.2, the emission of DSFGs cannot be entirely reproduced without taking into account the presence of dust in the galaxy. For this reason, we included in the SED fitting the modules representing dust attenuation and re-emission.

We selected the `dustatt_modified_CF00` (Charlot and Fall, 2000) template to model the attenuation by dust (see Figure 3.4 for some examples of dust attenuation laws).

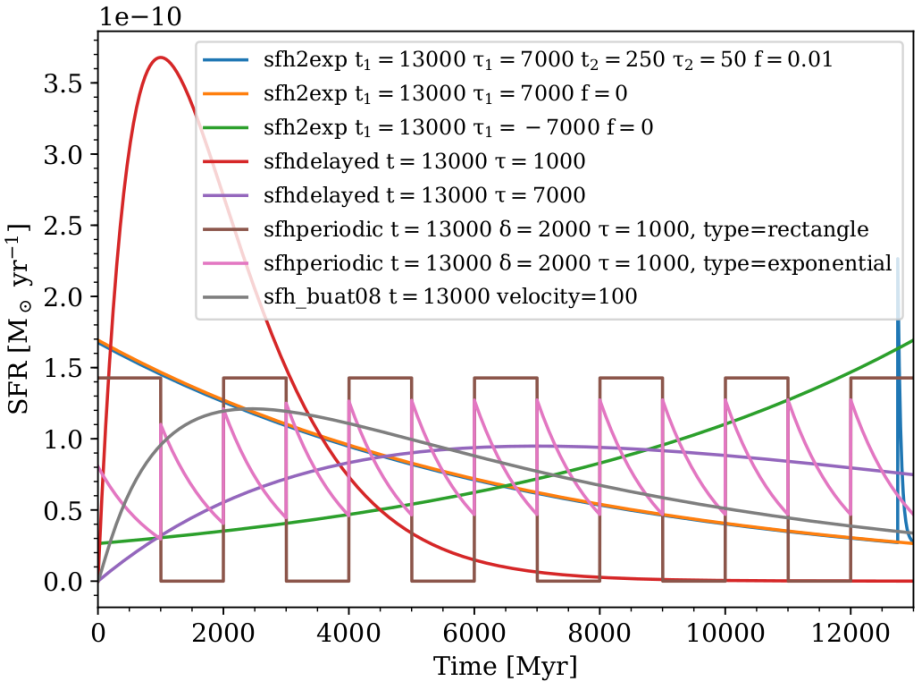

Figure 3.3: CIGALE possible SFHs. Blue, orange and green lines indicate the double exponential SFHs. Red and light-purple curves are two different SFHs with a delayed burst. Brown and magenta curves are the periodic SFHs avalaible in CIGALE. Finally, the grey line shows a rotation velocity dependent SFH. Adapted from Boquien et al. (2019).

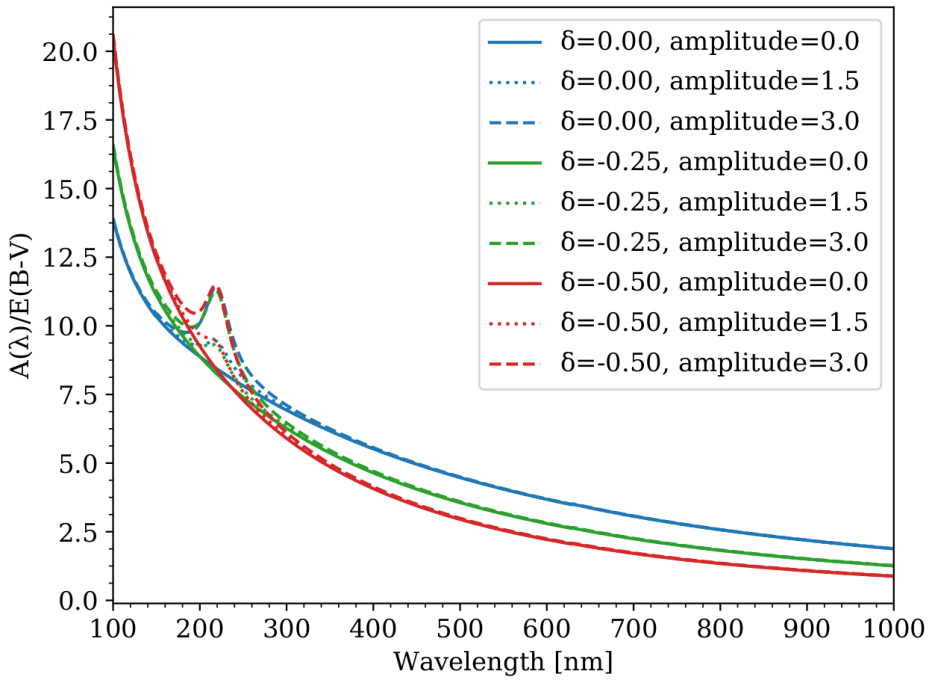

Figure 3.4: Different attenuation laws available in CIGALE, with different slopes and amplitudes of the bumps. From Boquien et al. (2019).

The `dustatt_modified_CF00` assumes the presence of both the diffuse interstellar medium (ISM) and a birth cloud (BC) in the surroundings of stars. In particular, the light of both young and old stellar populations is affected by the ISM attenuation, whereas the BCs attenuate only the emission from young stars, as they recently formed inside the clouds. Considering these two different but coexisting situations, two attenuation laws were computed with different slopes for the ISM and BCs. The V-band attenuation was then derived as the ratio between the ISM and the total attenuation (i.e., ISM + BCs).

To consistently model the dust emission, we used the `dl2014` (Draine et al., 2014) template. Indeed, the `dl2014` module is based on the same ISM and BCs environment used for the dust attenuation. This module takes the PAH mass fraction and the minimum radiation field as main input parameters. In Figure 3.5 we show the Draine et al. (2014) dust emission templates, with the main parameters of the emission having different possible values that can significantly affect the shape of the SED.

Active galactic nucleus component

Finally, we used the `fritz2006` module (Fritz et al., 2006; Feltre et al., 2012) to model the AGN component in the SED. We choose to adopt the `fritz2006` module (which considers a smooth distribution for the dust in the torus) instead of the SKIRTOR module (which assumes a clumpy torus scenario) for the following reasons: *i)* Feltre et al. (2012)

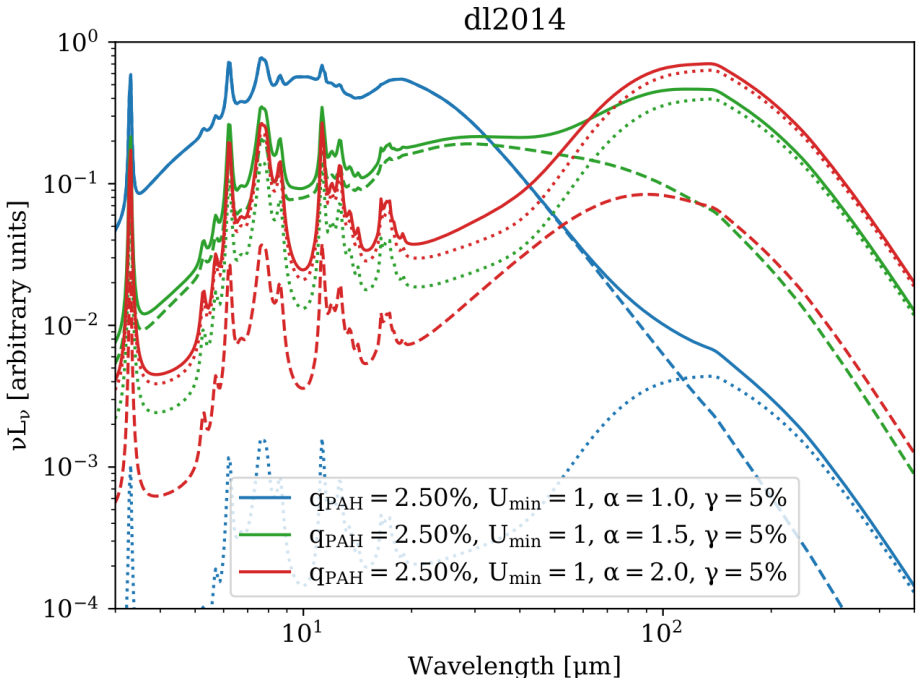

Figure 3.5: The Draine et al. (2014) dust emission templates, with different values of the main parameters. From Boquien et al. (2019).

have shown that even though there are differences between the SED from the torus models with different dust configurations, however, they are due to models assumptions instead of the torus morphology; *ii)* discriminate between the two scenarios using only the SED may lead to ambiguous results, given the degeneracy between the geometrical parameters of the torus, that are unconstrained and that can be better studied through X-ray spectral fitting; *iii)* with the poor sampling of the MIR part of our SEDs (limited to the four IRAC filters and the 24μm Sptizer filter) it is not possible to distinguish between a smooth and a clumpy torus. Thus, we limited our analysis to a smooth geometry which perfectly suites our main aim of accounting for the AGN contribution to the total emission of the galaxy, irrespectively from the torus geometry. The AGN emission is described with a radiative transfer model, which takes into account a primary emission coming from the engine (i.e., the accretion disc), a scattered emission produced by dust, and a thermal component of the dust emission. In particular, the main input parameters are the following: the ratio between the inner and outer radii of the dusty torus; the equatorial optical depth at 9.7 μm; the dust density distribution described by two parameters ($\propto r^{\beta} e^{-\gamma |cos\theta|}$); the opening angle of the dusty torus; the angle Ψ between the equatorial axis and the line of sight; and the AGN fraction (f_{AGN}), defined as the ratio between the AGN IR luminosity and the total IR luminosity (i.e., AGN + SF) in the same bands. In Figure 3.6, we show some AGN models with different τ and Ψ obtained in the SED fitting. It is possible to see how different

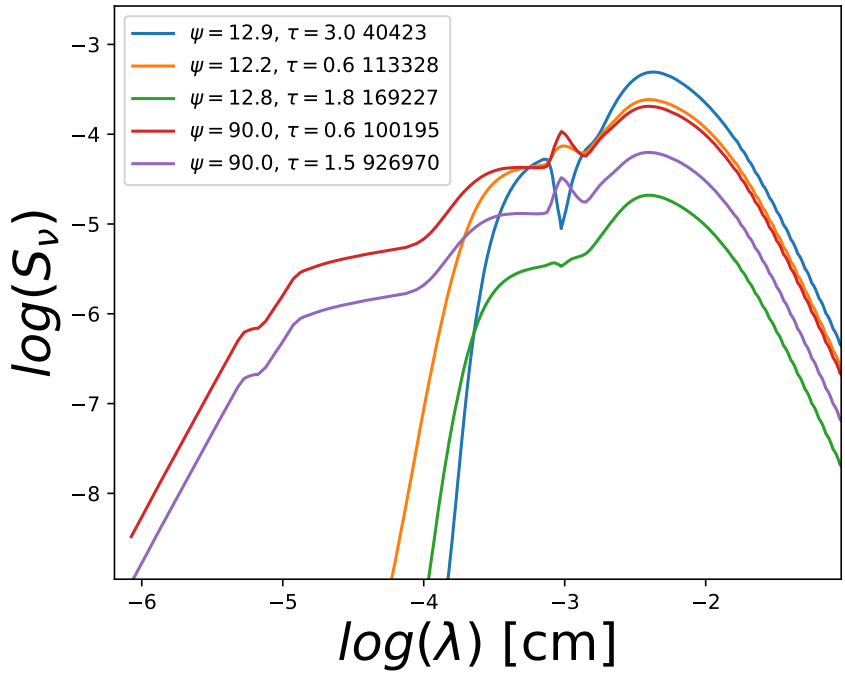

Figure 3.6: Examples of AGN templates adopted in the SED fitting with different values of the optical depth at 9.7 μm (τ) and the angle between the equatorial axis and the line of sight (Ψ).

combinations of these parameters give rise to different shapes and types of AGN (i.e., Type 1 and Type 2). In Table 3.1 we report a summary of all the input parameters used for SED fitting with CIGALE.

3.3.3 SED-fitting results

We performed the SED fitting for the 1620 sources of our sample using CIGALE with the modules described above. For our purposes, we obtained the following output parameters: dust luminosity (i.e., the IR 8-1000 μm luminosity); stellar mass; AGN fraction (f_{AGN},i.e., the ratio between the luminosity due to the AGN and the total emission in the 5-40μm range); τ (equatorial optical depth at 9.7μm); Ψ (angle between equatorial axis and line of sight) parameters of the `fritz2006` model. In addition we also obtained photometric redshift for 110 sources.

Among the 1620 sources for which we performed the fit, we first removed those presenting a high reduced χ^2 (>10). Since our goals are strictly linked to the IR emission of these sources, we also computed the ratio between the ALMA observed flux and the best-fit flux at the same wavelength; sources with a ratio greater than the 5σ (the observed flux error) of the ratio distribution were removed and classified as "bad SED" if we were not able to obtain an acceptable fit. The 5σ threshold was selected in order to be consistent with

Table 3.1: CIGALE parameters used for the SED fitting. The first column reports the name of the templates as well as each individual parameter. In the second column the parameters are reported, and in the third column the descriptions of the parameters are given.

Parameter	Values	Description
SFH (sfhdelayed)		
τ_{main}	1.0, 2.0, 5.0, 7.0 [Gyr]	e-folding time of the main stellar population
age$_{main}$	1.0, 3.0, 5.0, 8.0, 11.0, 12.0 [Gyr]	Age of the main stellar population in the galaxy
τ_{burst}	10.0 [Gyr]	e-folding time of the late starburst population
age$_{burst}$	0.001, 0.01, 0.1, 0.3 [Gyr]	Age of the late burst
f$_{burst}$	0.0, 0.15, 0.30	Mass fraction of the late burst population
Stellar component (bc03)		
IMF	1	Initial mass function: 1 (Chabrier 2003)
Z	0.02	Metallicity
Separation age	10 [Myr]	Age of the separation between the young and the old star populations
Dust attenuation (dustatt_modified_cf00)		
A_V^{ISM}	0.3, 1.7, 2.8, 3.3	V-band attenuation in the interstellar medium
μ	0.3, 0.5, 0.8, 1.0	Ratio of the BC-to-ISM attenuation
slope ISM	-0.7	Power law slope of the attenuation in the ISM
slope BC	-0.7	Power law slope of the attenuation in the BC
Dust emission (dl2014)		
q$_{PAH}$	0.47, 2.5, 3.9	Mass fraction of PAH
U$_{min}$	5.0, 10.0, 25.0, 40.0	Minimum radiation field
α	1.0, 2.0, 3.0	Dust emission power law slope
γ	0.0, 0.02	Illuminated fraction
AGN component (fritz2006)		
r$_{ratio}$	60.0	Ratio of the maximum to minimum radii of the dusty torus
τ	0.6, 1.0, 3.0	Equatorial optical depth at 9.7 μm
β	-0.5	Radial dust distribution within the torus
γ	0.0	Angular dust distribution within the torus
Opening angle	100.0	Full opening angle of the dusty torus
Ψ	0.001, 30.100, 89.99	Angle between equatorial axis and line of sight
f_{AGN}	0.0, 0.1, 0.15, 0.25, 0.50	AGN fraction (1-1000 μm

the "good SED" selection performed by Liu et al. (2019b) and Adscheid et al. (2024) in the catalog construction. We obtained a good fit for 1411 of the 1620 galaxies, with 43 having a new photometric redshift. The remaining 67 galaxies without redshift had a bad fit (i.e., the IR-millimeter photometry did not match the optical part of the SED or the we did not obtain a reduced χ^2 lower than 10), so we decided to exclude them from the final sample, but we consider them in the incompleteness estimate (by correcting with a multiplicative factor the remaining sample). In Figure 3.7 we show the best-fitting SED of three representative objects: a Type II AGN, a Type I AGN, and a galaxy without an AGN component.

In Figure 3.8, we report the redshift distribution (top-left panel) of the sample as well as the results from the SED fitting for stellar mass (bottom left), dust luminosity (bottom right), and AGN fraction (top-right panel) for both the initial (1411) and final (189 after the cut; see Section 3.4) sample of galaxies. The redshift distribution peaks between $z \sim 1.5$ and $z \sim 3$.

The galaxies in the sample are massive, with a peak in the distribution of stellar mass at $\log(M_\star/M_\odot) \sim 11$, consistent with them being SMGs (Chapman et al., 2005; Simpson et al., 2014), although our sample contains sources with masses as low as 10^8 $M_\odot$. The A^{3}COSMOS galaxies are on average IR-bright, most of which have IR luminosities spanning from 10^{11} $L_\odot$ to 10^{13} $L_\odot$. Using the best-fitting templates for each source, we were able to compute the AGN luminosity in a given wavelength range and thus the fractional AGN contribution to the total emission in that range. The 5-40 μm range is particularly sensitive to the presence of an AGN. Therefore, we considered this wavelength interval to derive the fraction of AGN, f_{AGN}, contributing to the luminosity in this range. As can be seen based on Figure 3.8, the distribution is bimodal, and most of the sources ($\sim 65\%$) have an AGN fraction near zero (i.e., they likely do not host an AGN), and the remainder have a f_{AGN} higher than ~ 0.2, peaking at ~ 0.4, with a tail up to $0.8 - 0.9$. The gap between $f_{AGN} = 0$ and higher values is due to the grid we adopted for the SED fitting. Despite the fact that 35% of sources likely host an AGN component (the mean f_{AGN} is ~ 0.4) in the best-fit SED, only a small fraction ($\sim 15\%$) is AGN dominated (i.e., with $f_{\rm AGN} > 0.5$). Also, since the AGN emission is mostly present in the $5 - 40$ μm range, the contribution og the AGN to the $8 - 1000$ μm emission is only a very small fraction. For consistency with Gruppioni et al. (2013) and other SFRD estimates, we used the total (AGN+galaxy) IR emission, stressing that the AGN is strongly subdominant, although a more quantitative analysis is left to a future stand-alone work on the AGN-hosting sub-sample. For these reasons, we did not remove the AGN contribution from the total $L_{\rm IR}$. For those sources that required the computation of a photometric redshift, we find the median error on the photo-z to be ~ 0.25, which is small enough not to affect significantly the results on the IR-LF, derived in the next Chapter.

Finally, we derived the dust-obscured SFR for each galaxy using the Kennicutt (1998b) relation, which assumes the SFR to be proportional to the IR luminosity:

$$SFR(\mathrm{M_\odot yr^{-1}}) \simeq 1.09 \times 10^{-10} \mathrm{L_{IR}(L_\odot)}. \tag{3.2}$$

The resulting SFRs are consistent with those derived as output from the SED fitting (with a ~ 0.15 dex difference in the median values). We compare the $SFR - M_\star$ distribution with respect to the star-forming main sequence (MS, e.g., Speagle et al., 2014, see Figure 3.9). Our sample is characterized by star-forming galaxies with SFRs up to $\sim 10^3\ M_\odot$ yr^{-1}, typical of starbursting galaxies at the considered redshift. In each panel in the figure, we plot the MS from Speagle et al. (2014) computed at the mean redshift of the bin (black solid line) and an upper line (in black dashed line) corresponding to four times the SFR on the MS, at a fixed $M_\star$, which is indicative of the starbursting regime (Rodighiero et al., 2011). Starburst galaxies tend to cluster on a "sequence" above and parallel to the MS, as also noted in other works (Caputi et al., 2017; Bisigello et al., 2018). As our SFR is derived directly from the IR luminosity, this bimodality cannot be simply explained with the parametrization of the SFH or the presence of dust. However, in our case, the selection of pre-selected targets can affect the MS distribution. In particular, we show in Figure 3.9 the distribution of the sources on the MS plane before (1411 sources) and after (189 sources) removing the targeted sources (i.e., the target of the individual pointing) in blue and red. As can be noticed, the red circles mostly occupy the region on the MS. In fact, many of the ALMA observations were targeting bright sub-mm galaxies selected with ground based facilities, likely highly star forming and in the starburst locus of the MS

As previously mentioned, for six out of 189 sources, we were unable to obtain a reasonable fit. The common characteristic of these sources is that they have an SED characterized by optical and ALMA photometry that does not appear to belong to the same object and can only be fitted by assuming extreme, unrealistic templates of dust emission. For this reason, and by inspecting the ALMA and optical cutouts, we decided to treat these sources statistically in the derivation of the LF. The details of the procedure, as well as some examples, are shown in Section 4.1.1.

3.4 Turning an heterogeneous pointed survey into a blind-like survey

As mentioned in Chapter 2 the A^{3}COSMOS survey is based on observations with different sensitivities (i.e., limiting fluxes), resolutions, and ALMA observed-frame wavelengths. The result is a survey of observations with different selection functions. Being a collection of several observations, almost every pointing is centered on a targeted source of interest

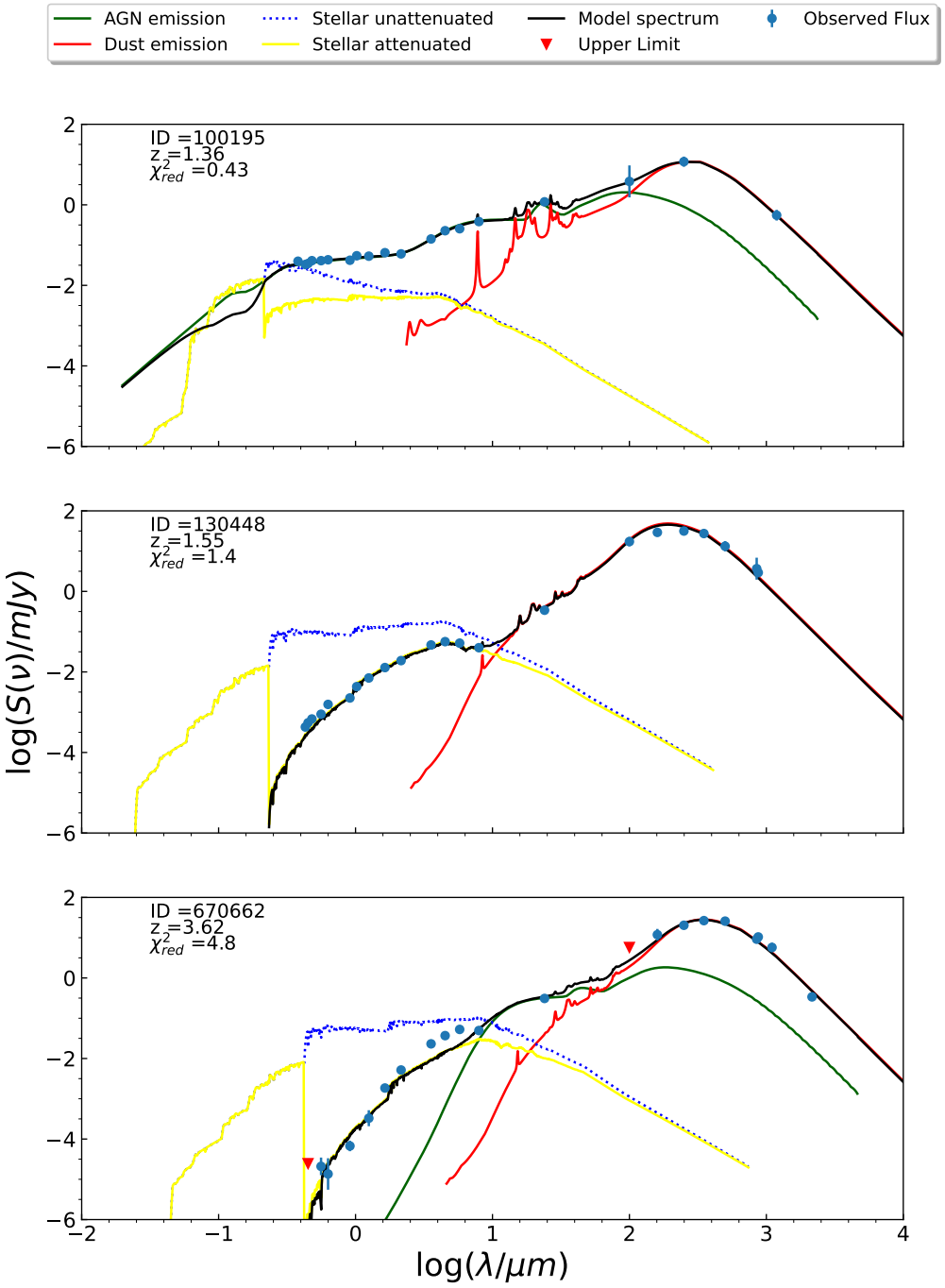

Figure 3.7: Examples of SED-fitting results for three different classes of objects. From left to right: Unobscured AGN SED, SED without an AGN contribution, and obscured AGN component. The blue circles and the red triangles represent data points and upper limits, respectively. The best-fit model is plotted as a black solid line. The stellar attenuated and unattenuated, the dust emission, and the AGN emission are respectively reported as a yellow solid line, a blue dashed line, a red solid line, and a green solid line.

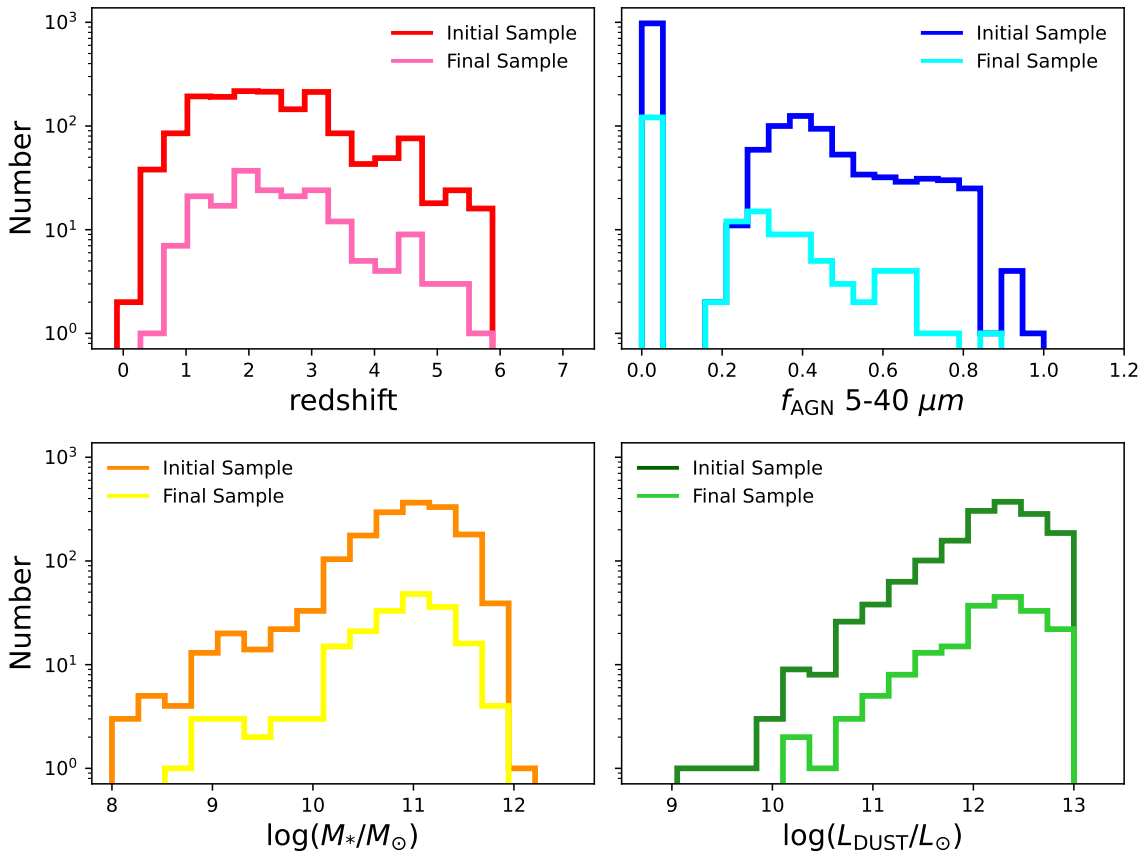

Figure 3.8: Distributions of the main physical parameters obtained through SED fitting for the initial and final, reduced, sample. Top-left panel: Redshift distribution. Top-right panel: AGN fraction distribution, computed in the 5-40 μm range. Bottom-left panel: Stellar mass distribution, in units of solar masses. Bottom-right panel: dust luminosity distribution in solar luminosities.

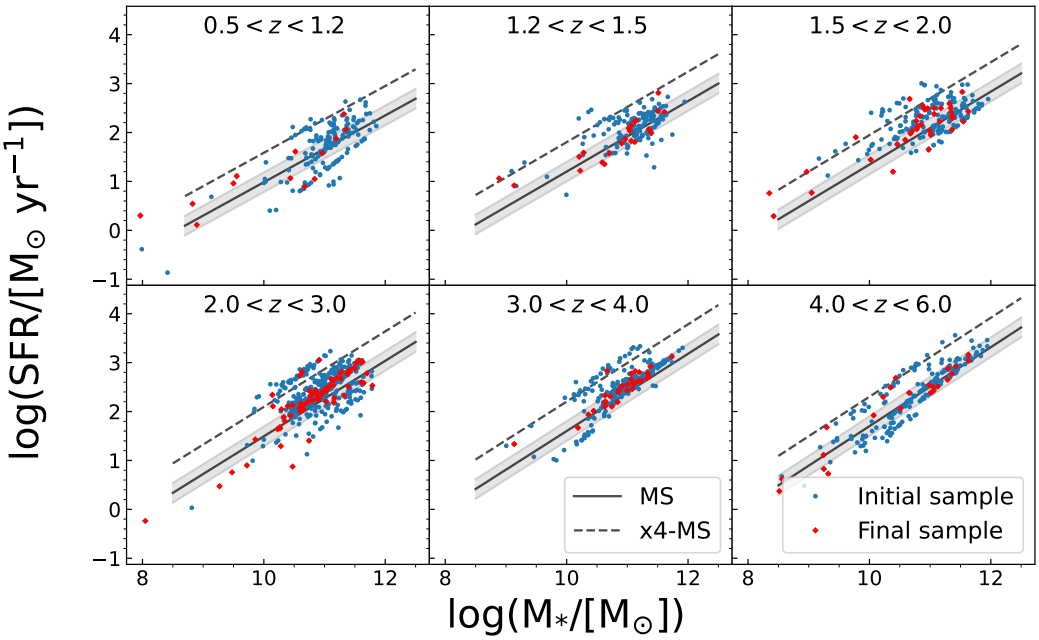

Figure 3.9: Main sequence of galaxies computed in six different redshift bins: 0.5-1.2, 1.2-1.5, 1.5-2.0, 2.0-3.0, 3.0-4.0, 4.0-6.0. Data of the full sample are reported as blue circles, while the red diamonds represent the final sample (3.4.4) used in our analysis. The black solid line and shaded area indicate the main sequence (Speagle et al., 2014) (computed at the mean values of the redshift bins) and 1σ dispersion. Finally, the black dashed lines represent the 4x MS, indicative of the starburst regime.

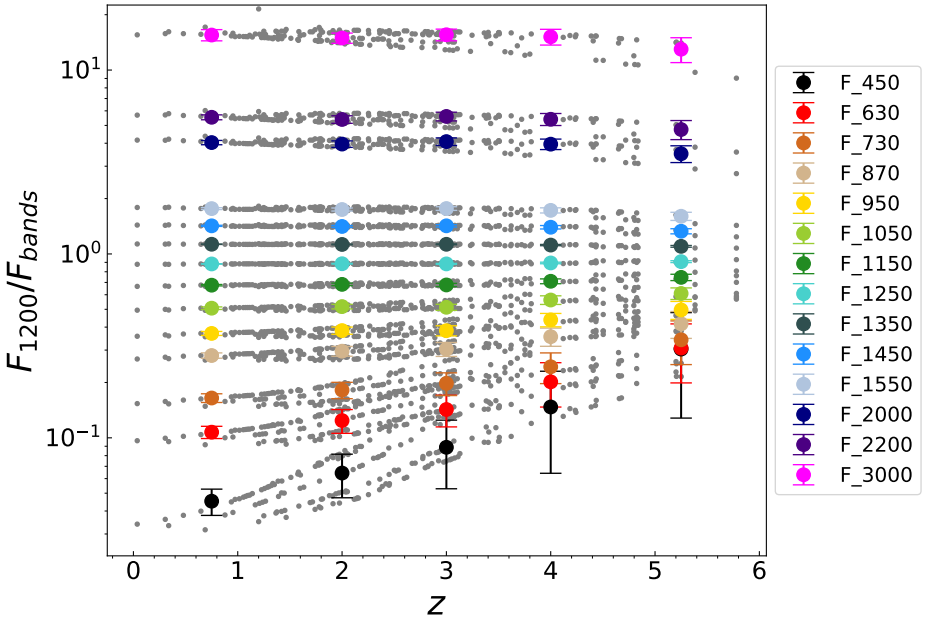

Figure 3.10: Ratio between the flux at 1200 μm and other bands against redshift. The gray circles in the background indicate the values for individual sources in each band, while the colored circles refer to the median values in each redshift bin and for each ALMA band, as described in Section 3.4.2.

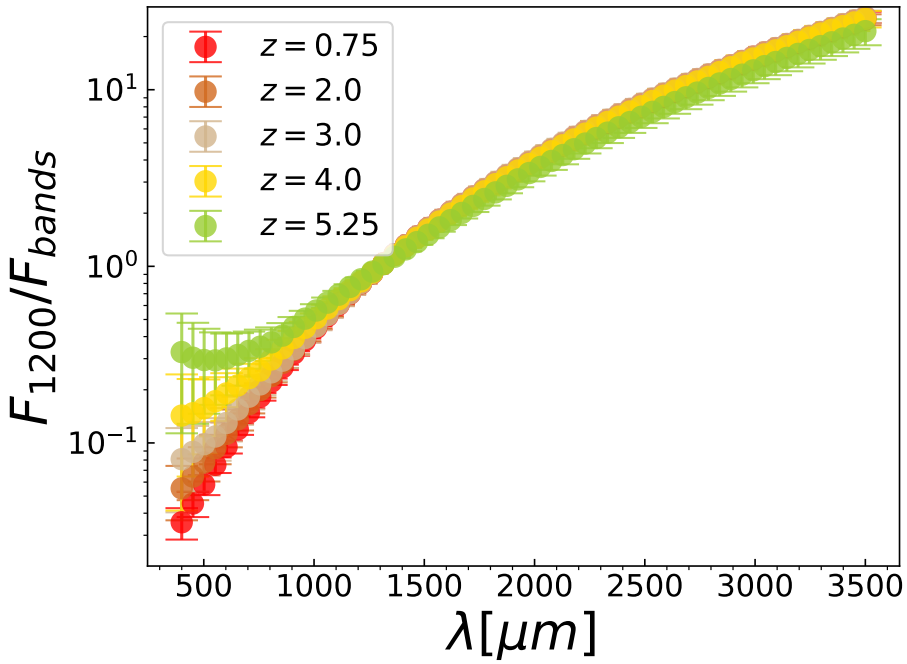

Figure 3.11: Ratio between the flux at 1200μm and in other bands against observed wavelength. Each circle is the median value computed as described in Section 3.4.2. The red, brown, gray, and yellow circles are at $z < 4.5$, while the green circles represent the higher redshift bin at $z > 4.5$.

for that observation. In this perspective, the use of the A^{3}COSMOS survey for statistical purposes (e.g., LF, SFRD) needs a dedicated analysis for turning it into a blind survey. In this section, we discuss the method we used to turn a generic (F)IR-millimeter ensemble of pointed observations into a blind survey (see also Adscheid et al., sub.).

3.4.1 Blind surveys

To derive statistical properties of the sample through the corresponding areal coverage, a blind survey is needed. In order to achieve the construction of a blind survey, the next step should be followed. In determining the limiting flux of A^{3}COSMOS, we scaled the RMS of each individual pointing to the corresponding RMS at our reference wavelength of 1.2 mm based on the corresponding best-fit SED template (Section 3.4.2). We then determined the total area spanned by our survey, accounting for the primary beam attenuation and overlapping pointings (Section 3.4.3). Finally, any possible bias due to the presence of a target was taken into account (Section 3.4.4).

3.4.2 Wavelength homogenisation

The first step in obtaining an unbiased survey from the A^{3}COSMOS sample was the conversion of all observing wavelengths to a reference one. In our case, we chose the $\lambda_{\rm ref} = 1200$ μm wavelength in the observed frame, which falls in ALMA Band 6, as it is the most populated. This way, we could rescale all the fluxes at each observing wavelength ($\lambda_{\rm obs}$) to a reference one ($\lambda_{\rm ref}$) using the fluxes at the observed SEDs in order to infer the observed ratio between $\lambda_{\rm ref}$ and $\lambda_{\rm obs}$ for each source. In particular, we expected a decrease of the flux ratios when going to a higher z and shorter wavelengths, since the two fluxes approaches the rest-frame peak of dust emission in the SED.

As reported in Figure 3.10, we divided the sample into five redshift bins (z<1.5, 1.5-2.5, 2.5-3.5, 3.5-4.5, 4.5-6). For visualization purposes, we plotted only the most populated bands as gray circles. The colored points indicate the median value for a certain λ_{obs} for a specific redshift bin. It can be seen in the figure that for shorter λ_{obs} (close to $\lambda_{\rm ref}$), the ratios are unsurprisingly low and almost redshift independent, while at longer $\lambda_{\rm obs}$ the ratios become larger and more redshift dependent, especially in the highest z-bin.

Figure 3.11 shows the differences between the ratios in the different z-bins. We note that for $z < 4.5$, the correction curves are very similar to each other. For this reason, we used only one mean curve (up to $z = 4.5$) and a different one for $z > 4.5$ in our analysis.

3.4.3 Sensitivity homogenisation

We used the conversion curves obtained as explained in the previous section to convert the RMS in each pointing as if it was observed at 1200 μm. Subsequently, the pointings became characterized by a uniform (in wavelength) sensitivity across their field of view (FoV). However, observing with the ALMA interferometer leads to a primary beam in which the sensitivity of the observation varies radially from the center to the outer regions.

We regrid the full survey into 1" pixels, assigning a specific primary beam correction ($pbcor$) to each pixel, and dividing the RMS by the corresponding $pbcor$. This correction follows a Gaussian function reaching unity at the center of each pointing and decreasing radially to zero:

$$pbcor = e^{-\frac{d^2}{2\sigma^2}}, \tag{3.3}$$

with d being the distance of each pixel from the pointing center, while σ being $FWHM/2.35$. For simplicity, we delimit the area of each pointing to where $pbcor > 0.2$.

For this reason, we divided the sky region covered by our pointings into 1" pixels and flagged the pixels inside a pointing with a flux value corresponding to the sensitivity of that pointing (i.e., primary beam correction higher than 0.2). This approach allowed us to obtain a corrected RMS at the position of each pixel within the pointing. We then converted this corrected RMS to a limiting flux by multiplying it by 4.35, which is the sensitivity cutoff of the prior catalog of A^{3}COSMOS. After this procedure, we ended up with a pixel map of limiting fluxes inside the pointings. However, in the case of overlapping pointings, the selection of an exclusive area was not straightforward. Indeed, the common area between two overlapping pointings has to be counted only once, and the limiting flux from one of the two pointings needs to be assigned to the common area.

This issue has been dealt with by following the Avni and Bahcall (1980) method, which coherently combines multiple samples at different depths. As shown in Figure 3.12, the limiting flux in the common area covered by two or more pointings is the one corresponding to the most sensitive observation at the reference frequency (i.e., the lowest limiting flux among the pointings).

3.4.4 Total areal coverage

We proceeded by deriving the cumulative areal coverage of our survey by combining the effective area accessible by all pointings at each limiting flux. This was done by counting the number of pixels having 4.35xRMS above a given $S_{\rm LIM}$, and deriving the cumulative effective area that is accessible above each corresponding $S_{\rm LIM}$. This method enables us to assign an effective area to each $S_{\rm LIM}$.

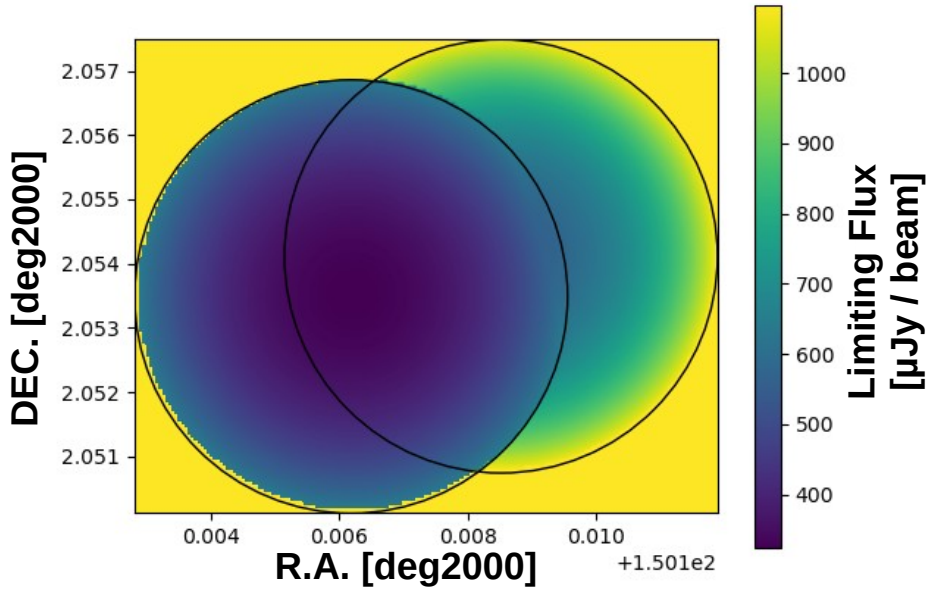

Figure 3.12: Two overlapping pointings in band 6. The black circle represents the adopted pointing size (out to a *pbcor* of 0.2), color-coded by the inferred RMS. Lower RMS values are represented by darker colors and higher values by lighter ones. Outside our primary beam boundary, we set values to the arbitrary high value of 10^6 μJy. In such cases, we adopted the area from the deepest pointing in the overlapping region.

In order to minimize potential biases due to pre-targeted ALMA sources contaminating the selection function, we disregarded central targets as follows. First, we removed the target and all sources within the central 1" of the pointing. Then, to take also into account possible positional offsets between the ALMA follow-up sources and the SMG pointed targets, which are 5" on average (Hodge et al., 2013), we removed the pointings without any ALMA detections in the central 1". In this way we excluded 2060 out of 3215 pointings with potentially wrong serendipitous detections. By removing pointings having no central target, we were confident not to bias our sample towards possible off-center targeted galaxies. The 1" masking was chosen through a simulation varying the mask radius, increasing its size and comparing the retrieved masked number counts with an input distribution (Adscheid et al., sub.). It has been shown that when increasing the central mask radius, no benefit is observed in the convergence of the retrieved number counts. In order to avoid biased statistics due to possible clustering around the pointed targets, we also removed 104 of the 1620 sources with a redshift similar to that of the target by following the criterion from Weaver et al. (2022). For the adopted criterion a source of z_s can be considered to be at the same redshift of another source (z_t) if $|z_s - z_t| < 0.04(1 + z_t)$.

Starting from our initial pool of 1620 sources, after removing potential targets and clustered sources, we end up with 189 sources, which make our final sample. In Figure 3.13 we

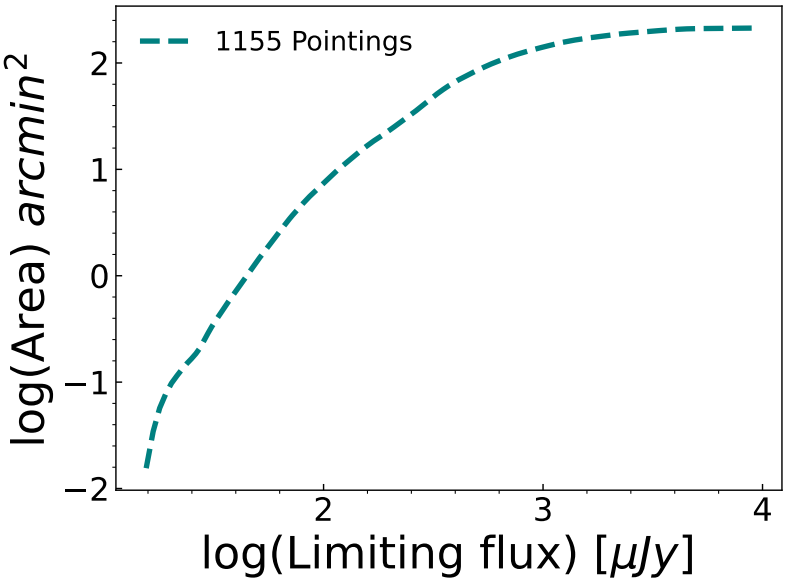

Figure 3.13: Total areal coverage of the final 1155 considered in our work.

show the areal coverage for the final 1155 pointings.

In the next Chapters, we will refer to the sample presented in this Chapter for all the analysis and results.

CHAPTER 4

The total IR luminosity function and dust-obscured star formation rate density

4.1 The A^{3}COSMOS luminosity function

Deriving the areal coverage of our survey allowed us to properly compute the luminosity function with the $1/V_{\rm MAX}$ method (Schmidt, 1970). In the following sections, we describe the method applied to derive the total infrared luminosity function and compare it with previous works.

4.1.1 Method

We used the $1/V_{\rm MAX}$ Schmidt (1970) method to compute the observed IR LF ($\Phi(L_{\rm IR}, z)$) for our final sample, which consists of 1155 individual pointings that can be considered as independent fields. For this reason, by following the Avni and Bahcall (1980) method, we were able to derive the effective areal coverage at each $S_{\rm LIM}$ across all pointings. We then used the relation between area and limiting fluxes, shown in Figure 3.13), to associate an accessible area above a certain flux to each source.

To compute the LF, we divided our sample into eight redshift bins from $z \sim 0.5$ to $z \sim 6$ and into eight logarithmic $L_{\rm IR}$ bins of 0.5 dex width, from $L_{\rm IR} = 10^{10}$ to $L_{\rm IR} = 10^{14}$ L$_\odot$. For each source in a z-$L_{\rm IR}$ bin, we measured the contribution to the LF in that bin by applying a redshift step of $dz = 0.02$ and K-correcting its best-fit SED from the lower to the upper boundary of the corresponding redshift bin, each time computing the observed flux at 1200 μm. We used this flux to infer the corresponding areal coverage at each dz by interpolating the previously derived areal coverage curve (Figure 3.13). Lastly, we combined the effective area obtained in this way with the volume element at each redshift step and obtained a

comoving volume over which a given source is detectable:

$$V_{\rm MAX} = V_{\rm zmax} - V_{\rm zmin}, \tag{4.1}$$

where $V_{\rm zmax}$ and $V_{\rm zmin}$ are the sum of the subvolume in each dz shell up to the upper and lower limits of the bin, respectively. In particular, $V_{\rm zmax}$ can either be the volume at the upper bound of each dz bin or the maximum volume reachable by considering the S/N limit of the survey (i.e., corresponding to the z at which the source would reach the limiting flux, given its luminosity). Finally, we corrected the $V_{\rm MAX}$ by taking into account the completeness and spuriousness corrections derived by Liu et al. (2019b), and we obtained the $\Phi(L_{\rm IR}, z)$ by summing all the $1/V_{\rm MAX}$ in a certain $L_{\rm IR}$-redshift bin.

4.1.2 Unidentified sources

As described in Section 3.3.3, we were unable to obtain a satisfactory fit for the SED of six of the 189 sources. We identified these six sources as potential HST-dark objects. Consequently, having to rely solely on ALMA fluxes (the photo-z is associated with optical photometry), these objects were disgregated from the $1/V_{\rm MAX}$ method but included statistically in the LF analysis. Specifically, we assumed that these sources exist at a redshift greater than $z = 3$, and we utilized the following procedure: first, we computed the cumulative redshift distribution for the rest of the sample, then, for each N-th ($N = 100$) random extraction during the LF calculation, we assigned a redshift ($z > 3$) to each of the sources by drawing from the cumulative distribution function as a random sampler. Once a redshift was drawn, we used the median SED of the sample to "fit" the ALMA flux and consequently to obtain an infrared luminosity to be incorporated into the LF calculation.

4.1.3 The Infrared luminosity function

We obtained the IR LF by using the total (i.e., including all the SED components) $L_{\rm IR}$ computed in the $8 - 1000$ μm range. The z-bins (0.5-1.0; 1.0-1.5; 1.5-2.0; 2.0-2.5; 2.5-3.0; 3.0-3.5; 3.5-4.5; 4.5-6.0) are nearly equally populated, apart from the first bin, which contains slightly fewer sources than the others. The LF is shown in Figure 4.2 as black circles, with the red boxes representing the Poissonian uncertainties: the values are reported in Table 4.1. In each panel, we have overplotted the $L_{\rm IR}$ completeness limit as a vertical black dashed line. This threshold was computed by rescaling the 1200μm flux of each source's SED (within a given $L_{\rm IR} - z$ bin) down to the same $S_{\rm LIM}$, and then taking the highest $L_{\rm IR}$ values at that limit as the 100% completeness $L_{\rm IR}$ limit. The points below the completeness limit are reported as white boxes (with red borders) in Figure 4.2. For comparison, we also report existing IR LF estimates obtained from other studies. In particular, we compared our

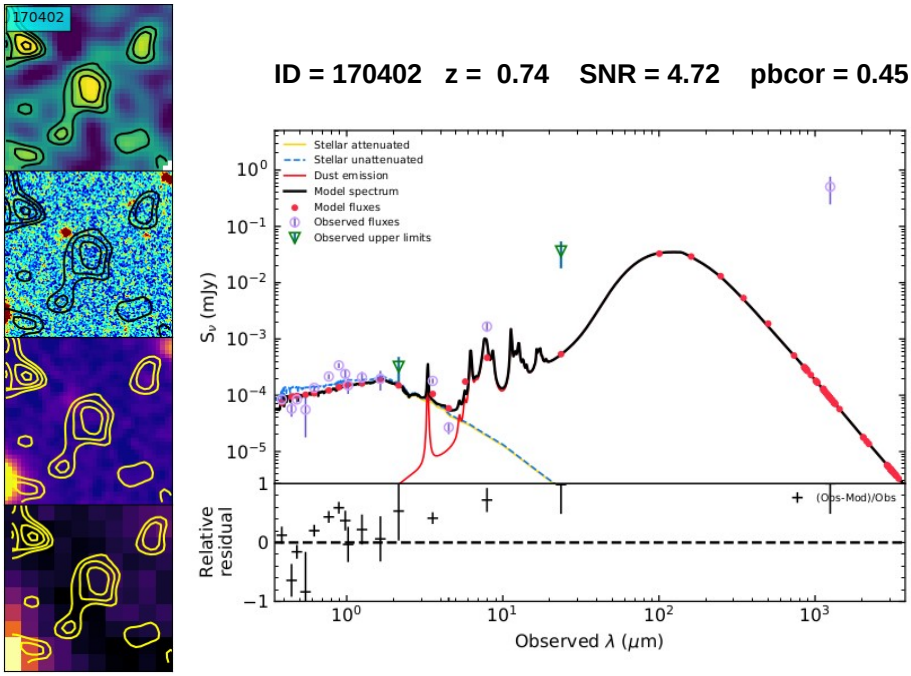

Figure 4.1: Example of a source with optical identification (photo-z = 0.74) likely distinct from the ALMA galaxy. Left panel (from top to bottom): ALMA, acs-I, UltraVista-j, and IRAC1 images are displayed with ALMA contours overlaid. It can be inferred that the optical/NIR object near the ALMA position is not centered in the ALMA galaxy. Right panel: SED of the same object showing how the code struggles to fit the optical and ALMA photometry with a single SED template.

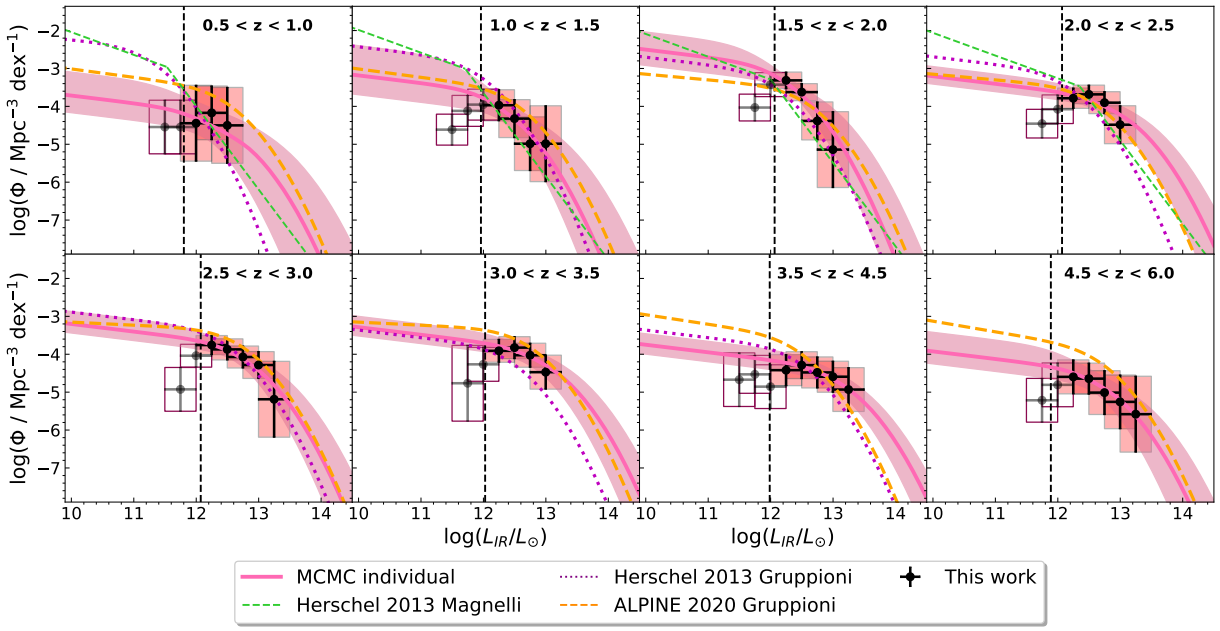

Figure 4.2: A^{3}COSMOS luminosity function (black circles and red boxes). The individual redshift bin MCMC best fit is plotted as pink solid lines and shaded error bands. The redshift ranges are reported in the upper-right corner of each subplot, while the luminosity bins are centered at each 0.25 dex, with a width of 0.5 dex (overlapping bins). The black vertical dashed lines represent the completeness limit of the L_{IR}. The orange dashed, purple dotted, and green dashed lines are the best-fit LFs obtained by Gruppioni et al. (2013), Magnelli et al. (2013), and Gruppioni et al. (2020).

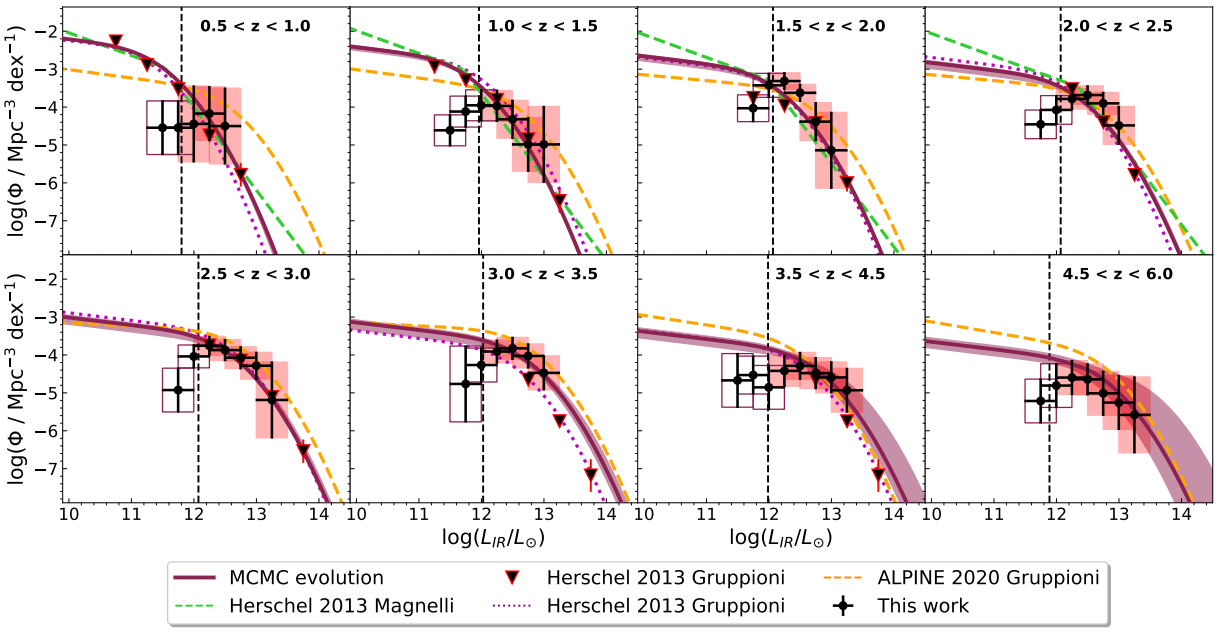

Figure 4.3: A^{3}COSMOS (red boxes and black circles) + *Herschel* (black triangles) luminosity function. The dark-red lines and shaded areas are the best fit obtained by using all the LF points from different z-bins together. The redshift ranges are reported in the upper-right corner of each subplot, while the luminosity bins are centered at each 0.25 dex, with a width of 0.5 dex (overlapping bins). The black vertical dashed lines represent the completeness limit of the $L_{\rm IR}$. The orange dashed, purple dotted, and green dashed lines are the best-fit LFs obtained by Gruppioni et al. (2013), Magnelli et al. (2013), and Gruppioni et al. (2020).

results with the best fit from previous IR works, either from ALMA (ALPINE; Gruppioni et al., 2020) or *Herschel* (PEP+GOODS-H and PEP+HerMES; Gruppioni et al., 2013; Magnelli et al., 2013), when available at consistent redshifts.

As can be seen from Figure 4.2, we mostly sampled the bright end of the luminosity function, as our complete points are only above $\log(L_{\rm IR}/{\rm L}_{\odot}) \simeq 12$ at each redshift bin. This is mainly a consequence of the fact that, at lower redshift, ALMA samples down the Rayleigh-Jeans tail, and therefore even if deep pointings are available, they are inefficient compared to *Herschel*, which samples the peak of the IR SED. The peak of dust emission can be better probed by ALMA (Band 6 and 7 mainly) only at high-redshifts ($z > 3$). Despite this, our data points are in good agreement, within the errors, with the black triangles from *Herschel* (Gruppioni et al., 2013, Figure 4.3), whose $z < 3$ LF estimates are characterized by much higher statistics (smaller error bars) and better sensitivity and are thus able probe the IR LF down to the knee of the IR LF ($log(L_{\rm IR}/L_{\odot}) \sim 11$) and its faint-end. The consistency with independent estimates inferred from *Herschel* (Gruppioni et al., 2013), is reassuring in terms of methodology, despite the poorer ALMA statistics at the faint-end and at low-z. At $z > 3 - 3.5$, where *Herschel* probes further down the peak of the dust emission and ALMA starts probing the peak, our estimates show a systematically higher normalization. Indeed, as stated by Gruppioni et al. (2013), in the $3 < z < 4.2$ range, most of the *Herschel* sources have a photometric redshift, and the PEP selection may be missing a fraction of high redshift galaxies, making their estimate a lower limit. However, it has to be underlined, that our results may be affected by uncertainties on the parameters estimated form the SED fitting. In particular, uncertainties on the IR luminosities, related to a proper characterization of the dust attenuation, may affect the number of galaxies in each luminosity bin, causing possible variations on the knee of the IR-LF. Also, for those galaxies that needed a photo-z computation, errors on the estimate of the redshift may have similar effect of the errors on $L_{\rm IR}$, shifting sources from one redshift bin to the other.

4.1.4 Luminosity function evolution with redshift

In order to trace the number density of galaxies at all redshifts and IR luminosities, we use a functional form to reproduce the IR LF. To this purpose, we modeled our LF with a modified Schechter function (Saunders et al., 1990a) described by four free parameters:

$$\Phi(L)dlogL = \Phi^* \left(\frac{L}{L^*}\right)^{1-\alpha_S} exp\left[-\frac{1}{2\sigma_S^2} log_{10}^2\left(1+\frac{L}{L^*}\right)\right] dlogL, \tag{4.2}$$

where α_S and σ_S represent the faint-end slope and the parameter shaping the bright-end slope, respectively, whereas L^* and Φ^* represent the luminosity and normalization at the knee, respectively. The modified Schechter function is similar to a power law for $L \ll L^*$ and behaves as a Gaussian for $L \gg L^*$.

Table 4.1: Infrared luminosity function as inferred using the A^{3}COSMOS database. In the first column, the luminosity bins are reported, while columns 2-8 report the Φ values in each luminosity and redshift bins. Bold (or italic) values represent independent luminosity bins. Values in round brackets indicate luminosity bins that are below the completeness limit, and numbers in square brackets are the number of sources in each L-z bin.

$\log(L_{\rm IR}/L_{\odot})$	$\log(\Phi/{\rm Mpc}^{-3}{\rm dex}^{-1})$			
	$0.5 < z \leq 1.0$	$1.0 < z \leq 1.5$	$1.5 < z \leq 2.0$	$2.0 < z \leq 2.5$
11.25-11.75	(*-4.54 ± 0.71 [3]*)	(*-4.61 ± 0.41 [8]*)		
11.50-12.00	(**-4.54 ± 0.71 [2]**)	(**-4.12 ± 0.41 [9]**)	(**-4.03 ± 0.35 [9]**)	(**-4.46 ± 0.38 [7]**)
11.75-12.25	*-4.44 ± 1.00 [1]*	(*-3.95 ± 0.41 [9]*)	(*-3.43 ± 0.32 [12]*)	(*-4.08 ± 0.38 [7]*)
12.00-12.50	**-4.17 ± 0.71 [2]**	**-3.97 ± 0.41 [8]**	**-3.31 ± 0.22 [21]**	**-3.79 ± 0.27 [14]**
12.25-12.75	*-4.50 ± 1.00 [1]*	*-4.32 ± 0.50 [5]*	*-3.62 ± 0.22 [20]*	*-3.68 ± 0.24 [17]*
12.50-13.00		**-4.99 ± 0.71 [2]**	**-4.38 ± 0.5 [4]**	**-3.90 ± 0.29 [12]**
12.75-13.25		*-4.99 ± 1.00 [1]*	*-5.14 ± 1.00 [1]*	*-4.48 ± 0.50 [4]*
	$2.5 < z \leq 3.0$	$3.0 < z \leq 3.5$	$3.5 < z \leq 4.5$	$4.5 < z \leq 6.0$
11.25-11.75			(*-4.67 ± 0.71 [2]*)	
11.50-12.00	**(-4.93 ± 0.58 [3])**	**(-4.76 ± 1.00 [1])**	**(-4.53 ± 0.50 [3])**	**(-5.21 ± 0.58 [2])**
11.75-12.25	(*-4.04 ± 0.30 [11]*)	(*-4.27 ± 0.45 [3]*)	(*-4.85 ± 0.58 [2]*)	(*-4.81 ± 0.58 [3]*)
12.00-12.50	**-3.76 ± 0.25 [16]**	**-3.91 ± 0.30 [9]**	**-4.42 ± 0.41 [6]**	**-4.60 ± 0.45 [5]**
12.25-12.75	*-3.87 ± 0.28 [13]*	*-3.83 ± 0.29 [13]*	*-4.29 ± 0.35 [8]*	*-4.64 ± 0.41 [6]*
12.50-13.00	**-4.07 ± 0.29 [12]**	**-4.03 ± 0.32 [11]**	**-4.48 ± 0.41 [6]**	**-5.01 ± 0.58 [3]**
12.75-13.25	*-4.28 ± 0.35 [8]*	*-4.47 ± 0.45 [5]*	*-4.59 ± 0.41 [7]*	*-5.25 ± 0.71 [2]*
13.00-13.50	**-5.19 ± 1.00 [1]**		**-4.93 ± 0.58 [4]**	**-5.58 ± 1.00 [1]**

To find the L^* and Φ^* that best reproduce our LF, we performed a Monte Carlo Markov chain (MCMC) analysis using the PYTHON package `emcee` (Foreman-Mackey et al., 2013), which uses a set of walkers to explore the parameter space simultaneously. We carried out the MCMC analysis using 50 walkers with 10000 steps (draws), discarding the first 1000 sampled draws of each walker (burnin). The likelihood was built in the following form:

$$L = -\frac{1}{2}\sum\left(\frac{\Phi_{\rm Model} - \Phi}{\delta\Phi}\right)^2. \tag{4.3}$$

We ran the MCMC using flat prior distributions for the two free parameters and with α_S and σ_S fixed to the values of Gruppioni et al. (2013) (i.e., α_S=1.2 and σ_S=0.5), with $\log(\Phi^*)$ free to vary between -5 and -2 and $\log(L^*)$ between 10 and 13. The prior distribution was then combined with the likelihood function to obtain the posterior distribution.

We fitted the ALMA points alone (Figure 4.2) in the lower redshift bins (i.e., $0.5 < z < 1.0$ and $1.0 < z < 1.5$). The individual fit showed a very low normalization with respect to the *Herschel* best-fit and large error bands, and it did not allow us to constrain the fit parameters L^* and Φ^* in an accurate way. The discrepancy at $z < 2$ between these estimates and those by Gruppioni et al. (2013) are mainly due to the poorer capability of ALMA, with respect to *Herschel*, in sampling the dust emission peak at low redshift, leading to larger uncertainties in the IR-LF estimates and on its parameters. Between redshift 1.5 and 3.0, the best-fit LF is in good agreement with the *Herschel* one, except for a slightly higher normalization in the $1.5 < z < 2.0$ redshift bin. Finally, between $z = 3$ and $z = 3.5$, our best fit is consistent with that of the ALPINE survey (Gruppioni et al., 2020) but has lower Φ^* at the knee at $z > 3.5$.

Since the ALMA-only LF (Figure 4.3, red boxes) is not able to trace the lowest luminosities, we decided to take advantage of the great number of galaxies and wide coverage in luminosity of the *Herschel* PEP+HerMES survey by Gruppioni et al. (2013) up to $z \sim 3$, with which our sample is consistent, while extending to higher redshifts using our ALMA measurements. This approach enabled us to best characterize the faint-end and the knee of the LF at $z > 3$. Indeed, by using *Herschel*'s LF data at all available redshifts (in Figure 4.3, only those at $0.5 < z < 6$ are shown), our MCMC analysis allowed us to constrain the best-fit parameters of the Schechter function and trace its evolution at higher z.

Previous works already claimed a joint density and luminosity evolution of the IR LF with redshift (see e.g., Caputi et al., 2007; Béthermin et al., 2011; Marsden et al., 2011; Gruppioni et al., 2013) characterized by an increase in luminosity and a decrease in density with increasing redshift. In particular, Caputi et al. (2007) and Béthermin et al. (2011) and Gruppioni et al. (2013) found a break in the redshift evolution resulting in a steepening of the density evolution a $z > 1$ and a flattening of the luminosity one at $z > 2$. For these reasons, we performed a second MCMC fit across all redshift bins, assuming an exponential decline

of the local number density, and two different $z_{\rm break}$ values ($z_{\rho 0}$ and z_{l0}) for the evolution of $\Phi(z)^*$ and $L(z)^*$, expressed as:

$$\begin{cases} \Phi^* = \Phi_0^*(1+z)^{k_{\rho 1}} & z < z_{\rho 0} \\ \Phi^* = \Phi_0^*(1+z)^{k_{\rho 2}}(1+z_{\rho 0})^{(k_{\rho 1}-k_{\rho 2})} & z > z_{\rho 0}, \end{cases} \tag{4.4}$$

$$\begin{cases} L^* = L_0^*(1+z)^{k_{\rm l1}} & z < z_{\rm l0} \\ L^* = L_0^*(1+z)^{k_{\rm l2}}(1+z_{\rm l0})^{(k_{\rm l1}-k_{\rm l2})} & z > z_{\rm l0}, \end{cases} \tag{4.5}$$

where Φ_0^* and L_0^* are the normalization and characteristic luminosity at $z = 0$ and $k_{\rho 1}$, $k_{\rho 2}$, $k_{\rm l1}$, and $k_{\rm l2}$ are the exponents for values lower and greater than $z_{\rho 0}$ and $z_{\rm l0}$ for Φ and L, respectively. In this second fit, each point of the LF is associated with a redshift corresponding to the median value of the galaxy population inside the individual redshift bin. By using these values, we could provide a broader and smoother description of the evolving Φ^* and L^*. From this fit, we obtained two evolution curves (L^* and Φ^* versus z) that take into account the shape of the LF at each z. The priors used in this MCMC are given for the parameters that regulate the evolution of the LF, while α_S and σ_S are fixed to 1.2 and 0.5 (found by Gruppioni et al. (2013) at $z \sim 0.15$) which anchor Φ^* and L^* to their value at $z \sim 0.7$ found with *Herschel*-only measurements. In particular, we fixed the L^* and Φ^* at $z \sim 0.7$ to be the same found by *Herschel*. The best-fit curve at each z-bin is shown in Figure 4.3 as a dark-red solid line and shaded errors.

The trend with redshift of L^* and Φ^* is reported in Figure 4.4, and the results of the MCMC fit are reported in Tables 4.2 and 4.3, representing the 16th and 84th percentiles' error bands and the best-fit values at $z = 0$. The curve from the evolutionary MCMC and uncertainties are reported as dark-red lines and shaded areas. For comparison, the estimates of the individual fit are plotted as pink diamonds for the ALMA-only case. From Figure 4.4, it is possible to observe that the values of L^* and Φ^* estimated by fitting only the A^{3}COSMOS data points are slightly inconsistent with the results obtained using A^{3}COSMOS plus *Herschel* (at $z < 2$). As mentioned before, this is due to the limited ability of ALMA to trace the dust peak emission at $z < 2$ and to the larger weight of *Herschel* data (containing more sources) in the combination. The evolution of Φ changes from $z < z_{\rho 0} = 0.89^{+0.07}_{-0.14}$ to lower values, with an evolutionary trend of $\Phi^* \propto (1+z)^{-0.55}$ for $z < z_{\rho 0}$ and $\Phi^* \propto (1+z)^{-3.41}$ for $z > z_{\rho 0}$. Overall, a decreasing trend was observed. This can be interpreted as a decreasing density of the bulk of star-forming galaxies at a given redshift. Notably, L^* shows two different trends with redshift below and above the break. In particular, for $z < z_{l0} = 3.03^{+0.87}_{-0.73}$, L^* evolves as $(1+z)^{3.41}$ and for $z > z_{\rm l0}$ as $L^* \propto (1+z)^{0.59}$, thus becoming flatter at higher redshifts. The evolutionary trend of L^* can be ascribed to downsizing (Thomas et al., 2010b), that is, brighter (massive, according to the $SFR-M$ relation) galaxies formed earlier than

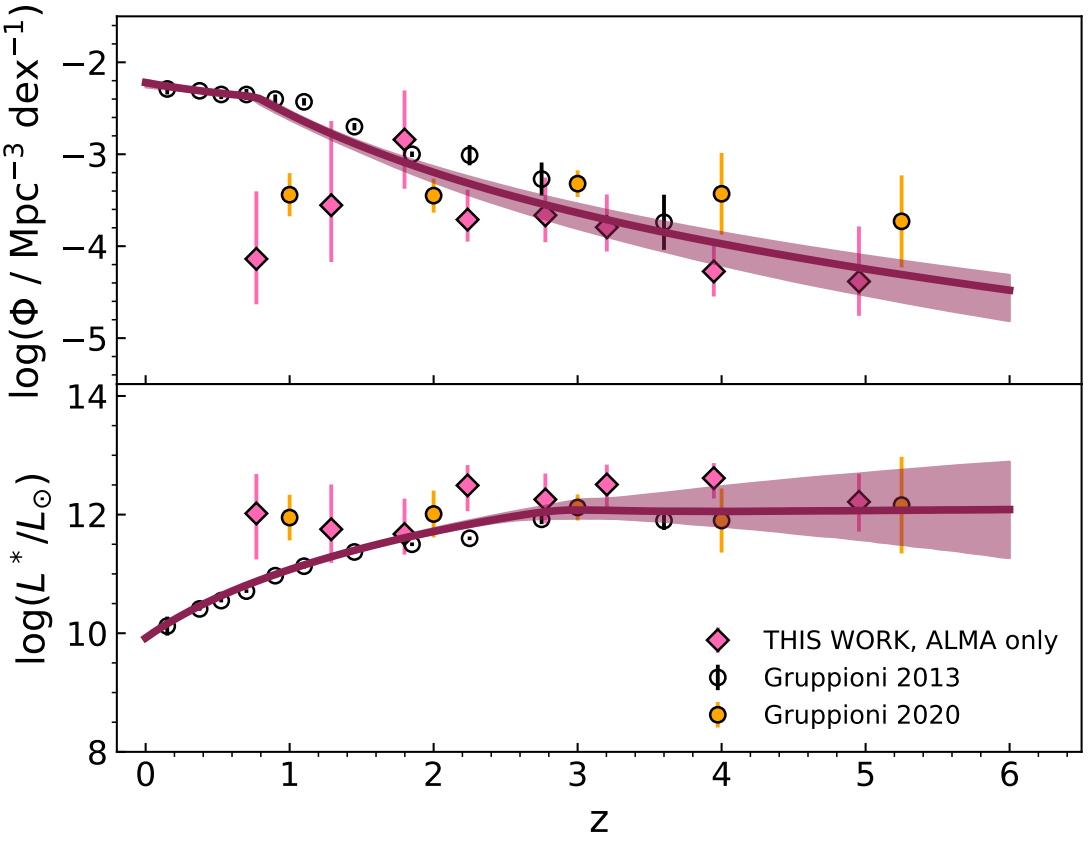

Figure 4.4: Evolutionary trends of Φ^* (top panel) and L^* (bottom panel) with redshift. The solid dark-red lines and shaded areas show the MCMC-based redshift evolution of Φ^* and L^* across all the redshifts, while the pink diamonds are the estimates obtained when fitting each redshift bin individually in the ALMA-only case. Finally, the empty black circles and yellow circles represent estimates for L^* and Φ^* from Gruppioni et al. (2013) and Gruppioni et al. (2020), which we include for comparison.

their fainter (less massive) counterparts. A similar analysis has already been performed by Gruppioni et al. (2013) using the *Herschel* PEP/HerMES LF (indicated with black empty circles in Figure 4.4), finding a consistently decreasing Φ^* and increasing L^*. However, their value of z_{10} (i.e., $z_{10} \sim 2$) is lower than ours ($z_{10} \sim 3$). The evolution is in very good agreement with the *Herschel*-only results (empty black circles) and with the ALPINE estimates at $z > 4$.

4.2 Dust-obscured SFRD up to $z \sim 6$

Finally, using the best-fit luminosity function in each redshift bin, we derived the co-moving SFRD. In particular, we first obtained the IR luminosity density ($\rho_{\rm IR}$) by integrating the

Table 4.2: Best-fit parameters at the knee of the IR-LF. Luminosities (L^*) and normalizations (Φ^*) with 16th, 50th, and 84th percentiles at the knee in the eight redshift bins obtained through the MCMC analysis or, in the ALMA+*Herschel* case, using the information from all the redshifts together.

z	$\log(L^*/L_\odot)$ 16th	$\log(L^*/L_\odot)$ 50th	$\log(L^*/L_\odot)$ 84th	$\log(\Phi^*/\mathrm{Mpc}^{-3}\mathrm{dex}^{-1})$ 16th	$\log(\Phi^*/\mathrm{Mpc}^{-3}\mathrm{dex}^{-1})$ 50th	$\log(\Phi^*/\mathrm{Mpc}^{-3}\mathrm{dex}^{-1})$ 84th
$0.5-1.0$	10.93	10.94	10.95	-2.49	-2.44	-2.40
$1.0-1.5$	11.27	11.29	11.31	-2.84	-2.77	-2.73
$1.5-2.0$	11.58	11.61	11.66	-3.19	-3.09	-3.04
$2.0-2.5$	11.79	11.84	11.90	-3.44	-3.32	-3.24
$2.5-3.0$	11.93	12.05	12.15	-3.71	-3.55	-3.46
$3.0-3.5$	11.93	12.07	12.27	-3.90	-3.71	-3.61
$3.5-4.5$	11.81	12.05	12.47	-4.20	-3.97	-3.84
$4.5-6.0$	11.57	12.07	12.69	-4.53	-4.24	-4.10

Table 4.3: Values at $z = 0$ obtained from the MCMC fit across all redshifts. Values at $z = 0$ obtained from the MCMC evolutive fit. The slope priors α_S and σ_S are fixed to the values found by Gruppioni et al. (2013).

$\log(L_0^*)$	$\log\Phi_0^*$	kl_1	kl_2	z_l	$k\rho_1$	$k\rho_2$	z_ρ	α	σ
$9.90^{+0.07}_{-0.07}$	$-2.20^{+0.07}_{-0.07}$	$3.41^{+0.83}_{-0.16}$	0.59^{+*}_{-*}	$3.03^{+0.87}_{-0.73}$	$-0.55^{+0.62}_{-0.16}$	$-3.41^{+0.31}_{-0.67}$	$0.89^{+0.07}_{-0.14}$	1.2^f	0.5^f

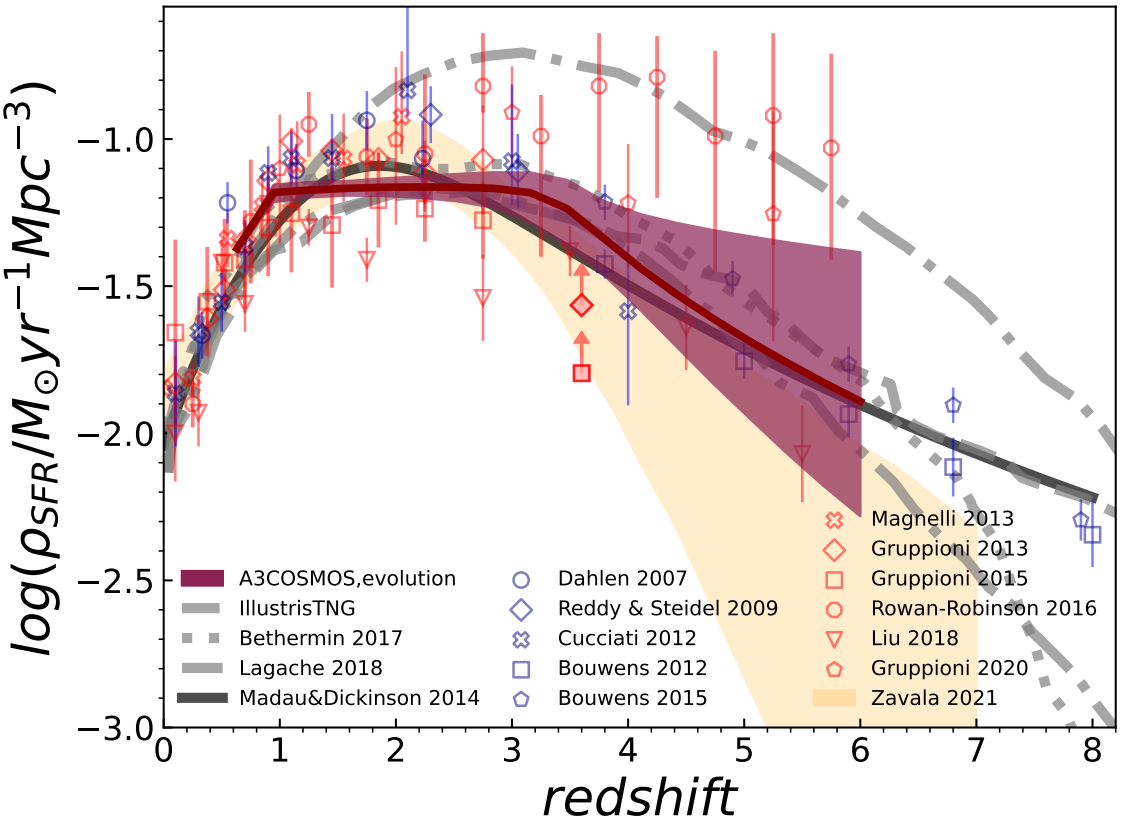

Figure 4.5: Co-moving SFRD evolution with z. The dark-red shaded area was obtained by integrating the evolutionary LF from $z = 0.5$ to 6. Comparison curves from the literature are reported as gray dash-dotted (pessimistic and optimistic cases; Lagache et al. 2018), dashed (IllustrisTNG), dotted (Bethermin et al. 2017), and black solid lines Madau & Dickinson (2014). The empty red circles with different symbols represent different IR/millimeter estimates of the SFRD from Gruppioni et al. (2013), Magnelli et al. (2013), Gruppioni et al. (2015a), Rowan-Robinson et al. (2016), Liu et al. (2018), and Gruppioni et al. (2020), and the orange shaded area is the dust-obscured SFRD by Zavala et al. (2021b), from the MORA survey. The SFRD from UV surveys is plotted as empty blue circles with different markers (Dahlen et al., 2007; Reddy and Steidel, 2009; Bouwens et al., 2012; Cucciati et al., 2012; Bouwens et al., 2015).

Table 4.4: Star formation rate density obtained by integrating the LF best-fit in our eight redshift bins. The second column is the median value, while third and fourth columns show the lower and upper 16th boundaries.

z	$\log\rho_{\rm SFR}$ $[{\rm M}_\odot{\rm yr}^{-1}{\rm Mpc}^{-3}]$	$\log\rho_{\rm SFR}$	$\log\rho_{\rm SFR}$
	50th	16th	84th
$0.5-1.0$	-1.25	-1.27	-1.23
$1.0-1.5$	-1.17	-1.20	-1.15
$1.5-2.0$	-1.16	-1.19	-1.14
$2.0-2.5$	-1.16	-1.20	-1.13
$2.5-3.0$	-1.17	-1.23	-1.12
$3.0-3.5$	-1.19	-1.29	-1.12
$3.5-4.5$	-1.40	-1.53	-1.24
$4.5-6.0$	-1.67	-1.92	-1.32

IR LF in each z bin from $log(L_{\rm IR}) = 8$ (to be consistent with other IR-based SFRDs) to $log(L_{\rm IR}) = 14$:

$$\rho_{\rm IR}(z) = \int_{8}^{14} \Phi(logL_{\rm IR,z}) L_{\rm IR}\, dlogL_{\rm IR}. \tag{4.6}$$

Then, we could convert the IR luminosity density into a SFRD by applying the Kennicutt (1998b) relation to convert $L_{\rm IR}$ to SFR, assuming a Chabrier (2003) IMF. As described in Section 4.1.4, in addition to the individual fit, we performed an MCMC fit by taking the information from all the redshift bins together in order to derive the redshift evolution of L^* and Φ^*. In this way, we obtained the LF at each redshift from $z \sim 0.5$ to $z \sim 6$, and we integrated the LF[$L^*(z)$,$\Phi^*(z)$)] in the full redshift range (for clarity, we report the results of the fit for the eight bins of our IR LF). The result was an evolution curve of the SFRD with the redshift, shown in Figure 5.4. The values of the SFRD and error bands are reported in Table 4.4. The dark-red solid lines with the shaded area represents the SFRD and its lower and upper boundaries derived as the errors on the integration of the LF at each redshift. In order to compare our values with those from the literature, in the figure we have overplotted previous SFRD measurements or model estimates Madau and Dickinson (2014), Béthermin et al. (2017), and Lagache (2018) and the IllustrisTNG simulation (Pillepich et al., 2018a). Estimates of the dust-obscured SFRD from other IR-millimeter works (Gruppioni et al., 2013; Magnelli et al., 2013; Gruppioni et al., 2015a; Rowan-Robinson et al., 2016; Liu et al., 2018; Gruppioni et al., 2020) are reported as empty red circles with different markers. The empty blue circles represent the SFRD from UV works, corrected from dust attenuation, by Dahlen et al. (2007), Reddy and Steidel (2009), Bouwens et al. (2012), Cucciati et al. (2012), and Bouwens et al. (2015).

Thanks to the use of the *Herschel* data points, combined with the ALMA ones, in the LF fit, we were able to derive accurate estimates of the dust-obscured SFRD at $z < 3$ as welll as at higher redshifts. We found that the SFRD computed at $z \sim 0.5 - 1.0$ follows the rise described by Madau and Dickinson (2014) (dark-gray curve) and is consistent with the IR and UV estimates from previous works. Although our points up to $z \sim 2$ have a lower normalization with respect to those from Gruppioni et al. (2013) and Magnelli et al. (2013), this discrepancy may be explained by the different types of fit performed, which results in a different extrapolation to the faint end. From $z \sim 2$ to $z \sim 3.5$, the SFRD follows a flat trend, being above the Madau and Dickinson (2014). This flattening of the SFRD is compatible with predictions from models that envisage the early formation of massive spheroids (see Calura and Matteucci, 2003). As mentioned before, at $z > 3$, our estimates were derived using ALMA alone (last three redshift bins). The observed trend is a decrease of the dust-obscured SFRD up to $z \sim 6$, even though the limited number of sources does not allow us to strictly constrain the SFRD evolution at those redshifts. We found the $z > 3$ dust-obscured SFRD to be consistent with the dust-corrected UV estimates and with the estimate of Madau

and Dickinson (2014), while in the lower boundary, we found it to be consistent with the dust-obscured SFRD derived by Zavala et al. (2021b), although with a ~ 0.5 dex difference between the mean values. The upper boundary is consistent with Gruppioni et al. (2020), pointing toward a possibly underestimated SFRD at $z > 3$. However, this underestimation, as traced by our data, seems not to be as extreme as suggested by Rowan-Robinson et al. (2016) and Gruppioni et al. (2020).

4.3 Summary and conclusions

Owing to the photometric coverage of COSMOS2020 + ALMA, we were able to perform SED fittings using the CIGALE code to constrain the SFR, $L_{\rm IR}$, and $M_\star$ of the full ALMA sample. Applying the Avni and Bahcall (1980) method, we were able to reconcile the overlapping regions between several pointings and correctly evaluate the depth of such regions. Moreover, we derived an SED-based method to homogenize the pointings at different observing wavelengths, converting the RMS noise into that of the reference wavelength. By removing pointings without a detected target and by correcting for clustering, we were able to turn A^{3}COSMOS into an untargeted, "blind-like" survey. We thus derived the total infrared luminosity function in the $8 - 1000\mu$m band using the $1/V_{MAX}$ (Schmidt, 1970) method and using the already available data from *Herschel*. We estimated the LF from $z \sim 0.5$ to $z \sim 6$ and performed an MCMC simulation to fit the LF data, including the possibility for the characteristic parameters (Φ^* and L^*) to evolve with redshift. By integrating the LF, we derived the infrared luminosity density and thus the dust-obscured SFRD up to $z \sim 6$. We summarize the conclusions of this work as follows:

- We find the A^{3}COSMOS sample to be characterized by galaxies that are massive ($\log(M_\star/\mathrm{M}_\odot) = 10-12$) and bright in the IR ($8-1000\mu$m) domain, with $\log(L_{\rm IR}/\mathrm{L}_\odot) = 11-13.5$. Converting $L_{\rm IR}$ into SFR, we obtained values typical of normal star-forming (SFR $\sim 1 - 100$ $\mathrm{M}_\odot\mathrm{yr}^{-1}$) and starbursting galaxies (SFR $\sim 100 - 1000$ $\mathrm{M}_\odot\mathrm{yr}^{-1}$).

- We find our LF to be in good agreement with the existing literature (in particular at $z > 1$), though it pushes the SFRD to $z \sim 6$ with unprecedented statistics.

- Our MCMC analysis suggests a joint redshift-decreasing number density and a redshift-increasing IR luminosity for ALMA-selected star-forming galaxies. This result is consistent with these galaxies being less frequent and more luminous (i.e., massive) when going toward higher redshift.

- Our estimates of the dust-obscured SFRD are consistent with those from other IR surveys and with the UV dust-corrected estimates. Also, we found a broader peak in the SFRD, with a smooth decrease at $z > 4$, which suggests a significant contribution from the obscured SFRD at high redshift. Furthermore, a contribution to the SFRD, particularly at high redshifts, could originate from HST-dark sources (Franco et al., 2018b; Wang et al., 2019; Talia et al., 2021; Enia et al., 2022; Behiri et al., 2023), which are not, a priori, included in a prior sample, with the exception of the six added sources.

Our study of the physical (i.e., stellar mass, dust luminosity, star formation rate) and statistical (LF and SFRD) properties of the ALMA sample of galaxies in the COSMOS field resulted in the detection and characterization of a star-forming and starbursting dominated population, $\sim 40\%$ of which likely host an AGN. We also found that the A^{3}COSMOS sample evolves both in luminosity (L^*) and density (Φ^*) and significantly contributes to the total (IR+UV) SFRD also at $z > 3$. However, in order to improve our knowledge and put tighter constraints on the evolution and formation of galaxies at higher z, more statistics are needed. Being constantly updated, the A^{3}COSMOS catalog represents a key survey for reaching newer results with better statistics. With JWST, the future COSMOS-Web survey (Casey et al., 2022) will also play an important role in covering the COSMOS field, allowing surveys to obtain better photometric coverage and thus allowing the physical properties of galaxies to be better constrained.

CHAPTER 5

The total Star Formation Rate Function: comparison with state-of-the art models

5.1 Introduction

Understanding how galaxies form and evolve has been a topic of interest of both observational and numerical astrophysics from the past decades up to present days. In fact, the characterization of all the physical mechanisms behind the evolution of galaxies is not an easy task and may require a variety of different observation types (i.e., photometric as well as spectroscopic) and models and/or numerical simulations. In particular, large use has been made of simulations and semi-analytical models (SAMs) in the past years (White and Frenk, 1991; Kauffmann et al., 1993; Springel et al., 2001; Bower et al., 2006; Croton et al., 2006; Monaco et al., 2007; Somerville et al., 2008; Fontanot et al., 2009; Guo et al., 2011; Benson, 2012; Menci et al., 2012; Somerville et al., 2012; Henriques et al., 2013; Gruppioni et al., 2015b; Henriques et al., 2015) to widely investigate the physics that rules galaxy formation and evolution. In order to probe the formation of stars, the star formation rate (SFR) represents the most accurate indicator for retrieving information on the instantaneous growth in stellar mass ($M_\star$), rather than using a cumulative quantity such as the total $M_\star$ of the galaxy.

Although SFR of galaxies is an informative parameter to investigate galaxy evolution, their derivation can be subject to several limits, due to the bands of observation. Indeed, different estimates of the SFR of a galaxy can be provided by measuring luminosities in different observing bands like the ultraviolet (UV) or the infrared (IR), as well as individual emission lines (e.g., Hα). Different relations have been derived and calibrated to convert from these luminosities into a corresponding SFR (e.g., Kennicutt, 1998a; Kennicutt, 1998b; Kennicutt and Evans, 2012b; Smit et al., 2012). In the last ten years, many works have been

performed, devoted to the investigation of the main components that regulate the SF and have compared observational results (i.e., the observed star formation rate function, SFRF, Reddy et al., 2008; Oesch et al., 2010; van der Burg et al., 2010; Ly et al., 2011; Magnelli et al., 2011; Cucciati et al., 2012; Smit et al., 2012; Gruppioni et al., 2013; Magnelli et al., 2013; Patel et al., 2013; Sobral et al., 2013; Duncan et al., 2014; Bouwens et al., 2015; Alavi et al., 2016; Parsa et al., 2016; Gruppioni et al., 2020) with predictions from simulations and models (Davé et al., 2011; Fontanot et al., 2012; Tescari et al., 2014; Gruppioni et al., 2015b; Katsianis et al., 2017; Katsianis et al., 2021). These studies have highlighted a tension between observational results in different bands as well as observational results and simulations. On the one hand, UV and IR estimates seem to sample different regimes of SFRs, being in certain cases complementary. On the other hand, simulations and models without the addition of an active galactic nucleus (AGN) and without a proper characterization of supernovae (SNe) are not able to reproduce both the faint and the bright ends of the star formation rate functions (SFRFs), especially at the higher redshifts ($z \geq 2$ Gruppioni et al., 2015b).

In order to further investigate the evolution of the SFR with z, and the reason of this tension, large surveys are needed. To this purpose, the A^{3}COSMOS represents an ideal test-bed for simulation and SAMs, probing the IR-mm SFRF over a wide redshift range ($z \sim 0 - 6$). The physical and statistical analysis of the A^{3}COSMOS sample have already been performed in Chapter 4, aimed at deriving the total IR-LF and SFRD at different redshifts. In this Chapter, we present new estimates of the SFRF covering redshifts from 0 to 6 and compare our results with those from UV studies, as well as to those from simulations and SAMs.

The Chapter is organized as follow: in Section 5.2 we present the sample used to derive the SRFR; in Section 5.3 we explain how we derive the SFRF for the A^{3}COSMOS survey and compare it with other observational results and estimates from simulations; in Section 5.4 we show the comparison between observed and predicted SFRD; in Section 5.5 the conclusions will be presented.

5.2 The data

5.2.1 IR-mm Sample

In this analysis, we used the sample described and obtained in Chapter 2 and 3, which is well suited for statistically studying star formation properties and compare them with models. Figure 5.1 shows the SFR distribution of the full 1620 galaxies sample (cyan histogram) and for the subsample of 189 sources (teal histogram). Both distributions peak at SFR $\sim$

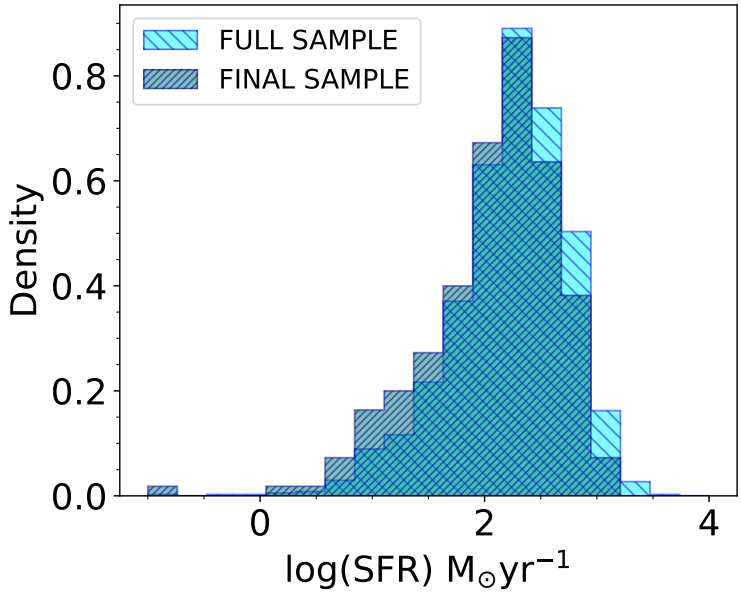

Figure 5.1: Density distributions of the IR-SFR obtained through SED fitting for total A3COSMOS sample (cyan) and for the sub-sample considered in this work (teal).

$100 - 1000$ M$_\odot$yr^{-1}, most of which were excluded from the parent A^{3}COSMOS sample because they were pre-targeted sources.

In order to accurately constrain the parameters of the best-fit SFRFs, we have combined the A^{3}COSMOS IR-SFRFs with those obtained from *Herschel* (Gruppioni et al., 2015b), containing a much larger number of sources, as done also in thre previous Chapter for the IR-LF. How the combination of the two dataset is performed, will be explained in Section 5.3.1.

5.2.2 UV datasets

Although the star formation derived using the $L_{\rm IR}$ has been proven to account for a large fraction of the total SFR of a galaxy (Wuyts et al., 2011; Pannella et al., 2015), it traces only the obscured part, the fractional contribution of the IR to UV derived SFRs may change at $z > 3$. For this reason, we included in our analysis the UV-SFRF from seven works from the literature, broadly spanning the redshift range from 0 to 6 (to be consistent with our IR/mm sample):

- van der Burg et al., 2010 derive the UV-SFRF in the range $3 < z < 5$, using $\sim 10^5$ Lyman-break galaxies from the CFHT Legacy Survey Deep fields.

- Cucciati et al., 2012 study the UV-SFRF of I-band selected galaxies using the VVDS surveys, from the local Universe up to $z \sim 4.5$.

- Parsa et al., 2016 explore the UV-SFRF from $z \sim 2$ to $z \sim 4$ combining the HUDF, CANDELS/GOODS-south and UltraVISTA/COSMOS surveys.
- Mehta et al., 2017 use the UVUDF to derive the UV-SFRF of Lyman-break galaxies at $z \sim 1.5 - 3$.
- Ono et al., 2018 study the UV-SFRF towards higher redshifts ($z \sim 4 - 7$) through the Great Optically Luminous Dropout Research Using Subaru HSC (GOLDRUSH).
- Adams et al., 2020 derive the SFRF at $z \sim 4$ combining the COSMOS survey and the *XMM-Newton* Large-Scale Structure fileds.
- Bouwens et al., 2021, 2022 use a combination of several fields to derive the UV-SFRF at $z \sim 2 - 9$.

Using this data, we will take into account the unobscured contribution to the total SFRF at each redshift. similarly to what we do with the ALMA+*Herschel* SFRFs, we combine together also the different UV-SFRF estimates (see Section 5.3.1).

5.3 The IR and UV SFR function

To derive the SFRF, we start from the IR and UV luminosity functions, converting $L_{\rm IR}$ and UV magnitudes into SFRs. Specifically, for the conversion of $L_{\rm IR}$ to SFR, we employed the Kennicutt (1998b) relation (for a Chabrier IMF):

$$SFR_{\rm IR}({\rm M_\odot yr^{-1}}) = 1.09 \times 10^{-10} \frac{L_{\rm IR}}{L_\odot}. \tag{5.1}$$

To derive the SFR from the UV luminosity, we used the UV LF estimates corrected for dust attenuation. We first converted the absolute UV magnitude into UV luminosity:

$$L_{\rm UV,corr} = 10^{-0.4(M_{\rm UV,corr} - 51.60)} \tag{5.2}$$

Finally, from $L_{\rm UV,corr}$, we then calculated the UV corrected component of the SFR as follows (see Kennicutt and Evans, 2012b):

$$SFR_{\rm UV,corr}({\rm M_\odot yr^{-1}}) = 0.82 \times 10^{-28} \frac{L_{\rm UV,corr}}{\rm ergs^{-1}Hz^{-1}}, \tag{5.3}$$

5.3.1 The method

In order to measure the IR and UV SFRFs, we first fitted our data (IR and UV separately) by performing a Monte Carlo Markov chain (MCMC) analysis, thus obtaining a best-fit IR

and UV SFRF for each of our redshift bins. We ran the MCMC using the PYTHON package `emcee` (Foreman-Mackey et al., 2013), which allows us to explore the parameter space simultaneously, using a set of walkers. While the UV SFRFs can be fitted with a classical Schechter function (Schechter, 1976), the IR SFRFs typically show an excess in the bright-end, that cannot be simply modeled with a Schechter (Lawrence et al., 1986; Soifer et al., 1987; Saunders et al., 1990a; Rush et al., 1993; Shupe et al., 1998; Sanders et al., 2003). For this reason, we adopted a modified Schechter (Saunders et al., 1990a) for the IR-SFRF fit. The classical Schechter is characterized by three free parameters, which are the knee luminosity (SFR*) and density Φ^* of the galaxy population, plus the slope of the faint-end (α). The modified Schechter has, in addition, a fourth parameter, σ, describing the shape of the bright-end. The Schechter function is described in the following way:

$$\Phi(L)dlogL = \Phi^* \left(\frac{L}{L^*}\right)^{\alpha} exp\left[-\frac{L}{L^*}\right] dlogL. \tag{5.4}$$

The modified Schechter can be written as:

$$\Phi(L)dlogL = \Phi^* \left(\frac{L}{L^*}\right)^{1-\alpha_S} exp\left[-\frac{1}{2\sigma_S^2} log_{10}^2\left(1+\frac{L}{L^*}\right)\right] dlogL, \tag{5.5}$$

Previous studies (e.g., Caputi et al., 2007; Béthermin et al., 2011; Gruppioni et al., 2013) have shown that these parameters, in particular L^* and Φ^*, evolve with redshift. Indeed, in the IR domain, while the typical IR luminosity (hence the dust-obscured SFR), of the galaxy population increases with redshift, Φ^* decreases towards higher z (e.g., Gruppioni et al., 2013). This evolution can be described by a functional form, assuming a $z_{\rm break}$ for both parameters, that characterizes the change in their evolution with the redshift. We adopted a similar redshift evolution for the UV SFRF, for which we factored in an evolving faint-end slope, following Parsa et al., 2016. The equations which describe the IR- and UV-SFRF evolutions are reported below:

$$\begin{cases} \Phi^* = \Phi_0^*(1+z)^{k_{\rho 1}} & z < z_{\rho 0} \\ \Phi^* = \Phi_0^*(1+z)^{k_{\rho 2}}(1+z_{\rho 0})^{(k_{\rho 1}-k_{\rho 2})} & z > z_{\rho 0} \end{cases} \tag{5.6}$$

$$\begin{cases} SFR^* = SFR_0^*(1+z)^{k_{\rm l1}} & z < z_{\rm l0} \\ SFR^* = SFR_0^*(1+z)^{k_{\rm l2}}(1+z_{\rm l0})^{(k_{\rm l1}-k_{\rm l2})} & z > z_{\rm l0} \end{cases} \tag{5.7}$$

where Φ_0^* and SFR$_0^*$ are the normalization and characteristic SFR at $z = 0$, $k_{\rho 1}$, $k_{\rho 2}$, $k_{\rm l1}$ and $k_{\rm l2}$ are the exponents for values lower and greater than $z_{\rho 0}$ and $z_{\rm l0}$ for Φ^* and SFR*, respectively. The evolution of α in the UV (dust corrected) SFRF fit, is parametrized by the following power law:

$$\alpha(z) = k_{a1} + k_{a2} \times z. \tag{5.8}$$

By taking advantage of the wide redshift range and the plethora of independent datasets considered in this analysis, we can constrain the best-fit parameters, identifying the local Schechter function and its evolution, through a MCMC fitting approach. Then, using the functional forms for the evolution described before, we can obtain the best-fit IR and UV-SFRFs for each redshift bin. In this way, we can easily combine SFRF data from different studies (in the same bands and completeness-corrected) and characterize with great accuracy the best-fit IR and UV-SFRFs at different redshifts. In order to accurately constrain the parameters of the best-fit SFRFs, we also combined the A^{3}COSMOS IR-SFRFs with those obtained from Herschel (Gruppioni et al., 2015b), containing a much larger number of sources, as we did in Chapter 4 for the IRLFs.

5.3.2 Comparison between UV- and IR-SFRF

We found the IR-SFRF to be characterized by a slowly decreasing Φ^* up to $z \sim 1$ and followed by a steeper decreasing trend toward the higher redshifts. On the other hand, the IR-SFR* smoothly increases toward higher redshifts. For the UV, we found a similar evolutionary trend with the redshift, with α also decreasing at higher z. The IR and UV SFRFs, along with their best-fits, are shown in Figure 5.2. The IR-mm data are tracing the most extreme SFRs, from SFR$\sim 10^2$ to SFR$\sim 10^{3.5}$ M$_\odot$ yr^{-1}, while the UV (corrected) SFRFs cover mostly the fainter SFR values $1 - 100$ M$_\odot$ yr^{-1}.

5.3.3 Comparison with simulations and semi-analytical models

In order to compare our results to simulations and SAMs, which predict the total SFRF, we need to trace the total SFRF from the data. We thus performed and MCMC fit under the following assumptions: in principle, for a complete sample, in which the UV and IR fluxes are available for each galaxy, the total SFR would be computed as the sum of the obscured component (traced by the IR) and the unobscured one (traced by the observed UV), for each galaxy; however, in this analysis, we are dealing with different samples in the IR and UV (for which multiple surveys are used), thus we cannot derive the total SFR of the individual galaxies. Nevertheless, we can assume that the faint-end of the UV-SFRF (corrected for dust attenuation) is tracing $\sim 100\%$ of the SFR and, in a similar way, that the bright-end of the total SFRF is almost entirely traced by the bright-end of the IR-SFRF. With this assumptions, we can therefore fit the UV-SFRF at SFR $<$ SFR$^*_{\rm UV}$ together with the IR-SFRF at SFR $>$ SFR$^*_{\rm IR}$, which are valid tracers of the total SFRF. To perform the fit, we followed the same procedure described before, with the addition of the possibility for σ to evolve with the redshift ($\sigma(z) = k_{s1} + k_{s2} \times z$, as we did for α in the UV-SFRF fit). The results of the total SFRF fit is reported in Figure 5.2 (black solid line). As it can be seen

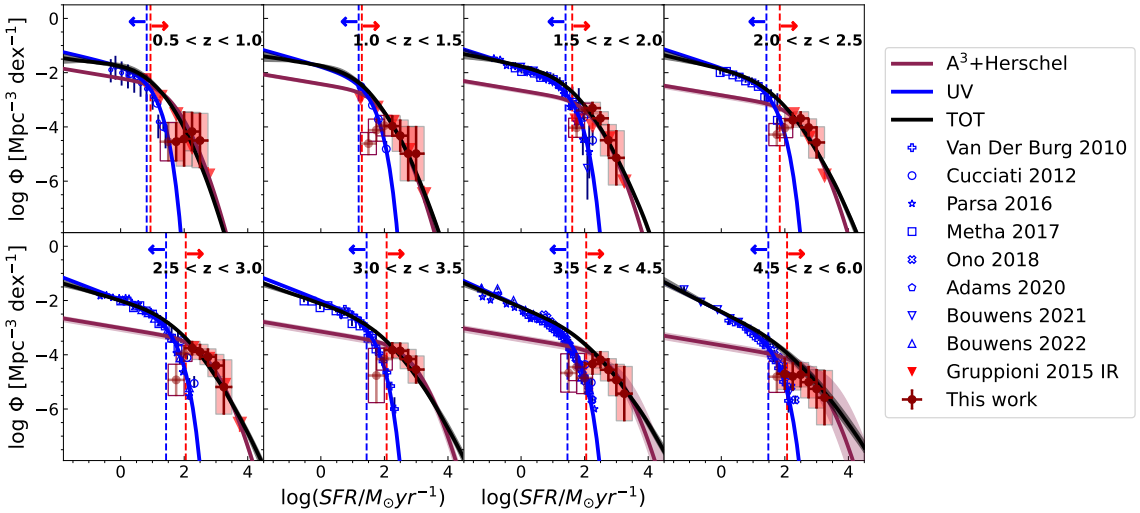

Figure 5.2: IR and UV star formation rate functions. The red points and square errors are the estimates of the SFRF obtained in this work. The red triangles are those obtained by Gruppioni et al. (2015b). Blu points with different symbols are the observed SFRF by van der Burg et al. (2010), Cucciati et al. (2012), Parsa et al. (2016), Mehta et al. (2017), Ono et al. (2018), Adams et al. (2020), and Bouwens et al. (2021, 2022), uncorrected for dust attenuation. The red and blu curves are the MCMC best-fit for the IR and UV SFRF, respectively. Finally, the black line is the total IR+UV SFRF and the blue and red vertical lines represent the higher (for the UV) and lower (for the IR) limits below and above which we took the SFRF data to perform the fit.

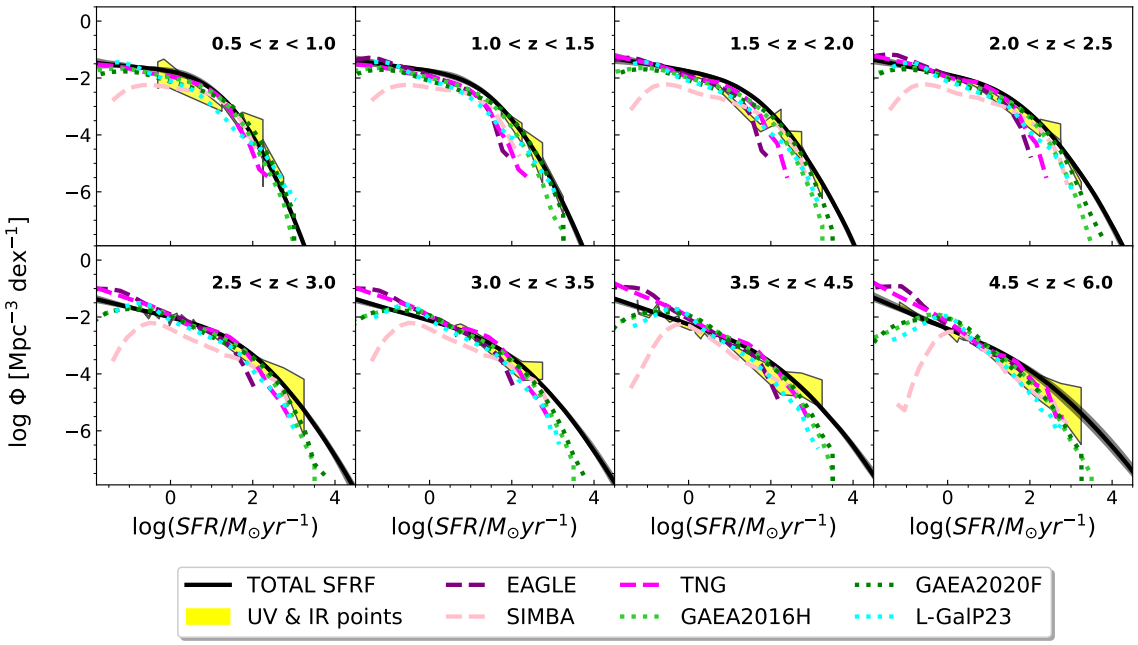

Figure 5.3: Observed SFRF compared with the prediction from simulations and SAMs. The yellow area represents the observed data used for the fit. The best-fit curve is reported in black. The purple dashed line represents the SFRF from the Evolution and Assembly of GaLaxies and their Environments (EAGLE) simulation; the pink dashed curve is the result from the SIMBA simulation and the magenta line is from the IllustrisTNG. The limegreen and green dotted curves are the prediction by Hirschmann et al. (2016) and Fontanot et al. (2020), from the GAEA SAM. Finally, the cyan dotted curves are the predictions by Parente et al. (2023a).

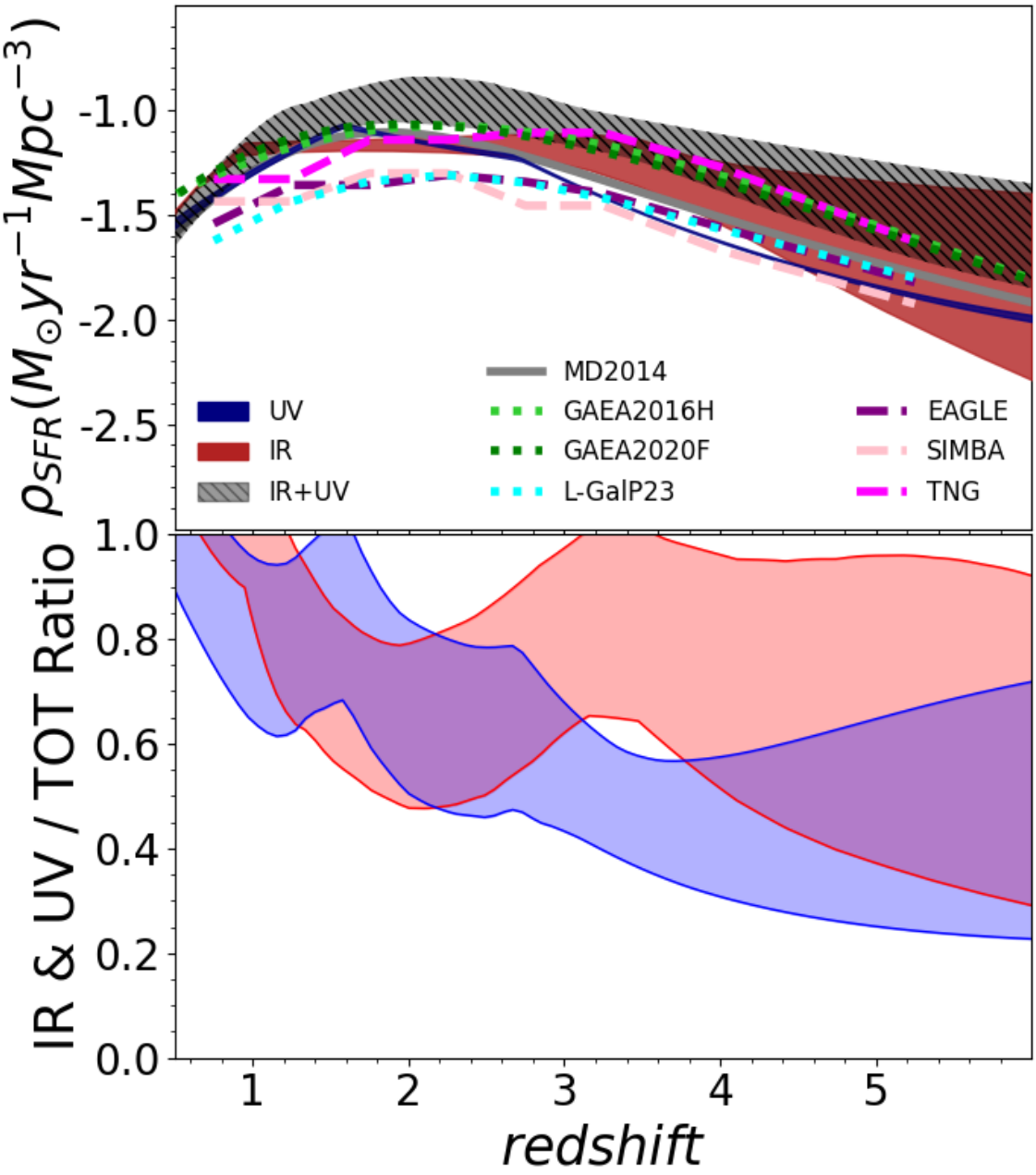

Figure 5.4: SFRD at redshift $0.5 - 6$ and fraction that can be estimated by IR or UV (dust-corrected) contribution. The top panel shows the individual IR (red band) and UV dust-corrected (blue band) SFRD, as well as the total SFRD (black band). For comparison, the SFRDs from the models are also shown, with the same colors as in Figure 5.3. In the bottom panel, the fractional contribution between IR and total and UV (dust-corrected) and total is presented. The blue region is the UV contribution, while the red one represents that from the IR. This ratio represents how much of the total we can reproduce using only UV (dust-corrected) or IR.

Table 5.1: Best fit parameters for the total SFRF.

$log(SFR_0^*)$	$log(\Phi_0^*)$	k_{l1}	k_{l2}	z_l	$k_{\rho 1}$	$k_{\rho 2}$	z_ρ	k_{a1}	k_{a2}	k_{s1}	k_{s2}
$-0.27^{+0.10}_{-0.10}$	$-1.94^{+0.05}_{-0.11}$	$2.43^{+0.38}_{-0.39}$	$0.28^{+0.23}_{-0.35}$	$1.00^{+0.06}_{-0.07}$	$-0.16^{+0.23}_{-0.13}$	$-3.46^{+0.25}_{-0.21}$	$2.54^{0.06}_{-0.06}$	$-0.05^{+0.01}_{-0.01}$	$1.25^{+0.01}_{-0.02}$	$0.14^{+0.02}_{-0.02}$	$0.54^{+0.03}_{-0.01}$

* Values at $z = 0$ obtained from the MCMC evolutive fit

from the Figure, at each z, the total SFRF almost reproduces the UV-SFRF faint-end and the IR-SFRF bright-end. Moreover it shows a non-negligible contribution in the region at $\mathrm{SFR}^*_{\mathrm{UV}} < \mathrm{SFR} < \mathrm{SFR}^*_{\mathrm{IR}}$.

We compare our results on the total IR+UV SFRF with prediction some from state-of-the-art simulations and semy-analytical models. In particular, we discuss the comparison with the SFRF from the EAGLE simulation (Crain et al., 2015; Schaye et al., 2015) by Katsianis et al. (2017), IllustrisTNG (Pillepich et al., 2018b) and SIMBA (Davé et al., 2019) hydrodynamical simulations, the GAEA (Hirschmann et al., 2016; Fontanot et al., 2020) and L-GALAXIES2020 (Henriques et al., 2020) upgraded version by Parente et al., 2023a SAMs. In the following, we briefly describe these theoretical frameworks. The predicted SFRF are shown in Figure 5.3, along with our estimates.

EAGLE

In the context of stellar formation, the EAGLE simulation incorporates the methodology proposed by Dalla Vecchia and Schaye (2008), wherein the gaseous medium is categorized into distinct phases: cold molecular clouds, warm atomic gas, and ionized hot gas bubbles. The star formation rate is estimated through the Kennicutt-Schmidt relation (Schmidt, 1959), derived from the surface density of both stars and gas. Presence of supermassive black holes (SMBHs) is included as well, with seeds placed at the center of massive dark matter (DM) halos. The feedback from AGNs is constructed to be responsible for the quenching of star formation and reproduces the high-mass end of the stellar mass function. The prediction of the EAGLE simulation are shown in Figure 5.3 (magenta dashed curve). The SFR range covered by the SFRF prediction are spanning between $0.01 < \mathrm{SFR}[\mathrm{M}_\odot \mathrm{yr}^{-1}] < 2$, thus, we are able to compare it with our results between the faint-end and the knee of the SFRFs. While at lower redshifts the prediction reproduce the faint-end of the total SFRFs, at $z > 2.5$, it begins to reproduce with better accuracy the knee region of the Schechter.

IllustrisTNG

The IllustrisTNG (Pillepich et al., 2018b) is an improvement of the cosmological simulation Illustris (Genel et al., 2014; Vogelsberger et al., 2014), based on the AREPO (Springel, 2010) code. The IllustrisTNG incorporates an updated galaxy formation model, specifically

addressing limitations found in the original Illustris run. Noteworthy enhancements in the new model include improvements to the prescriptions for supernova and AGN feedback. The IllustrisTNG implementation features enhanced feedback mechanisms, particularly for objects within the 10^{12} - 10^{14} solar mass halo range. Galactic winds are injected in a isotropic way, with increased wind factors in terms of velocity and energy, resulting in a more efficient overall quenching process in IllustrisTNG compared to its predecessor. Regarding AGN feedback for high BH accretion rates relative to the Eddington limit, the model assumes that a fraction of the accreted rest-mass energy thermally heats the surrounding gas. In cases of low accretion rates, a pure kinetic feedback component is employed, imparting momentum to the surrounding gas in a stochastic manner. Unlike the EAGLE predictions, the IllustrisTNG SFRF estimates can reach values up to $log(\mathrm{SFR}) \sim 3$, allowing us to compare it with a more star forming portion of the total SFRF. The comparison is similar to that of the EAGLE simulation, with the IllustrisTNG SFRF showing slightly higher values of Φ at SFR of the knee and larger. Notably, at $z > 3$, where other predictions struggle in reproducing the knee of the total SFRF, this simulation predicts quite well the observed SFRF up to SFR $\sim 5 \times 10^2$, at $z \sim 5$.

SIMBA

The SIMBA (Davé et al., 2019) simulation is the upgraded version of the MUFASA (Davé et al., 2017), based on the GIZMO code (Hopkins, 2015). The main enhancement lies in the inclusion of seeding and evolution of BHs, playing a role in the quenching, overcoming the precedent mass quenching feedback scheme used in the the MUFASA simulation. BH accretion is facilitated through two channels, with a component sourced from cold gas and one originating from hot gas. This propels feedback mechanisms that suppress galaxy activity in the form of kinetic bi-polar outflows and X-ray heating. As already observed for the previous two simulations, also SIMBA reproduces well the total SFRF at $z < 2.5$, missing the most star forming population.

GAEA2016H and GAEA2020F

In this study, we also compare our SFRF results with predictions from semi-analytic models. Specifically, we employ the epredictions from the GAlaxy Evolution and Assembly (GAEA) code, both in its standard realization presented in Hirschmann et al. (2016) , GAEA2016H hereafter, and in the updated version from Fontanot et al. (2020), GAEA2020F, which correspond to the F06-GAEA run in that paper. In this section, we provide a brief overview of the key defining aspects of the two iterations of the GAEA model. Both models delineate baryonic evolution within four compartments: the stellar component of galaxies, cold gas

within the galactic disk, hot gas in the halo of dark matter, and the ejected gas component. Physically or observationally motivated prescriptions are employed for astrophysical processes incorporated into the model (e.g., cooling, star formation, stellar feedback, gas recycling, metal enrichment). The model further features a non-instantaneous treatment for chemical enrichment, that accounts for individual lifetimes of stellar populations and a redshift-dependent stellar feedback scheme that includes stellar driven outflows. This model has been calibrated to reproduce the GSMF up to $z \sim 3$, but it also provide a good agreement with higher redshift observations (Fontanot et al., 2017). In more recent rendition of the model (Fontanot et al., 2020), the modeling of cold gas accretion onto supermassive black holes (SMBHs) has been improved and better characterized, taking into account several triggering mechanisms (such as mergers and disk instabilities) for the loss of angular momentum of the cold gas, leading to the formation of a reservoir from which its could get accreted to the central BH,. Various triggering mechanisms for accretion are incorporated, such as mergers and disk instabilities. Finally, AGN feedback is also introduced in the form of AGN-driven outflows.

Both the GAEA2016H and GAEA2020F are in good agreement with our data points and best-fit up to $z \sim 3.5$. At higher redshifts, the models begin to diverge from the data, especially at the highest star-forming end.

L-GalP23

The L-Galaxies SAM (Henriques et al., 2020) is the last public release of the Munich galaxy formation model. It is run on top of the Millennium simulation (Springel, 2005) and it models the evolution of both the stellar and gaseous components of DM haloes by taking into account a number astrophysical processes. These include, e.g., gas cooling, chemical enrichment, bulge growth during mergers and disk instabilities, environmental processes like ram pressure and tidal stripping. The model spatially resolves to some extent the stellar and gaseous discs of galaxies, with star formation being modelled based on the molecular H2 content as predicted by the model. Feedback from SNe and AGNs (radio mode) is also taken into account. Here we compare with the predictions of the L-Galaxies model, incorporating updates introduced in Parente et al. (2023a). These updates include a detailed treatment of dust evolution and a novel prescription for disk instabilities, which considers the instability of both the stellar and gaseous disc, with the latter being capable of inducing starbursts and accreting the central SMBH. Similarly to other models, the L-GalP23 predictions mostly reproduce the faint-end of the SFRF.

The comparison between our results and the simulations described above shows that, despite some limitations are still present in reproducing the very highest star forming end of

the SFRF (at the higher redshifts) by most of the models, some progresses have been made in the characterization of the physical processes regulating the star formation in galaxies. Indeed, the agreement between data and models has significantly improved with respect to similar works carried out in the past years (e.g., Gruppioni et al., 2015a), making the good agreement with data up to $z \sim 3.5 - 4$ possible.

5.4 The total SFRD

In this Section, we show the cosmic SFR obtained by integrating the total SFRFs and compare the $\mathrm{SFRD_{TOT}}$ to the estimates we obtain when integrating the predictions by simulations and SAMs.

5.4.1 Total SFRD

To compute the total SFRD, we integrated the total SFRF down to SFR$= 0.3$ $\mathrm{M_\odot\ yr^{-1}}$, to prevent the integration to diverge while integrating the faint-end of the UV-SFRF (Oesch et al., 2018). The result is shown in Figure 5.4 as the black shaded area (top panel). The total SFRD follows an increasing trend at $0 < z < 1$, between which it increases of ~ 1 dex. This rise continues up to $z \sim 2$, at which the SFRD reaches its peak value, while a broad peak can be identified at $1 < z < 2.5$. At higher redshifts ($z > 2.5 - 3$) the total SFRD starts decreasing towards $z \sim 6$, by a factor $\sim 0.3 - 0.5$ dex. We investigated the fraction of the total SFRD that can be estimated by either the IR or the UV (dust-corrected) SFRDs. This comparison is shown in the bottom panel of Figure 5.4. Both the IR and the UV are able to trace the whole SFRD from $z \sim 0$ to $z \sim 1$. Towards higher redshifts, the fraction of the SFRD estimated by the IR and the UV decreases, reaching the minimum at $z \sim 6$, at which they are able to recover just the $\sim 50\%$ of the total SFRD.

5.4.2 Comparison with models

We further studied the SFRD by comparing it with the SFRD from the models considered in this work. As expected, the EAGLE SFRD (magenta line) is not able to reproduce the observed SFRD in the covered SFR range as it does not extend at values higher than ~ 100 $\mathrm{M_\odot\ yr^{-1}}$. The SFRD from the SIMBA simulation (cyan curve) shows a similar trend as for the EAGLE, being lower than the total SFRD. The IllustrisTNG simulation is instead able to reproduce the SFRD at high redshift ($z > 2$). The GAEA SFRDs are instead consistent with our results up to $z \sim 2.5$ and slightly lower at higher redshifts, still predicting a SFRD higher than that derived by Madau and Dickinson (2014), and consistent with the lower uncertainty border of our total SFRD. Finally, the modified version of the `L-GalP23` models by Parente

et al. (2023a) is producing a SFRD similar to those obtained using the EAGLE and SIMBA simulations. In addition, at low redshifts ($z < 1$), semi-analytical models appear to predict a higher SFRD than observed. This discrepancy may be attributed to an overproduction of star-forming galaxies in the local universe by the SAMs. Conversely, at high redshifts ($z > 2.5$), there seems to be a deficiency in the fraction of galaxies exhibiting particularly active star formation (e.g., SFR > 1000 $M_\odot$ yr^{-1}), which characterizes the bright end of the IR-SFRF at those redshifts. However, in the work by Gruppioni et al. (2015b), SAMs were able to reproduce the bright end up to $z < 1 - 1.5$, but now, the recent models by Hirschmann et al. (2016) and Fontanot et al. (2020) are consistent with the observations up to $z \sim 2 - 2.5$.

5.5 Summary and Conclusions

By combining the recent IR-LF and SFRD obtained by **traina2024sfrd** with the dust corrected UV-SFRF derived in various literature works, we estimated the total (IR+UV) SFRFs and SFRD over the $z = 0.5 - 6$ redshift range. Furthermore, we compared these results with predictions from state-of-the-art SAMs and hydrodinamical simulations to assess how well these models can reproduce the observational estimates. The obtained results can be summarized as follows:

- The IR and UV dust-corrected star formation functions sample different ranges of SFRs. Indeed, the UV-SFRF extends at values below 10 $M_\odot yr^{-1}$ up to $z \sim 2$ and reaches values of 100 $M_\odot yr^{-1}$ at higher redshifts. The IR-SFRF, on the other hand, is dominant at higher SFRs, particularly in the range of 100-1000 $M_\odot yr^{-1}$.

- Using the dust-corrected UV-SFRF data points at values of SFR lower than the knee and the IR-SFRF at values higher than the knee, we derived the total best-fitting SFRF. Comparing the total SFRF with predictions from simulations and SAMs reveals that they are capable of reproducing the faint-end quite well at all redshifts, but the bright-end only up to $z \sim 2.5$. At higher redshifts, there appears to be a lack of galaxies with very high SFR, responsible for the bright-end.

- The total SFRD shows a typical increasing trend at $0.5 < z < 1.5$, a broad peak up to $z \sim 3$ and decreases towards $z \sim 6$. The models predict an SFRD consistent with observed values up to approximately $z \sim 2.5 - 3$. At higher redshifts, they are weakly consistent within the errors. The ratios between IR and total SFRD and UV (dust-corrected) and total SFRD is useful to quantify how good are both tracers in reproducing the evolution of the total SFRD. We found both of them able to reproduce

it up to $z \sim 1$, but, at higher redshifts, they only accounts for the $\sim 50 - 70\%$ of the total.

CHAPTER 6

Dust mass function and dust mass density

In Chapter 4 and 5 we found that the IR, dust-driven, emission in galaxies dominates the contribution to the total SFRD in both the local and high redshift Universe. In particular, in order to explain the high fraction ($\sim 50\%$) of the total SFRD traced by the IR at $z > 4$, large dust reservoirs should be present in those galaxies. Moreover, we have also found cutting-edge cosmological simulations and SAMs are typically unable to reproduce the bright (thus the highly star forming) end of the LF (and SFRF), where the emission by bright IR galaxies dominates. For these reasons, in this Chapter, we investigate the shape and evolution of the dust mass density in the Universe out to $z \sim 6$ from the A^{3}COSMOS sample (Sections 6.2 and 6.3).

6.1 Introduction

Recent estimates of the star formation rate density (SFRD) by IR and mm-based studies (e.g., Gruppioni et al., 2020; Khusanova et al., 2021; Traina et al., 2024) imply the presence of large quantities of dust, even at high redshifts (e.g., $z > 3$), in order to explain the significant fraction of the SFRD coming from dust-obscured galaxies. To understand the origin of these large SFRDs, a possibility is to investigate the mass of dust ($M_{\rm D}$) in galaxies and the dust mass content of the Universe at different cosmic times. Such a study is not only crucial for our understanding of dust-obscured SFRD, but also because dust plays a major role in most astrophysical processes in the evolution of galaxies and AGNs, and the question of how and when dust emerges is still debated. Deriving the dust mass function (DMF) and the evolution with redshift of the dust mass density (DMD) offers the opportunity to address this issue via a statistical approach.

In the past years, a number of works have been devoted to the estimation of the $M_{\rm D}$ in galaxies, mostly using data from the *Herschel* observatory (Rodighiero et al., 2011; Lemaux

et al., 2014). However, while these studies were able to trace the DMD since $z \sim 2-3$ to the present days, they did not constrain its evolution at higher redshifts, because of the limitation of the FIR in tracing the Rayleigh-Jeans (hereafter R-J) regime of the dust emission (needed for deriving $M_{\rm D}$, see Section 6.2), at higher redshifts. Sampling the dust emission at longer wavelengths such as the sub-millimeter (sub-mm) and millimeter (mm) bands is then crucial to explore the high-z dust content of the Universe. Different studies, using sub-mm/mm facilities (e.g., IRAM, ALMA) have investigated $M_{\rm D}$ at higher redshifts (Magnelli et al., 2019b; Magnelli et al., 2020; Pozzi et al., 2020). Despite the relevance of this topic in understanding the buildup of interstellar dust, the number of studies aimed at tracing the evolution of $M_{\rm D}$ over cosmic time is still poor, while existing DMD estimates at high-redshift are quite uncertain. Moreover, simulations (Popping et al., 2017; Aoyama et al., 2018; Li et al., 2019; Vijayan et al., 2019) fail to accurately reproduce the observed evolution of the DMD with redshift, and in particular very few are able to reproduce the observed drop at $z < 1$ (Gioannini et al., 2017; Parente et al., 2023a). In order to shed light on the evolution of galaxy's dust content across cosmic time, deep (sub-)mm surveys of large galaxy samples and covering a wide redshift range need to be carried out. Altough ALMA is characterized by a small field of view, which makes wide-area surveys too observationally demanding, as described in Chapter 3, the recent A^{3}COSMOS survey Liu et al. (2019a,b) circumvents this limitation by collecting and homogeneously analysing archival ALMA images of dusty star-forming galaxies. This unique survey can also be exploited for characterizing the dust mass content and evolution. As extensively discussed in Chapters 2 and 3, we estimated the star-forming properties (number counts, $L_{\rm IR}$, SFR) of the A^{3}COSMOS sample via SED-fitting. In this Chapter, we build on our previous analysis (Traina et al., 2024, Adsceid et al. sub.) to constrain the DMF and DMD in the redshift range $0.5 < z < 6$. This Chapter is organized as follows. In Section 6.2 we describe the methods used to derive $M_{\rm D}$ and discuss analogies and differences between various approaches; in Section 6.3 we present the DMF and DMD, comparing them with previous literature estimates and simulations. Finally, we highlight and interpret our results in Section 6.4. The galaxy sample used for this analysis is the same already described in Chapter 2 and 3, used for the derivation of the LF, SFRF and SFRD. This sample, constituted of dusty star forming galaxies and having a sub-mm/mm detection with ALMA, is particularly well suited for the characterization of the dust properties of these type of galaxies. In the next Section, we indeed derive the dust mass for the final sample (using different methods) and we investigate possible dependencies of $M_{\rm D}$ on both dust temperature and redshift.

6.2 Dust mass estimation

The IR emission in galaxies originates from dust heated either by UV emission from recently formed stars or from the AGN. The dust thermalizes with the radiation and re-emits at longer wavelengths, in the IR bands, with a spectrum that can reliably described by a grey body emission (i.e., less efficient than a black body Bianchi, 2013), whose shape is linked to the different dust phases in a galaxy. The warm dust component, close to the heating source (stars or AGN) emits large quantities of luminosity per unit of mass and dominates the far-infrared emission (where dust emission peaks). The diffuse dust component in the galaxy, which dominates in mass, is instead heated by a weaker radiation field, thus having lower temperatures. This implies a much lower luminosity per unit mass and an emission peaked at longer wavelengths (sub-mm/mm). The composite contribution of the different dust phases produces the observed peak of the dust emission ($\lambda_{\rm peak}$). At $\lambda > \lambda_{\rm peak}$, the grey body emission is in the R-J regime (where cold dust peaks) and can be used to trace the global dust mass in the galaxy. In particular, the R-J emission traces the bulk of the dust reservoir in the galaxy, which is at the "mass-weighted" temperature, in contrast to the "luminosity-weighted" temperature, that would be associated to strongly heated dust, emitting in the FIR, but not representative of the total dust mass (see Liang et al., 2019, for a detailed discussion on the different dust temperature definitions). From the observed dust emission fluxes, assuming a dust temperature value, one can retrieve the dust mass. In this work, we compute the $M_{\rm D}$ relying on the spectral energy distribution (SED) fitting or directly from the observed ALMA flux. In the following Sections (6.2.1 and 6.2.2), we describe these two possible approaches to derive $M_{\rm D}$.

6.2.1 $M_{\rm D}$ from SED fitting

The first method to infer $M_{\rm D}$ of a galaxy is to perform SED fitting of the FIR/mm photometry, that is tracing dust emission. In this paper, we use the PYTHON "Code Investigating GALaxy Emission" (CIGALE; Boquien et al., 2019) SED-fitting tool. CIGALE is based on the energy balance between the UV and optical emission by stars and the re-emission in the IR and mm by the dust and it allows one to choose among different individual templates for each emission component (e.g., stellar optical/UV emission, cold dust emission, AGN) across a broad parameter space. For the dust emission component, we use the DL14 (Draine et al., 2014) module. Consistently with the dust attenuation component used, DL14 assumes the presence of both the diffuse interstellar medium (ISM), heated by the general stellar population in the galaxy, and birth clouds (BCs), heated by newly formed massive stars. The main input parameters are the PAH mass fraction and the minimum radiation field. The dust mass of the cold component is computed by dividing the dust luminosity

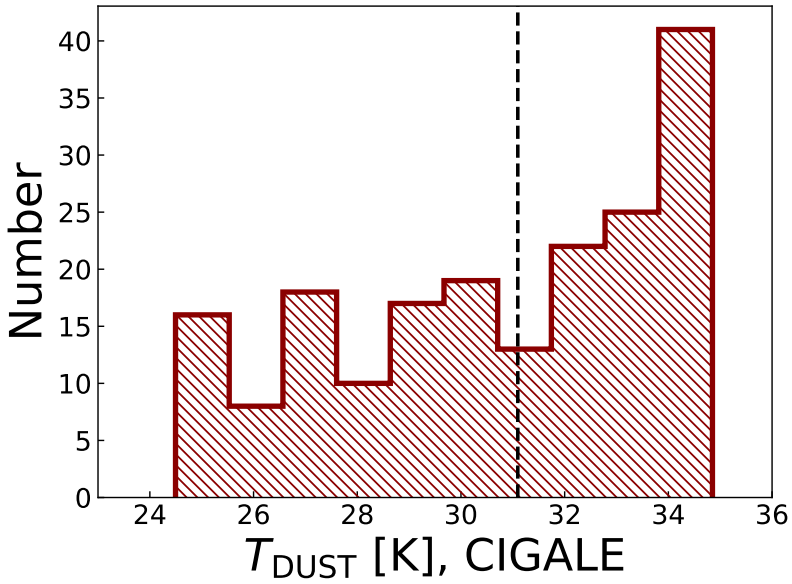

Figure 6.1: Mass-weighted dust temperature in K computed by using the output radiation field given by the SED fitting analysis. The vertical dashed line indicates the median value for the sample.

(i.e., the luminosity arising from the dust heated by stars) by the dust emissivity, and it is returned as output from the SED-fitting. The radiation field (U, returned from CIGALE) that is responsible for heating the dust can be linked to the mass-weighted dust temperature as follows:

$$T_{\mathrm{D,CIGALE}} = 18 \cdot U^{1/6}[\mathrm{K}]. \tag{6.1}$$

Figure 6.1 shows the $T_{\mathrm{D,CIGALE}}$ distribution, which follows a nearly flat trend, with a smoothly rising distribution which peaks at $T_{\mathrm{D,CIGALE}} \sim 34$K, with a median value ~ 31K, in agreement to what is found by Pozzi et al., 2020.

This method allow us to obtain M_{D} as an output of the SED fitting, using information from all the bands from the optical to the mm. We further verify wether there are or not systematics between the dust mass measured in sources with a flux in ALMA bands 3 or 4 and those with ALMA observations at shorter wavelengths. To do this, we selected those galaxies with observations in band 3 or 4 and performed an SED fitting removing those fluxes. Then, we compared the outputs for the dust masses with the dust masses obtained including band 3 and 4. This comparison is shown in Figure 6.2. As it can be seen, most of the sources are lying on the 1:1 relation, without showing any possible systematics on the M_D measurement.

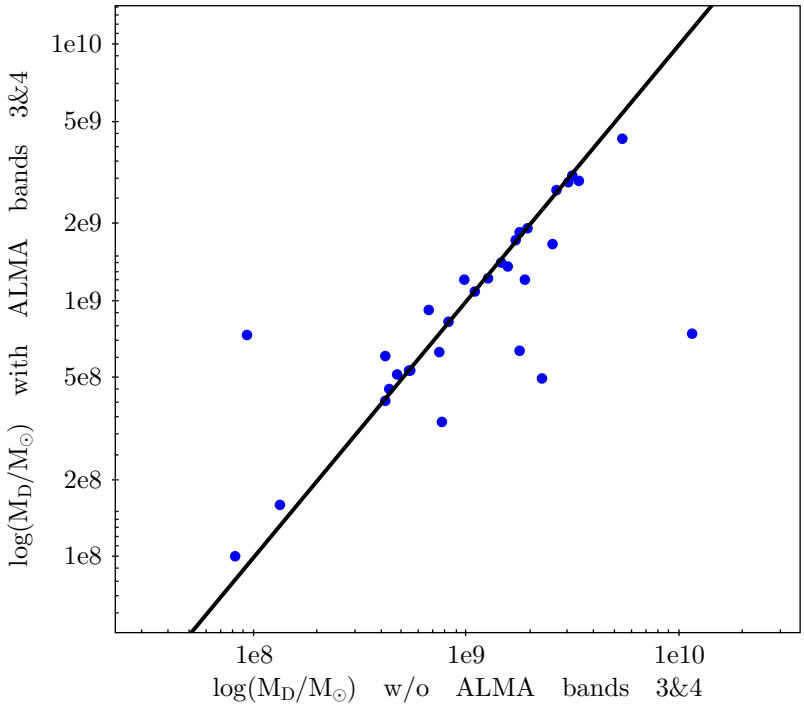

Figure 6.2: Comparison of the dust masses measured from the SED fitting with (y-axis) and without (x-axis) including observations in bands 3 and 4 of ALMA.

6.2.2 $M_{\rm D}$ from R-J flux density

An alternative method to derive $M_{\rm D}$ consists in using the flux at a certain wavelength in the R-J part of the SED. Following the optically thin approximation, $M_{\rm D}$ can be computed as follows (see e.g., Magnelli et al., 2020):

$$M_{\rm D} = \frac{5.03 \times 10^{-31} \cdot S_{\nu_{\rm obs}} \cdot D_{\rm L}^2}{(1+z)^4 \cdot B_{\nu_{\rm obs}}(T_{\rm obs}) \cdot \kappa_{\nu_o}} \cdot \left(\frac{\nu_o}{\nu_{\rm rest}}\right)^{\beta}; \tag{6.2}$$

where $B_{\nu_{\rm obs}}(T_{\rm obs})$ is the black-body Planck function computed at the observed frame, mass-weighted, temperature ($T_{\rm obs} = T_{\rm D}/(1+z)$); $S_{\nu_{\rm obs}}$ is the flux density at the observed frequency $\nu_{\rm obs}$, with $\nu_{\rm rest} = (1+z)\nu_{\rm obs}$; κ_{ν_o} is the photon cross-section to mass ratio of dust at the rest-frame ν_0 and β is the dust emissivity spectral index (see e.g., Magnelli et al., 2020). In our analysis, we adopted a value of $\kappa = 0.0469$ m^{2}kg^{-1}, derived for a wavelength of 850μm (Draine et al., 2014) to be consistent with the CIGALE prescriptions used. For the spectral index of the dust emissivity, β, typical values are between 1.5 and 2.0 (with a good agreement between empirical measurements and theoretical predictions Dunne and Eales, 2001; Clements et al., 2010; Draine, 2011). Here we used the suggested value by Scoville et al., 2014, $\beta = 1.8$, found by the Planck Collaboration et al., 2011.

Once κ_{ν_0} and β have been fixed, the main parameters that affect $M_{\rm D}$ are the flux at the observed frequency $\nu_{\rm obs}$ and the rest-frame, mass-weighted, temperature $T_{\rm D}$. Several

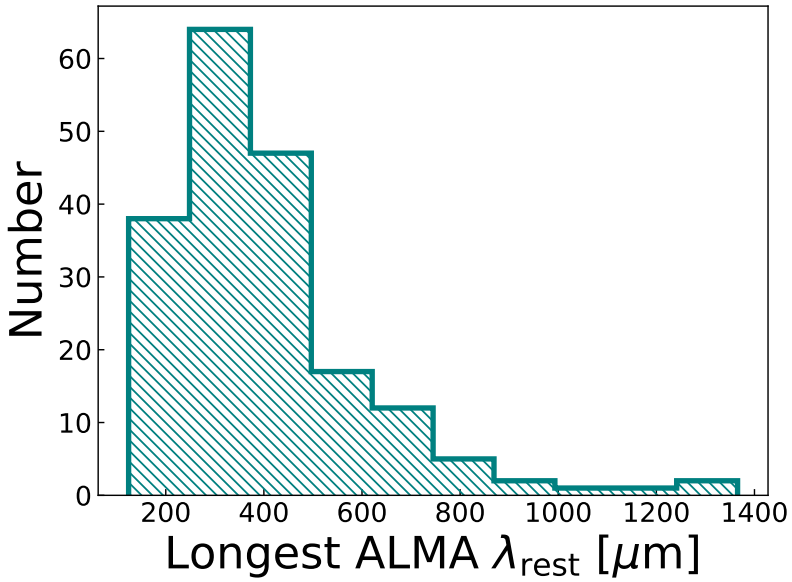

Figure 6.3: Rest-frame wavelength in μm of the longest observed ALMA fluxes for each galaxy in the sample.

works suggest (or use) the dust temperature in a range between $\sim$ 15K and $\sim$ 40K (see e.g., Dunne et al., 2011; Dale et al., 2012; Magnelli et al., 2014; Pozzi et al., 2020, 2021). As it can be calculated using Equation 6.2, higher dust masses corresponds to lower dust temperatures and vice versa, leading to uncertainties between 25% and 50% for $M_{\rm D}$ with a different $T_{\rm D}$ assumption (Magnelli et al., 2020). Here we choose to use two values of rest-frame temperature, namely $T_{\rm D} = 25$K and $T_{\rm D} = 35$K, that encompass the range of possible values for the mass-weighted $T_{\rm D}$, supported by observations and models (see e.g., Magnelli et al., 2014; Sommovigo et al., 2020). Magnelli et al., 2014 found indeed that only a small fraction of galaxies with high sSFR shows a $T_{\rm D} > 35$K.

We also select three different fluxes to be used in the $M_{\rm D}$ estimation: two fluxes interpolated from the best-fitting SED for each galaxy (the observed and the rest-frame 850μm fluxes, $S_{850,\rm obs}$ and $S_{850,\rm rest}$) and one observed ALMA flux at the longest available wavelength ($S_{\rm ALMA,long}$). By using the interpolated flux in the SED, we always sample the R-J regime between the rest-frame the 850μm and the observed-frame 850μm flux up to $z \sim 4$. The longest observed ALMA band correspond to rest-frame values above $\lambda \sim 200\mu$m, enabling us to to probe the R-J tail for every galaxy in our sample (see Figure 6.3).

In Figures 6.4, we show the distributions for $M_{\rm D}$ computed with the two different methods (SED-fit or single MBB) and with two different temperatures of the MBB (25K and 35K). The median values of the 25K dust mass is $7.6^{+8.6}_{-4.7} \times 10^8$ M$_\odot$ and the 35K median $M_{\rm D}$ having values of $3.7^{+4.8}_{-2.1} \times 10^8$ M$_\odot$. In this case the 25K $M_{\rm D}$ is a factor $\sim$ 2 larger than the 35K one. Moreover, as expected from the $T_{\rm D}$ distribution of the CIGALE SEDs (see Fig. 6.1,

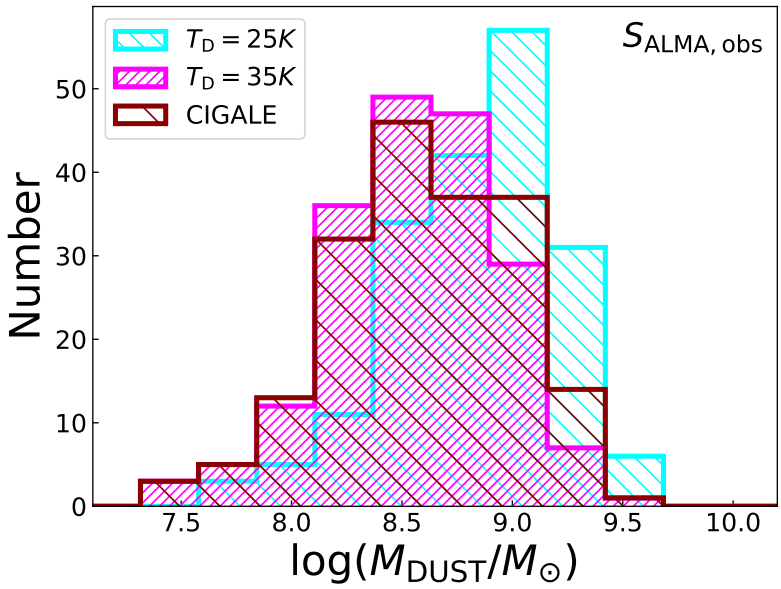

Figure 6.4: Logarithm of the dust mass derived using the longest observed ALMA fluxes and assuming a dust temperature of 25K (cyan histogram) or 35K (magenta histogram). The red distribution corresponds to the dust masses given as an output of the CIGALE SED fitting.

the $M_{\rm D,35K}$ and $M_{\rm D,CIGALE}$ are in good agreement, with a difference of ~ 0.04 dex in their median values.

For our analysis, we decide to use three different $M_{\rm D}$ estimates to derive the DMF and DMD. One is the CIGALE dust mass (hereafter $M_{\rm D,cigale}$), which is independent of the assumption made on the dust temperature, and of the reference wavelength of the monochromatic flux. The other two are the dust masses derived using the actual observed ALMA flux at the longest wavelength, with $T_{\rm D} = 25$ and 35K. This flux is chosen because it provides a more purely (sub-)mm based $M_{\rm D}$ measurements, which can be easily compared with literature studies by simply matching in dust temperatures. We refer to these dust masses with $M_{\rm D,ALMA,25}$ and $M_{\rm D,ALMA,35}$, respectively.

6.3 Dust mass function and dust mass density

6.3.1 $V_{\rm MAX}$ method

In order to derive the DMF, we applied the Schmidt, 1970 "maximum comoving volume" ($V_{\rm MAX}$) method that, based on the data, allowed us to derive the observed DMF without making any assumption relative to its shape. The areal coverage as a function of the flux has already been derived by Traina et al., 2024 for the A^{3}COSMOS survey at a reference observed wavelength of 1200μm. This relation between cumulative area and limiting fluxes

is here used to associate an accessible area above a certain flux with each source.

We derive the DMF in eight redshift bins from $z \sim 0.5$ to $z \sim 6$ and into dust mass bins of 0.5 dex width from $\log(M_{\rm D}/{\rm M}_{\odot}) = 6$ to $\log(M_{\rm D}/{\rm M}_{\odot}) = 10$. For each source in a z-$M_{\rm D}$ bin, we measured the contribution to the DMF in that bin by applying a redshift step of $dz = 0.02$ and K-correcting its best-fit SED from the lower to the upper boundary of the corresponding redshift bin, each time computing the observed flux at 1200 μm. We used this flux to infer the corresponding areal coverage at each dz by interpolating the previously derived areal coverage vs flux density curve. Lastly, we combined the effective area obtained in this way with the element of volume at each redshift step and obtained a co-moving volume over which a given source is accessible:

$$V_{\rm MAX} = V_{\rm zmax} - V_{\rm zmin}, \tag{6.3}$$

where $V_{\rm zmax}$ and $V_{\rm zmin}$ are the sum of the subvolume in each dz shell up to the upper and lower limits of the bin, respectively. In particular, $V_{\rm zmax}$ can either be the volume at the upper bound of each dz bin or the maximum volume reachable by considering the S/N limit of the survey (i.e., corresponding to the z at which the area would be zero). Finally, we corrected the $V_{\rm MAX}$ by taking into account the completeness and spuriousness corrections derived by Liu et al., 2019b, and we obtained the $\Phi(M, z)$ by summing each $1/V_{\rm MAX}$ in a certain luminosity-redshift bin. The completeness threshold is computed by rescaling all the observed 1200μm fluxes of each SED to the faintest observed 1200 μm flux density in this redshift bin and then taking the $M_{\rm D}$ of that SED, which gives the highest $M_{\rm D}$ value at that limit. This latter value represents the $M_{\rm D}$ below which our sample is not 100% complete. We derived the DMF using this method for the three different $M_{\rm D}$ estimates.

6.3.2 The dust mass function

We derived the DMFs using either the dust mass inferred from CIGALE or from the ALMA observed flux at the longest wavelength available and assuming $T_{\rm D} = 25$K, $T_{\rm D} = 35$K. In each case we divided the sample in eight, similarly populated, redshift bins (0.5-1.0; 1.0-1.5; 1.5-2.0; 2.0-2.5; 2.5-3.0; 3.0-3.5; 3.5-4.5; 4.5-6.0).

We compare our DMF results with the few estimates available in similar redshift ranges from the literature. In particular, at $0.5 < z < 2.5$, we compare the A^{3}COSMOS DMFs with the results by Pozzi et al. (2020). Firstly, it is important to underline the main differences between the two samples. The *Herschel* data sample is much larger than the A^{3}COSMOS sample (~ 7000 and ~ 190 galaxies, respectively), leading to lower Poissonian uncertainties on the estimated DMFs. Moreover, the *Herschel* sample traces a wider range in dust masses, both at the faint (due to a better sensitivity) and the bright-ends (larger co-moving volume probed). In the redshift and luminosity range in common, in the A^{3}COSMOS and

the *Herschel* results, we find a weak agreement with the $\mathrm{DMF}_{25\mathrm{K}}$ and a better consistency when using the 35K dust masses, as well as the CIGALE M_{D}. This difference could be explained by the method used in Pozzi et al. (2020) to derive T_{D}, which considers the dust temperature as a function of the redshift and the specific star formation rate (Magnelli et al., 2014), which leads to $T_{\mathrm{D}} > 25$K (thus lower M_{D} values) for the same sample of star-forming galaxies. At higher redshifts, very few works have investigated the DMF. In Figure 6.5 and 6.6, we report the Dunne et al. (2003) DMF at $1 < z < 5$, the point by Magnelli et al. (2019b) at $3.1 < z < 4.6$ and the ALPINE DMF at $z \sim 4.5$ (Pozzi et al., 2021). We find a good agreement between our estimates (using $T_{\mathrm{D}} \sim 35$K and the CIGALE estimates) and the aforementioned works.

To obtain the best-fit parameters characterizing the DMF at different redshifts, we performed a Markov chain Monte Carlo (MCMC) fitting analysis, modeling the DMF with a Schechter function (that has been found to be a better parametrization than the modified-Schechter, often used to fit the IR-LF, Pozzi et al., 2020):

$$\Phi(M_{\mathrm{D}})dlogM_{\mathrm{D}} = \Phi^{*}\left(\frac{M_{\mathrm{D}}}{M^{*}_{\mathrm{D}}}\right)^{\alpha} exp\left[-\frac{M_{\mathrm{D}}}{M^{*}_{\mathrm{D}}}\right] dlogM_{\mathrm{D}}, \tag{6.4}$$

where α is the slope of the faint end and M^{*}_{D} and Φ^{*} represent the dust mass and normalization at the knee, respectively. Previous works on the IR-LF characterization pointed toward a redshift evolution of both the typical density and luminosity of the IR galaxy population (see e.g., Caputi et al., 2007; Béthermin et al., 2011; Marsden et al., 2011; Gruppioni et al., 2013; Traina et al., 2024) characterized by an increase in luminosity and a decrease in density with increasing redshift. In Pozzi et al., 2020, the authors found also a similar evolutionary trend with redshift for the DMF. Assuming that the evolution of the DMF is similar to that of the IR-LF, we performed an MCMC fit using simultaneously the information from all redshift bins, assuming an exponential shape and two different z_{break} values ($z_{\rho 0}$ and z_{l0}), that are let free to vary, for the evolution of $\Phi(z)^{*}$ and $M(z)^{*}_{\mathrm{D}}$, expressed as:

$$\begin{cases} \Phi^{*} = \Phi^{*}_{0}(1+z)^{k_{\rho 1}} & z < z_{\rho 0} \\ \Phi^{*} = \Phi^{*}_{0}(1+z)^{k_{\rho 2}}(1+z_{\rho 0})^{(k_{\rho 1}-k_{\rho 2})} & z > z_{\rho 0}, \end{cases} \tag{6.5}$$

$$\begin{cases} M^{*}_{\mathrm{D}} = M^{*}_{D,0}(1+z)^{k_{\mathrm{l}1}} & z < z_{\mathrm{l}0} \\ M^{*}_{\mathrm{D}} = M^{*}_{D,0}(1+z)^{k_{\mathrm{l}2}}(1+z_{\mathrm{l}0})^{(k_{\mathrm{l}1}-k_{\mathrm{l}2})} & z > z_{\mathrm{l}0}, \end{cases} \tag{6.6}$$

where Φ^{*}_{0} and $M^{*}_{D,0}$ are the normalization and characteristic dust mass at $z = 0$ and $k_{\rho 1}$, $k_{\rho 2}$, $k_{\mathrm{l}1}$, and $k_{\mathrm{l}2}$ are the exponents for values lower and greater than $z_{\rho 0}$ and $z_{\mathrm{l}0}$ for Φ and M_{D}, respectively. In this fit, each point of the DMF is associated with a redshift corresponding to the median redshift value of the underlying galaxy population in the same bin.

Table 6.1: Dust mass function inferred from the A^{3}COSMOS database.

$\log(M_{\rm D,CIGALE}/M_\odot)$	$\log(\Phi/{\rm Mpc}^{-3}{\rm dex}^{-1})$			
	$0.5 < z \leq 1.0$	$1.0 < z \leq 1.5$	$1.5 < z \leq 2.0$	$2.0 < z \leq 2.5$
7.75-8.25		(*-4.68*$^{+0.22}_{-0.35}$)		
8.00-8.50	(**-4.46**$^{+0.54}_{-0.86}$)	(**-4.68**$^{+0.22}_{-0.36}$)	(**-3.73**$^{+0.29}_{-0.42}$)	(**-3.90**$^{+0.30}_{-0.40}$)
8.25-8.75	(*-3.98*$^{+0.45}_{-0.71}$)	(*-3.68*$^{+0.24}_{-0.37}$)	(*-3.40*$^{+0.18}_{-0.31}$)	*-3.56*$^{+0.19}_{-0.32}$
8.50-9.00	**-4.15**$^{+0.55}_{-0.89}$	**-3.65**$^{+0.25}_{-0.41}$	**-3.59**$^{+0.19}_{-0.31}$	**-3.62**$^{+0.17}_{-0.30}$
8.75-9.25		*-4.46*$^{+0.41}_{-0.75}$	*-3.92*$^{+0.22}_{-0.35}$	*-3.95*$^{+0.21}_{-0.36}$
9.00-9.50		**-4.65**$^{+0.56}_{-0.88}$	**-4.04**$^{+0.24}_{-0.40}$	**-4.51**$^{+0.39}_{-0.61}$
9.25-9.75			*-4.68*$^{+0.60}_{-0.87}$	*-5.21*$^{+0.82}_{-1.21}$
	$2.5 < z \leq 3.0$	$3.0 < z \leq 3.5$	$3.5 < z \leq 4.5$	$4.5 < z \leq 6.0$
7.75-8.25				(*-4.84*$^{+0.85}_{-1.19}$)
8.00-8.50	(**-4.05**$^{+0.23}_{-0.34}$)	(**-4.19**$^{+0.42}_{-0.71}$)	(**-4.33**$^{+0.28}_{-0.44}$)	(**-4.59**$^{+0.44}_{-0.70}$)
8.25-8.75	*-3.91*$^{+0.28}_{-0.41}$	*-3.77*$^{+0.29}_{-0.42}$	*-4.11*$^{+0.29}_{-0.41}$	(*-4.78*$^{+0.45}_{-0.65}$)
8.50-9.00	**-3.84**$^{+0.20}_{-0.28}$	**-3.73**$^{+0.27}_{-0.38}$	**-4.27**$^{+0.28}_{-0.39}$	(**-4.83**$^{+0.46}_{-0.61}$)
8.75-9.25	*-3.90*$^{+0.22}_{-0.32}$	*-3.95*$^{+0.27}_{-0.40}$	*-4.56*$^{+0.37}_{-0.51}$	*-4.77*$^{+0.43}_{-0.71}$
9.00-9.50	**-4.64**$^{+0.44}_{-0.65}$	**-4.39**$^{+0.46}_{-0.62}$	**-4.84**$^{+0.49}_{-0.67}$	**-5.14**$^{+0.59}_{-0.92}$
9.25-9.75	*-5.02*$^{+0.62}_{-0.87}$	*-5.08*$^{+0.88}_{-1.17}$	*5.01*$^{+0.62}_{-0.91}$	*-5.42*$^{+0.90}_{-1.22}$
9.50-10.00				**-5.42**$^{+0.90}_{-1.22}$
9.75-10.25				
10.00-10.50				*-5.39*$^{+0.88}_{-1.20}$
10.25-10.75				**-5.39**$^{+0.88}_{-1.20}$

* Bold (or italic) values represent independent mass bins. Values in brackets indicate mass bins that are below the completeness limit.

We carried out the MCMC analysis using the PYTHON package `emcee` (Foreman-Mackey et al., 2013), which uses a set of walkers to explore the parameter space simultaneously. We carried out the MCMC analysis using 50 walkers with 10000 steps (draws), discarding the first 1000 sampled draws of each walker (burnin). The log-likelihood was built in the following form:

$$L = -\frac{1}{2}\sum\left(\frac{\Phi_{\rm Model}-\Phi}{\delta\Phi}\right)^2. \tag{6.7}$$

Given the small number of DMF points, however, we are not able to tightly constrain the faint and bright-end of the Schechter function. For $\rm DMF_{25K}$, $M^*_{\rm D}$ is significantly higher than what is found by Pozzi et al. (2020) and the best-fit has a very different shape. The $\rm DMF_{35K}$ is instead more consistent with the Pozzi et al. (2020) estimate and the best-fit is also more in agreement, even though the $M^*_{\rm D}$ is still higher. Indeed, by fitting the DMF using only the A^{3}COSMOS data, we cannot robustly constrain all parameters of the Schechter function.

As already done by Traina et al. (2024) for deriving the LF best fit, we exploit the *Herschel* data derived by Pozzi et al. (2020) to fit the DMF. The greater statistic of the *Herschel* data at $0 < z < 2.5$, allows us to combine the accuracy of the DMF by Pozzi et al. (2020) at lower-mid redshifts, with the capability of ALMA to explore the dust content of galaxies in the high-z Universe. With this combined datasets, we are able to better constrain the shape of the DMF. We ran the MCMC using flat prior distributions for the two free parameters and with α fixed to the values found by Pozzi et al. (2020) (i.e., α=1.48), with $\log(\Phi^*_0)$ between -2.5 and -2 and $\log(M^*_{\rm D,0})$ between 6 and 7.5. The *Herschel* DMF was derived by assuming that the dust temperature is a function of z and of the sSFR. This means that the galaxies in that sample do not have a fixed temperature, so it is not possible to coherently combine those estimates of the DMF with ours $\rm DMF_{25K}$ or $\rm DMF_{35K}$. For this reason, we decided to combine the Pozzi et al. (2020) DMF with the CIGALE DMF, since it does not assume a fixed temperature and is also more consistent with the Pozzi et al. (2020) data. The results of these DMF fits in each redshift bin and for each method are shown in Figure 6.5, considering only A^{3}COSMOS data, and 6.6, combining A^{3}COSMOS with *Herschel* results, which are summarized in Table 6.2.

We compare our DMF data points with the few estimates available in similar redshift ranges from the literature. In particular, at $0.5 < z < 2.5$, we compare the A^{3}COSMOS DMFs with the results by Pozzi et al. (2020). Firstly, it is important to underline the main differences between the two samples. The *Herschel* data sample is much larger than the A^{3}COSMOS sample (~ 7000 and ~ 190 galaxies, respectively), leading to lower uncertainties on the estimated DMFs. Moreover, the *Herschel* sample traces a wider range of dust masses, both at the faint (due to a better sensitivity) and the bright-ends (larger co-moving volume probed). In the redshift and luminosity range in common, in the A^{3}COSMOS and

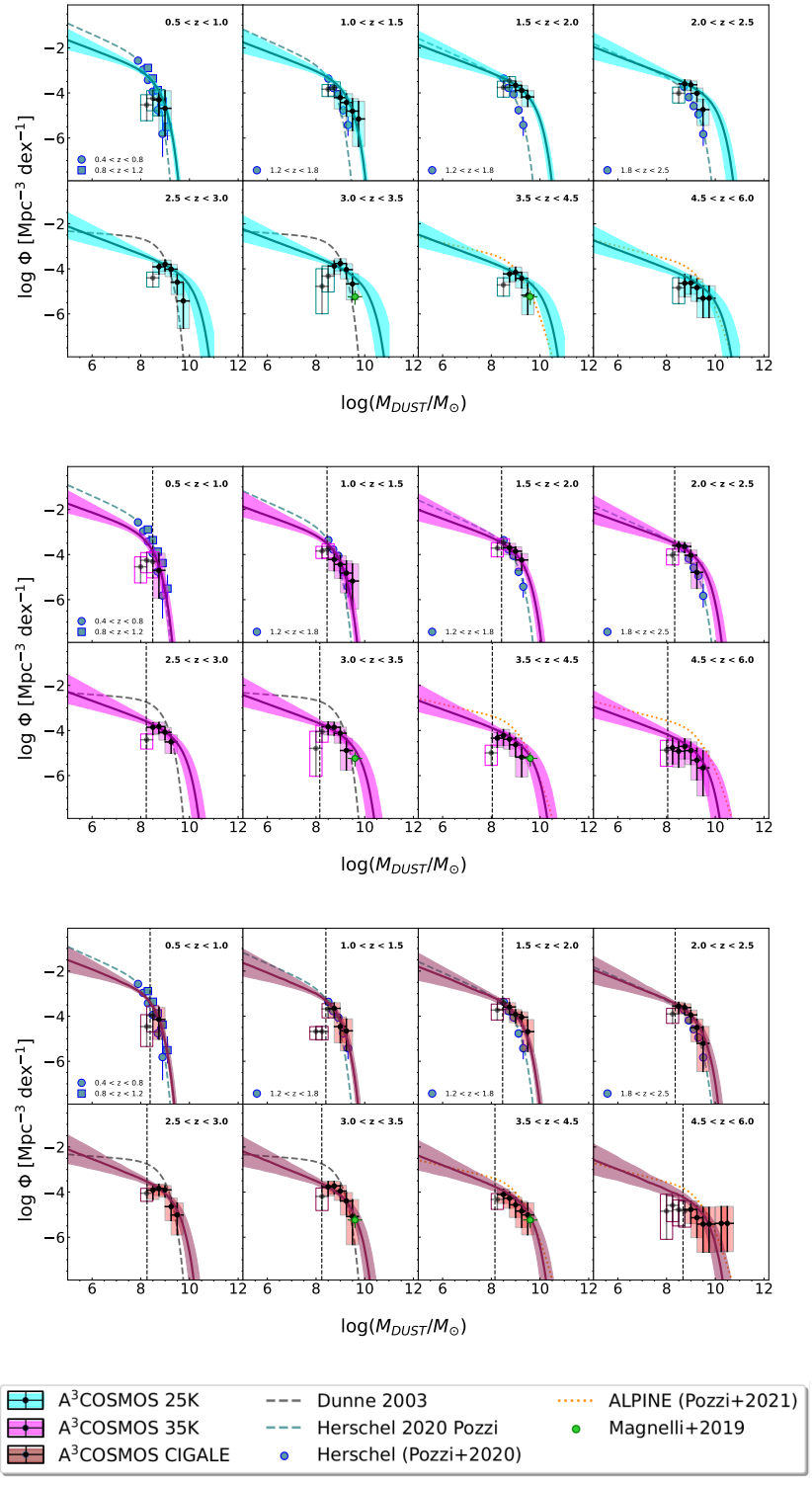

Figure 6.5: Dust mass function derived using the $V_{\rm MAX}$ method for dust masses of the galaxies computed assuming $T_{\rm D} = 25$K (cyan squares and black circles with errors, computed following Gehrels (1986), upper panel), $T_{\rm D} = 35$K (magenta squares and black circles with errors, central panel) and using the dust mass from CIGALE (red squares and black circles with errors, lower panel). The best-fit, computed using the A^{3}COSMOS data points, is displayed as a red solid line, with shaded errorbands of the same colors. For this fit, $M^*_{\rm D}$, $\Phi^*_{\rm D}$ and α are free to vary. For comparison, different estimates from the literature are reported. The light blue circles and squares are the values obtained by Pozzi et al., 2020 and the black dashed lines correspond to the best-fit. The green dashed curves are from Dunne et al., 2003. The blue circle is the estimate by Magnelli et al., 2019b and the dashed line is the ALPINE dust mass function by Pozzi et al., 2021.

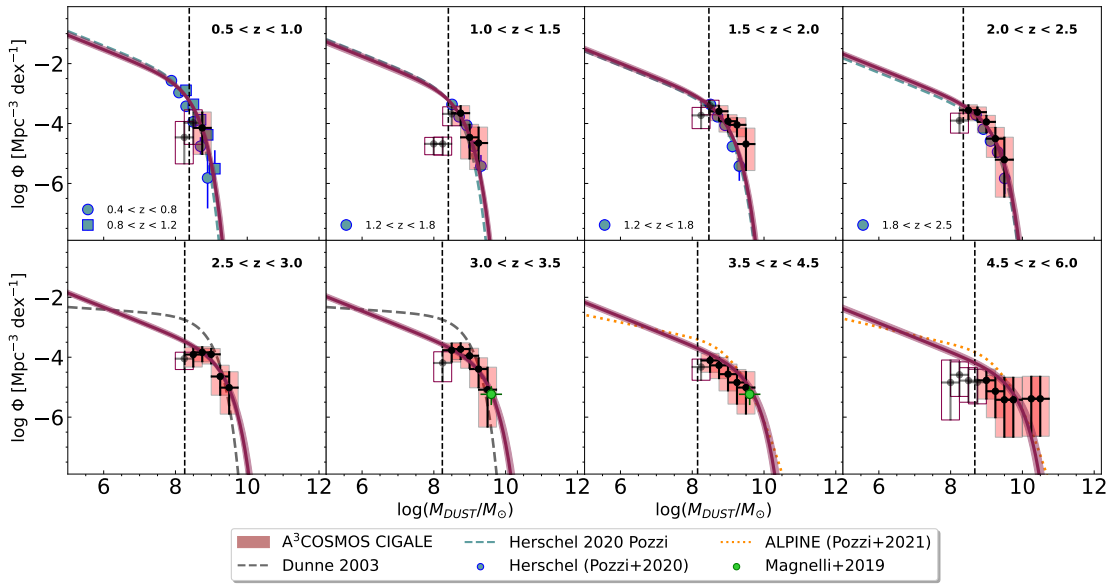

Figure 6.6: Dust mass functions derived using the $V_{\rm MAX}$ method for dust masses of the galaxies obtained via SED fitting (red boxes and black circles with errors, computed following Gehrels (1986)). The best-fit is displayed as a red solid line, with shaded errorbands of the same colors. For comparison, different estimates from the literature are reported. The light blue circles and squares are the values obtained by Pozzi et al., 2020 and the black dashed lines correspond to the best-fit. The green dashed curves are from Dunne et al., 2003. The blue circle is the estimate by Magnelli et al., 2019b and the dashed line is the ALPINE dust mass function by Pozzi et al., 2021.

Table 6.2: Best-fit parameters at the knee of the DMF. Dust masses ($M_{\rm D}^*$) and normalizations (Φ^*) with 16th, 50th, and 84th percentiles at the knee in the eight redshift bins obtained through the MCMC analysis or, in the ALMA+*Herschel* case, using the information from all the redshifts together.

z	$\log(M_{\rm D}^*/M_\odot)$	$\log(M_{\rm D}^*/M_\odot)$	$\log(M_{\rm D}^*/M_\odot)$	$\log(\Phi^*/{\rm Mpc}^{-3}{\rm dex}^{-1})$	$\log(\Phi^*/{\rm Mpc}^{-3}{\rm dex}^{-1})$	$\log(\Phi^*/{\rm Mpc}^{-3}{\rm dex}^{-1})$
	16th	50th	84th	16th	50th	84th
$0.5-1.0$	8.06	8.24	8.41	-2.89	-2.50	-2.09
$1.0-1.5$	8.28	8.51	8.74	-3.27	-2.87	-2.44
$1.5-2.0$	8.47	8.72	8.96	-3.63	-3.20	-2.78
$2.0-2.5$	8.61	8.87	9.12	-3.89	-3.45	-3.01
$2.5-3.0$	8.75	9.02	9.29	-4.15	-3.70	-3.26
$3.0-3.5$	8.85	9.13	9.41	-4.34	-3.88	-3.43
$3.5-4.5$	9.00	9.30	9.59	-4.63	-4.16	-3.70
$4.5-6.0$	9.17	9.49	9.79	-4.95	-4.46	-3.99

the *Herschel* results, we find a weak agreement with the DMF$_{25\rm K}$ and a much better consistency when using the 35K dust masses, as well as the CIGALE $M_{\rm D}$. This agreement could be explained by the method used in Pozzi et al. (2020) to derive $T_{\rm D}$, which considers the dust temperature as a function of the redshift and the specific star formation rate (Magnelli et al., 2014), which leads to $T_{\rm D} > 25$K (thus lower $M_{\rm D}$ values), increasing with redshift up to $\sim 35-40$ K at $z \sim 2$. At higher redshifts, very few works have investigated the DMF. In Figure 6.5 and 6.6, we report the Dunne et al. (2003) DMF at $1 < z < 5$ (obtained from a SCUBA sample of dusty galaxies), the point by Magnelli et al. (2019b) at $3.1 < z < 4.6$, derived using the IRAM/GISMO 2mm Survey in the COSMOS field, and the ALPINE DMF at $z \sim 4.5$ (Pozzi et al., 2021). Within the large uncertainties of our data points, the three DMF estimates agree with the best-fit by Dunne et al., 2003. While the DMF$_{35K}$ and DMF$_{CIGALE}$ agree very well with the data point by Magnelli et al., 2019b at $z \sim 3.5$, the DMF$_{25}$ is weakly consistent within the errors. Finally, our DMF$_{25}$, as expected, is in a good agreement with the ALPINE DMF estimate, derived assuming $T_D = 25$K.

The typical dust mass at each redshift bin (i.e., $M_{\rm D}^*$) is almost constantly increasing by ~ 1 dex, from $z \sim 0.5$ to $z \sim 6$. This means that, as for $L_{\rm IR}^*$, massive galaxies are typically more dust rich at higher redshifts than their local counterparts. Similarly, the density Φ^* decreases steeply towards higher redshifts (by ~ 2 dex).

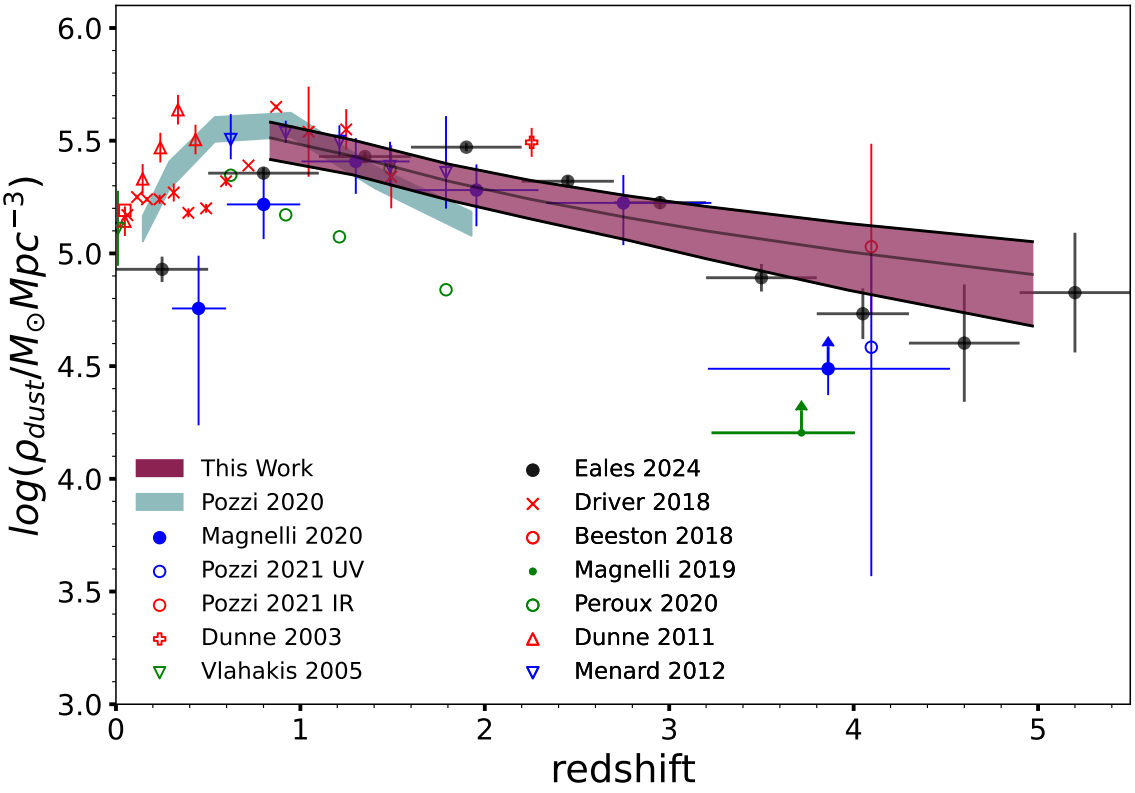

Figure 6.7: Dust mass density evolution with redshift, derived by integrating the CIGALE dust mass function in each redshift bin (red shaded area). Different estimates are shown as different colored points with different markers. The red plus marker shows the values by Dunne et al., 2003; the green triangles are the estimates by Vlahakis et al., 2005; the red triangles are the DMD points by Dunne et al., 2011; the blue triangles indicates the estimate by Ménard and Fukugita, 2012; the red crosses are the data points by Driver et al., 2018; the red circles are the data by Beeston et al., 2018; the estimate by Magnelli et al., 2019b is shown as a green filled circle; the green empty circles are the points by Péroux and Howk, 2020; the estimates by Pozzi et al., 2021 are shown as blue and red circles; the dust mass densities from Magnelli et al., 2020 are displayed as blue filled circles; the black points are the DMD estimates by Eales and Ward, 2024; finally, the light blue shaded area represents the estimate of the dust mass density by Pozzi et al., 2020. For a self-consistent comparison, we rescaled the data by Magnelli et al., 2020 and Pozzi et al., 2021 to a $T_{\rm D} = 35$K.

6.3.3 Dust mass density

By integrating the DMF best-fit (at $4 < log(M_{\rm D}) < 11$) in each redshift bin, we can measure the amount of dust, per unit of co-moving volume, in the Universe, obtaining the DMD. Figure 6.7 shows the DMD obtained by integrating the combined CIGALE and *Herschel* DMF best-fit. We report the values of the DMD in Table 6.3. To allow the comparison of the results by Magnelli et al., 2020 and Pozzi et al., 2021 with ours, we rescaled their DMDs from $T = 25$K to $T = 35$K. We find the DMD to be following the shape of the Pozzi et al., 2020 DMD, with a smoother decrease from $z = 1$ to higher redshifts. Our results are in excellent agreement with the estimates by Ménard and Fukugita, 2012, obtained for MgII absorbers. We are also consistent with the DMD from Driver et al., 2018 between $z \sim 1$ and $z \sim 2$. We are consistent with Magnelli et al., 2020 (rescaled from a temperature of 25K to 35K) at $z \sim 1.5 - 3$. The DMD by Péroux and Howk, 2020 is instead significantly lower between $z \sim 1.5$ and $z \sim 4$. At $z \sim 4.5$, we are fully consistent with the results obtained from the rest-frame FIR selected galaxies in the ALPINE ALMA survey (Pozzi et al., 2021). Comparing our results with the recent estimates by Eales and Ward, 2024, obtained using *Herschel*-ATLAS, we find a good agreement at $z \sim 1.5$, while our DMD is lower at $2 < z < 3$ and slightly higher at $3 < z < 5$.

Although using a $M_{\rm D}$ estimate computed without assuming a fixed $T_{\rm D}$ may lead to a DMD estimate unbiased towards the choice of $T_{\rm D}$, however, to compare the DMD with some of the literature estimates, one must be careful in considering different temperature assumptions by different authors. For example, both Magnelli et al., 2020 and Pozzi et al., 2021 assume $T_{\rm D} = 25$K. For our sample, assuming $T_{\rm D} = 25$K instead of $T_{\rm D} = 35$K, leads to a $\sim 54\%$ higher dust mass, meaning that we will expect higher values of $M^*_{\rm D}$ and corresponding larger values of the $\rho(z)_{\rm D}$. In this way, a disagreement with other datasets is likely due to different $T_{\rm D}$ assumptions. Here we derive also the DMDs by integrating the DMFs obtained assuming $T_{\rm D} = 25$K and $T_{\rm D} = 35$K. Here we use the A^{3}COSMOS data only, since we cannot consistently combine them with the Pozzi et al., 2020 data, which are obtained using a varying $T_{\rm D}$. The results are shown in Figure 6.8. As expected, $\rho(z)_{\rm D,T=35K}$ is typically lower than $\rho(z)_{\rm D,T=25K}$.

6.4 Discussion

In this Section, we compare our results with predictions for the DMF and DMD from models in the literature. In particular, we consider the semi-analytical model by Parente et al., 2023b for comparison to the DMF, and the predictions by Gioannini et al., 2017, Popping et al., 2017, Aoyama et al., 2018, Li et al. (2019), Vijayan et al., 2019, Triani et al., 2020, Parente et al., 2023b and Yates et al. (2024) to compare with the DMD. Although different in

Table 6.3: Dust mass density obtained by integrating the DMF best-fit in our eight redshift bins, for the CIGALE A^{3}COSMOS + *Herschel* fit.

z	$\log\rho_{\rm DUST}$ $[\mathrm{M_\odot Mpc^{-3}}]$		
	16th	50th	84th
$0.5-1.0$	5.42	5.51	5.58
$1.0-1.5$	5.35	5.43	5.50
$1.5-2.0$	5.24	5.32	5.40
$2.0-2.5$	5.15	5.24	5.32
$2.5-3.0$	5.06	5.16	5.25
$3.0-3.5$	4.98	5.10	5.21
$3.5-4.5$	4.84	5.01	5.13
$4.5-6.0$	4.68	4.91	5.05

* The third column is the median value, while second and fourth columns show the lower and upper 16th boundaries.

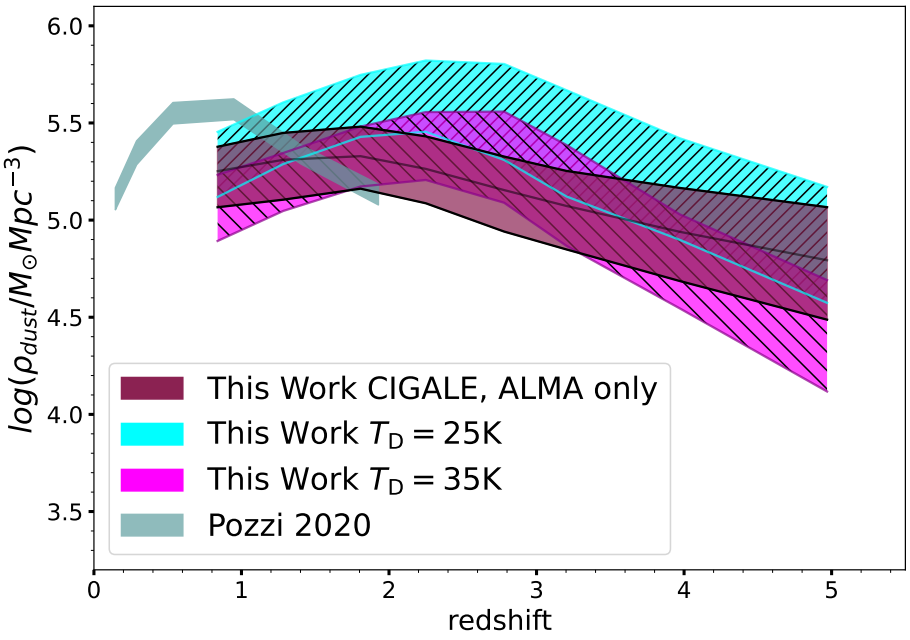

Figure 6.8: DMDs obtained by integrating the DMFs in Figure 6.5. The darkred area is the DMD computed from the ALMA-only DMF; the cyan and magenta areas are obtained from the DMFs derived considering a dust temperature of 25K and 35K, respectively. The light blue shaded area is the DMD estimated by Pozzi et al. (2020).

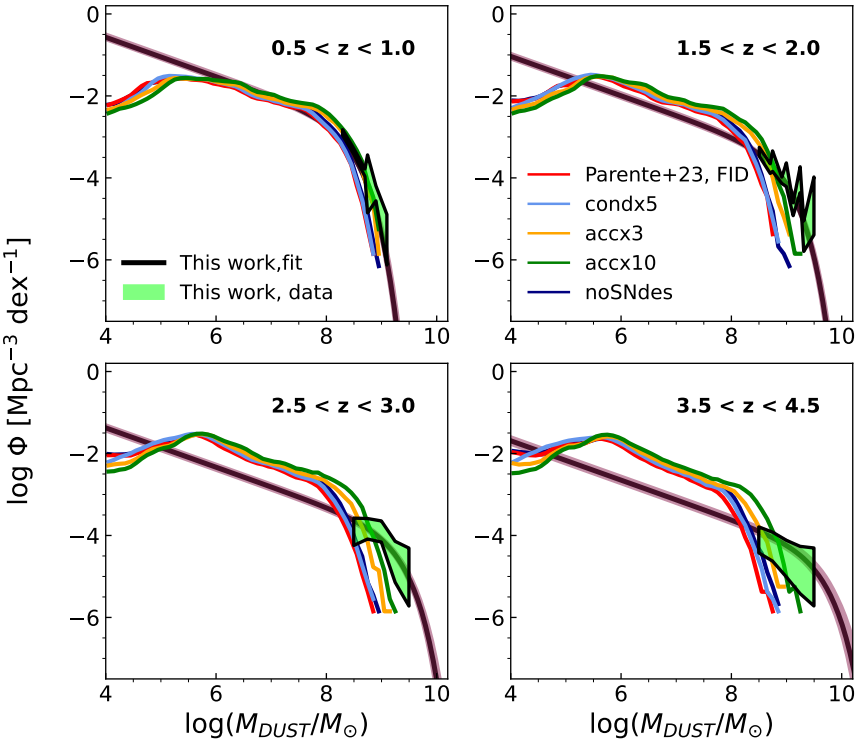

Figure 6.9: Comparison between the DMF derived in this work (black solid line and light-green points, with black borders) and the predictions by Parente et al., 2023b, with different prescriptions.

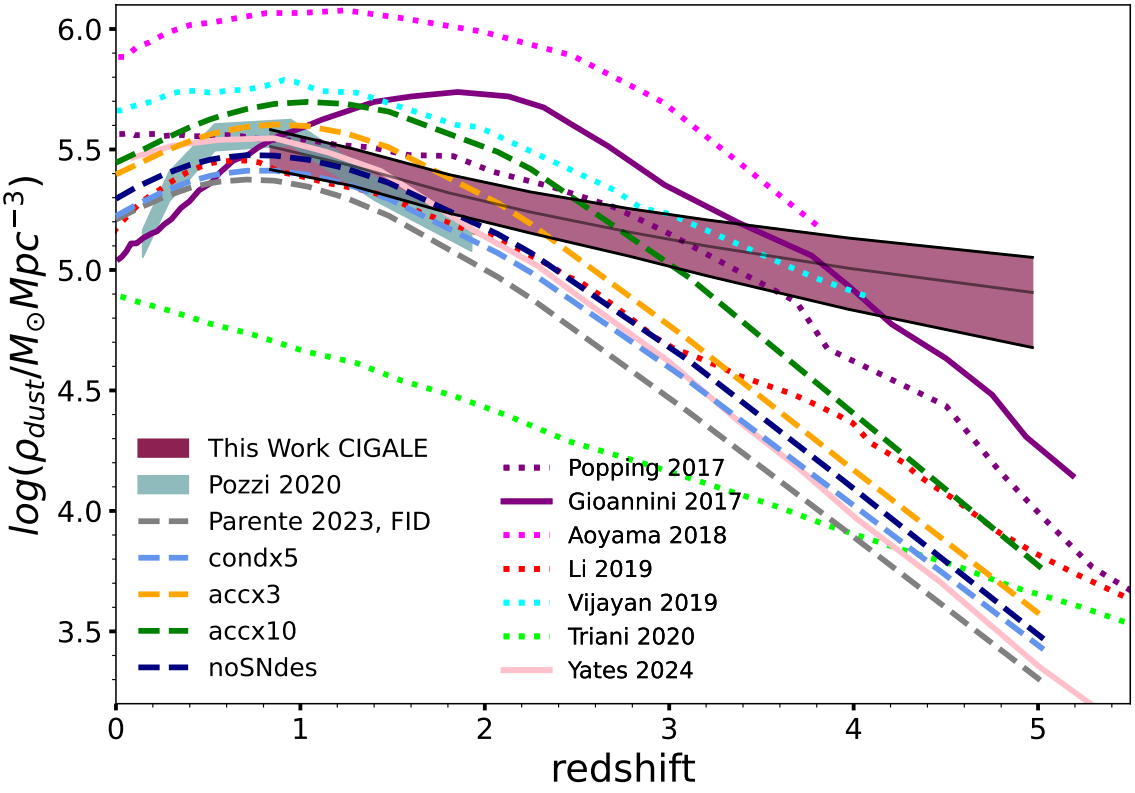

Figure 6.10: Comparison between our DMD (derived using the CIGALE dust masses) and predictions from simulations. The purple solid line is the DMD by Gioannini et al., 2017, while the purple dashed line represents the prediction by Popping et al., 2017. The magenta dotted line is the prediction by Aoyama et al., 2018, the cyan dotted line is the DMD predicted by Vijayan et al., 2019, the light-green dotted curve is by Triani et al., 2020, red dotted line is the prediction by Li et al. (2019) and the pink solid line is the DMD from Yates et al. (2024). The grey, light blue, yellow, green and blue dashed lines are the DMDs estimated using the models by Parente et al., 2023b with different prescriptions.

the details implementation, the dust models in the aforementioned works are conceptually similar. They all include: (i) dust production by stellar sources (SNe and AGB stars) (ii) dust evolution in the ISM, in particular accretion of gas-phase metals onto pre-existing grains, and destruction of grains in hostile environments (e.g. SN shocks and the hot phase) (iii) astration of grains, that is grains returning into newly formed stars. All these processes play a role in determining the amount of dust present in galaxies. Specifically, the evolution of dust within the ISM turns out to be very important. Simulations indicate that the bulk of the dust mass observed today originates from grain accretion within the ISM, while stellar production only contributes a small fraction ($< 10\%$) to the overall dust budget (e.g. Vijayan et al. 2019, Parente et al. 2023b). The DMD predicted by the aforementioned models is shown in Fig. 6.10. There is a great dispersion, spanning about one order of magnitude at all redshifts. Also, there is no agreement in terms of shape. In some of the models (e.g. Triani et al. 2020, Popping et al. 2017) we observe a $\rho_{\rm dust}$ increasing with cosmic time, while some others (e.g. Gioannini et al. 2017, Aoyama et al. 2018, Li et al. 2019, Parente et al. 2023b) predict a clear drop from $z \simeq 1-2$ to $z = 0$, which is more in line with our results. In general, none of the models is able to match both the shape and normalization of the observed $\rho_{\rm dust}$. The different performances among the various models in predicting cosmic dust abundance originate from distinct underlying reasons that are challenging to pinpoint. Firstly, while the theoretical frameworks of these models are conceptually similar, their practical numerical implementation can vary significantly. Secondly, a major contributing factor could be that the dust model is implemented on top of different galaxy evolution models, each incorporating sub-grid recipes for processes (e.g. star formation, chemical enrichment) which are crucial for the production and evolution of dust mass. Analyzing these disparities is not trivial and goes beyond the scope of the current work. Instead, we adopt an alternative approach, aiming to quantify the influence of specific dust-related mechanisms — namely stellar production, ISM accretion, and SN-driven destruction — on the overall dust budget. To do this, we standardize the galaxy evolution framework to accentuate the impacts of the targeted processes. Specifically, we conduct multiple simulations using the L-Galaxies (Parente et al., 2023b) model[1] to explore potential ways for increasing the dust mass at the redshifts investigated here.

The conducted simulations are as follows:

- **condx5**: the dust condensation efficiency is enhanced by a factor of 5, to mimic a larger dust production by stellar sources (both AGBs and SNe);
- **accx3**: the ISM grains accretion timescale is reduced by a factor of 3, to mimic a more

[1]It is noteworthy that this model is able to reproduce the general trend of redshift evolution of the dust mass density within the uncertainties (see Fig 10 of Parente et al. 2023b).

efficient accretion in molecular clouds;

- **accx10**: same as before, but the timescale is reduced by a factor of 10;
- **noSNdes**: grains destruction is SN shocks is switched off.

In Fig. 6.10, we present the DMD results from these experiments. Switching off grains destruction by SNe only marginally increases the overall dust abundance compared to the fiducial run. This occurs because the metals generated by the SNe-driven destruction rapidly recombine into dust grains through the highly efficient accretion process. Similarly, increasing the stellar production of grains has a minor effect on the DMD, raising it by a factor of $\simeq 1.4$ at $z > 1$. Conversely, increasing the efficiency of grains accretion has a stronger impact on the DMD, boosting it by a factor of 2 compared to the fiducial model, bringing it closer to our A^{3}COSMOS estimation. Nevertheless, both the accx3 and accx10 simulations overestimate the DMD at $z < 0.5$.

Since the A^{3}COSMOS DMD is derived from the integration of the observed DMF, it is also interesting to compare the latter for the aforementioned SAM-based experiments, as shown in Fig. 6.9. As previously mentioned, modifying the stellar production and switching off the SNe-driven grains destruction has a minimal impact on the predicted DMF. Conversely, enhancing the accretion efficiency brings the SAM predictions closer to the observed DMF, particularly at $z > 2$ in the accx10 run. Among our experiments, this is the only way to generate objects with dust masses akin to those observed ($\simeq 10^9, M_\odot$). We additionally note a discrepancy between the simulated DMFs and the extrapolated Schechter fit at $M_{\rm dust} < 10^8, M_\odot$, where direct observations are unavailable. It is worth noting that this constitutes an important source of tension when examining the DMD since the integration of the DMF up to $M_{\rm dust} \sim 10^8, M_\odot$ accounts for $< 95\%$ of the DMD.

We conclude this section with two caveats regarding our numerical experiments. The first concerns the underlying galaxy evolution framework of the model. Specifically, the SAM by Parente et al., 2023b has been noted to exhibit a lack of highly star-forming galaxies at $z > 1$ (see Chapter 5). These galaxies also host substantial amounts of dust, the same dust missing in Fig. 6.9. Secondly, while increasing accretion alleviates discrepancies with observations, we caution that it may affect the relationship between the dust-gas ratio and ISM metallicity (Parente et al., 2022), a topic beyond the scope of this study.

6.5 Summary and Conclusions

In this Chapter, we investigated the properties of the dust mass budget in high-redshift galaxies. To this end, we studied a sample of 189 ALMA-selected star-forming galaxies in

a wide redshift range ($0.5 < z < 6$), drawn from the A^{3}COSMOS database. By performing SED fitting analysis, we measured the dust content of each galaxy (i.e., dust mass and temperature) and we used these estimates to derive the DMF and the DMD. We summarize our results as follows:

- The A^{3}COSMOS star-forming galaxies are dust-rich, with SED-based dust masses between 10^8 and 10^9 M$_\odot$ and the bulk of them showing a $T_{\rm D} \sim 30 - 35$K;
- We compare SED fit-based dust measurement, taking advantage of the multiwavelength information and assuming energy balance, to RJ-based dust mass estimates being more direct but limited by the assumed dust temperature. RJ-based dust masses are in good agreement with the SED fit-based ones, when the assumed dust temperature is roughly consistent with those inferred from our SED fit (∼35K), while the dust mass estimate with $T = 25$ are $\sim 54\%$ higher;
- Using $M_{\rm D}$ derived from the SED fitting, we estimated the DMF and fitted it in combination with the *Herschel* DMF by Pozzi et al. (2020), that are in excellent agreement with our A^{3}COSMOS estimates. We obtained a DMD showing a decrease of the dust content towards higher redshifts, consistently with other results from the literature;
- The DMF inferred from the $M_{\rm D}$ derived from the SED fit are in good agreement with those derived by Pozzi et al., 2020 in the luminosity and redshift range in common between these two studies;
- Combining the Herschel and ALMA DMFs measurement we inferred, from the first time, the evolution of the DMFs over a wide range of redshifts ($0.5 < z < 6$). The characteristic density (Φ^*) and mass (M_D^*) of the DMFs are evolving with a decreasing and increasing trend with redshift, respectively;
- Integrating the DMFs down to 10^4 M$_\odot$, we found that the DMD evolves with a smoothly decreasing trend from $z \sim 0.75$ to $z \sim 5.25$, without showing a drastic drop towards higher redshifts.
- None of the models available in literature is able to match both the shape and normalization of the observed DMD at $0.5 < z < 5$. Through dedicated numerical experiments, we find that the grains accretion in the ISM is the most effective dust-related process for increasing the dust content of galaxies.

With this study, we were able to explore the dust content of the Universe at high redshift, were still little is known about the mean mechanisms responsible for their production in the galaxies that are populating it. As some other studies has already found, our result

confirm that the dust mass density seems to be decreasing smoothly from $z \sim 1$ to $z \sim 6$. However, a key role is played by the assumptions on the dust temperature, which can significantly change the results. Further detailed studies on the dust content in individual, as well as on large samples of galaxies, especially with the ALMA interferometer (in particular with the "ALMA Wideband Sensitivity Upgrade", that is going to improve significantly the performances and the sensitivity of the interferometer), will surely improve our knowledge of the properties characterizing the dust and its evolution with the cosmic time.

CHAPTER 7

AGN in A^{3}COSMOS

In the previous Chapters we derived the main physical properties (i.e., $M_\star$, $L_{\rm IR}$, $M_{\rm D}$ and SFR) that characterize dusty star forming galaxies selected in the (sub-)mm, which are fundamental in understanding their evolution. Indeed, we investigated as well the key statistical quantities (IR LF, SFRD, DMD) that allow us to measure at which rate galaxies are building up their masses through the formation of stars, but also to study how their reservoirs of gas and dust are evolving with cosmic time. Nevertheless, a fundamental role in shaping evolution of galaxies can be played by the possible presence of AGN activity (see Section 1.5), affecting the properties of the host galaxy. In this perspective, it is thus important to characterize the aforementioned physical properties of galaxies hosting an AGN with respect to their non-active counterparts (or in galaxies where the AGN contribution is less significant). Hence, in this Chapter, we will analyze the physical properties of galaxies hosting an AGN in the A^{3}COSMOS (Section 7.1) and their contribution to the IR LF and dust obscured SFRD (Section 7.2). Through this Chapter, with AGN host galaxies we refer to those sources having an AGN fraction (in the wavelength range between 5 and 40 μm) higher than 0.3 (i.e., the AGN emission contributes for more than 30$\%$ to the total emission, in the MIR part of the SED).

7.1 AGN properties

In Section 3.3.2 we have described the parameters characterizing the IR emission due to an AGN. This emission can be described as a three component emission: one coming from central the engine (i.e., the accretion disc); a scattered emission produced by dust and a thermal component due to dust emission. In order to select AGN host galaxies within the A^{3}COSMOS sample, we selected a threshold in one of the parameters that is given as an output from the SED fitting, i.e., the AGN fraction, defined as the ratio between the IR emission due to the AGN and the total IR emission computed in the $5 < \lambda < 40 \mu$m wavelength

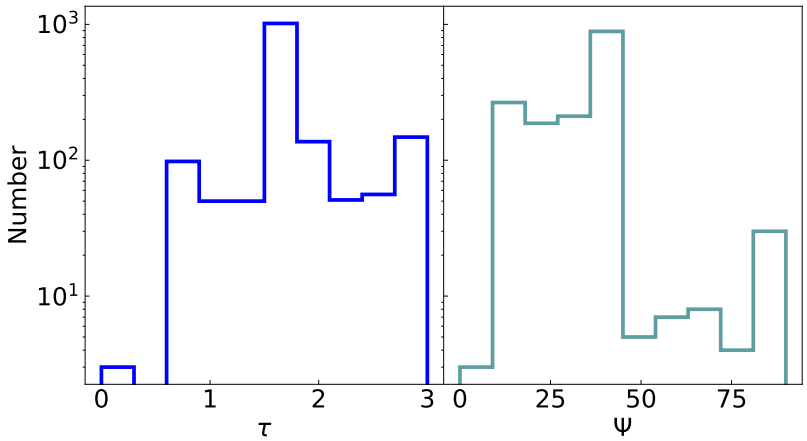

Figure 7.1: Distributions of the optical depth at 9.7μm (left panel) and of the angle between the line of sight and the equatorial axis of the torus (right panel).

range. This value can indeed be used as a measure of the dominance of the AGN-driven emission over the galaxy one. From the SED fitting and the best-fit torus model, for each galaxy we were able to obtain the value of the optical depth at 9.7 μm (τ), indicative of the thickness of the dusty torus and the angle between the line of sight and the equatorial axis (Ψ). In Figure 7.1 we show the histogram of the values of τ and Ψ obtained for our sources containing an AGN. The optical depth has an almost uniform distribution over the whole range $1-3$ (which was the input grid range selected), with a shallow peak at $\tau \sim 1.5-2$. Most galaxies have an inclination angle of the torus, with respect to the line of sight, between 0° and 50°, meaning that the majority of the AGN in the A^{3}COSMOS sample are likely to be obscured by the torus.

We thus selected AGN host galaxies by using $f_{\rm AGN,5-40} = 0.3$ as a threshold (although different, more conservative, selections could be based on this parameter). We found 576 galaxies to be AGN dominated in the initial A^{3}COSMOS sample and 47 in the final sample. For the galaxies hosting an AGN, we checked the presence of the Spitzer/MIPS detection, to validate the robustness of the AGN fractions we derived, finding that only 8/47 galaxies have not detection at $24\mu m$. We compare the stellar mass, SFR and dust mass of those galaxies with the same quantity in galaxies with a less significant AGN fraction. In Figure 7.2 we report the density distribution of the SFR, stellar mass and redshift of the sources hosting an AGN compared to those of sources with $f_{\rm AGN,5-40} < 0.3$. The SFR distributions are very similar for galaxies with and without AGN, with median values $< SFR_{\rm AGN} >= 183^{+263}_{-143}$ M$_\odot$ yr^{-1} and $< SFR_{\rm NO-AGN} >= 193^{+381}_{-138}$ M$_\odot$ yr^{-1}, respectively. The stellar mass and redshift distributions show a slight difference, with galaxies with higher AGN significance being on average less massive and at higher redshifts ($< log(M_{\star,\rm AGN}/{\rm M}_\odot >) = 10.87^{+0.91}_{-0.32}$, $< z_{AGN} >= 2.55^{+1.68}_{-0.78}$; $< log(M_{\star,\rm NO-AGN} > /{\rm M}_\odot >) = 11.04^{+0.60}_{-0.29}$, $< z_{NO-AGN} >=$

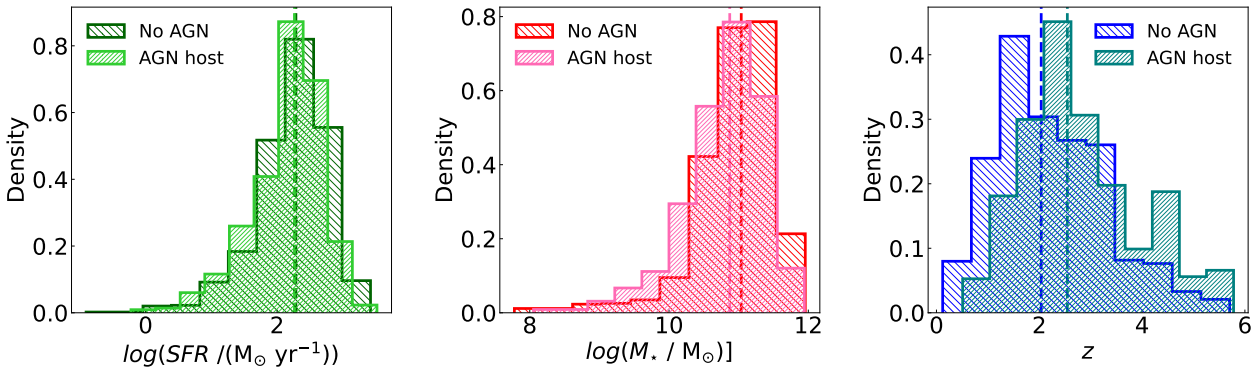

Figure 7.2: Density distributions of SFR, $M_\star$ and redshift of the galaxies with $f_{\rm AGN,5-40}$ lower and higher than 0.5, represented with different colors.

$2.04^{+1.15}_{-0.85}$). Galaxies hosting AGNs have been found to be more present at higher redshifts also in previous works (e.g., Gruppioni et al., 2013; Yang et al., 2023). Gruppioni et al. (2013) also found that, in general, galaxies hosting an AGN tend to be more massive than their non-active counterparts. Also, Mountrichas et al. (2024) are finding that, at a given stellar mass (below 10^11 $M_\odot$), AGN host galaxies are usually more star forming than normal galaxies at $\sim 0 < z < 2$.

7.2 Contribution of the AGN host galaxies to the star formation rate density

Finally, here we investigated the contribution of the AGN host galaxies to the IR LF and SFRD. In particular, we computed and fitted the LF with the same method described in Section 4.1, for the sub-sample of galaxies with $f_{\rm AGN,5-40} > 0.3$. The result is reported in Figure 7.3. We compare the best fit,of the IR LF of galaxies hosting an AGN to that obtained for the IR LF derived in Chapter 4. As it can be seen from the figure, the best-fit of the AGN population is lower than the total IR LF, except for the bright-end of the LF, which seems to be mostly due to galaxies hosting an AGN at any redshifts. In Figure 7.4 we also show the ratio between the AGN host IR LF and the total IR LF, as a function of the luminosity, in each redshift bin. We notice that, on average, the ratio seems to increase with redshift, while it remains almost constant with luminosity, except for the the redshift bins between $z \sim 1.5$ and $z \sim 3.5$, in which the ratio increases from $R \sim 0.3$ to $R \sim 0.6$, at the higher $L_{\rm IR}$, i.e., $12 < log(L_{\rm IR}) < 13$, although in this luminosity range the uncertainties become very large.

By integrating the AGN host IR LF we obtain the SFRD from the host population (Figure 7.5). We compare the dust obscured SFRD derived here with the total SFRD derived in

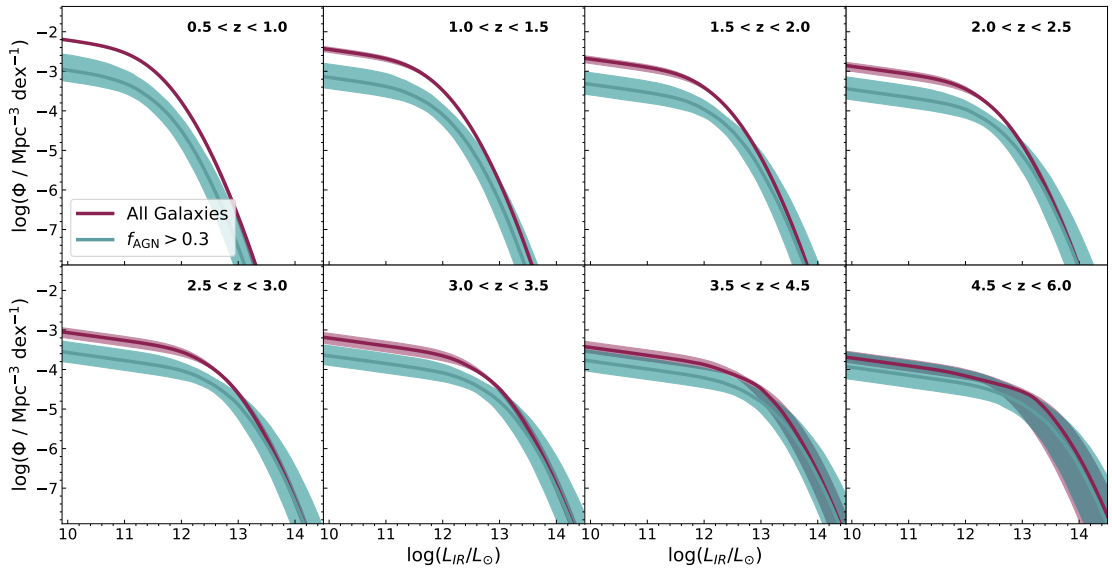

Figure 7.3: IR LF from AGN host galaxies (teal curve) compared to the best fit obtained for all the galaxies (red curve).

Chapter 4. From $z \sim 0.5$ to $z \sim 3.5$, the AGN host contribution is ~ 0.5dex lower than the total. At higher redshifts ($4 < z < 6$) the contribution is more significant, suggesting that the SFRD at high redshifts is likely to be dominated by galaxies hosting an AGN.

A similar analysis has been performed by Symeonidis and Page (2021), at $0 < z < 2.5$, in which they investigated the contribution of the presence of an AGN in the IR-LF and dust-obscured SFRD. In this work, they found the IR-LF to be dominated by star-forming galaxies at $L < L^*$, and by the AGN host galaxies at higher luminosities, in agreement with our results. Moreover, they found the ratio between the total IR luminosity and the IR luminosity from AGN host galaxies to be strongly increasing at all redshifts, in weak agreement with our results, which show a significant increase at $1.5 < z < 4.5$, at $L_{\rm IR} > 5 \times 10^{12}$ L$_\odot$.

7.3 Conclusions

In this Chapter we analyzed the effect of the AGN presence on the galaxies physical properties (i.e., SFR, stellar mass) and the contribution of galaxies hosting an AGN in the IR-LF and SFRD. The results can be summarized as follows:

- The A^{3}COSMOS sample is characterized by $\sim 36\%$ of sources that are likely hosting an AGN (i.e., $f_{\rm AGN,5-40} > 0.3$. The SFRs of galaxies with an AGN contribution are similar to those of galaxies without an AGN, while the stellar masses are slightly different, yet consistent within the errors. This could be interpreted with the AGN

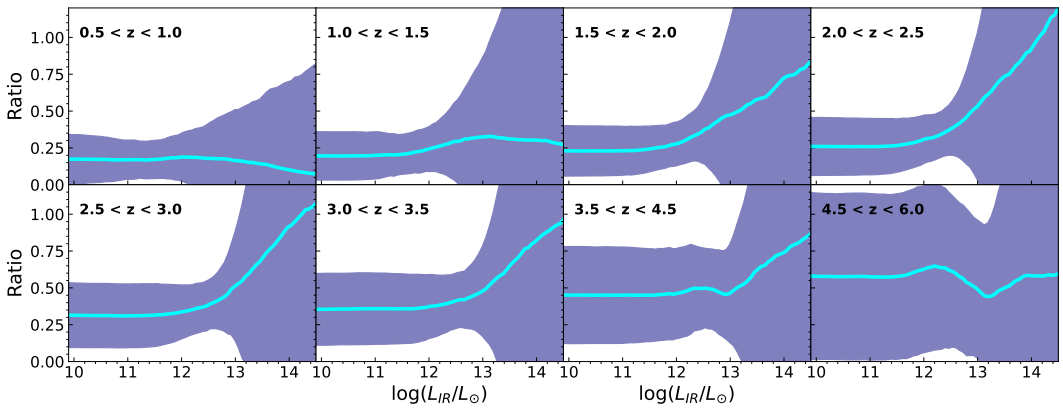

Figure 7.4: Ratio between the AGN host IR LF and the total IR LF, as a function of the luminosity and for eight redshift bins.

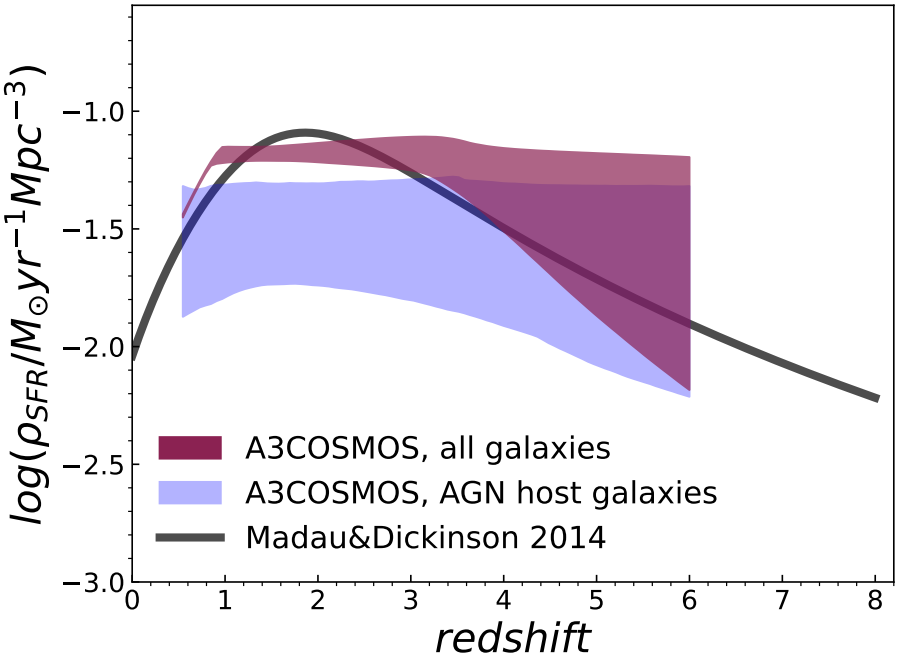

Figure 7.5: Star formation rate density contribution from galaxies hosting an AGN (light blue area), compared to the total dust obscured SFRD (red shaded area) and the Madau and Dickinson (2014) curve (black).

presence not being strongly affecting the properties of the host galaxies. In addition, galaxies hosting an AGN are located typically at higher redshifts, at which large reservoirs of gas and dust are though to be present in the host galaxies and can trigger the AGN activity.

- The IR-LF is dominate by star-forming galaxies in the faint-end, but it is mostly due to AGN host galaxies at the bright luminosities. Galaxies with extreme IR luminosity (and SFR) are therefore more likely to host an AGN.

- The contribution to the SFRD is mostly due to non-active star-forming galaxies, at $0.5 < z < 4$, but becomes dominated by those galaxies hosting an AGN at higher redshifts, where the contribution to the IR-LF is more significant.

CHAPTER 8

Conclusions and future prospects

The study of the evolution of galaxies with cosmic time implies the derivation of the main physical parameters for large samples of galaxies, enabling to study how these vary with redshift. Building large galaxy samples across a wide range of redshift and luminosities allows us to derive statistical properties as a function of the redshift, such as the LF and the cosmic SFRD. These quantities are fundamental for probing the statistical nature of various galaxy populations at different cosmic times, as well as for studying the mass assembly process in galaxies at different epochs. Since the majority of the star formation activity at cosmic noon ($z \sim 1 - 3$) is enshrouded by dust, the use of mm-selected samples of dusty star-forming galaxies with widemultiwavelength coverage allows us to characterize both obscured and unobscured star formation. The unprecedented sensitivity reached by ALMA, coupled with the selection of unbiased samples in the mm bands allows us to study the evolution of dusty galaxies up to higher redshifts than reached before, thus exploring the $z > 3$ previously uncovered by IR surveys. In this perspective, the A^{3}COSMOS survey, represents the largest existing ALMA survey, composed by all the available observations in the ALMA archive. However, A^{3}COSMOS is very heterogeneous in observing wavelength, as well as in sensitivity and resolutions. The unparalleled wealth of multiwavelength ancillary data available in the COSMOS field, including the cutting-edge COSMOS2020 optical-near infrared catalogue, make the A^{3}COSMOS survey a unique baseline for statistical studies on the nature and evolution of star-forming galaxies over a wide redshift and luminosity range, while being unaffected by dust extinction. For this reason, we have developed a technique that allowed us to use the heterogeneous A^{3}COSMOS survey as a blind-like survey, thus taking advantage of the large and deep galaxy sample for performing statistical studies.

This PhD Thesis primarily focused on a statistical assessment of the demography, star formation rate, dust content and cosmic evolution of the largest ALMA sample of star-forming galaxies available to-date. In this last Chapter, we summarize the main results obtained in this Thesis and discuss some on-going projects, as well as potential follow-up

studies based on this PhD Thesis.

8.1 Summary of the main results

Physical properties and statistical analysis

The large wealth of data present in the ALMA archive over the A3COSMOS survey has allowed us to study the physical properties of a large sample (> 1500) of dusty star forming galaxies, selected in the mm band. For this sources we performed a multiwavelength SED fitting, with photometric data covering from the optical/UV to the mm emission. We found the A^{3}COSMOS sample to be characterized by massive galaxies ($M_\star \sim 10^{10} - 10^{12}$ M$_\odot$) and IR-bright galaxies, with $L_{\rm IR} \sim 10^{11} - 10^{13}$ L$_\odot$ (corresponding to SFR up to ~ 1000 M$_\odot$ yr^{-1}).

In order to investigate the statistical quantities tracing galaxies evolution, we developed a method to turn the A^{3}COSMOS (inhomogeneous and targeted survey) into a "blind-like" survey, by taking into consideration the possible biases related to the observational targets and the possible clustering of sources.

Infrared luminosity function (Sec. 4.1) and star formation rate density (Sec. 4.2, 5.4)

The detailed analysis of the sample in the A^{3}COSMOS, coupled with the homogenisation of all the pointings, enabled us to investigate the IR-LF and its evolution with redshift, from $z \sim 0.5$ up to $z \sim 6$, finding that the typical luminosity (L^*) is increasing while its normalization (Φ^*) decreases. The derivation of the IR-LF allowed us to compute the first ALMA archival estimate of the dust-obscured SFRD at $0.5 < z < 6$. Our study corroborates the presence of a broad peak at $1 < z < 3.5$, preceded by a mildly rising trend from $z \sim 6$ to $z \sim 3.5$, and followed by a decreasing trend from $z \sim 1$ towards the local Universe.

Moreover, we compared the IR-LF and SFRD with predictions from hydrodynamical simulations and semi-analytical models. We found that models generally underpredict the bright (more star forming)-end of the LF (SFRF), which estimate much higher IR luminosities and larger SFRS, especially at high redshift.

Dust mass density (Sec. 6.3)

In addition, we took advantage of the mm selection of our sample to assess the main physical properties (mass, temperature) of interstellar dust for ALMA-selected star-forming galaxies, as well as their evolution over a wide redshift range. The dust masses of the A^{3}COSMOS

sources range between $M_{\rm D} \sim 10^8$ and $M_{\rm D} \sim 10^9$ $M_\odot$ and are characterized by a relatively low temperature ($25 < T_{\rm D} < 35$ K). We derive the DMF and DMD and their evolution with cosmic time, since $z \sim 6$ to $z \sim 0.5$. We found a slowly increasing DMD in the redshift range covered by our data, that, combined with lower-z estimates, suggests the presence of a broad peak at $0.5 < z < 1.5$.

8.2 On-going projects

JWST MIRI proposal

In order to investigate in more detail the properties of the AGN in the A^{3}COSMOS sample, especially around the cosmic noon ($2 < z < 3$), we decided to put in a JWST MIRI Cycle 3 proposal. In particular, we proposed to observe 29 AGN candidates selected from the SED fitting, which were already observed with MIRI at 7.7μm within the COSMOS-Web JWST survey (PI: Kartaltepe, PID:1727). Our goal was to follow them up with MIRI filters also at 10, 15 and 18 μm, which are sensitive to the IR emission driven by the AGN (if present). This study will eventually allow us to better characterize the AGN dominance in star forming galaxies and to investigate whether or not (and at which level) the MIR coverage helps constraining the presence of the AGN in the host galaxy.

8.3 Future works

In the past years, several works have exploited the ALMA archive, using the A^{3}COSMOS database, to investigate the properties of star forming, gas and dust-rich galaxies, at different cosmic epochs. In particular, the statistical studies performed in this Thesis have contributed to unveil the properties of the dust-obscured galaxies in the high-z Universe and their evolution. However, further analysis will be crucial in understanding more deeply the evolution of the star formation across cosmic time and the interplay between star forming / starbursting galaxies with the central AGN.

BH accretion rate density through cosmic time

The natural continuation of this Thesis work, is the comprehensive study of the statistical properties characterizing galaxies hosting an AGN, as well as the properties of the AGNs themselves within the A^{3}COSMOS sample. This sets the stage for deriving BH accretion rate density and its evolution over time, which describes the rate at which active SMBHs accrete and grow in mass at various epochs. Indeed, several studies suggest that the evolution of BHARD over cosmic time resembles that of the SFRD. Deriving the BHARD from

an ALMA-based survey would provide an estimate unaffected by obscuration, either due to dust in the galaxy or the dusty torus heated by the AGN. This study might help us contrain the currently-debated BHARD at high-redshifts ($z > 3$), where recent studies argue for a substantial contribution from obscured AGN (e.g., Yang et al., 2023), being ~ 0.5 dex higher than existing BHARD estimates based on the deepest X-ray surveys (Vito et al., 2018; Pouliasis et al., 2024).

A^{3}COSMOS and A^{3}GOODS: increasing the sample

Finally, the pipelines developed by the A^{3}COSMOS team will be able, in the future, to easily collect data from the ever growing ALMA archive, leading to an increase in the sample of galaxies after each ALMA cycle of observation. Thus, combining the larger statistics, with the inclusion of other fields (such as the GOODS), will allow us to constrain the properties regulating the evolution of galaxies with much smaller uncertainties. In this, new data from the COSMOS-WEB survey and from the SMILES survey are going to improve the photometric coverage and redshift estimation for galaxies without a spectroscopic redshift.

ALMA vs JWST morphology

Another future project that can be carried out exploiting the ALMA archive along with the newest observations by JWST programs will be aimed at investigating the JWST and ALMA morphological properties, for a subsample of galaxies selected to be observed in the COSMOS field by ALMA, MIRI and NIRCam. In order to more deeply understand how star formation is occurring in galaxies, studying their morphology provides a method to directly observe the regions where stars are actually forming. In particular, using different observing wavelenghts permits to distinguish between regions in which un-obscured and obscured star formation is ongoing and to compare the structures in which these processes are taking place. Moreover, by investigating the morphological properties of the star forming structures over a wide redshift range, it is possible to study how star formation is occurring in galaxies at different evolutive stages and, eventually, to probe the presence of relaxed or merger-like systems. These analysis will improve our knowledge of the processes of evolution and formation of massive, luminous galaxies, especially at the higher redshifts, where these type of studies have been impossible to do in the pre-JWST era.

For this reasons, by exploiting the co-existence of the A3COSMOS ALMA observations with the NIRCam and MIRI data (that will soon be public) in the COSMOS-WEB survey, it will be possible to study the (sub-)mm, optical/NIR and MIR morphology of the galaxies in a subsample of the A3COSMOS database. On the one hand, the optical/NIR emission, from HST ancillary data in the COSMOS field and from the NIRCam C-WEB data, sample

the stellar component of the SED of the galaxy. If the resolution is high enough, as provided by the NIRCam instrument, these observations trace the spatial distribution of such component. On the other hand, at the MIR wavelenghts, PAH, which are tracers of the dust-obscured star formation, can be observed. Also, the (sub-)mm continuum, measured by ALMA observations, directly traces the dust reservoirs in galaxies and how these are spatially distributed, thanks to its resolution. By mean of this, thanks to the unparalleled resolution provided by JWST instruments (~ 2.4 kpc at $z \sim 1$ for MIRI and ~ 1.2 kpc for NIRCam), we will be able to resolve stellar regions and clumps of obscured star formation up to $z \sim 3$. This allow us to explore the resolved star formation in galaxies with different masses and SFRs, belonging both to the main sequence of galaxies and to the starbursting region of the stellar mass – SFR relation.

In conclusion, the large wealth of data in the ALMA archive has truly unlocked the in-depth analysis of obscured star formation and dust mass build up from the cosmic dawn to the nearby Universe. Despite the growing number of studies focusing on the very first stages of galaxy evolution, larger and more representative galaxy samples are needed in order to tightly constrain the properties of the bulk population of star-forming galaxies up to the highest redshifts ($z > 3 - 4$). In particular, expanding the sample of star-forming galaxies will give us the possibility to shed light on the dust enrichment of the Universe and to understand at which epoch it began. Moreover, this would also allow us to study in more detail the connection between the presence of an AGN and the evolution of its host galaxy. On the other hand, the improvement and development of new models to simulate the observational results will advance our understanding of the physical processes undergoing in the evolutionary phases of galaxies.
By harnessing the unparalleled combination of the JWST, that is exploring the faintest and furthest galaxies with its unique resolution and sensitivity, and ALMA (that is unveiling the dusty, obscured side of the Universe), it will be possible to draw a more detailed picture of galaxy evolution at different epochs of the Universe history.

Bibliography

Salpeter, Edwin E. (Jan. 1955). “The Luminosity Function and Stellar Evolution.” In: 121, p. 161. DOI: 10.1086/145971.

Schmidt, Maarten (Mar. 1959). “The Rate of Star Formation.” In: 129, p. 243. DOI: 10.1086/146614.

— (Nov. 1970). “Space Distribution and Luminosity Functions of Quasars”. In: 162, p. 371. DOI: 10.1086/150668.

Schechter, P. (Jan. 1976). “An analytic expression for the luminosity function for galaxies.” In: 203, pp. 297–306. DOI: 10.1086/154079.

White, S. D. M. and M. J. Rees (May 1978). “Core condensation in heavy halos: a two-stage theory for galaxy formation and clustering.” In: 183, pp. 341–358. DOI: 10.1093/mnras/183.3.341.

Avni, Y. and J. N. Bahcall (Feb. 1980). “On the simultaneous analysis of several complete samples. The V/Vmax and Ve/Va variables, with applications to quasars.” In: 235, pp. 694–716. DOI: 10.1086/157673.

Peebles, P. J. E. (Dec. 1982). “Large-scale background temperature and mass fluctuations due to scale-invariant primeval perturbations”. In: 263, pp. L1–L5. DOI: 10.1086/183911.

Leger, A. and J. L. Puget (Aug. 1984). “Identification of the Unidentified Infrared Emission Features of Interstellar Dust”. In: 137, pp. L5–L8.

Sellgren, K. (Feb. 1984). “The near-infrared continuum emission of visual reflection nebulae.” In: 277, pp. 623–633. DOI: 10.1086/161733.

Allamandola, L. J. et al. (Mar. 1985). “Polycyclic aromatic hydrocarbons and the unidentified infrared emission bands: auto exhaust along the milky way.” In: 290, pp. L25–L28. DOI: 10.1086/184435.

Davis, M. et al. (May 1985). “The evolution of large-scale structure in a universe dominated by cold dark matter”. In: 292, pp. 371–394. DOI: 10.1086/163168.

Gehrels, N. (Apr. 1986). “Confidence Limits for Small Numbers of Events in Astrophysical Data”. In: 303, p. 336. DOI: 10.1086/164079.

Lawrence, A. et al. (Apr. 1986). “Studies of IRAS sources at high galactic latitudes - II. Results froma redshift survey at b>60 : distribution in depth, luminosity function, and physical nature of IRAS galaxies.” In: 219, pp. 687–701. DOI: 10.1093/mnras/219.3.687.

Soifer, B. T. et al. (Sept. 1987). “The IRAS Bright Galaxy Sample. II. The Sample and Luminosity Function”. In: 320, p. 238. DOI: 10.1086/165536.

Sanders, D. B. et al. (Feb. 1988). “Ultraluminous Infrared Galaxies and the Origin of Quasars”. In: 325, p. 74. DOI: 10.1086/165983.

Solomon, P. M. and L. J. Sage (Nov. 1988). “Star-Formation Rates, Molecular Clouds, and the Origin of the Far-Infrared Luminosity of Isolated and Interacting Galaxies”. In: 334, p. 613. DOI: 10.1086/166865.

Leger, A. et al. (June 1989). “Physics of IR emission by interstellar PAH molecules”. In: 216.1-2, pp. 148–164.

Saunders, W. et al. (Jan. 1990a). “The 60-mu.m and far-infrared luminosity functions of IRAS galaxies.” In: 242, pp. 318–337. DOI: 10.1093/mnras/242.3.318.

— (Jan. 1990b). “The 60-mu.m and far-infrared luminosity functions of IRAS galaxies.” In: 242, pp. 318–337. DOI: 10.1093/mnras/242.3.318.

White, Simon D. M. and Carlos S. Frenk (Sept. 1991). “Galaxy Formation through Hierarchical Clustering”. In: 379, p. 52. DOI: 10.1086/170483.

Condon, J. J. (Jan. 1992). “Radio emission from normal galaxies.” In: 30, pp. 575–611. DOI: 10.1146/annurev.aa.30.090192.003043.

Kauffmann, G. et al. (Sept. 1993). “The formation and evolution of galaxies within merging dark matter haloes.” In: 264, pp. 201–218. DOI: 10.1093/mnras/264.1.201.

Rush, Brian et al. (Nov. 1993). “The Extended 12 Micron Galaxy Sample”. In: 89, p. 1. DOI: 10.1086/191837. arXiv: astro-ph/9306013 [astro-ph].

Blain, A. W. and M. S. Longair (Apr. 1996). “Observing strategies for blank-field surveys in the submillimetre waveband”. In: 279.3, pp. 847–858. DOI: 10.1093/mnras/279.3.847.

Lilly, S. J. et al. (Mar. 1996). “The Canada-France Redshift Survey: The Luminosity Density and Star Formation History of the Universe to Z approximately 1”. In: 460, p. L1. DOI: 10.1086/309975. arXiv: astro-ph/9601050 [astro-ph].

Madau, Piero et al. (Dec. 1996). “High-redshift galaxies in the Hubble Deep Field: colour selection and star formation history to z∼4”. In: 283.4, pp. 1388–1404. DOI: 10.1093/mnras/283.4.1388. arXiv: astro-ph/9607172 [astro-ph].

Steidel, Charles C. et al. (Aug. 1996). "Spectroscopy of Lyman Break Galaxies in the Hubble Deep Field". In: 112, p. 352. DOI: 10.1086/118019. arXiv: astro-ph/9604140 [astro-ph].

Sawicki, M. J. et al. (Jan. 1997). "Evolution of the Galaxy Population Based on Photometric Redshifts in the Hubble Deep Field". In: 113, pp. 1–12. DOI: 10.1086/118231. arXiv: astro-ph/9610100 [astro-ph].

Smail, Ian et al. (Nov. 1997). "A Deep Sub-millimeter Survey of Lensing Clusters: A New Window on Galaxy Formation and Evolution". In: 490.1, pp. L5–L8. DOI: 10.1086/311017. arXiv: astro-ph/9708135 [astro-ph].

Barger, A. J. et al. (July 1998). "Submillimetre-wavelength detection of dusty star-forming galaxies at high redshift". In: 394.6690, pp. 248–251. DOI: 10.1038/28338. arXiv: astro-ph/9806317 [astro-ph].

Hughes, David H. et al. (July 1998). "High-redshift star formation in the Hubble Deep Field revealed by a submillimetre-wavelength survey". In: 394.6690, pp. 241–247. DOI: 10.1038/28328. arXiv: astro-ph/9806297 [astro-ph].

Ivison, R. J. et al. (Aug. 1998). "A hyperluminous galaxy at z=2.8 found in a deep submillimetre survey". In: 298.2, pp. 583–593. DOI: 10.1046/j.1365-8711.1998.01677.x. arXiv: astro-ph/9712161 [astro-ph].

Kennicutt (May 1998a). "The Global Schmidt Law in Star-forming Galaxies". In: 498.2, pp. 541–552. DOI: 10.1086/305588. arXiv: astro-ph/9712213 [astro-ph].

Kennicutt Robert C., Jr. (Jan. 1998b). "Star Formation in Galaxies Along the Hubble Sequence". In: 36, pp. 189–232. DOI: 10.1146/annurev.astro.36.1.189. arXiv: astro-ph/9807187 [astro-ph].

Madau, Piero et al. (May 1998). "The Star Formation History of Field Galaxies". In: 498.1, pp. 106–116. DOI: 10.1086/305523. arXiv: astro-ph/9708220 [astro-ph].

Magorrian, John et al. (June 1998). "The Demography of Massive Dark Objects in Galaxy Centers". In: 115.6, pp. 2285–2305. DOI: 10.1086/300353. arXiv: astro-ph/9708072 [astro-ph].

Shupe, David L. et al. (July 1998). "The Local Luminosity Function at 25 Microns". In: 501.2, pp. 597–607. DOI: 10.1086/305825. arXiv: astro-ph/9803149 [astro-ph].

Allamandola, L. J. et al. (Feb. 1999). "Modeling the Unidentified Infrared Emission with Combinations of Polycyclic Aromatic Hydrocarbons". In: 511.2, pp. L115–L119. DOI: 10.1086/311843.

Moore, Ben et al. (Oct. 1999). "Dark Matter Substructure within Galactic Halos". In: 524.1, pp. L19–L22. DOI: 10.1086/312287. arXiv: astro-ph/9907411 [astro-ph].

Steidel, Charles C. et al. (July 1999). "Lyman-Break Galaxies at z>∼4 and the Evolution of the Ultraviolet Luminosity Density at High Redshift". In: 519.1, pp. 1–17. DOI: 10.1086/307363. arXiv: astro-ph/9811399 [astro-ph].

Charlot, Stéphane and S. Michael Fall (Aug. 2000). "A Simple Model for the Absorption of Starlight by Dust in Galaxies". In: 539.2, pp. 718–731. DOI: 10.1086/309250. arXiv: astro-ph/0003128 [astro-ph].

Dunne, Loretta and Stephen A. Eales (Nov. 2001). "The SCUBA Local Universe Galaxy Survey - II. 450-μm data: evidence for cold dust in bright IRAS galaxies". In: 327.3, pp. 697–714. DOI: 10.1046/j.1365-8711.2001.04789.x. arXiv: astro-ph/0106362 [astro-ph].

Springel, Volker et al. (Dec. 2001). "Populating a cluster of galaxies - I. Results at [formmu2]z=0". In: 328.3, pp. 726–750. DOI: 10.1046/j.1365-8711.2001.04912.x. arXiv: astro-ph/0012055 [astro-ph].

Blain, Andrew W. et al. (Oct. 2002). "Submillimeter galaxies". In: 369.2, pp. 111–176. DOI: 10.1016/S0370-1573(02)00134-5. arXiv: astro-ph/0202228 [astro-ph].

Ferrarese, Laura (Oct. 2002). "Beyond the Bulge: A Fundamental Relation between Supermassive Black Holes and Dark Matter Halos". In: 578.1, pp. 90–97. DOI: 10.1086/342308. arXiv: astro-ph/0203469 [astro-ph].

Peng, Chien Y. et al. (July 2002). "Detailed Structural Decomposition of Galaxy Images". In: 124.1, pp. 266–293. DOI: 10.1086/340952. arXiv: astro-ph/0204182 [astro-ph].

Bell, Eric F. (Apr. 2003). "Estimating Star Formation Rates from Infrared and Radio Luminosities: The Origin of the Radio-Infrared Correlation". In: 586.2, pp. 794–813. DOI: 10.1086/367829. arXiv: astro-ph/0212121 [astro-ph].

Bruzual, G. and S. Charlot (Oct. 2003). "Stellar population synthesis at the resolution of 2003". In: 344.4, pp. 1000–1028. DOI: 10.1046/j.1365-8711.2003.06897.x. arXiv: astro-ph/0309134 [astro-ph].

Calura, Francesco and Francesca Matteucci (Oct. 2003). "The Cosmic Evolution of the Galaxy Luminosity Density". In: 596.2, pp. 734–747. DOI: 10.1086/378195. arXiv: astro-ph/0307014 [astro-ph].

Chabrier, Gilles (July 2003). "Galactic Stellar and Substellar Initial Mass Function". In: 115.809, pp. 763–795. DOI: 10.1086/376392. arXiv: astro-ph/0304382 [astro-ph].

Chapman, S. C. et al. (Apr. 2003). "A median redshift of 2.4 for galaxies bright at submillimetre wavelengths". In: 422.6933, pp. 695–698. DOI: 10.1038/nature01540. arXiv: astro-ph/0304235 [astro-ph].

Dunne, Loretta et al. (May 2003). "A census of metals at high and low redshift and the connection between submillimetre sources and spheroid formation". In: 341.2, pp. 589–598. DOI: 10.1046/j.1365-8711.2003.06440.x. arXiv: astro-ph/0210260 [astro-ph].

Lu, Nanyao et al. (May 2003). "Infrared Emission of Normal Galaxies from 2.5 to 12 Micron: Infrared Space Observatory Spectra, Near-Infrared Continuum, and Mid-Infrared Emission Features". In: 588.1, pp. 199–217. DOI: 10.1086/374043. arXiv: astro-ph/0301481 [astro-ph].

Ranalli, P. et al. (Feb. 2003). "The 2-10 keV luminosity as a Star Formation Rate indicator". In: 399, pp. 39–50. DOI: 10.1051/0004-6361:20021600. arXiv: astro-ph/0211304 [astro-ph].

Sanders, D. B. et al. (Oct. 2003). "The IRAS Revised Bright Galaxy Sample". In: 126.4, pp. 1607–1664. DOI: 10.1086/376841. arXiv: astro-ph/0306263 [astro-ph].

Takeuchi, Tsutomu T. et al. (Apr. 2003). "The Luminosity Function of IRAS Point Source Catalog Redshift Survey Galaxies". In: 587.2, pp. L89–L92. DOI: 10.1086/375181. arXiv: astro-ph/0303181 [astro-ph].

Ueda, Yoshihiro et al. (Dec. 2003). "Cosmological Evolution of the Hard X-Ray Active Galactic Nucleus Luminosity Function and the Origin of the Hard X-Ray Background". In: 598.2, pp. 886–908. DOI: 10.1086/378940. arXiv: astro-ph/0308140 [astro-ph].

Blain, A. W. et al. (Aug. 2004). "Accurate Spectral Energy Distributions and Selection Effects for High-Redshift Dusty Galaxies: A New Hot Population to Discover with the Spitzer Space Telescope?" In: 611.1, pp. 52–58. DOI: 10.1086/422026. arXiv: astro-ph/0404438 [astro-ph].

Chapman, S. C. et al. (Aug. 2004). "Evidence for Extended, Obscured Starbursts in Submillimeter Galaxies". In: 611.2, pp. 732–738. DOI: 10.1086/422383. arXiv: astro-ph/0412051 [astro-ph].

Yan, Haojing et al. (Nov. 2004). "High-Redshift Extremely Red Objects in the Hubble Space Telescope Ultra Deep Field Revealed by the GOODS Infrared Array Camera Observations". In: 616.1, pp. 63–70. DOI: 10.1086/424898. arXiv: astro-ph/0408070 [astro-ph].

Borys, C. et al. (Dec. 2005). "The Relationship between Stellar and Black Hole Mass in Submillimeter Galaxies". In: 635.2, pp. 853–863. DOI: 10.1086/491617. arXiv: astro-ph/0507610 [astro-ph].

Chapman, S. C. et al. (Apr. 2005). "A Redshift Survey of the Submillimeter Galaxy Population". In: 622.2, pp. 772–796. DOI: 10.1086/428082. arXiv: astro-ph/0412573 [astro-ph].

Maraston, Claudia (Sept. 2005). "Evolutionary population synthesis: models, analysis of the ingredients and application to high-z galaxies". In: 362.3, pp. 799–825. DOI: 10.1111/j.1365-2966.2005.09270.x. arXiv: astro-ph/0410207 [astro-ph].

Pérez-González, Pablo G. et al. (Sept. 2005). "Spitzer View on the Evolution of Star-forming Galaxies from z = 0 to z ~3". In: 630.1, pp. 82–107. DOI: 10.1086/431894. arXiv: astro-ph/0505101 [astro-ph].

Springel, Volker (Dec. 2005). "The cosmological simulation code GADGET-2". In: 364.4, pp. 1105–1134. DOI: 10.1111/j.1365-2966.2005.09655.x. arXiv: astro-ph/0505010 [astro-ph].

Vlahakis, Catherine et al. (Dec. 2005). "The SCUBA Local Universe Galaxy Survey - III. Dust along the Hubble sequence". In: 364.4, pp. 1253–1285. DOI: 10.1111/j.1365-2966.2005.09666.x. arXiv: astro-ph/0510768 [astro-ph].

Bower, R. G. et al. (Aug. 2006). "Breaking the hierarchy of galaxy formation". In: 370.2, pp. 645–655. DOI: 10.1111/j.1365-2966.2006.10519.x. arXiv: astro-ph/0511338 [astro-ph].

Croton, Darren J. et al. (Jan. 2006). "The many lives of active galactic nuclei: cooling flows, black holes and the luminosities and colours of galaxies". In: 365.1, pp. 11–28. DOI: 10.1111/j.1365-2966.2005.09675.x. arXiv: astro-ph/0508046 [astro-ph].

Flagey, N. et al. (July 2006). "Spitzer/IRAC and ISOCAM/CVF insights on the origin of the near to mid-IR Galactic diffuse emission". In: 453.3, pp. 969–978. DOI: 10.1051/0004-6361:20053949. arXiv: astro-ph/0604238 [astro-ph].

Fritz, J. et al. (Mar. 2006). "Revisiting the infrared spectra of active galactic nuclei with a new torus emission model". In: 366.3, pp. 767–786. DOI: 10.1111/j.1365-2966.2006.09866.x. arXiv: astro-ph/0511428 [astro-ph].

Kovács, A. et al. (Oct. 2006). "SHARC-2 350 μm Observations of Distant Submillimeter-selected Galaxies". In: 650.2, pp. 592–603. DOI: 10.1086/506341. arXiv: astro-ph/0604591 [astro-ph].

Lodato, Giuseppe and Priyamvada Natarajan (Oct. 2006). "Supermassive black hole formation during the assembly of pre-galactic discs". In: 371.4, pp. 1813–1823. DOI: 10.1111/j.1365-2966.2006.10801.x. arXiv: astro-ph/0606159 [astro-ph].

Bertoldi, F. et al. (Sept. 2007). "COSBO: The MAMBO 1.2 Millimeter Imaging Survey of the COSMOS Field". In: 172.1, pp. 132–149. DOI: 10.1086/520511.

Capak, P. et al. (Sept. 2007). "The First Release COSMOS Optical and Near-IR Data and Catalog". In: 172.1, pp. 99–116. DOI: 10.1086/519081. arXiv: 0704.2430 [astro-ph].

Caputi, K. I. et al. (May 2007). "The Infrared Luminosity Function of Galaxies at Redshifts z = 1 and z ∼2 in the GOODS Fields". In: 660.1, pp. 97–116. DOI: 10.1086/512667. arXiv: astro-ph/0701283 [astro-ph].

Dahlen, Tomas et al. (Jan. 2007). "Evolution of the Luminosity Function, Star Formation Rate, Morphology, and Size of Star-forming Galaxies Selected at Rest-Frame 1500 and 2800 Å". In: 654.1, pp. 172–185. DOI: 10.1086/508854. arXiv: astro-ph/0609016 [astro-ph].

Leauthaud, Alexie et al. (Sept. 2007). "Weak Gravitational Lensing with COSMOS: Galaxy Selection and Shape Measurements". In: 172.1, pp. 219–238. DOI: 10.1086/516598. arXiv: astro-ph/0702359 [astro-ph].

Monaco, Pierluigi et al. (Mar. 2007). "The MORGANA model for the rise of galaxies and active nuclei". In: 375.4, pp. 1189–1219. DOI: 10.1111/j.1365-2966.2006.11253.x. arXiv: astro-ph/0610805 [astro-ph].

Salim, Samir et al. (Dec. 2007). "UV Star Formation Rates in the Local Universe". In: 173.2, pp. 267–292. DOI: 10.1086/519218. arXiv: 0704.3611 [astro-ph].

Sanders, D. B. et al. (Sept. 2007). "S-COSMOS: The Spitzer Legacy Survey of the Hubble Space Telescope ACS 2 deg^2 COSMOS Field I: Survey Strategy and First Analysis". In: 172.1, pp. 86–98. DOI: 10.1086/517885. arXiv: astro-ph/0701318 [astro-ph].

Scoville, N. et al. (Sept. 2007). "The Cosmic Evolution Survey (COSMOS): Overview". In: 172.1, pp. 1–8. DOI: 10.1086/516585. arXiv: astro-ph/0612305 [astro-ph].

Taniguchi, Y. et al. (Sept. 2007). "The Cosmic Evolution Survey (COSMOS): Subaru Observations of the HST Cosmos Field". In: 172.1, pp. 9–28. DOI: 10.1086/516596. arXiv: astro-ph/0612295 [astro-ph].

Zamojski, M. A. et al. (Sept. 2007). "Deep GALEX Imaging of the COSMOS HST Field: A First Look at the Morphology of z ∼0.7 Star-forming Galaxies". In: 172.1, pp. 468–493. DOI: 10.1086/516593. arXiv: astro-ph/0701478 [astro-ph].

da Cunha, Elisabete et al. (Aug. 2008). "A simple model to interpret the ultraviolet, optical and infrared emission from galaxies". In: 388.4, pp. 1595–1617. DOI: 10.1111/j.1365-2966.2008.13535.x. arXiv: 0806.1020 [astro-ph].

Dalla Vecchia, Claudio and Joop Schaye (July 2008). "Simulating galactic outflows with kinetic supernova feedback". In: 387.4, pp. 1431–1444. DOI: 10.1111/j.1365-2966.2008.13322.x. arXiv: 0801.2770 [astro-ph].

Dey, Arjun et al. (Apr. 2008). "A Significant Population of Very Luminous Dust-Obscured Galaxies at Redshift z ∼2". In: 677.2, pp. 943–956. DOI: 10.1086/529516. arXiv: 0801.1860 [astro-ph].

Hopkins, Philip F. et al. (Apr. 2008). "A Cosmological Framework for the Co-Evolution of Quasars, Supermassive Black Holes, and Elliptical Galaxies. I. Galaxy Mergers and Quasar Activity". In: 175.2, pp. 356–389. DOI: 10.1086/524362. arXiv: 0706.1243 [astro-ph].

Reddy, Naveen A. et al. (Mar. 2008). "Multiwavelength Constraints on the Cosmic Star Formation History from Spectroscopy: The Rest-Frame Ultraviolet, Hα, and Infrared Luminosity Functions at Redshifts 1.9 lesssim z lesssim 3.4". In: 175.1, pp. 48–85. DOI: 10.1086/521105. arXiv: 0706.4091 [astro-ph].

Sajina, Anna et al. (Aug. 2008). "Spitzer Mid-Infrared Spectroscopy of Infrared Luminous Galaxies at z $\sim$2. III. Far-IR to Radio Properties and Optical Spectral Diagnostics". In: 683.2, pp. 659–682. DOI: 10.1086/589914. arXiv: 0805.0263 [astro-ph].

Somerville, Rachel S. et al. (Dec. 2008). "A semi-analytic model for the co-evolution of galaxies, black holes and active galactic nuclei". In: 391.2, pp. 481–506. DOI: 10.1111/j.1365-2966.2008.13805.x. arXiv: 0808.1227 [astro-ph].

Casey, C. M. et al. (Oct. 2009). "Confirming a population of hot-dust dominated, star-forming, ultraluminous galaxies at high redshift". In: 399.1, pp. 121–128. DOI: 10.1111/j.1365-2966.2009.15291.x. arXiv: 0906.5346 [astro-ph.CO].

Elvis, Martin et al. (Sept. 2009). "The Chandra COSMOS Survey. I. Overview and Point Source Catalog". In: 184.1, pp. 158–171. DOI: 10.1088/0067-0049/184/1/158. arXiv: 0903.2062 [astro-ph.CO].

Fontanot, Fabio et al. (Aug. 2009). "The many manifestations of downsizing: hierarchical galaxy formation models confront observations". In: 397.4, pp. 1776–1790. DOI: 10.1111/j.1365-2966.2009.15058.x. arXiv: 0901.1130 [astro-ph.CO].

Ilbert, O. et al. (Jan. 2009). "Cosmos Photometric Redshifts with 30-Bands for 2-deg^2". In: 690.2, pp. 1236–1249. DOI: 10.1088/0004-637X/690/2/1236. arXiv: 0809.2101 [astro-ph].

Le Floc'h, Emeric et al. (Sept. 2009). "Deep Spitzer 24 μm COSMOS Imaging. I. The Evolution of Luminous Dusty Galaxies—Confronting the Models". In: 703.1, pp. 222–239. DOI: 10.1088/0004-637X/703/1/222. arXiv: 0909.4303 [astro-ph.CO].

Magnelli, B. et al. (Mar. 2009). "The 0.4 < z < 1.3 star formation history of the Universe as viewed in the far-infrared". In: 496.1, pp. 57–75. DOI: 10.1051/0004-6361:200811443. arXiv: 0901.1543 [astro-ph.CO].

Murphy, Eric J. (Nov. 2009). "The Far-Infrared-Radio Correlation at High Redshifts: Physical Considerations and Prospects for the Square Kilometer Array". In: 706.1, pp. 482–496. DOI: 10.1088/0004-637X/706/1/482. arXiv: 0910.0011 [astro-ph.CO].

Reddy, Naveen A. and Charles C. Steidel (Feb. 2009). "A Steep Faint-End Slope of the UV Luminosity Function at z $\sim$2-3: Implications for the Global Stellar Mass Density and

Star Formation in Low-Mass Halos". In: 692.1, pp. 778–803. DOI: 10.1088/0004-637X/692/1/778. arXiv: 0810.2788 [astro-ph].

Stadel, J. et al. (Sept. 2009). "Quantifying the heart of darkness with GHALO - a multibillion particle simulation of a galactic halo". In: 398.1, pp. L21–L25. DOI: 10.1111/j.1745-3933.2009.00699.x. arXiv: 0808.2981 [astro-ph].

Clements, D. L. et al. (Mar. 2010). "The submillimetre properties of ultraluminous infrared galaxies". In: 403.1, pp. 274–286. DOI: 10.1111/j.1365-2966.2009.16064.x. arXiv: 0911.3593 [astro-ph.CO].

Eales, S. et al. (May 2010). "The Herschel ATLAS". In: 122.891, p. 499. DOI: 10.1086/653086. arXiv: 0910.4279 [astro-ph.CO].

Gruppioni, C. et al. (July 2010). "PEP: First Herschel probe of dusty galaxy evolution up to z ~3". In: 518, L27, p. L27. DOI: 10.1051/0004-6361/201014608. arXiv: 1005.1473 [astro-ph.CO].

Laird, Elise S. et al. (Feb. 2010). "On the X-ray properties of sub-mm-selected galaxies". In: 401.4, pp. 2763–2772. DOI: 10.1111/j.1365-2966.2009.15860.x. arXiv: 0910.2464 [astro-ph.CO].

McCracken, H. J. et al. (Jan. 2010). "The COSMOS-WIRCam Near-Infrared Imaging Survey. I. BzK-Selected Passive and Star-Forming Galaxy Candidates at z gsim 1.4". In: 708.1, pp. 202–217. DOI: 10.1088/0004-637X/708/1/202. arXiv: 0910.2705 [astro-ph.CO].

Oesch, P. A. et al. (Dec. 2010). "The Evolution of the Ultraviolet Luminosity Function from z ~0.75 to z ~2.5 Using HST ERS WFC3/UVIS Observations". In: 725.2, pp. L150–L155. DOI: 10.1088/2041-8205/725/2/L150. arXiv: 1005.1661 [astro-ph.CO].

Peng, Chien Y. et al. (June 2010). "Detailed Decomposition of Galaxy Images. II. Beyond Axisymmetric Models". In: 139.6, pp. 2097–2129. DOI: 10.1088/0004-6256/139/6/2097. arXiv: 0912.0731 [astro-ph.CO].

Rodighiero, G. et al. (June 2010). "Mid- and far-infrared luminosity functions and galaxy evolution from multiwavelength Spitzer observations up to z ~2.5". In: 515, A8, A8. DOI: 10.1051/0004-6361/200912058. arXiv: 0910.5649 [astro-ph.CO].

Schinnerer, E. et al. (June 2010). "The VLA-COSMOS Survey. IV. Deep Data and Joint Catalog". In: 188.2, pp. 384–404. DOI: 10.1088/0067-0049/188/2/384. arXiv: 1005.1641 [astro-ph.CO].

Springel, Volker (Jan. 2010). "E pur si muove: Galilean-invariant cosmological hydrodynamical simulations on a moving mesh". In: 401.2, pp. 791–851. DOI: 10.1111/j.1365-2966.2009.15715.x. arXiv: 0901.4107 [astro-ph.CO].

Thomas, Daniel et al. (June 2010a). "Environment and self-regulation in galaxy formation". In: 404.4, pp. 1775–1789. DOI: 10.1111/j.1365-2966.2010.16427.x. arXiv: 0912.0259 [astro-ph.CO].

— (June 2010b). "Environment and self-regulation in galaxy formation". In: 404.4, pp. 1775–1789. DOI: 10.1111/j.1365-2966.2010.16427.x. arXiv: 0912.0259 [astro-ph.CO].

Treister, Ezequiel et al. (Oct. 2010). "Heavily Obscured Active Galactic Nuclei in High-redshift Luminous Infrared Galaxies". In: 722.2, pp. L238–L243. DOI: 10.1088/2041-8205/722/2/L238. arXiv: 1009.2501 [astro-ph.CO].

van der Burg, R. F. J. et al. (Nov. 2010). "The UV galaxy luminosity function at z = 3-5 from the CFHT Legacy Survey Deep fields". In: 523, A74, A74. DOI: 10.1051/0004-6361/200913812. arXiv: 1009.0758 [astro-ph.CO].

Volonteri, Marta and Mitchell C. Begelman (Dec. 2010). "Quasi-stars and the cosmic evolution of massive black holes". In: 409.3, pp. 1022–1032. DOI: 10.1111/j.1365-2966.2010.17359.x. arXiv: 1003.5220 [astro-ph.HE].

Aretxaga, I. et al. (Aug. 2011). "AzTEC millimetre survey of the COSMOS field - III. Source catalogue over 0.72 deg^2 and plausible boosting by large-scale structure". In: 415.4, pp. 3831–3850. DOI: 10.1111/j.1365-2966.2011.18989.x. arXiv: 1105.0890 [astro-ph.CO].

Béthermin, M. et al. (May 2011). "Modeling the evolution of infrared galaxies: a parametric backward evolution model". In: 529, A4, A4. DOI: 10.1051/0004-6361/201015841. arXiv: 1010.1150 [astro-ph.CO].

Davé, Romeel et al. (July 2011). "Galaxy evolution in cosmological simulations with outflows - I. Stellar masses and star formation rates". In: 415.1, pp. 11–31. DOI: 10.1111/j.1365-2966.2011.18680.x. arXiv: 1103.3528 [astro-ph.CO].

Draine, Bruce T. (2011). *Physics of the Interstellar and Intergalactic Medium.*

Dunne, L. et al. (Oct. 2011). "Herschel-ATLAS: rapid evolution of dust in galaxies over the last 5 billion years". In: 417.2, pp. 1510–1533. DOI: 10.1111/j.1365-2966.2011.19363.x. arXiv: 1012.5186 [astro-ph.CO].

Georgantopoulos, I. et al. (Oct. 2011). "On the L_x - $L_{6\mu m}$ ratio as a diagnostic for Compton-thick AGN". In: 534, A23, A23. DOI: 10.1051/0004-6361/201117400. arXiv: 1107.3777 [astro-ph.CO].

Guo, Qi et al. (May 2011). "From dwarf spheroidals to cD galaxies: simulating the galaxy population in a ΛCDM cosmology". In: 413.1, pp. 101–131. DOI: 10.1111/j.1365-2966.2010.18114.x. arXiv: 1006.0106 [astro-ph.CO].

Hainline, Laura J. et al. (Oct. 2011). "The Stellar Mass Content of Submillimeter-selected Galaxies". In: 740.2, 96, p. 96. DOI: 10.1088/0004-637X/740/2/96. arXiv: 1006.0238 [astro-ph.CO].

Hao, Cai-Na et al. (Nov. 2011). "Dust-corrected Star Formation Rates of Galaxies. II. Combinations of Ultraviolet and Infrared Tracers". In: 741.2, 124, p. 124. DOI: 10.1088/0004-637X/741/2/124. arXiv: 1108.2837 [astro-ph.CO].

Hatsukade, B. et al. (Feb. 2011). "AzTEC/ASTE 1.1-mm survey of the AKARI Deep Field South: source catalogue and number counts". In: 411.1, pp. 102–116. DOI: 10.1111/j.1365-2966.2010.17658.x. arXiv: 1010.0585 [astro-ph.CO].

Lindner, R. R. et al. (Aug. 2011). "A Deep 1.2 mm Map of the Lockman Hole North Field". In: 737.2, 83, p. 83. DOI: 10.1088/0004-637X/737/2/83. arXiv: 1106.0344 [astro-ph.CO].

Lutz, D. et al. (Aug. 2011). "PACS Evolutionary Probe (PEP) - A Herschel key program". In: 532, A90, A90. DOI: 10.1051/0004-6361/201117107. arXiv: 1106.3285 [astro-ph.CO].

Ly, Chun et al. (Jan. 2011). "The Hα Luminosity Function and Star Formation Rate Volume Density at z = 0.8 from the NEWFIRM Hα Survey". In: 726.2, 109, p. 109. DOI: 10.1088/0004-637X/726/2/109. arXiv: 1011.2759 [astro-ph.CO].

Magnelli, B. et al. (Apr. 2011). "Evolution of the dusty infrared luminosity function from z = 0 to z = 2.3 using observations from Spitzer". In: 528, A35, A35. DOI: 10.1051/0004-6361/200913941. arXiv: 1101.2467 [astro-ph.CO].

Marsden, Gaelen et al. (Oct. 2011). "A Monte Carlo approach to evolution of the far-infrared luminosity function with BLAST". In: 417.2, pp. 1192–1209. DOI: 10.1111/j.1365-2966.2011.19336.x. arXiv: 1010.1176 [astro-ph.CO].

Murphy, E. J. et al. (Aug. 2011). "Calibrating Extinction-free Star Formation Rate Diagnostics with 33 GHz Free-free Emission in NGC 6946". In: 737.2, 67, p. 67. DOI: 10.1088/0004-637X/737/2/67. arXiv: 1105.4877 [astro-ph.CO].

Planck Collaboration et al. (Dec. 2011). "Planck early results. XXV. Thermal dust in nearby molecular clouds". In: 536, A25, A25. DOI: 10.1051/0004-6361/201116483. arXiv: 1101.2037 [astro-ph.GA].

Popescu, C. C. et al. (Mar. 2011). "Modelling the spectral energy distribution of galaxies. V. The dust and PAH emission SEDs of disk galaxies". In: 527, A109, A109. DOI: 10.1051/0004-6361/201015217. arXiv: 1011.2942 [astro-ph.CO].

Robotham, A. S. G. and S. P. Driver (June 2011). "The GALEX-SDSS NUV and FUV flux density and local star formation rate". In: 413.4, pp. 2570–2582. DOI: 10.1111/j.1365-2966.2011.18327.x. arXiv: 1101.5187 [astro-ph.CO].

Rodighiero, G. et al. (Oct. 2011). "The Lesser Role of Starbursts in Star Formation at z = 2". In: 739.2, L40, p. L40. DOI: 10.1088/2041-8205/739/2/L40. arXiv: 1108.0933 [astro-ph.CO].

Salvato, M. et al. (Dec. 2011). "Dissecting Photometric Redshift for Active Galactic Nucleus Using XMM- and Chandra-COSMOS Samples". In: 742.2, 61, p. 61. DOI: 10.1088/0004-637X/742/2/61. arXiv: 1108.6061 [astro-ph.CO].

Wardlow, J. L. et al. (Aug. 2011). "The LABOCA survey of the Extended Chandra Deep Field-South: a photometric redshift survey of submillimetre galaxies". In: 415.2, pp. 1479–1508. DOI: 10.1111/j.1365-2966.2011.18795.x. arXiv: 1006.2137 [astro-ph.CO].

Wuyts, Stijn et al. (Sept. 2011). "On Star Formation Rates and Star Formation Histories of Galaxies Out to z ~3". In: 738.1, 106, p. 106. DOI: 10.1088/0004-637X/738/1/106. arXiv: 1106.5502 [astro-ph.CO].

Benson, Andrew J. (Feb. 2012). "G ALACTICUS: A semi-analytic model of galaxy formation". In: 17.2, pp. 175–197. DOI: 10.1016/j.newast.2011.07.004. arXiv: 1008.1786 [astro-ph.CO].

Bouwens, R. J. et al. (Aug. 2012). "UV-continuum Slopes at z ~4-7 from the HUDF09+ERS+CANDELS Observations: Discovery of a Well-defined UV Color-Magnitude Relationship for z >= 4 Star-forming Galaxies". In: 754.2, 83, p. 83. DOI: 10.1088/0004-637X/754/2/83. arXiv: 1109.0994 [astro-ph.CO].

Casey, Caitlin M. (Oct. 2012). "Far-infrared spectral energy distribution fitting for galaxies near and far". In: 425.4, pp. 3094–3103. DOI: 10.1111/j.1365-2966.2012.21455.x. arXiv: 1206.1595 [astro-ph.CO].

Civano, F. et al. (Aug. 2012). "The Chandra COSMOS Survey. III. Optical and Infrared Identification of X-Ray Point Sources". In: 201.2, 30, p. 30. DOI: 10.1088/0067-0049/201/2/30. arXiv: 1205.5030 [astro-ph.CO].

Cucciati, O. et al. (Mar. 2012). "The star formation rate density and dust attenuation evolution over 12 Gyr with the VVDS surveys". In: 539, A31, A31. DOI: 10.1051/0004-6361/201118010. arXiv: 1109.1005 [astro-ph.CO].

Dale, D. A. et al. (Jan. 2012). "Herschel Far-infrared and Submillimeter Photometry for the KINGFISH Sample of nearby Galaxies". In: 745.1, 95, p. 95. DOI: 10.1088/0004-637X/745/1/95. arXiv: 1112.1093 [astro-ph.CO].

Feltre, A. et al. (Oct. 2012). "Smooth and clumpy dust distributions in AGN: a direct comparison of two commonly explored infrared emission models". In: 426.1, pp. 120–127. DOI: 10.1111/j.1365-2966.2012.21695.x. arXiv: 1207.2668 [astro-ph.CO].

Fontanot, Fabio et al. (Nov. 2012). "Semi-analytic galaxy formation in early dark energy cosmologies". In: 426.3, pp. 2335–2341. DOI: 10.1111/j.1365-2966.2012.21880.x. arXiv: 1207.1723 [astro-ph.CO].

Hsieh, Bau-Ching et al. (Dec. 2012). "The Taiwan ECDFS Near-Infrared Survey: Ultra-deep J and K_S Imaging in the Extended Chandra Deep Field-South". In: 203.2, 23, p. 23. DOI: 10.1088/0067-0049/203/2/23. arXiv: 1210.4519 [astro-ph.CO].

Kennicutt and Evans (Sept. 2012a). "Star Formation in the Milky Way and Nearby Galaxies". In: 50, pp. 531–608. DOI: 10.1146/annurev-astro-081811-125610. arXiv: 1204.3552 [astro-ph.GA].

Kennicutt, Robert C. and Neal J. Evans (Sept. 2012b). "Star Formation in the Milky Way and Nearby Galaxies". In: 50, pp. 531–608. DOI: 10.1146/annurev-astro-081811-125610. arXiv: 1204.3552 [astro-ph.GA].

Magdis, Georgios E. et al. (Nov. 2012). "The Evolving Interstellar Medium of Star-forming Galaxies since z = 2 as Probed by Their Infrared Spectral Energy Distributions". In: 760.1, 6, p. 6. DOI: 10.1088/0004-637X/760/1/6. arXiv: 1210.1035 [astro-ph.CO].

Magnelli, B. et al. (Mar. 2012). "A Herschel view of the far-infrared properties of submillimetre galaxies". In: 539, A155, A155. DOI: 10.1051/0004-6361/201118312. arXiv: 1202.0761 [astro-ph.CO].

McCracken, H. J. et al. (Aug. 2012). "UltraVISTA: a new ultra-deep near-infrared survey in COSMOS". In: 544, A156, A156. DOI: 10.1051/0004-6361/201219507. arXiv: 1204.6586 [astro-ph.CO].

Ménard, Brice and Masataka Fukugita (Aug. 2012). "Cosmic Dust in Mg II Absorbers". In: 754.2, 116, p. 116. DOI: 10.1088/0004-637X/754/2/116. arXiv: 1204.1978 [astro-ph.CO].

Menci, N. et al. (Apr. 2012). "Galaxy formation in warm dark matter cosmology". In: 421.3, pp. 2384–2394. DOI: 10.1111/j.1365-2966.2012.20470.x. arXiv: 1201.1617 [astro-ph.CO].

Michałowski, M. J. et al. (May 2012). "The stellar masses and specific star-formation rates of submillimetre galaxies". In: 541, A85, A85. DOI: 10.1051/0004-6361/201016308. arXiv: 1108.6058 [astro-ph.CO].

Mineo, S. et al. (Jan. 2012a). "X-ray emission from star-forming galaxies - I. High-mass X-ray binaries". In: 419.3, pp. 2095–2115. DOI: 10.1111/j.1365-2966.2011.19862.x. arXiv: 1105.4610 [astro-ph.HE].

— (Nov. 2012b). "X-ray emission from star-forming galaxies - II. Hot interstellarmedium". In: 426.3, pp. 1870–1883. DOI: 10.1111/j.1365-2966.2012.21831.x. arXiv: 1205.3715 [astro-ph.HE].

Oliver, S. J. et al. (Aug. 2012). "The Herschel Multi-tiered Extragalactic Survey: HerMES". In: 424.3, pp. 1614–1635. DOI: 10.1111/j.1365-2966.2012.20912.x. arXiv: 1203.2562 [astro-ph.CO].

Sajina, Anna et al. (Sept. 2012). "Spitzer- and Herschel-based Spectral Energy Distributions of 24 μm Bright z ~0.3-3.0 Starbursts and Obscured Quasars". In: 757.1, 13, p. 13. DOI: 10.1088/0004-637X/757/1/13. arXiv: 1207.4963 [astro-ph.CO].

Scott, K. S. et al. (June 2012). "The source counts of submillimetre galaxies detected at λ= 1.1 mm". In: 423.1, pp. 575–589. DOI: 10.1111/j.1365-2966.2012.20905.x. arXiv: 1203.2609 [astro-ph.CO].

Smit, Renske et al. (Sept. 2012). "The Star Formation Rate Function for Redshift z ~4-7 Galaxies: Evidence for a Uniform Buildup of Star-forming Galaxies during the First 3 Gyr of Cosmic Time". In: 756.1, 14, p. 14. DOI: 10.1088/0004-637X/756/1/14. arXiv: 1204.3626 [astro-ph.CO].

Somerville, Rachel S. et al. (July 2012). "Galaxy properties from the ultraviolet to the far-infrared: Λ cold dark matter models confront observations". In: 423.3, pp. 1992–2015. DOI: 10.1111/j.1365-2966.2012.20490.x. arXiv: 1104.0669 [astro-ph.CO].

Vattakunnel, S. et al. (Mar. 2012). "The radio-X-ray relation as a star formation indicator: results from the Very Large Array-Extended Chandra Deep Field-South". In: 420.3, pp. 2190–2208. DOI: 10.1111/j.1365-2966.2011.20185.x. arXiv: 1111.3285 [astro-ph.CO].

Yun, Min S. et al. (Feb. 2012). "Deep 1.1 mm-wavelength imaging of the GOODS-S field by AzTEC/ASTE - II. Redshift distribution and nature of the submillimetre galaxy population". In: 420.2, pp. 957–985. DOI: 10.1111/j.1365-2966.2011.19898.x. arXiv: 1109.6286 [astro-ph.CO].

Béthermin, Matthieu et al. (Sept. 2013). "The redshift evolution of the distribution of star formation among dark matter halos as seen in the infrared". In: 557, A66, A66. DOI: 10.1051/0004-6361/201321688. arXiv: 1304.3936 [astro-ph.CO].

Bianchi, S. (Apr. 2013). "Vindicating single-T modified blackbody fits to Herschel SEDs". In: 552, A89, A89. DOI: 10.1051/0004-6361/201220866. arXiv: 1302.5699 [astro-ph.CO].

Bothwell, M. S. et al. (Mar. 2013). "A survey of molecular gas in luminous sub-millimetre galaxies". In: 429.4, pp. 3047–3067. DOI: 10.1093/mnras/sts562. arXiv: 1205.1511 [astro-ph.CO].

Foreman-Mackey, Daniel et al. (Mar. 2013). "emcee: The MCMC Hammer". In: 125.925, p. 306. DOI: 10.1086/670067. arXiv: 1202.3665 [astro-ph.IM].

Gruppioni, C. et al. (June 2013). "The Herschel PEP/HerMES luminosity function - I. Probing the evolution of PACS selected Galaxies to z 4". In: 432.1, pp. 23–52. DOI: 10.1093/mnras/stt308. arXiv: 1302.5209 [astro-ph.CO].

Henriques, Bruno M. B. et al. (June 2013). "Simulations of the galaxy population constrained by observations from z = 3 to the present day: implications for galactic winds and the fate of their ejecta". In: 431.4, pp. 3373–3395. DOI: 10.1093/mnras/stt415. arXiv: 1212.1717 [astro-ph.CO].

Hodge, J. A. et al. (May 2013). "An ALMA Survey of Submillimeter Galaxies in the Extended Chandra Deep Field South: Source Catalog and Multiplicity". In: 768.1, 91, p. 91. DOI: 10.1088/0004-637X/768/1/91. arXiv: 1304.4266 [astro-ph.CO].

Johnson, Jarrett L. et al. (July 2013). "Supermassive Seeds for Supermassive Black Holes". In: 771.2, 116, p. 116. DOI: 10.1088/0004-637X/771/2/116. arXiv: 1211.0548 [astro-ph.CO].

Kormendy, John and Luis C. Ho (Aug. 2013). "Coevolution (Or Not) of Supermassive Black Holes and Host Galaxies". In: 51.1, pp. 511–653. DOI: 10.1146/annurev-astro-082708-101811. arXiv: 1304.7762 [astro-ph.CO].

Magnelli, B. et al. (May 2013). "The deepest Herschel-PACS far-infrared survey: number counts and infrared luminosity functions from combined PEP/GOODS-H observations". In: 553, A132, A132. DOI: 10.1051/0004-6361/201321371. arXiv: 1303.4436 [astro-ph.CO].

Muzzin, Adam et al. (May 2013). "A Public K_s -selected Catalog in the COSMOS/ULTRA-VISTA Field: Photometry, Photometric Redshifts, and Stellar Population Parameters". In: 206.1, 8, p. 8. DOI: 10.1088/0067-0049/206/1/8. arXiv: 1303.4410 [astro-ph.CO].

Patel, Shannon G. et al. (Mar. 2013). "HST/WFC3 Confirmation of the Inside-out Growth of Massive Galaxies at 0 < z < 2 and Identification of Their Star-forming Progenitors at z ~3". In: 766.1, 15, p. 15. DOI: 10.1088/0004-637X/766/1/15. arXiv: 1208.0341 [astro-ph.CO].

Riechers, Dominik A. et al. (Apr. 2013). "A dust-obscured massive maximum-starburst galaxy at a redshift of 6.34". In: 496.7445, pp. 329–333. DOI: 10.1038/nature12050. arXiv: 1304.4256 [astro-ph.CO].

Shankar, Francesco et al. (Jan. 2013). "Size evolution of spheroids in a hierarchical Universe". In: 428.1, pp. 109–128. DOI: 10.1093/mnras/sts001. arXiv: 1105.6043 [astro-ph.CO].

Sobral, David et al. (Jan. 2013). "A large Hα survey at z = 2.23, 1.47, 0.84 and 0.40: the 11 Gyr evolution of star-forming galaxies from HiZELS". In: 428.2, pp. 1128–1146. DOI: 10.1093/mnras/sts096. arXiv: 1202.3436 [astro-ph.CO].

Wang, S. X. et al. (Dec. 2013). "An ALMA Survey of Submillimeter Galaxies in the Extended Chandra Deep Field-South: The AGN Fraction and X-Ray Properties of Submillimeter Galaxies". In: 778.2, 179, p. 179. DOI: 10.1088/0004-637X/778/2/179. arXiv: 1310.6364 [astro-ph.CO].

Bonoli, Silvia et al. (Jan. 2014). "Massive black hole seeds born via direct gas collapse in galaxy mergers: their properties, statistics and environment". In: 437.2, pp. 1576–1592. DOI: 10.1093/mnras/stt1990. arXiv: 1211.3752 [astro-ph.CO].

Bouwens, R. J. et al. (Nov. 2014). "A Census of Star-forming Galaxies in the Z ~9-10 Universe based on HST+Spitzer Observations over 19 Clash Clusters: Three Candidate Z ~9-10 Galaxies and Improved Constraints on the Star Formation Rate Density at Z ~9.2". In: 795.2, 126, p. 126. DOI: 10.1088/0004-637X/795/2/126. arXiv: 1211.2230 [astro-ph.CO].

Casey, Caitlin M. et al. (Aug. 2014). "Dusty star-forming galaxies at high redshift". In: 541.2, pp. 45–161. DOI: 10.1016/j.physrep.2014.02.009. arXiv: 1402.1456 [astro-ph.CO].

Delvecchio, I. et al. (Apr. 2014). "Tracing the cosmic growth of supermassive black holes to z $\sim$ 3 with Herschel". In: 439.3, pp. 2736–2754. DOI: 10.1093/mnras/stu130. arXiv: 1401.4503 [astro-ph.GA].

Draine, B. T. et al. (Jan. 2014). "Andromeda's Dust". In: 780.2, 172, p. 172. DOI: 10.1088/0004-637X/780/2/172. arXiv: 1306.2304 [astro-ph.CO].

Duncan, K. et al. (Nov. 2014). "The mass evolution of the first galaxies: stellar mass functions and star formation rates at 4 < z < 7 in the CANDELS GOODS-South field". In: 444.3, pp. 2960–2984. DOI: 10.1093/mnras/stu1622. arXiv: 1408.2527 [astro-ph.GA].

Genel, Shy et al. (Nov. 2014). "Introducing the Illustris project: the evolution of galaxy populations across cosmic time". In: 445.1, pp. 175–200. DOI: 10.1093/mnras/stu1654. arXiv: 1405.3749 [astro-ph.CO].

Lemaux, B. C. et al. (Dec. 2014). "Hidden starbursts and active galactic nuclei at 0 < z < 4 from the Herschel-VVDS-CFHTLS-D1 field: Inferences on coevolution and feedback". In: 572, A90, A90. DOI: 10.1051/0004-6361/201323089. arXiv: 1311.5228 [astro-ph.CO].

Madau, Piero and Mark Dickinson (Aug. 2014). "Cosmic Star-Formation History". In: 52, pp. 415–486. DOI: 10.1146/annurev-astro-081811-125615. arXiv: 1403.0007 [astro-ph.CO].

Magnelli, B. et al. (Jan. 2014). "The evolution of the dust temperatures of galaxies in the SFR-M_* plane up to z $\sim$ 2". In: 561, A86, A86. DOI: 10.1051/0004-6361/201322217. arXiv: 1311.2956 [astro-ph.CO].

Scoville, N. et al. (Mar. 2014). "The Evolution of Interstellar Medium Mass Probed by Dust Emission: ALMA Observations at z = 0.3-2". In: 783.2, 84, p. 84. DOI: 10.1088/0004-637X/783/2/84. arXiv: 1401.2987 [astro-ph.GA].

Simpson, J. M. et al. (June 2014). "An ALMA Survey of Submillimeter Galaxies in the Extended Chandra Deep Field South: The Redshift Distribution and Evolution of Submillimeter Galaxies". In: 788.2, 125, p. 125. DOI: 10.1088/0004-637X/788/2/125. arXiv: 1310.6363 [astro-ph.CO].

Speagle, J. S. et al. (Oct. 2014). "A Highly Consistent Framework for the Evolution of the Star-Forming "Main Sequence" from z ~0-6". In: 214.2, 15, p. 15. DOI: 10.1088/0067-0049/214/2/15. arXiv: 1405.2041 [astro-ph.GA].

Staguhn, Johannes G. et al. (July 2014). "The GISMO Two-millimeter Deep Field in GOODS-N". In: 790.1, 77, p. 77. DOI: 10.1088/0004-637X/790/1/77. arXiv: 1311.1485 [astro-ph.CO].

Swinbank, A. M. et al. (Feb. 2014). "An ALMA survey of sub-millimetre Galaxies in the Extended Chandra Deep Field South: the far-infrared properties of SMGs". In: 438.2, pp. 1267–1287. DOI: 10.1093/mnras/stt2273. arXiv: 1310.6362 [astro-ph.CO].

Symeonidis, M. et al. (Oct. 2014). "Linking the X-ray and infrared properties of star-forming galaxies at z < 1.5". In: 443.4, pp. 3728–3740. DOI: 10.1093/mnras/stu1441. arXiv: 1407.4511 [astro-ph.GA].

Tescari, E. et al. (Mar. 2014). "Simulated star formation rate functions at z ∼ 4-7, and the role of feedback in high-z galaxies". In: 438.4, pp. 3490–3506. DOI: 10.1093/mnras/stt2461. arXiv: 1312.5310 [astro-ph.CO].

Ueda, Yoshihiro et al. (May 2014). "Toward the Standard Population Synthesis Model of the X-Ray Background: Evolution of X-Ray Luminosity and Absorption Functions of Active Galactic Nuclei Including Compton-thick Populations". In: 786.2, 104, p. 104. DOI: 10.1088/0004-637X/786/2/104. arXiv: 1402.1836 [astro-ph.CO].

Vignali, Cristian (July 2014). "Obscured accretion from AGN surveys". In: *Multiwavelength AGN Surveys and Studies*. Ed. by Areg M. Mickaelian and David B. Sanders. Vol. 304, pp. 132–138. DOI: 10.1017/S1743921314003548. arXiv: 1401.5061 [astro-ph.GA].

Vito, F. et al. (Dec. 2014). "The hard X-ray luminosity function of high-redshift (3 < z 5) active galactic nuclei". In: 445.4, pp. 3557–3574. DOI: 10.1093/mnras/stu2004. arXiv: 1409.6918 [astro-ph.GA].

Vogelsberger, Mark et al. (Oct. 2014). "Introducing the Illustris Project: simulating the coevolution of dark and visible matter in the Universe". In: 444.2, pp. 1518–1547. DOI: 10.1093/mnras/stu1536. arXiv: 1405.2921 [astro-ph.CO].

Aird, J. et al. (Aug. 2015). "The evolution of the X-ray luminosity functions of unabsorbed and absorbed AGNs out to z∼ 5". In: 451.2, pp. 1892–1927. DOI: 10.1093/mnras/stv1062. arXiv: 1503.01120 [astro-ph.HE].

Béthermin, Matthieu et al. (Jan. 2015). "Evolution of the dust emission of massive galaxies up to z = 4 and constraints on their dominant mode of star formation". In: 573, A113, A113. DOI: 10.1051/0004-6361/201425031. arXiv: 1409.5796 [astro-ph.GA].

Bouwens, R. J. et al. (Apr. 2015). "UV Luminosity Functions at Redshifts z ∼ 4 to z ∼ 10: 10,000 Galaxies from HST Legacy Fields". In: 803.1, 34, p. 34. DOI: 10.1088/0004-637X/803/1/34. arXiv: 1403.4295 [astro-ph.CO].

Capak, P. L. et al. (June 2015). "Galaxies at redshifts 5 to 6 with systematically low dust content and high [C II] emission". In: 522.7557, pp. 455–458. DOI: 10.1038/nature14500. arXiv: 1503.07596 [astro-ph.GA].

Carniani, S. et al. (Dec. 2015). "ALMA constraints on the faint millimetre source number counts and their contribution to the cosmic infrared background". In: 584, A78, A78. DOI: 10.1051/0004-6361/201525780. arXiv: 1502.00640 [astro-ph.GA].

Crain, Robert A. et al. (June 2015). "The EAGLE simulations of galaxy formation: calibration of subgrid physics and model variations". In: 450.2, pp. 1937–1961. DOI: 10.1093/mnras/stv725. arXiv: 1501.01311 [astro-ph.GA].

da Cunha, E. et al. (June 2015a). "An ALMA Survey of Sub-millimeter Galaxies in the Extended Chandra Deep Field South: Physical Properties Derived from Ultraviolet-to-radio Modeling". In: 806.1, 110, p. 110. DOI: 10.1088/0004-637X/806/1/110. arXiv: 1504.04376 [astro-ph.GA].

— (June 2015b). "An ALMA Survey of Sub-millimeter Galaxies in the Extended Chandra Deep Field South: Physical Properties Derived from Ultraviolet-to-radio Modeling". In: 806.1, 110, p. 110. DOI: 10.1088/0004-637X/806/1/110. arXiv: 1504.04376 [astro-ph.GA].

Georgakakis, A. et al. (Oct. 2015). "The X-ray luminosity function of active galactic nuclei in the redshift interval z=3-5". In: 453.2, pp. 1946–1964. DOI: 10.1093/mnras/stv1703. arXiv: 1507.07558 [astro-ph.HE].

Gruppioni, C. et al. (Aug. 2015a). "Star formation in Herschel's Monsters versus semi-analytic models". In: 451.4, pp. 3419–3426. DOI: 10.1093/mnras/stv1204. arXiv: 1506.01518 [astro-ph.GA].

— (Aug. 2015b). "Star formation in Herschel's Monsters versus semi-analytic models". In: 451.4, pp. 3419–3426. DOI: 10.1093/mnras/stv1204. arXiv: 1506.01518 [astro-ph.GA].

Henriques, Bruno M. B. et al. (Aug. 2015). "Galaxy formation in the Planck cosmology - I. Matching the observed evolution of star formation rates, colours and stellar masses". In: 451.3, pp. 2663–2680. DOI: 10.1093/mnras/stv705. arXiv: 1410.0365 [astro-ph.GA].

Hopkins, Philip F. (June 2015). "A new class of accurate, mesh-free hydrodynamic simulation methods". In: 450.1, pp. 53–110. DOI: 10.1093/mnras/stv195. arXiv: 1409.7395 [astro-ph.CO].

Mohan, Niruj and David Rafferty (Feb. 2015). *PyBDSF: Python Blob Detection and Source Finder*. Astrophysics Source Code Library, record ascl:1502.007. ascl: 1502.007.

Oesch, P. A. et al. (July 2015). "First Frontier Field Constraints on the Cosmic Star Formation Rate Density at z $\sim$ 10—The Impact of Lensing Shear on Completeness of High-redshift Galaxy Samples". In: 808.1, 104, p. 104. DOI: 10.1088/0004-637X/808/1/104. arXiv: 1409.1228 [astro-ph.GA].

Pannella, M. et al. (July 2015). "GOODS-Herschel: Star Formation, Dust Attenuation, and the FIR-radio Correlation on the Main Sequence of Star-forming Galaxies up to z 4". In: 807.2, 141, p. 141. DOI: 10.1088/0004-637X/807/2/141. arXiv: 1407.5072 [astro-ph.GA].

Schaye, Joop et al. (Jan. 2015). "The EAGLE project: simulating the evolution and assembly of galaxies and their environments". In: 446.1, pp. 521–554. DOI: 10.1093/mnras/stu2058. arXiv: 1407.7040 [astro-ph.GA].

Sijacki, Debora et al. (Sept. 2015). "The Illustris simulation: the evolving population of black holes across cosmic time". In: 452.1, pp. 575–596. DOI: 10.1093/mnras/stv1340. arXiv: 1408.6842 [astro-ph.GA].

Smolcic, V. et al. (Apr. 2015). "VizieR Online Data Catalog: The VLA-COSMOS Survey. V. 324MHz (Smolcic+, 2014)". In: *VizieR Online Data Catalog*, J/MNRAS/443/2590, J/MNRAS/443/2590.

Taniguchi, Yoshiaki et al. (Dec. 2015). "The Subaru COSMOS 20: Subaru optical imaging of the HST COSMOS field with 20 filters*". In: 67.6, 104, p. 104. DOI: 10.1093/pasj/psv106. arXiv: 1510.00550 [astro-ph.GA].

Alavi, Anahita et al. (Nov. 2016). "The Evolution of the Faint End of the UV Luminosity Function during the Peak Epoch of Star Formation (1 < z < 3)". In: 832.1, 56, p. 56. DOI: 10.3847/0004-637X/832/1/56. arXiv: 1606.00469 [astro-ph.GA].

Aravena, M. et al. (Dec. 2016). "The ALMA Spectroscopic Survey in the Hubble Ultra Deep Field: Continuum Number Counts, Resolved 1.2 mm Extragalactic Background, and Properties of the Faintest Dusty Star-forming Galaxies". In: 833.1, 68, p. 68. DOI: 10.3847/1538-4357/833/1/68. arXiv: 1607.06769 [astro-ph.GA].

Civano, F. et al. (Mar. 2016). "The Chandra Cosmos Legacy Survey: Overview and Point Source Catalog". In: 819.1, 62, p. 62. DOI: 10.3847/0004-637X/819/1/62. arXiv: 1601.00941 [astro-ph.GA].

Hatsukade, Bunyo et al. (June 2016). "SXDF-ALMA 2-arcmin^2 deep survey: 1.1-mm number counts". In: 68.3, 36, p. 36. DOI: 10.1093/pasj/psw026. arXiv: 1602.08167 [astro-ph.GA].

Hirschmann, Michaela et al. (Sept. 2016). "Galaxy assembly, stellar feedback and metal enrichment: the view from the GAEA model". In: 461.2, pp. 1760–1785. DOI: 10.1093/mnras/stw1318. arXiv: 1512.04531 [astro-ph.GA].

Laigle, C. et al. (June 2016). "The COSMOS2015 Catalog: Exploring the 1 < z < 6 Universe with Half a Million Galaxies". In: 224.2, 24, p. 24. DOI: 10.3847/0067-0049/224/2/24. arXiv: 1604.02350 [astro-ph.GA].

Lang, Dustin et al. (Apr. 2016). *The Tractor: Probabilistic astronomical source detection and measurement*. Astrophysics Source Code Library, record ascl:1604.008. ascl: 1604.008.

Laporte, N. et al. (Apr. 2016). "Young Galaxy Candidates in the Hubble Frontier Fields. III. MACS J0717.5+3745". In: 820.2, 98, p. 98. DOI: 10.3847/0004-637X/820/2/98. arXiv: 1602.02775 [astro-ph.GA].

Lehmer, B. D. et al. (July 2016). "The Evolution of Normal Galaxy X-Ray Emission through Cosmic History: Constraints from the 6 MS Chandra Deep Field-South". In: 825.1, 7, p. 7. DOI: 10.3847/0004-637X/825/1/7. arXiv: 1604.06461 [astro-ph.GA].

Marchesi, S. et al. (Jan. 2016). "The Chandra COSMOS Legacy survey: optical/IR identifications". In: 817.1, 34, p. 34. DOI: 10.3847/0004-637X/817/1/34. arXiv: 1512.01105 [astro-ph.GA].

Oteo, I. et al. (May 2016). "ALMACAL I: First Dual-band Number Counts from a Deep and Wide ALMA Submillimeter Survey, Free from Cosmic Variance". In: 822.1, 36, p. 36. DOI: 10.3847/0004-637X/822/1/36. arXiv: 1508.05099 [astro-ph.GA].

Parsa, Shaghayegh et al. (Mar. 2016). "The galaxy UV luminosity function at z 2-4; new results on faint-end slope and the evolution of luminosity density". In: 456.3, pp. 3194–3211. DOI: 10.1093/mnras/stv2857. arXiv: 1507.05629 [astro-ph.GA].

Ranalli, P. et al. (May 2016). "The 2-10 keV unabsorbed luminosity function of AGN from the LSS, CDFS, and COSMOS surveys". In: 590, A80, A80. DOI: 10.1051/0004-6361/201527013. arXiv: 1512.05563 [astro-ph.HE].

Rowan-Robinson, Michael et al. (Sept. 2016). "The star formation rate density from z = 1 to 6". In: 461.1, pp. 1100–1111. DOI: 10.1093/mnras/stw1169. arXiv: 1605.03937 [astro-ph.GA].

Vito, F. et al. (Nov. 2016). "The deepest X-ray view of high-redshift galaxies: constraints on low-rate black hole accretion". In: 463.1, pp. 348–374. DOI: 10.1093/mnras/stw1998. arXiv: 1608.02614 [astro-ph.GA].

Volonteri, M. et al. (Aug. 2016). "The cosmic evolution of massive black holes in the Horizon-AGN simulation". In: 460.3, pp. 2979–2996. DOI: 10.1093/mnras/stw1123. arXiv: 1602.01941 [astro-ph.GA].

Walter, Fabian et al. (Dec. 2016). "ALMA Spectroscopic Survey in the Hubble Ultra Deep Field: Survey Description". In: 833.1, 67, p. 67. DOI: 10.3847/1538-4357/833/1/67. arXiv: 1607.06768 [astro-ph.GA].

Béthermin, Matthieu et al. (Nov. 2017). "The impact of clustering and angular resolution on far-infrared and millimeter continuum observations". In: 607, A89, A89. DOI: 10.1051/0004-6361/201730866. arXiv: 1703.08795 [astro-ph.GA].

Brisbin, Drew et al. (Dec. 2017). "An ALMA survey of submillimeter galaxies in the COSMOS field: Multiwavelength counterparts and redshift distribution". In: 608, A15, A15. DOI: 10.1051/0004-6361/201730558. arXiv: 1708.05748 [astro-ph.GA].

Caputi, K. I. et al. (Nov. 2017). "Star Formation in Galaxies at z $\sim$ 4-5 from the SMUVS Survey: A Clear Starburst/Main-sequence Bimodality for Hα Emitters on the SFR-M* Plane". In: 849.1, 45, p. 45. DOI: 10.3847/1538-4357/aa901e. arXiv: 1705.06179 [astro-ph.GA].

Ciesla, L. et al. (Dec. 2017). "The SFR-M_* main sequence archetypal star-formation history and analytical models". In: 608, A41, A41. DOI: 10.1051/0004-6361/201731036. arXiv: 1706.08531 [astro-ph.GA].

Davé, Romeel et al. (May 2017). "MUFASA: Galaxy star formation, gas, and metal properties across cosmic time". In: 467.1, pp. 115–132. DOI: 10.1093/mnras/stx108. arXiv: 1610.01626 [astro-ph.GA].

Davidzon, I. et al. (Sept. 2017). "The COSMOS2015 galaxy stellar mass function . Thirteen billion years of stellar mass assembly in ten snapshots". In: 605, A70, A70. DOI: 10.1051/0004-6361/201730419. arXiv: 1701.02734 [astro-ph.GA].

Delvecchio, I. et al. (June 2017). "The VLA-COSMOS 3 GHz Large Project: AGN and host-galaxy properties out to z 6". In: 602, A3, A3. DOI: 10.1051/0004-6361/201629367. arXiv: 1703.09720 [astro-ph.GA].

Dunlop, J. S. et al. (Apr. 2017). "A deep ALMA image of the Hubble Ultra Deep Field". In: 466.1, pp. 861–883. DOI: 10.1093/mnras/stw3088. arXiv: 1606.00227 [astro-ph.GA].

Fontanot, Fabio et al. (June 2017). "Strong Stellar-driven Outflows Shape the Evolution of Galaxies at Cosmic Dawn". In: 842.2, L14, p. L14. DOI: 10.3847/2041-8213/aa74bd. arXiv: 1703.02983 [astro-ph.GA].

Fujimoto, Seiji et al. (Nov. 2017). "Demonstrating a New Census of Infrared Galaxies with ALMA (DANCING-ALMA). I. FIR Size and Luminosity Relation at z = 0-6 Revealed with 1034 ALMA Sources". In: 850.1, 83, p. 83. DOI: 10.3847/1538-4357/aa93e6. arXiv: 1703.02138 [astro-ph.GA].

Geach, J. E. et al. (Feb. 2017). "The SCUBA-2 Cosmology Legacy Survey: 850 μm maps, catalogues and number counts". In: 465.2, pp. 1789–1806. DOI: 10.1093/mnras/stw2721. arXiv: 1607.03904 [astro-ph.GA].

Gioannini, L. et al. (Nov. 2017). "The cosmic dust rate across the Universe". In: 471.4, pp. 4615–4627. DOI: 10.1093/mnras/stx1914. arXiv: 1707.06784 [astro-ph.GA].

Katsianis, A. et al. (Nov. 2017). "The evolution of the star formation rate function in the EAGLE simulations: a comparison with UV, IR and Hα observations from z $\sim$ 8 to z $\sim$ 0". In: 472.1, pp. 919–939. DOI: 10.1093/mnras/stx2020. arXiv: 1708.01913 [astro-ph.GA].

Lee, G. -H. et al. (Sept. 2017). "VizieR Online Data Catalog: WISE MIR properties of galaxies in compact groups (Lee+, 2017)". In: *VizieR Online Data Catalog*, J/ApJ/835/280, J/ApJ/835/280.

Lo Faro, B. et al. (Dec. 2017). "Characterizing the UV-to-NIR shape of the dust attenuation curve of IR luminous galaxies up to z $\sim$ 2". In: 472.2, pp. 1372–1391. DOI: 10.1093/mnras/stx1901. arXiv: 1707.09805 [astro-ph.GA].

Mehta, Vihang et al. (Mar. 2017). "UVUDF: UV Luminosity Functions at the Cosmic High Noon". In: 838.1, 29, p. 29. DOI: 10.3847/1538-4357/aa6259. arXiv: 1702.06953 [astro-ph.GA].

Popping, Gergö et al. (Nov. 2017). "The dust content of galaxies from z = 0 to z = 9". In: 471.3, pp. 3152–3185. DOI: 10.1093/mnras/stx1545. arXiv: 1609.08622 [astro-ph.GA].

Scoville, N. et al. (Mar. 2017). "Evolution of Interstellar Medium, Star Formation, and Accretion at High Redshift". In: 837.2, 150, p. 150. DOI: 10.3847/1538-4357/aa61a0. arXiv: 1702.04729 [astro-ph.GA].

Smolčić, V. et al. (June 2017). "The VLA-COSMOS 3 GHz Large Project: Continuum data and source catalog release". In: 602, A1, A1. DOI: 10.1051/0004-6361/201628704. arXiv: 1703.09713 [astro-ph.GA].

Umehata, Hideki et al. (Jan. 2017). "ALMA Deep Field in SSA22: Source Catalog and Number Counts". In: 835.1, 98, p. 98. DOI: 10.3847/1538-4357/835/1/98. arXiv: 1611.09857 [astro-ph.GA].

Aoyama, Shohei et al. (Aug. 2018). "Cosmological simulation with dust formation and destruction". In: 478.4, pp. 4905–4921. DOI: 10.1093/mnras/sty1431. arXiv: 1802.04027 [astro-ph.GA].

Beeston, R. A. et al. (June 2018). "GAMA/H-ATLAS: the local dust mass function and cosmic density as a function of galaxy type - a benchmark for models of galaxy evolution". In: 479.1, pp. 1077–1099. DOI: 10.1093/mnras/sty1460. arXiv: 1712.07261 [astro-ph.GA].

Bisigello, L. et al. (Jan. 2018). "Analysis of the SFR-M* plane at z < 3: single fitting versus multi-Gaussian decomposition". In: 609, A82, A82. DOI: 10.1051/0004-6361/201731399. arXiv: 1706.06154 [astro-ph.GA].

Casey, Caitlin M. et al. (July 2018). "The Brightest Galaxies in the Dark Ages: Galaxies' Dust Continuum Emission during the Reionization Era". In: 862.1, 77, p. 77. DOI: 10.3847/1538-4357/aac82d. arXiv: 1805.10301 [astro-ph.GA].

Driver, Simon P. et al. (Apr. 2018). "GAMA/G10-COSMOS/3D-HST: the 0 < z < 5 cosmic star formation history, stellar-mass, and dust-mass densities". In: 475.3, pp. 2891–2935. DOI: 10.1093/mnras/stx2728. arXiv: 1710.06628 [astro-ph.GA].

Franco, M. et al. (Dec. 2018a). "GOODS-ALMA: 1.1 mm galaxy survey. I. Source catalog and optically dark galaxies". In: 620, A152, A152. DOI: 10.1051/0004-6361/201832928. arXiv: 1803.00157 [astro-ph.GA].

— (Dec. 2018b). "GOODS-ALMA: 1.1 mm galaxy survey. I. Source catalog and optically dark galaxies". In: 620, A152, A152. DOI: 10.1051/0004-6361/201832928. arXiv: 1803.00157 [astro-ph.GA].

Hatsukade, Bunyo et al. (Dec. 2018a). "ALMA twenty-six arcmin^2 survey of GOODS-S at one millimeter (ASAGAO): Source catalog and number counts". In: 70.6, 105, p. 105. DOI: 10.1093/pasj/psy104. arXiv: 1808.04502 [astro-ph.GA].

— (Dec. 2018b). "ALMA twenty-six arcmin^2 survey of GOODS-S at one millimeter (ASAGAO): Source catalog and number counts". In: 70.6, 105, p. 105. DOI: 10.1093/pasj/psy104. arXiv: 1808.04502 [astro-ph.GA].

Jin, Shuowen et al. (Sept. 2018). ""Super-deblended" Dust Emission in Galaxies. II. Far-IR to (Sub)millimeter Photometry and High-redshift Galaxy Candidates in the Full COSMOS Field". In: 864.1, 56, p. 56. DOI: 10.3847/1538-4357/aad4af. arXiv: 1807.04697 [astro-ph.GA].

Lagache, Guilaine (May 2018). "Exploring the dusty star-formation in the early Universe using intensity mapping". In: *Peering towards Cosmic Dawn*. Ed. by Vibor Jelić and Thijs van der Hulst. Vol. 333, pp. 228–233. DOI: 10.1017/S1743921318000558. arXiv: 1801.08054 [astro-ph.GA].

Liu, Daizhong et al. (Feb. 2018). ""Super-deblended" Dust Emission in Galaxies. I. The GOODS-North Catalog and the Cosmic Star Formation Rate Density out to Redshift 6". In: 853.2, 172, p. 172. DOI: 10.3847/1538-4357/aaa600. arXiv: 1703.05281 [astro-ph.GA].

Małek, K. et al. (Nov. 2018). "HELP: modelling the spectral energy distributions of Herschel detected galaxies in the ELAIS N1 field". In: 620, A50, A50. DOI: 10.1051/0004-6361/201833131. arXiv: 1809.00529 [astro-ph.GA].

Oesch, P. A. et al. (Mar. 2018). "The Dearth of z ∼ 10 Galaxies in All HST Legacy Fields—The Rapid Evolution of the Galaxy Population in the First 500 Myr". In: 855.2, 105, p. 105. DOI: 10.3847/1538-4357/aab03f. arXiv: 1710.11131 [astro-ph.GA].

Ono, Yoshiaki et al. (Jan. 2018). "Great Optically Luminous Dropout Research Using Subaru HSC (GOLDRUSH). I. UV luminosity functions at z ∼ 4-7 derived with the half-million dropouts on the 100 deg^2 sky". In: 70, S10, S10. DOI: 10.1093/pasj/psx103. arXiv: 1704.06004 [astro-ph.GA].

Pearson, W. J. et al. (July 2018). "Main sequence of star forming galaxies beyond the Herschel confusion limit". In: 615, A146, A146. DOI: 10.1051/0004-6361/201832821. arXiv: 1804.03482 [astro-ph.GA].

Pillepich, Annalisa et al. (Mar. 2018a). "First results from the IllustrisTNG simulations: the stellar mass content of groups and clusters of galaxies". In: 475.1, pp. 648–675. DOI: 10.1093/mnras/stx3112. arXiv: 1707.03406 [astro-ph.GA].

Pillepich, Annalisa et al. (Jan. 2018b). "Simulating galaxy formation with the IllustrisTNG model". In: 473.3, pp. 4077–4106. DOI: 10.1093/mnras/stx2656. arXiv: 1703.02970 [astro-ph.GA].

Stach, Stuart M. et al. (June 2018). "An ALMA Survey of the SCUBA-2 Cosmology Legacy Survey UKIDSS/UDS Field: Number Counts of Submillimeter Galaxies". In: 860.2, 161, p. 161. DOI: 10.3847/1538-4357/aac5e5. arXiv: 1805.05362 [astro-ph.GA].

Vito, F. et al. (Jan. 2018). "High-redshift AGN in the Chandra Deep Fields: the obscured fraction and space density of the sub-L$_*$ population". In: 473.2, pp. 2378–2406. DOI: 10.1093/mnras/stx2486. arXiv: 1709.07892 [astro-ph.GA].

Zavala, J. A. et al. (Dec. 2018). "Constraining the Volume Density of Dusty Star-forming Galaxies through the First 3 mm Number Counts from ALMA". In: 869.1, 71, p. 71. DOI: 10.3847/1538-4357/aaecd2. arXiv: 1810.12300 [astro-ph.GA].

Aihara, Hiroaki et al. (Dec. 2019). "Second data release of the Hyper Suprime-Cam Subaru Strategic Program". In: 71.6, 114, p. 114. DOI: 10.1093/pasj/psz103. arXiv: 1905.12221 [astro-ph.IM].

Boquien, M. et al. (Feb. 2019). "CIGALE: a python Code Investigating GALaxy Emission". In: 622, A103, A103. DOI: 10.1051/0004-6361/201834156. arXiv: 1811.03094 [astro-ph.GA].

Buat, V. et al. (Dec. 2019). "Cold dust and stellar emissions in dust-rich galaxies observed with ALMA: a challenge for SED-fitting techniques". In: 632, A79, A79. DOI: 10.1051/0004-6361/201936643.

Davé, Romeel et al. (June 2019). "SIMBA: Cosmological simulations with black hole growth and feedback". In: 486.2, pp. 2827–2849. DOI: 10.1093/mnras/stz937. arXiv: 1901.10203 [astro-ph.GA].

González-López, Jorge et al. (Sept. 2019). "The Atacama Large Millimeter/submillimeter Array Spectroscopic Survey in the Hubble Ultra Deep Field: CO Emission Lines and 3 mm Continuum Sources". In: 882.2, 139, p. 139. DOI: 10.3847/1538-4357/ab3105. arXiv: 1903.09161 [astro-ph.GA].

Li, Qi et al. (Nov. 2019). "The dust-to-gas and dust-to-metal ratio in galaxies from z = 0 to 6". In: 490.1, pp. 1425–1436. DOI: 10.1093/mnras/stz2684. arXiv: 1906.09277 [astro-ph.GA].

Liang, Lichen et al. (Oct. 2019). "On the dust temperatures of high-redshift galaxies". In: 489.1, pp. 1397–1422. DOI: 10.1093/mnras/stz2134. arXiv: 1902.10727 [astro-ph.GA].

Liu, Daizhong et al. (Oct. 2019a). *a3cosmos-gas-evolution: Galaxy cold molecular gas evolution functions*. Astrophysics Source Code Library, record ascl:1910.003. ascl: 1910.003.

— (Dec. 2019b). "Automated Mining of the ALMA Archive in the COSMOS Field (A^3COSMOS). II. Cold Molecular Gas Evolution out to Redshift 6". In: 887.2, 235, p. 235. DOI: 10.3847/1538-4357/ab578d. arXiv: 1910.12883 [astro-ph.GA].

Magnelli, B. et al. (May 2019a). "The IRAM/GISMO 2 mm Survey in the COSMOS Field". In: 877.1, 45, p. 45. DOI: 10.3847/1538-4357/ab1912. arXiv: 1904.10006 [astro-ph.GA].

— (May 2019b). "The IRAM/GISMO 2 mm Survey in the COSMOS Field". In: 877.1, 45, p. 45. DOI: 10.3847/1538-4357/ab1912. arXiv: 1904.10006 [astro-ph.GA].

Vijayan, Aswin P. et al. (Nov. 2019). "Detailed dust modelling in the L-GALAXIES semi-analytic model of galaxy formation". In: 489.3, pp. 4072–4089. DOI: 10.1093/mnras/stz1948. arXiv: 1904.02196 [astro-ph.GA].

Wang, T. et al. (Aug. 2019). "A dominant population of optically invisible massive galaxies in the early Universe". In: 572.7768, pp. 211–214. DOI: 10.1038/s41586-019-1452-4. arXiv: 1908.02372 [astro-ph.GA].

Adams, N. J. et al. (May 2020). "The rest-frame UV luminosity function at z 4: a significant contribution of AGNs to the bright end of the galaxy population". In: 494.2, pp. 1771–1783. DOI: 10.1093/mnras/staa687. arXiv: 1912.01626 [astro-ph.GA].

Béthermin, M. et al. (Nov. 2020). "The ALPINE-ALMA [CII] survey: Data processing, catalogs, and statistical source properties". In: 643, A2, A2. DOI: 10.1051/0004-6361/202037649. arXiv: 2002.00962 [astro-ph.GA].

Donevski, D. et al. (Dec. 2020). "In pursuit of giants. I. The evolution of the dust-to-stellar mass ratio in distant dusty galaxies". In: 644, A144, A144. DOI: 10.1051/0004-6361/202038405. arXiv: 2008.09995 [astro-ph.GA].

Faisst, A. L. et al. (Apr. 2020). "The ALPINE-ALMA [C II] Survey: Multiwavelength Ancillary Data and Basic Physical Measurements". In: 247.2, 61, p. 61. DOI: 10.3847/1538-4365/ab7ccd. arXiv: 1912.01621 [astro-ph.GA].

Fontanot, Fabio et al. (Aug. 2020). "The rise of active galactic nuclei in the galaxy evolution and assembly semi-analytic model". In: 496.3, pp. 3943–3960. DOI: 10.1093/mnras/staa1716. arXiv: 2002.10576 [astro-ph.CO].

Fudamoto, Yoshinobu et al. (Feb. 2020). "A3COSMOS: the dust attenuation of star-forming galaxies at z = 2.5-4.0 from the COSMOS-ALMA archive". In: 491.4, pp. 4724–4734. DOI: 10.1093/mnras/stz3248. arXiv: 1910.12885 [astro-ph.GA].

González-López, Jorge et al. (July 2020). "The ALMA Spectroscopic Survey in the HUDF: Deep 1.2 mm Continuum Number Counts". In: 897.1, 91, p. 91. DOI: 10.3847/1538-4357/ab765b. arXiv: 2002.07199 [astro-ph.GA].

Gruppioni, C. et al. (Nov. 2020). "The ALPINE-ALMA [CII] survey. The nature, luminosity function, and star formation history of dusty galaxies up to z 6". In: 643, A8, A8. DOI: 10.1051/0004-6361/202038487. arXiv: 2006.04974 [astro-ph.GA].

Henriques, Bruno M. B. et al. (Feb. 2020). "L-GALAXIES 2020: Spatially resolved cold gas phases, star formation, and chemical enrichment in galactic discs". In: 491.4, pp. 5795–5814. DOI: 10.1093/mnras/stz3233. arXiv: 2003.05944 [astro-ph.GA].

Hodge, J. A. and E. da Cunha (Dec. 2020). "High-redshift star formation in the Atacama large millimetre/submillimetre array era". In: *Royal Society Open Science* 7.12, 200556, p. 200556. DOI: 10.1098/rsos.200556. arXiv: 2004.00934 [astro-ph.GA].

Le Fèvre, O. et al. (Nov. 2020). "The ALPINE-ALMA [CII] survey. Survey strategy, observations, and sample properties of 118 star-forming galaxies at 4 < z < 6". In: 643, A1, A1. DOI: 10.1051/0004-6361/201936965. arXiv: 1910.09517 [astro-ph.CO].

Magnelli, Benjamin et al. (Mar. 2020). "The ALMA Spectroscopic Survey in the HUDF: The Cosmic Dust and Gas Mass Densities in Galaxies up to z $\sim$ 3". In: 892.1, 66, p. 66. DOI: 10.3847/1538-4357/ab7897. arXiv: 2002.08640 [astro-ph.GA].

Péroux, Céline and J. Christopher Howk (Aug. 2020). "The Cosmic Baryon and Metal Cycles". In: 58, pp. 363–406. DOI: 10.1146/annurev-astro-021820-120014. arXiv: 2011.01935 [astro-ph.GA].

Pozzi, F. et al. (Feb. 2020). "The dust mass function from z $\sim$0 to z $\sim$2.5". In: 491.4, pp. 5073–5082. DOI: 10.1093/mnras/stz2724. arXiv: 1909.11333 [astro-ph.GA].

Simpson, J. M. et al. (July 2020). "An ALMA survey of the brightest sub-millimetre sources in the SCUBA-2-COSMOS field". In: 495.3, pp. 3409–3430. DOI: 10.1093/mnras/staa1345. arXiv: 2003.05484 [astro-ph.GA].

Sommovigo, L. et al. (Sept. 2020). "Warm dust in high-z galaxies: origin and implications". In: 497.1, pp. 956–968. DOI: 10.1093/mnras/staa1959. arXiv: 2004.09528 [astro-ph.GA].

Triani, Dian P. et al. (Apr. 2020). "The origin of dust in galaxies across cosmic time". In: 493.2, pp. 2490–2505. DOI: 10.1093/mnras/staa446. arXiv: 2002.05343 [astro-ph.GA].

Bouwens, R. J. et al. (Aug. 2021). "New Determinations of the UV Luminosity Functions from z 9 to 2 Show a Remarkable Consistency with Halo Growth and a Constant Star Formation Efficiency". In: 162.2, 47, p. 47. DOI: 10.3847/1538-3881/abf83e. arXiv: 2102.07775 [astro-ph.GA].

Katsianis, Antonios et al. (Oct. 2021). "The Observed Cosmic Star Formation Rate Density Has an Evolution that Resembles a Γ(a, bt) Distribution and Can Be Described Successfully by Only Two Parameters". In: 919.2, 88, p. 88. DOI: 10.3847/1538-4357/ac11f2. arXiv: 2107.02733 [astro-ph.GA].

Khusanova, Y. et al. (May 2021). "The ALPINE-ALMA [CII] survey. Obscured star formation rate density and main sequence of star-forming galaxies at z > 4". In: 649, A152, A152. DOI: 10.1051/0004-6361/202038944. arXiv: 2007.08384 [astro-ph.GA].

Pozzi, F. et al. (Sept. 2021). "The ALPINE-ALMA [CII] survey. Dust mass budget in the early Universe". In: 653, A84, A84. DOI: 10.1051/0004-6361/202040258. arXiv: 2105.14789 [astro-ph.GA].

Symeonidis, M. and M. J. Page (May 2021). "AGN and star formation across cosmic time". In: 503.3, pp. 3992–4007. DOI: 10.1093/mnras/stab598. arXiv: 2102.11936 [astro-ph.GA].

Talia, Margherita et al. (Mar. 2021). "Illuminating the Dark Side of Cosmic Star Formation Two Billion Years after the Big Bang". In: 909.1, 23, p. 23. DOI: 10.3847/1538-4357/abd6e3. arXiv: 2011.03051 [astro-ph.CO].

Zavala, J. A. et al. (Mar. 2021a). "The Evolution of the IR Luminosity Function and Dust-obscured Star Formation over the Past 13 Billion Years". In: 909.2, 165, p. 165. DOI: 10.3847/1538-4357/abdb27. arXiv: 2101.04734 [astro-ph.GA].

— (Mar. 2021b). "The Evolution of the IR Luminosity Function and Dust-obscured Star Formation over the Past 13 Billion Years". In: 909.2, 165, p. 165. DOI: 10.3847/1538-4357/abdb27. arXiv: 2101.04734 [astro-ph.GA].

Algera, Hiddo et al. (Aug. 2022). "The ALMA REBELS Survey: The Dust-obscured Cosmic Star Formation Rate Density at Redshift 7". In: *arXiv e-prints*, arXiv:2208.08243, arXiv:2208.08243. arXiv: 2208.08243 [astro-ph.GA].

Bouwens, R. J. et al. (Nov. 2022). "z 2-9 Galaxies Magnified by the Hubble Frontier Field Clusters. II. Luminosity Functions and Constraints on a Faint-end Turnover". In: 940.1, 55, p. 55. DOI: 10.3847/1538-4357/ac86d1. arXiv: 2205.11526 [astro-ph.GA].

Casey, Caitlin M. et al. (Nov. 2022). "COSMOS-Web: An Overview of the JWST Cosmic Origins Survey". In: *arXiv e-prints*, arXiv:2211.07865, arXiv:2211.07865. DOI: 10.48550/arXiv.2211.07865. arXiv: 2211.07865 [astro-ph.GA].

Enia, Andrea et al. (Mar. 2022). "A New Estimate of the Cosmic Star Formation Density from a Radio-selected Sample, and the Contribution of H-dark Galaxies at $z \geq 3$". In: 927.2, 204, p. 204. DOI: 10.3847/1538-4357/ac51ca. arXiv: 2202.00019 [astro-ph.CO].

Gilli, R. et al. (Oct. 2022). "Supermassive black holes at high redshift are expected to be obscured by their massive host galaxies' interstellar medium". In: 666, A17, A17. DOI: 10.1051/0004-6361/202243708. arXiv: 2206.03508 [astro-ph.GA].

Gómez-Guijarro, C. et al. (Feb. 2022). "GOODS-ALMA 2.0: Source catalog, number counts, and prevailing compact sizes in 1.1 mm galaxies". In: 658, A43, A43. DOI: 10.1051/0004-6361/202141615. arXiv: 2106.13246 [astro-ph.GA].

Parente, Massimiliano et al. (Sept. 2022). "Dust evolution with MUPPI in cosmological volumes". In: 515.2, pp. 2053–2071. DOI: 10.1093/mnras/stac1913. arXiv: 2204.11884 [astro-ph.GA].

Wang, Tsan-Ming et al. (Apr. 2022). "A^{3}COSMOS: A census on the molecular gas mass and extent of main-sequence galaxies across cosmic time". In: 660, A142, A142. DOI: 10.1051/0004-6361/202142299. arXiv: 2201.12070 [astro-ph.GA].

Weaver, J. R. et al. (Jan. 2022). "COSMOS2020: A Panchromatic View of the Universe to z 10 from Two Complementary Catalogs". In: 258.1, 11, p. 11. DOI: 10.3847/1538-4365/ac3078. arXiv: 2110.13923 [astro-ph.GA].

Behiri, Meriem et al. (Aug. 2023). "Illuminating the Dark Side of Cosmic Star Formation II. A second date with RS-NIRdark galaxies in COSMOS". In: *arXiv e-prints*, arXiv:2309.00050, arXiv:2309.00050. DOI: 10.48550/arXiv.2309.00050. arXiv: 2309.00050 [astro-ph.GA].

Bing, L. et al. (Sept. 2023). "NIKA2 Cosmological Legacy Survey. Survey description and galaxy number counts". In: 677, A66, A66. DOI: 10.1051/0004-6361/202346579. arXiv: 2305.07054 [astro-ph.GA].

Gkogkou, A. et al. (Feb. 2023). "CONCERTO: Simulating the CO, [CII], and [CI] line emission of galaxies in a 117 deg^2 field and the impact of field-to-field variance". In: 670,

A16, A16. DOI: 10.1051/0004-6361/202245151. arXiv: 2212.02235 [astro-ph.CO].

Harikane, Yuichi et al. (Apr. 2023). "Pure Spectroscopic Constraints on UV Luminosity Functions and Cosmic Star Formation History From 25 Galaxies at $z_{\rm spec} = 8.61 - 13.20$ Confirmed with JWST/NIRSpec". In: *arXiv e-prints*, arXiv:2304.06658, arXiv:2304.06658. DOI: 10.48550/arXiv.2304.06658. arXiv: 2304.06658 [astro-ph.GA].

Moneti, A. et al. (Jan. 2023). "VizieR Online Data Catalog: The fourth UltraVISTA data release (DR4) (Moneti+, 2019)". In: *VizieR Online Data Catalog*, II/373, pp. II/373.

Parente, Massimiliano et al. (June 2023a). "The z 1 drop of cosmic dust abundance in a semi-analytic framework". In: 521.4, pp. 6105–6123. DOI: 10.1093/mnras/stad907. arXiv: 2302.03058 [astro-ph.GA].

— (June 2023b). "The z 1 drop of cosmic dust abundance in a semi-analytic framework". In: 521.4, pp. 6105–6123. DOI: 10.1093/mnras/stad907. arXiv: 2302.03058 [astro-ph.GA].

Yang, G. et al. (June 2023). "CEERS Key Paper. VI. JWST/MIRI Uncovers a Large Population of Obscured AGN at High Redshifts". In: 950.1, L5, p. L5. DOI: 10.3847/2041-8213/acd639. arXiv: 2303.11736 [astro-ph.GA].

Adscheid, Sylvia et al. (Mar. 2024). "A3COSMOS & A3GOODSS: Continuum Source Catalogues and Multi-band Number Counts". In: *arXiv e-prints*, arXiv:2403.03125, arXiv:2403.03125. DOI: 10.48550/arXiv.2403.03125. arXiv: 2403.03125 [astro-ph.GA].

Eales, Stephen and Bradley Ward (Apr. 2024). "The rise and fall of dust in the Universe". In: 529.2, pp. 1130–1137. DOI: 10.1093/mnras/stae403. arXiv: 2402.05181 [astro-ph.GA].

Mountrichas, G. et al. (Mar. 2024). "Comparative analysis of the SFR of AGN and non-AGN galaxies, as a function of stellar mass, AGN power, cosmic time, and obscuration". In: 683, A143, A143. DOI: 10.1051/0004-6361/202348952. arXiv: 2401.08760 [astro-ph.GA].

Pouliasis, E. et al. (Jan. 2024). "AGN X-ray luminosity function and absorption function in the Early Universe ($3 \leq z \leq 6$)". In: *arXiv e-prints*, arXiv:2401.13515, arXiv:2401.13515. DOI: 10.48550/arXiv.2401.13515. arXiv: 2401.13515 [astro-ph.GA].

Traina, A. et al. (2024). "A3COSMOS: The infrared luminosity function and dust-obscured star formation rate density at 0.5 < z < 6". In: *AA* 681, A118. DOI: 10.1051/0004-6361/202347048. URL: https://doi.org/10.1051/0004-6361/202347048.

Yates, Robert M. et al. (Jan. 2024). "The impact of binary stars on the dust and metal evolution of galaxies". In: 527.3, pp. 6292–6311. DOI: 10.1093/mnras/stad3419. arXiv: 2310.15218 [astro-ph.GA].